Le contrôle de réactivité d'aluminium en peinture anti-corrosion résistant à la haute température

Maria Serdechnova

**THESE DE DOCTORAT DE
L'UNIVERSITE PIERRE ET MARIE CURIE**

Spécialité

Chimie Physique et Chimie Analytique

Présentée par

Maria SERDECHNOVA

Pour obtenir le grade de

DOCTEUR de l'UNIVERSITÉ PIERRE ET MARIE CURIE

Sujet de la thèse :

Le contrôle de réactivité d'aluminium en peinture anticorrosion résistant à la haute température

soutenue le 20 juillet 2012

devant le jury composé de : (préciser la qualité de chacun des membres).

|		
M. K. OGLE	Professeur à ChimieParistech	Directeur de thèse
M. R. OLTRA	Directeur de recherche au CNRS	Rapporteur
Mme. M. RYAN	Professeur à l'Imperial College	Rapporteur
Mme. P. VOLOVITCH	Maître de conférence ChimieParistech	Examinateur
M. M. CASSIR	Professeur à ChimieParisTech	Examinateur
M. F. BRISSET	Ingénieur à L'Université Paris Sud	Examinateur
M. S. FRANGER	Maître de conférence L'Université Paris Sud	Examinateur
M. V. VIVIER	Directeur de recherche au CNRS	Examinateur
M. P. MARCUS	Directeur de recherche au CNRS	Invité

The control of Al reactivity for high temperature anticorrosion paint formulation

Sacrificial coatings containing metallic Al pigments and water soluble chromate inhibitors are widely used in aeronautic industry for high temperature applications. In the near future, however, they should be replaced because of Cr(VI) toxicity.

The aim of this work is to understand the fundamental Al reactivity in complex system and to use this knowledge for the development of new Cr(VI)-free protective paints.

The AESEC technique is used to isolate the individual phenomena during the corrosion processes. Pure 99.99% Al, Al intermetallics and alloys are studied to understand the Al behavior. The linear relationship between cathodic electrochemical current and Al dissolution rate is demonstrated and interpreted in terms of a simple model in which hydroxide generation, $Al(OH)_3$ formation/dissolution, and $Al(OH)_4^-$ diffusion are kinetically coupled.

For the first generation of studied paints, a significant dissolution of the siloxane binder is measured under cathodic polarization, while the Al cathodic reactivity is suppressed. Similar behavior was observed for Al-Mg intermetallics. In terms of cathodically generated hydroxide mechanism it was interpreted as the reaction of the second component of the system with generated OH^-:

either $\qquad (RO\text{-})_4Si \xrightarrow{OH^-} H_4SiO_4$

or $\qquad Mg^{2+} + 2OH^- \rightarrow Mg(OH)_2$
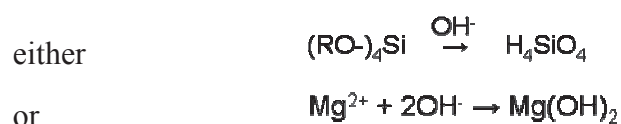
These results confirm the model of cathodic Al reactivity and were used to modify the coated system in order to activate Al.

The loss of anodic activity is explained by the loss of electrical contact at the metal/oxide/polymer/substrate interfaces. The research was focused on the modification of the oxide layer. It was found that Mg^{2+} ions retard Al passivation, due to the formation of a semiconducting spinel responsible for the improvement of conductivity.

Finally, two major factors are found to be critical for the control of Al reactivity: solution pH and oxide properties. Using additives to control these factors, the new coating formulation was proposed, stable up to 550 °C and protective more than 1000 H of salt spray test.

Content

Résumé

L'histoire de cette thèse (projet PHIACRE)

L'aluminium et ses alliages sont largement utilisés dans des nombreuses applications comme l'aéronautique, les réacteurs nucléaires, les traitements de surfaces, etc. Une des applications est la protection sacrificielle d'acier par des peintures contenant des pigments d'Al.

Ce projet de thèse a été lancé dans le cadre du projet PHIACRE (Peintures Hautes températures à Inhibiteurs Anti-Corrosion Respectueuses De l'Environnement). Le rôle de ce projet pour l'industrie aéronautique française est la formulation des peintures protectrices avec les nouvelles exigences spécifiques qui sont appropriées pour les normes environnementales modernes. Ces peintures peuvent être appliquées pour: (1) les parties de compresseurs et turbines, (2) les boîtiers en acier et les diffuseurs, (3) les composants de châssis, (4) les interfaces cellule / moteur.

Le cahier des charges pour le produit à développer est très spécifique: la nouvelle formulation doit être stable jusqu'à 550°C (d'où la raison du choix d'un liant inorganique), l'application doit se faire par "spray", la peinture doit être respectueuse d'environnement (remplacement du Cr(VI) en respectant la directive de REACH – Le Règlement sur l'enregistrement, l'évaluation, l'autorisation et les restrictions des substances chimiques –du 01.06.2007), etc.

L'objectif de ce travail est de comprendre les mécanismes fondamentaux de contrôle de la réactivité de particules d'Al dans une formulation de peinture très complexe et de développer une méthodologie "intelligente" de formulation de nouveaux revêtements résistants à haute température.

Evolution de la thèse

Ce manuscrit représente les principales étapes de l'évolution de l'étude. Dans le **chapitre 1** l'historique du projet et le contenu du sont présentés. L'état de l'art concernant différents mécanismes de protection par les revêtements est revu dans le **chapitre 2**. Les mécanismes de corrosion d'Al sont présentés au **chapitre 3**. Le **chapitre 4** explique les détails de la méthodologie du montage de spectroscopie d'émission atomique couplé à un plasma inductif avec une cellule électrochimique - spectroélectrochimie d'émission atomique (AESEC). Les **chapitres 5 à 9** présentent les résultats scientifiques de ces travaux et les discussions.

Les premiers essais de ce projet ont porté sur les revêtements avec les pigments de zinc dans un liant à la base de siloxane organique. Ces peintures offrent une protection galvanique à l'acier, ce qui était confirmé par les expériences électrochimiques et les essais au brouillard salin. Toutefois, le point de fusion du Zn (419 °C) rendait impossible l'utilisation des revêtements pour l'application choisie (chauffage jusqu'à 550 °C).

Pour éviter le problème de la décomposition thermique, les pigments de Zn ont été remplacés par des pigments d'Al dans le même liant avec une taille moyenne analogue des particules. Comme prévu, le comportement corrosif du système en fut changé. La protection galvanique a été perdue (**figure 1**), la formation de rouille rouge lors du test en brouillard salin a été accélérée considérablement ; et le revêtement a été rapidement détruit lors des expériences électrochimiques de polarisations cathodique et anodique.
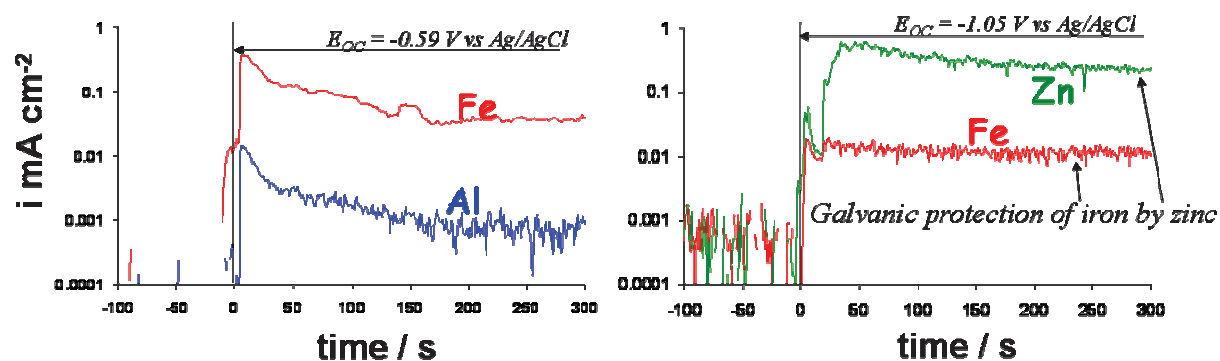
Figure 1. La corrosion spontanée des systèmes avec les peintures contenant les pigments d'Al (gauche) et de Zn (droite) dans un liant organique.

Ce changement majeur dans le comportement peut être liée à un grand nombre de phénomènes simultanés de dégradation qui contribuent à la corrosion atmosphérique des peintures. La **figure 2** illustre les phénomènes de dégradation majeurs, examinés dans cette thèse: (1) la dissolution des particules de métal sacrificielles, (2) la dissolution du liant (en présence d'hydroxyde, qui est cathodiquement généré), (3) la dissolution des additifs minéraux, qui sont solubles dans l'eau, (4) le détachement de particules métalliques individuelles et enfin (5) de la corrosion du substrat d'acier. Dans ce travail, la méthode AESEC a été proposée pour identifier et quantifier ces phénomènes (**chapitre 5**).
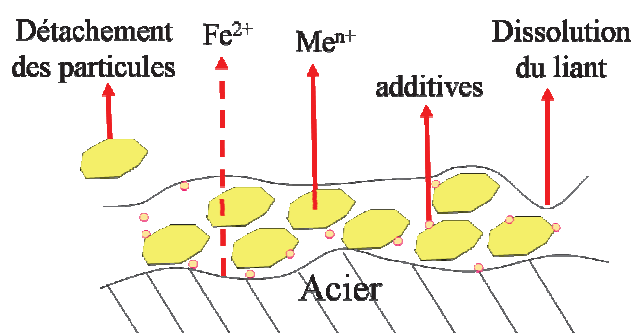
Figure 2. La présentation schématique de touts les phénomènes différents pendant la dégradation de la peinture.

Pour comprendre les mécanismes fondamentaux de la réactivité des particules de l'Al, l'Al pur (99,99%), ces intermétalliques et ces alliages ont été étudiés. Une particularité de l'Al est qu'il corrode seul la polarisation cathodique (**figure 3**) à cause de l'alcalinisation de surface par les réactions cathodiques. Ceci est important pour le couplage galvanique dans les peintures parce que les particules anodiques et le substrat cathodique sont à proximité. Le comportement cathodique de ces systèmes et les mécanismes fondamentaux de réactivité cathodique de l'Al ont été étudiés et quantifiés dans l'article "La dissolution cathodique d'Al, Al_2Cu et les alliages de l'Al» (**chapitre 6**).
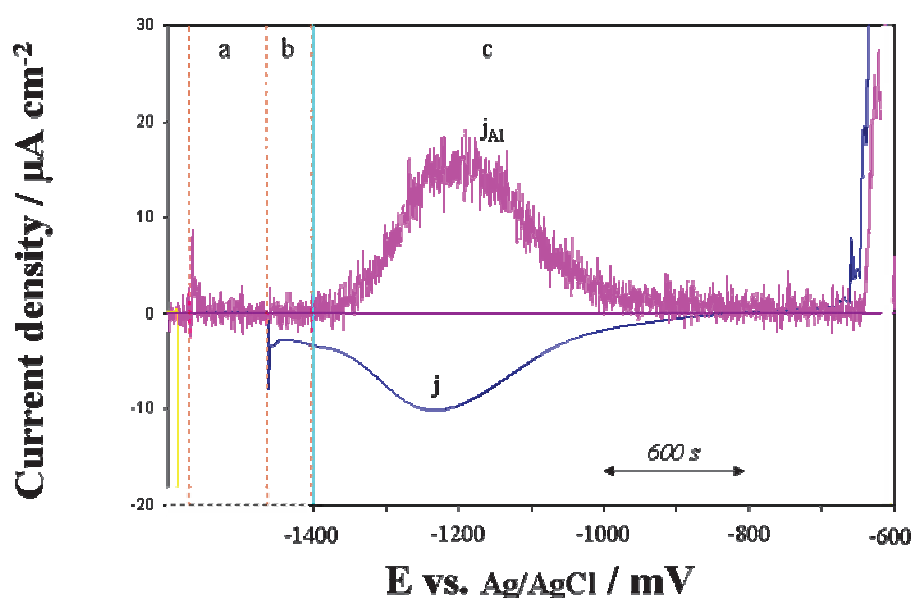
Figure 3. La réactivité (courant electrochimique, j, et dissolution d'Al, j_{Al}) en 3% NaCl (pH 6.1) : (a) – la réaction spontanée, (b) – potentielle appliquée (-1.4 V), (c) – courbe de polarisation cathodique.

Le rôle des éléments d'alliage pour la réactivité cathodique est présenté dans l'article "La dissolution cathodique de l'alliage AA6061 de l'aluminium" (**chapitre 7**). Dans ces deux articles, il a été montré que les phases d'alliage nobles (comme le Cu ou l'$Al_xFe_yMn_{1-y}Si$, par exemple) ne changent pas la stoechiométrie de la réaction entre l'Al et les hydroxydes, qui sont cathodiquement générés ; ils ont juste augmenté le courant total de la réaction et par conséquent la dissolution de l'Al grâce à l'augmentation de la surface de la cathode locale. Pour les additifs actifs d'alliage (comme le Mg ou le Si, par exemple), il a été montré qu'ils réagissent aussi avec des hydroxydes formés à la cathode, et ce processus augmente la stoechiométrie de la réaction de dissolution d'Al en comparaison avec la dissolution de l'Al 99,99%. Cette découverte a été utilisée pour comprendre de la diminution de la réactivité cathodique des pigments d'Al dans le liant de siloxane organique.

Le rôle des ions inorganiques pour la réactivité anodique et cathodique de l'Al est étudié au **chapitre 8**. Avec la mesure AESEC on a démontré que les ions Mg^{2+} retardent la formation d'oxyde passif sur l'Al pendant la réaction spontanée (**figure 4**) et modifient la couche d'oxyde sous un potentiel anodique.
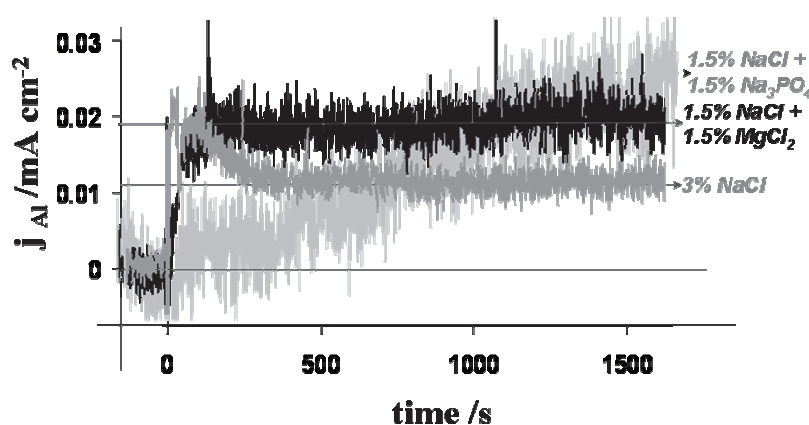
Figure 4. La vitesse de dissolution d'Al en presence de PO_4^{2-} et Mg^{2+} en solution (pH 9.4).

Ce mécanisme a été confirmé par des expériences de titration, des caractérisations en diffraction des rayons X, au MEB ainsi que par des mesures de conductivité. Nous avons interprété ces résultats comme la formation rapide d'un spinelle semi-conducteur qui est responsable de la diminution de la résistivité dans la couche d'oxyde. Ce concept de modification de couche d'oxyde de l'Al par les additifs a été transposé des échantillons massifs aux peintures dans le **chapitre 9**. La perte d'activité anodique a été expliquée par la perte de contact électrique au niveau des interfaces métal/oxyde/polymère/substrat et a été

attribuée à la résistance de l'Al$_2$O$_3$ et du liant siloxane. Les additifs inorganiques dans la formulation de peinture ont été utilisés pour modifier la conductivité de couche d'oxyde. Finalement, deux facteurs principaux sont jugés essentiels pour la réactivité d'Al: le pH de la solution et la conductivité de l'oxyde.

La compréhension des mécanismes de la réactivité de l'Al et du rôle des différents additifs nous a permis enfin de proposer une formulation de revêtement avec deux protections effectives : la protection barrière et la protection galvanique. Ces peintures peuvent finalement être utilisées par les partenaires industriels. Un brevet est actuellement en cours.

Conclusions

En **conclusion** de cette thèse, une nouvelle méthodologie a été développée pour la détection rapide de la dégradation des peintures sacrificielles, ce qui permet la compréhension des mécanismes de corrosion. La méthode AESEC nous permet de distinguer et de quantifier les phénomènes de dégradation élémentaires comme la dissolution des pigments métalliques, le détachement des particules de pigments sacrificiels, la dissolution du liant siloxane et la corrosion du substrat d'acier pour un système modèle résistant de haute température. La protection galvanique et la protection barrière du substrat par la peinture peuvent être distinguées par l'AESEC.

- Les principaux facteurs, qui contrôlent la réactivité des particules d'Al dans les pigments ont été déterminés:

    1. La dissolution cathodique de l'Al a été observée pour tous les systèmes et a été interprétée avec d'un modèle simple dans lequel la génération d'hydroxyde, la formation/dissolution de Al(OH)$_3$ et la diffusion de Al(OH)$_4^-$ sont cinétiquement couplées.
    2. Le rôle des additifs nobles (comme Cu ou Al$_x$Fe$_y$Mn$_{1-y}$Si) pour la dissolution de l'Al a été expliqué par les cathodes locales qui accélèrent la vitesse de dissolution de l'Al.
    3. Les additifs actifs comme du Mg ou du Si diminuent la dissolution cathodique de l'Al en raison des réactions compétitives avec des hydroxydes cathodiquement générés dans ce domaine fortement cathodique.

- La méthodologie d'AESEC a été développée pour la mesure de vitesse du détachement des particules:

  1. Le détachement de particules de l'Al pendant la polarisation a été observé par l'ICP et a été confirmé par le MEB. Il a été montré, que la technique de l'ICP ne détecte pas des particules qui ont un diamètre supérieur à 7 µm dans ces conditions opératoires (nébuliseur Meinhard K3, 3 ml/min de débit, etc.).

  2. L'étalonnage pour la distribution des particules avec la taille moyenne différente (3,2, 13,1 et 38,4 µm) a été réalisé et utilisé pour la quantification des particules détachées.

- L'utilisation de la nouvelle méthodologie pour les systèmes en acier avec peinture a montré que:

  1. La protection galvanique n'était pas observée au cours de la polarisation anodique des pigments de l'Al dans le liant du siloxane organique. Ces résultats peuvent être interprétés comme la présence de la couche d'oxyde d'Al passif à la surface des particules.

  2. La présence des ions de Mg^{2+} retarde la formation de la couche d'Al_2O_3; ce résultat a été attribué à la formation d'un spinelle semi-conducteur, responsable de l'augmentation de la conductivité dans la peinture.

  3. L'addition de $MgHPO_4$ ou d'une base de Lewis (pour l'augmentation de pH) dans la formulation de peinture augmente l'effet de couplage galvanique probablement en réduisant la résistance de l'oxyde par la modification de sa structure.

- La connaissance fondamentale de la réactivité du Zn et de l'Al a été appliquée pour la proposition de la formulation de peinture, qui s'est avérée stable jusqu'à 550 ° C et qui a résisté plus de 1000h au test de brouillard salin.

  1. Un modèle simple décrivant l'interruption de contact entre particules actives et l'acier a été proposé grâce à la comparaison de la protection galvanique de substrat par de pigments de l'Al et du Zn.

  2. La protection barrière de l'acier par la peinture avec des pigments métalliques actifs a été distinguée et améliorée par la modification de la distribution de la taille des particules.

Chapter I

Introduction

1. Introduction

1.1. The origin of the PhD study (project PHIACRE)

Al and its alloys are widely used in many engineering applications and scientific technologies, such as aerospace, advanced nuclear reactor, surface coating, metal/air batteries, etc. One of the applications is sacrificial coatings for steel containing sacrificial Al pigments.

This PhD project was started in the context of the PHIACRE (Peintures Hautes températures à Inhibiteurs Anti-Corrosion Respectueuses de l' Environnement) project. The role of this project for the French aeronautic industry is to make protective coatings with new specific applicable requirements and appropriate for the modern environmental standards. These coatings can be applied for: (1) the compressor parts and turbines, (2) the steel housing and diffusers, (3) the chassis components, (4) the interfaces airframe/motor.

The requirements for the developed product are specific: it should be stable up to 550 °C (that is why an inorganic binder is used for coating formulation), should be deposited by spray, should be environmentally-friendly (Cr(VI) should be excluded, the directive of REACH – Le Règlement sur l'enregistrement, l'évaluation, l'autorisation et les restrictions des substances chimiques – from 01.06.2007), etc.

The objective of this PhD work is to understand at a fundamental level how to control the Al particle reactivity in the complex paint formulation for the intelligent design of new high temperature protective coatings.

1.2. The evolution of this PhD research

In this manuscript the evolution of the PhD research is presented. In **chapter 1** (this chapter) short information about the history of the PHIACRE project and an overview of the PhD research is presented. In **Chapters 2 and 3** information about general protection with coatings and mechanisms of Al corrosion, respectively, are accumulated and analyzed. **Chapter 4** explains the details of the main technique used during this PhD research – atomic emission spectroelectrochemical (AESEC) technique. **Chapters 5 – 9** present the scientific results of this work and their discussion.

First attempts of this project were focused on zinc pigment containing coatings in an organic siloxane binder. These coatings provide galvanic protection to the steel, as confirmed by electrochemical and salt spray tests. However, the Zn melting point (419 °C) makes it impossible to use these coatings for the chosen application (heating up to 550 °C).

To avoid the problem of thermal decomposition, Zn pigments were replaced by Al pigments in the same binder with a similar average particle size. As expected, the corrosion behavior of the system changed. Galvanic protection was lost, red rust formation in SST dramatically accelerated and the coating was quickly destroyed in electrochemical experiments under both cathodic and anodic polarization.

So dramatic a change in the corrosion behavior can be related to a large number of simultaneous degradation phenomena that contribute to the atmospheric corrosion of the coatings (figure 1.1). **Figure 1.1** illustrates the major degradation phenomena, discussed in this dissertation: (1) the dissolution rate of sacrificial metal particles, (2) the dissolution of the binder especially in the presence of cathodically generated hydroxide, (3) the leaching of various water soluble inorganic pigments, (4) the detachment of individual metallic particles and finally (5) the corrosion of the steel substrate. In this work the AESEC method is proposed to identify and to quantify all these simultaneous phenomena (**Chapter 5**).
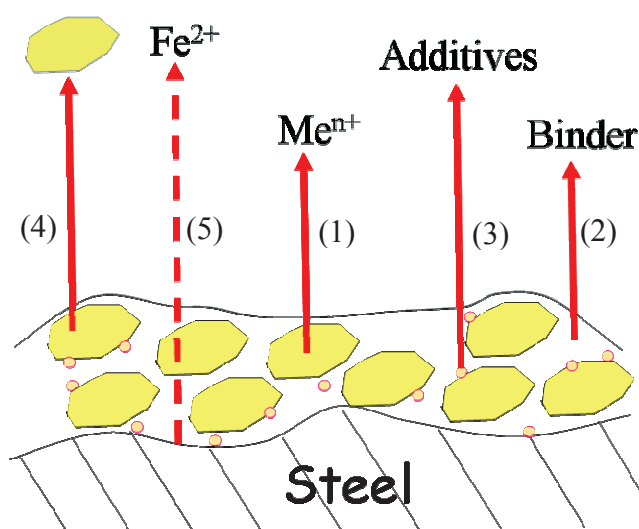
Figure 1.1. The schematic presentation of different phenomena during the coating degradation.

To understand the fundamental mechanisms of Al particle reactivity, pure 99.99% Al, Al intermetallics and alloys are studied. One of the curious phenomena associated with Al is that corrosion actually increases during a cathodic polarization due to hydroxide formation. This is important for galvanic coupling in paints since the anodic particles and cathodic substrate are in close proximity. The cathodic behavior of these systems and the fundamental mechanisms of Al cathodic reactivity are investigated in the article "The cathodic dissolution of Al, Al_2Cu, and Al alloys" (**Chapter 6**).

The role of alloying elements on cathodic reactivity is presented in the article "The cathodic dissolution of the AA6061 aluminum alloy" (**Chapter 7**). In these two works it was shown that noble alloying phases (like Cu or $Al_xFe_yMn_{1-y}Si$, for example) do not change the stoichiometry of the reaction between Al and cathodically generated hydroxides; they just increase the total current of the reaction and consequent Al dissolution due to the increase of the local cathode area. For the active alloying additives (like Mg or Si, for example) it was shown that they also react with cathodically formed hydroxides. This knowledge was useful for understanding the decrease of cathodic reactivity of Al pigment in the siloxane binder.

The role of inorganic ions for the anodic and cathodic Al reactivity is studied in **Chapter 8**. The AESEC measurement demonstrated that Mg^{2+} ions retard passive oxide formation on Al during spontaneous reaction and modify the oxide layer under anodic potential. This mechanism is confirmed by titration, XRD, SEM and conductivity measurements. We interpreted these results as due to the rapid formation of a semiconducting spinel which is responsible for the resistivity decrease in the oxide layer. This concept of *in-situ* Al oxide layer modification due to the additives in formulation was transposed from massive samples to the coatings in **Chapter 9**. The loss of the galvanic protection by the paint system without additives is related to the low conductivity of the metal/oxide/polymer/substrate interface and was attributed to the resistance of Al_2O_3 and the siloxane binder. Inorganic additives in paint formulation were used to modify the oxide layer conductivity. Two mechanisms were identified: (1) changing the pH of the local environment surrounding the particle or (2) by incorporating the inorganic ions directly into the oxide crystalline structure.

The understanding of the mechanism of Al reactivity and the role of different additives allowed us finally to propose a coating formulation with both effective barrier and galvanic protection types, which may ultimately be used by industrial partners. A patent is now being sought.

1.3. List of publications

The present PhD work is a summary of following papers. The author's contribution is also indicated. Such type of dissertation organization allows us to combine the logical parts of the work together and facilitate their reading due to the presence of all important information (like conditions of the experiment and used techniques) in one chapter.

Full-text articles

1. Atomic emission spectroelectrochemistry study of the degradation mechanism of model high-temperature paint containing sacrificial aluminum particles (chapter 5)

M. Serdechnova, P. Volovitch, K. Ogle
Surface & Coatings Technology **206** (2012) 2133–2139;

All experimental work on ICP analysis. Active participation in the SEM analysis, elemental microanalysis and coating formulation. Major part in data evaluation/interpretation and preparation of the manuscript.

2. The cathodic dissolution of Al, Al$_2$Cu, and Al alloys (chapter 6)

K. Ogle, M. Serdechnova, M. Mokaddem, P. Volovitch
Electrochimica Acta **56** (2011) 1711–1718;

Major part of the ICP experiments on the 99.99% Al and Al$_2$Cu intermetallic. Active participation in data evaluation/interpretation and preparation of the manuscript.

3. The cathodic dissolution of the AA6061 aluminum alloy (chapter 7)

M. Serdechnova, P. Volovitch, F. Brisset, K. Ogle
Electrochimica Acta, (submitted in June 2012)

All experimental work on ICP and XRD analysis. Active participation in the SEM analysis and elemental microanalysis. Major part in data evaluation/interpretation and preparation of the manuscript.

4. Aqueous corrosion of Al-Mg binary alloys: role of Al and Mg (chapter 8)

P. Volovitch, <u>M. Serdechnova</u>, K. Ogle
Corrosion **68(6)** (2012) 557-570

All experimental work on ICP, XRD and titration analysis. Active participation in data evaluation/interpretation and preparation of the manuscript.

5. Role of conductivity for sacrificial protection of steel by aluminum and zinc pigments in model high temperature coatings (chapter 9)

<u>M. Serdechnova</u>, P. Volovitch, S. Franger, K. Ogle
Surface & Coatings Technology, (submission in June 2012);

All experimental work on ICP and XRD analysis. Active participation in the SEM analysis, elemental microanalysis and conductivity measurement. Major part in data evaluation/interpretation and preparation of the manuscript.

Reviewed conference proceedings

1. Cathodic dissolution of pure aluminum, aluminum alloy AA6061 and aluminum particle based coating studied by AESEC method

<u>M. Serdechnova</u>, P. Volovitch, K. Ogle
Proceedings of *The XIII^s International conference of aluminum alloys*, Ed. Bob Demmler, Pittsburgh, USA, 03.06.2012-07.06.2012, *Wiley OnLine Library,* 6 p.

All experimental work on ICP and XRD analysis. Active participation in the SEM analysis and elemental microanalysis. Major part in data evaluation/interpretation and preparation of the manuscript.

2. Role of Mg^{2+} and PO$_4^{3-}$ for sacrificial protection of steel by aluminum pigment in model high temperature coatings

M. Serdechnova, P. Volovitch, K. Ogle

Proceedings of *Coating Science International* (COSI-2011), Noordwijk, The Netherlands, 27.06.2011-01.07.2011 *Book of abstract* pp.179-182

All experimental work on ICP analysis. Active participation in the SEM analysis, elemental microanalysis, conductivity measurement and coating formulation. Major part in data evaluation/interpretation and preparation of the manuscript.

Conference participation

1. Role of Mg^{2+} and PO_4^{3-} for sacrificial protection of steel by aluminum pigment in model high temperature coatings
Poster, COSI 2011, Noordwijk, 27.06.2011-01.07.2011
(3rd place in poster competition)

2. The aqueous degradation of model high temperature paint system
Oral presentation, Eurocorr2011, Stockholm, 04.09.2011-08.09.2011

3. Cathodic Dissolution of Pure Aluminum, Aluminum Alloy AA6016 and Aluminum Particle Based Coating Studied by AESEC Method
Oral presentation, ICAA13, Pittsburgh, 03.06.2012-07.06.2012

Chapter II

Basics of the protection by coatings

2. Basics of the protection by coatings

2.1. Typical structure and protection mechanisms

For protective, decorative or any specific technical aims, coatings can be applied on the surface to form a film. Coatings may contain numerous layers and pre-treatment steps [1, 2] depending on their applications. **Figure 2.1** shows an example of a cross section view for an idealized coated steel product. Three different types of coating material may be applied to steel:

1. Metallic coating – this may be both active and noble alloys. Al and Zn based alloys provide galvanic protection for the steel substrate while Sn alloys are essentially barrier films. Sometimes galvanized steel and Sn coated steel are used without further protection.

2. Conversion coating – an oxide film that offers some barrier protection and promotes adhesion of the polymer film. Sometimes conversion coatings are used as a final treatment for corrosion resistance however usually it is used in combination with a polymer film.

3. Polymer film – this could be a colorless transparent varnish film or a thick paint layer in the automotive or aeronautic industry. During this PhD research the polymeric coating, containing sacrificial Al pigments, are the center of the attention. The standard polymeric coating contains [3]:

   - Binder and/or mixture of binders;
   - Pigments (amount of small particles, practically not soluble in the binder, which change the properties of the coating);
   - Fillers;
   - Solvent;
   - Diluent;
   - Additives.
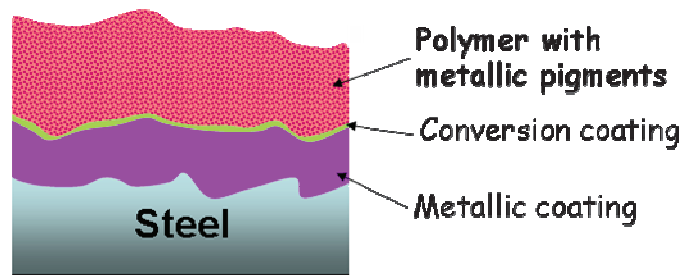
Figure 2.1 Schematic diagram of coated steel in cross sectional view. Small circles in the polymer film represent particles of pigments (not to scale).

Each component in the polymer coating formulation may serve different purposes. The active metallic pigments can be used for the sacrificial protection of the substrate as well as for other properties (metallic shine, weldability, etc.). The binder and fillers (they can be both organic and inorganic, according to the specific requirements for the surface formulation) provide the barrier layer and they hold the metallic pigments together and on the surface. Solvents and diluents facilitate the application of the coatings and their preparation.

Corrosion protection is generally achieved by one or by a combination of three mechanisms [4]:

a) The barrier protection by the paint, which limits the transport of water and aggressive species to the metallic surfaces;

b) The sacrificial protection by active metal which present as a metal coating or as a pigment;

c) The protection by inhibitors (additives) which are released during the contact of the coating with the environment.
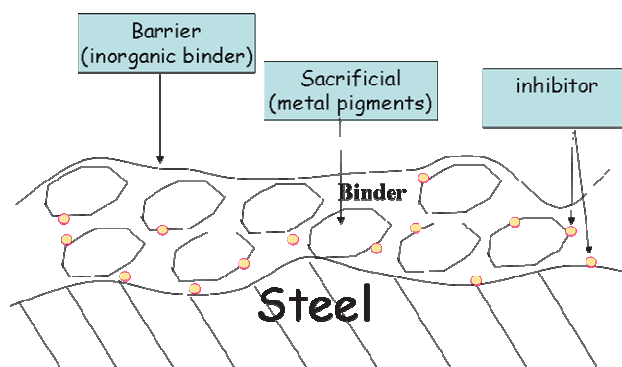
Figure 2.2. Three types of the protection of the steel substrate.

The barrier protection is not sufficient in the presence of defects and on cut-edges, but it still can modify the active coating reactivity. Protective properties may be improved by galvanic protection or the use of inhibitors.

The specific function of a selected component in a protection mechanism is not always clear. Some of them may be also multifunctional. As a result it is difficult to replace one component without affecting the whole protection mechanism and hence the durability of the system.

The elimination of the chromate treatment of the metal surfaces due to the chromium VI toxicity [5] has spurred the investigation of new methods for steel surface protection [6]. In the next section we will review the basic approaches for each protective mechanism separately.

2.1.1. Barrier protection

Barrier protection is typically offered by paints and, for complex systems, is related to the stability of the binder. The barrier coatings are used to suppress the corrosion reaction by limiting the diffusion of the electrolyte, oxygen and aggressive species like Cl^- to the substrate [6]. It also limits the transport of electrons to the metal interface [7, 8], suppressing the corrosion reactions.

Organic coatings widely used in the industry (like polyaniline or poly(2-iodoaniline)) are able to prevent both the anodic and the cathodic reactions [9, 10].

As alternative to organic barrier protective coatings, the inorganic high temperature paints with a silane base [11] were proposed by Air Force Research Laboratory [12]. They have formed the functionalized silica nanoparticles in-situ from hydrolyzed tetramethoxysilane and glycidoxypropyltrimethoxysilane in an aqueous sol-gel process, and then cross-linked these nanoparticles to form a thin, full dense, protective film on Al aerospace alloys. These nanostructured coatings have been shown to provide the good barrier to corrosion [12, 13].

Ceramic coatings are also very attractive [14] because they possess good thermal and electrical properties, and they are more resistant to oxidation, corrosion, erosion and wear than metals in high temperature environments [15].

In the present work, the binders based on siloxanes are used. The siloxanes can react with water. This reaction accelerates under strong acid [16, 17] or strong alkaline [17] conditions according to the reactions 2.1 and 2.2:

$$[2.1]$$

$$[2.2]$$
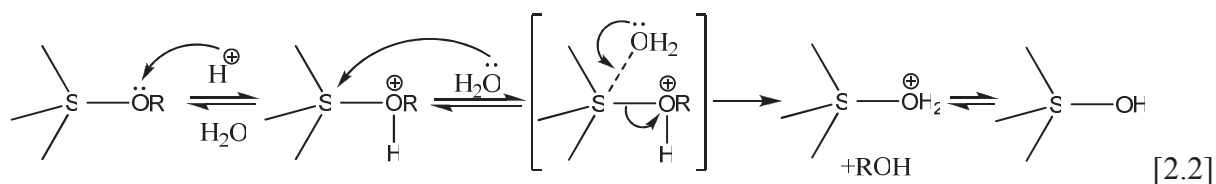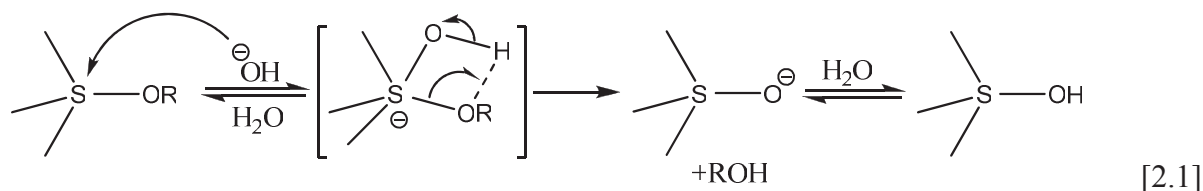
Further hydrolysis leads to the formation of small inorganic compounds (like $SiO_2 \cdot nH_2O$ [17]), which could not keep the metallic pigment together and therefore coating dissolution will be accompanied by pigment release. The hydrolyzed binder could not provide an appropriate barrier protection of the steel substrate and could not combine the active metal particles together for the sacrificial protection.

The barrier protection of the substrate can be effective due to the interruption of diffusion of the electrolyte, oxygen and aggressive species to the surface. The stability of the barrier protective coatings can be pH dependent. The efficiency of the barrier protection decreases with increase of porosity, cracks and other coating defects.

2.1.2. Sacrificial protection

The second type of the protection, particularly important in the presence of defects in the coating, is the sacrificial protection by the active metallic pigments. The sacrificial metallic coatings for corrosion protection must have the following attributes [18]: (1) excellent adhesion, (2) a suitable electrochemical potential relative to the substrate, and (3) formation of suitable corrosion product layer(s) [19]. Even the apparently simplest of them – a suitable electrochemical potential – is not so easy to predict in a continuously evolving environment especially for alloys [20].

The metallic film can have lower or higher potential than the substrate in different environments. The galvanic series cannot be predicted from the standard electromotic force

(EMF) series (See table 2.1). The situation is especially difficult for passivating materials, where the open circuit potential increases with time after a clean surface is exposed to an oxidizing environment due to the passive layer formation.

Table 2.1. Comparison of EMF and galvanic series: inversed order of elements (/ V vs Hg/Hg_2Cl_2) [18]

EMF series		Galvanic series, seawater, 25 °C	
Al^{3+}	-1.91	Zn	-1.03
Zn^{2+}	-1.00	Al	-0.78
Fe^{2+}	-0.68	Fe	-0.61
Ni^{2+}	-0.49	Cu	-0.36
Cu^{2+}	+0.10	Ni	-0.20

The conductivity of the environment can also modify the efficiency of galvanic protection, even if potential difference is sufficient. If the conductivity of the liquid is high (a common example is sea water) the anodic dissolution of the less noble metal will be spread over a larger area. The cathodic reaction of oxygen or water reduction (equation 2.3 and 2.4) [21, 22] appears on the protected metal :

$$2H_2O + O_2 + 4e \rightarrow 4\ OH^- \hspace{4cm} [2.3]$$

$$2H_2O + 2e \rightarrow H_2 + 2OH^- \hspace{4cm} [2.4]$$
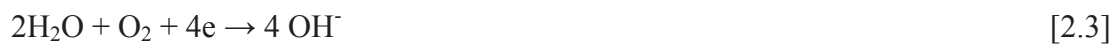
At the same time, in low conductivity liquids the corrosion will be localized to the part of the less noble metal near the junction.

Common examples of metals, used for sacrificial coatings are zinc [23, 24, 25], aluminum [26, 27, 28] magnesium [29, 30, 31, 32] and their alloys. Aluminum particles were chosen as the active metal in the industrial project associated with this work because of their relatively high melting temperature and relatively low price (in comparison with Mg, for example). Thus, the reactivity of aluminum is one of the most important parameters influencing the efficiency of protection.

Sacrificial protection is usually implemented together with a barrier coating, allowing to decrease the consumption of protectors and to increase their life time. The main problems in barrier protection comes from the failure caused during the application procedure,

transportation and operation, including modifications as a result of natural aging (swelling, raising, cracking, exfoliation) [33].

The accumulation of corrosion products in the breaches of the film adding an additional barrier to possible dissolution of the substrate can enhance the barrier protection as it is often discussed for Zn corrosion products [34, 35]. However, very voluminous products can result in stress accumulation and cracking of the paint layer. The formation of insulating layers between substrate and coating can disturb the electrical contact between them and interrupt the galvanic protection.

The presence of water-soluble contaminants at the metal/paint interface is an accelerating factor of the steel substrate corrosion process [36]. The presence of hydro-soluble species (SO_4^{2-} or Cl^-) can result in the formation of Fe^{2+} salts which by hydrolysis in the presence of oxygen contribute to the acidification of the interface and to the continuous degradation of the substrate by reactions 2.5 and 2.6:

$$4FeSO_4 + O_2 + 6H_2O \rightarrow 4FeOOH + 4H_2SO_4 \qquad [2.5]$$

$$H_2SO_4 + Fe + 1/2O_2 \rightarrow FeSO_4 + H_2O \qquad [2.6]$$

The loss of adhesion by an osmotic blistering process and the cathodic decomposition of the paint on the contaminated metallic surface take place. The blisters are first filled with water and later with corrosion products [37].

The corrosion potential during galvanic protection corresponds to the potential of active metal corrosion. Some approaches developed for metallic coatings (both active as Zn [38] or Al [39] and noble as Ni or Ti [40]) can be used for understanding metallic pigment reactivity. In this work we are focused on Al pigment and the reactivity of Al will be reviewed in **chapter 3**. When the galvanic protection is active, the total current between anode and cathode corresponds to the elemental dissolution of the sacrificial metal. If there is any difference between them, it can be attributed to the growth of the oxide film on the surface (see calculation in **chapter 9**) [41] or to the intense cathodic reaction (negative difference effect, NDE) [42].

Active coatings are widely used for steel protection. The efficiency of the protection depends on the environment (pH, ions presence, presence of corrosion products) and can not easily be predicted just from the galvanic series of the respective components.

2.1.3. Inhibitors

The inhibitor changes the kinetics of the dissolution reaction [43]. This will be manifest as a decrease in the dissolution rate and a modification of current-potential diagrams. The inhibitor released from the paint formulation can influence the reactivity of both the steel substrate and the sacrificial metal [6].

For several decades the most used anti-corrosion inhibitor for steel in the presence of halide ions [6, 44] and for Al [45, 46, 47] was CrO_4^{2-}. Its action is still not completely understood but it is generally attributed to the formation of a mono- or polyatomic oxide film on the metal surface, preventing the pitting corrosion (equation 2.5) [48].

$$Cr_2O_7^{2-} + 8H + 6e^+ = 2Cr(OH)_3 + H_2O \qquad [2.7]$$
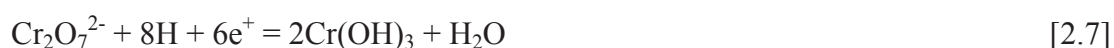
The necessity to exclude chromates from the surface treatment procedure has dramatically affected the aerospace industry due to its dependence on the use of steel and Al based alloys in aircraft manufacturing. In order to replace chromate inhibitors, for the protection of the steel and Al, both organic [49, 50, 51] or inorganic [52, 53] inhibitors were proposed.

Organic inhibitors

The corrosion protection of Al pigments by organic inhibitors is based on the adsorption of the organic molecules on the aluminum surface, preventing the contact of the solvent with aluminum particles [54, 55].

The organic molecules with a molecular weight lower than 200 g/mol do not adsorb on oxidized aluminum surfaces at all, unless they have functional groups such as carboxyl, phenolic hydroxyl, or amino groups that are capable to form complexes with the metallic ions on the surface of oxide [56].

For small aromatic acids the adsorption on Al in aqueous solutions becomes stronger with increasing number of functional groups, such as hydroxyl and carboxyl, in the aromatic ring and influenced by the position of these groups [57]. The inhibitive effect was found to be excellent for 2-amino-phenol while the regioisomer 4-amino-phenol were ineffective as inhibitors for the Al pigments. These results were explained by the fact that 4-aminophenol is not able to form chelate complexes, while 2(ortho-)aminophenol may form chelate complexes [58].
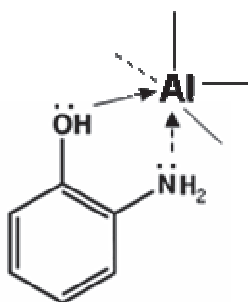
Figure 2.3. The possible structure of chelate structure (2-aminophenol) on the Al surface.

Fatty acids are usually added as a lubricating agent in the milling of Al foil [59]. They form complexes with Al(III) on the oxidized surface and makes it hydrophobic even if the Al_2O_3 surface under the organic layer is hydrophilic. Fatty acids provide some, although not sufficient, protection against aqueous solution. Commonly, stearic acid is used [60, 61].

Low molecular weight aromatic compounds (like salicylate [62], benzoate and phthalate [63]) are frequently used as inhibitors. It was demonstrated [63] that phthalate adsorbed stronger than benzoate, probably as a result of the additional carboxylate group in phthalate. The *ortho-* arrangement of the two carboxylate groups in phthalate should be suitable for formation of strong complexes with Al ions at the surface. The adsorption increased with increasing temperature for both benzoate and phalate, but decreased with pH, most likely due to deprotonation of the surface in alkaline solutions.

Surfactants are also used to protect the Al pigments from reaction with water [64]. They chemically react with surface of metal (or (hydro)oxide on the surface) with formation of protective hydrophobic coating in the internal layer (**figure 2.4**). If amount of the surfactant

compound is appropriate, it forms a second layer around the Al pigment with interaction between hydrophobic tails. As a result, around active metal particles there is a double layer, which protects against contact with an aggressive environment.

REGION I

REGION II

REGION III AND PLATEAU ADSORPTION REGION
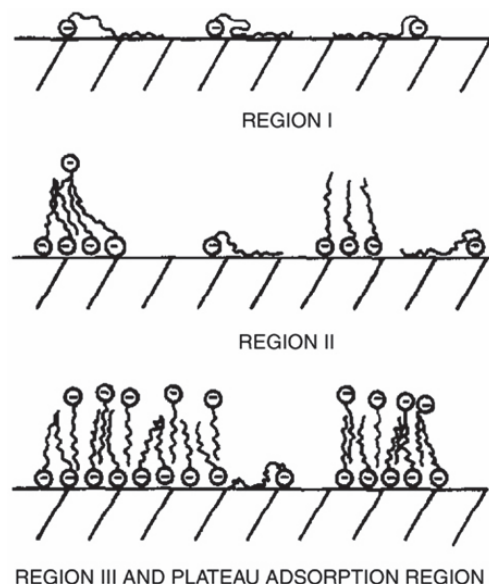
Figure 2.4 An illustration of the interactions of anionic surfactants with an oppositely charged surface in water from [54].

Adsorption increases with the surfactant chain length [65, 66]. The tail–to–tail interactions are usually stronger for linear than for branched tails because the former are able to pack more tightly.

Encapsulation [67] of Al particles by polymerization of monomers on the surface has been used for various purposes. One of application is the inhibition of Al pigment flakes for aqueous formulations allowing the stabilization of Al pigments in organic solvent and decreasing their corrosion in the aqueous media.

Inorganic inhibitors

Organic inhibitors can not be used for high temperature applications. As an alternative, inorganic inhibitors have been proposed for Al pigment [54] including cerium [45, 68, 69, 70] and lanthanum [69] compounds , molybdates [71], vanadates [71, 72], phosphates [73] and silica-based inhibitors [68].

The <u>silicate/cerium treatments</u> are supposed to improve the corrosion resistance forming an oxide layer that acts as a barrier for the oxygen diffusion to the metal surface. For efficient protection of Al by ceria sol-gel coatings, the preliminary surface modification of Al is necessary. The best protective layer was proposed to be formed by boiling of Al sample with 0.01 mol/l $CeCl_3$ in the presence of 0.01 M KOH which resulted in the mixed oxide film containing Al(III) and Ce(IV) oxides [74, 75].

The <u>silica coatings</u> are known as another alternative to chromate-inhibitors [76, 62]. Monomeric silica condenses together with hydrated Al, forming a stable [67], thermoresistant [77] three-dimensional dense film [78 ,79, 80] (equation 2.8).

$$\begin{array}{c}\text{—Al—OH}\\ |\\ \text{O}\\ |\\ \text{—Al—OH}\end{array} + Si(OH)_4 \longrightarrow \begin{array}{c}\text{—Al—O}\\ |\\ \text{O} \quad \text{Si}\\ |\\ \text{—Al—O}\end{array}\begin{array}{c}\text{OH}\\ \\ \text{OH}\end{array} \qquad\qquad [2.8]$$
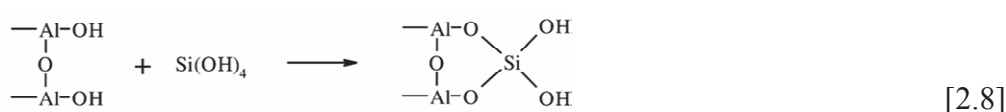
<u>Molybdates,</u> which are used as additives in conversion coatings or primer systems, have been tested extensively as a possible chromate replacement for Al [6]. A specific surface preparation by etching with KOH and oxide growing by heating prior to molybdate treatment was necessary for the efficiency of corrosion protection [71].

The pre-treatment of active metals like Al and Zn [72, 73] with salts of the phosphoric acid in low pH can result in significant decrease of the corrosion rate of the metal because of the insoluble film formation [81]. Hopeite ($Zn_3(PO_4)_2 \cdot 4\ H_2O$) or phosphophyllite ($Zn_2Fe(PO_4)_2 \cdot 4H_2O$) were proposed as one of the first Cr(VI) replacement for Al alloys [73].

The inhibitors control:

a) The corrosion rate of the steel substrate;

b) The reactivity of the components during the formulation of the paint (stability of the mixture);

c) The reactivity of metallic pigments;

The inhibitors simplify the coating application and increase the life time of the obtained system.

2.1.4. Conclusions

The effective corrosion protection can be achieved by a combination of 3 protective mechanisms: galvanic protection by active metal, barrier protection by organic or inorganic polymer (and corrosion products) and protection with inhibitors. The reactivity of all components should be well understood during both coating preparation and coating use.

2.2. References

1. Gabe, D. R. Protective layered electrodeposits. *Electrochimica Acta* **39**, 1115–1121 (1994).

2. Voevodin, A. A., Zabinski, J. S. & Muratore, C. Recent Advances in Hard, Tough, and Low Friction Nanocomposite Coatings. *Tsinghua Science & Technology* **10**, 665–679 (2005).

3. Laout, J.-C. Formulation des peintures - Physico-chimie et matières pulvérulentes | Techniques de l'ingénieur. (2005).at <http://www.techniques-ingenieur.fr/base-documentaire/download/j2270/formulation-des-peintures.html>

4. The Protection of Metal. at <http://www.zrcworldwide.com/t_protect.asp>

5. REACH. *http://europa.eu/rapid/pressReleasesAction.do?reference=MEMO/08/763&format=HTML&aged=0&language=EN&guiLanguage=en* (2008).

6. Twite, R. L. & Bierwagen, G. P. Review of alternatives to chromate for corrosion protection of aluminum aerospace alloys. *Progress in Organic Coatings* **33**, 91–100 (1998).

7. Onal, A. N. & Aksut, A. A. Corrosion inhibition of aluminium alloys by tolyltriazole in chloride solutions. *Anti-Corrosion Methods and Materials* **47**, 339–349 (2000).

8. Aksut, A. A. & Onal, A. N. The effect of some organic compounds on the corrosion of pure Fe, pure Cr and Fe---Cr alloys in acidic solutions. *Corrosion Science* **39**, 761–774 (1997).

9. Bereket, G., Hur, E. & Sahin, Y. Electrodeposition of polyaniline, poly(2-iodoaniline), and poly(aniline-co-2-iodoaniline) on steel surfaces and corrosion protection of steel. *Applied Surface Science* **252**, 1233–1244 (2005).

10. Wei, Y., Wang, J., Jia, X., Yeh, J.-M. & Spellane, P. Polyaniline as corrosion protection coatings on cold rolled steel. *Polymer* **36**, 4535–4537 (1995).

11. Parashar, G., Srivastava, D. & Kumar, P. Ethyl silicate binders for high performance coatings. *Progress in Organic Coatings* **42**, 1–14 (2001).

12. Voevodin, N. N., Kurdziel, J. W. & Mantz, R. Corrosion protection for aerospace aluminum alloys by Modified Self-assembled NAnophase Particle (MSNAP) sol-gel. *Surface and Coatings Technology* **201**, 1080–1084 (2006).

13. Ischenko, V., Harshe, R., Riedel, R. & Woltersdorf, J. Cross-linking of functionalised siloxanes with alumatrane: Reaction mechanisms and kinetics. *Journal of Organometallic Chemistry* **691**, 4086–4091 (2006).

14. Lee, K. N. Current status of environmental barrier coatings for Si-Based ceramics. *Surface and Coatings Technology* **133-134**, 1–7 (2000).

15. Shen, G. X., Chen, Y. C. & Lin, C. J. Corrosion protection of 316 L stainless steel by a TiO2 nanoparticle coating prepared by sol-gel method. *Thin Solid Films* **489**, 130–136 (2005).

16. Cypryk, M. & Apeloig, Y. Mechanism of the Acid-Catalyzed Si-O Bond Cleavage in Siloxanes and Siloxanols. A Theoretical Study. *Organometallics* **21**, 2165–2175 (2002).

17. Grigsby, C. O. *Kinetics of Rock-Water Reactions*. (1989).

18. Nowak, W. B. Thin metallic films for corrosion control. *Surface and Coatings Technology* **49**, 71–77 (1991).

19. Galvanic Corrosion Bimetallic Corrosion. *Corrosionist, The Website of Corrosion Protection and Corrosion Control* at <http://www.corrosionist.com/Galvanic_Corrosion.htm>

20. Munger, C. G. *Corrosion Prevention by Protective Coatings*. (Houston, 1999).

21. S. Szabó & I. Bakos Catalytic aspects of oxygen reduction in metal corrosion. *Corrosion reviews* **26**, 51–71 (2010).

22. Краснов, К. С. Равновесные электродные процессы. *Физическая химия* **2**, 49–93 (2001).

23. Zhang, X. G. & Valeriote, E. M. Galvanic protection of steel and galvanic corrosion of zinc under thin layer electrolytes. *Corrosion Science* **34**, 1957–1972 (1993).

24. Lindqvist, S. A., Meszaros, L. & Svenson, L. Aspects of Galvanic Action of Zinc-Rich Paints Electrochemical Investigation of Eight Commercial Primers. *Journal of the Oil and Colour Chemists' Association* **68**, 10–14 (1985).

25. Pereira, D., Scantlebury, J. D., Ferreira, M. G. S. & Almeida, M. E. The application of electrochemical measurements to the study and behaviour of zinc-rich coatings. *Corrosion Science* **30**, 1135–1147 (1990).

26. Kautek, W. The galvanic corrosion of steel coatings: aluminum in comparison to cadmium and zinc. *Corrosion Science* **28**, 173–199 (1988).

27. Mosser, M. F. Spherical aluminum particles in coatings. *United States Patent 4537632* (1985).

28. Parks, A. R. ALUMINUM SPRAYED COATINGS ON BOARD U.S. NAVY SHIPS A TEN YEAR OVERVIEW. *United States Navy, Naval Sea Systems Command, Washington, DC*

29. Parthiban, G. T. *et al.* Cathodic protection of steel in concrete using magnesium alloy anode. *Corrosion Science* **50**, 3329–3335 (2008).

30. Bierwagen, G., Brown, R., Battocchi, D. & Hayes, S. Active metal-based corrosion protective coating systems for aircraft requiring no-chromate pretreatment. *Progress in Organic Coatings* **67**, 195–208 (2010).

31. NANNA, M. E. & Bierwagen, G. P. Mg-rich coatings: A new paradigm for Cr-free corrosion protection of Al aerospace alloys. *Journal of Coatings Technology and Research* **1**, 69–80 (2004).

32. Battocchi, D., Sim�es, A. M., Tallman, D. E. & Bierwagen, G. P. Electrochemical behaviour of a Mg-rich primer in the protection of Al alloys. *Corrosion Science* **48**, 1292–1306 (2006).

33. Sacrificial Protection Systems. *Neftgazpromyshlennost* **23**, 3 (2006).

34. Schmidt, D. P., Shaw, B. A., Sikora, E., Shaw, W. W. & Laliberte, L. H. Corrosion protection assessment of sacrificial coating systems as a function of exposure time in a marine environment. *Progress in Organic Coatings* **57**, 352–364 (2006).

35. Shreepathi, S., Bajaj, P. & Mallik, B. P. Electrochemical impedance spectroscopy investigations of epoxy zinc rich coatings: Role of Zn content on corrosion protection mechanism. *Electrochimica Acta* **55**, 5129–5134 (2010).

36. Morcillo, M. Soluble salts: their effect on premature degradation of anticorrosive paints. *Progress in Organic Coatings* **36**, 137–147 (1999).

37. Zubielewicz, M. & Krolikowska, A. The influence of ageing of epoxy coatings on adhesion of polyurethane topcoats and protective properties of coating systems. *Progress in Organic Coatings* **66**, 129–136 (2009).

38. Song, G.-M. & Sloof, W. G. Effect of alloying element segregation on the work of adhesion of metallic coating on metallic substrate: Application to zinc coatings on steel substrates. *Surface and Coatings Technology* **205**, 4632–4639 (2011).

39. Barchi, L. *et al.* Electroplated bright aluminium coatings for anticorrosion and decorative purposes. *Progress in Organic Coatings* **68**, 120–125 (2010).

40. Jayaweera, P., Lowe, D. M., Sanjurjo, A., Lau, K. H. & Jiang, L. Corrosion-resistant metallic coatings on low carbon steel. *Surface and Coatings Technology* **86–87, Part 2**, 522–525 (1996).

41. Mokaddem, M., Volovitch, P. & Ogle, K. The anodic dissolution of zinc and zinc alloys in alkaline solution. I. Oxide formation on electrogalvanized steel. *Electrochimica Acta* **55**, 7867–7875 (2010).

42. Drazic, D. M. & Popic, J. P. Corrosion rates and negative difference effects for Al and some Al alloys. *J. Appl. Electrochem.* **29**, 43–50 (1999).

43. Никольский, Б. Р. Гомогенный катализ. *Физическая химия: теоретическое и практическое руководство* 757–763 (1987).

44. Ellersick, R. R. SERMETEL W. *http://www.boliven.com/patents/search?q=%28%22Sermetel%22%29&x=71&y=14*

45. B. Hinton Prevention and Control of corrosion in aircraft components - Changes over four decades. *Corrosion* **66**, 1–15 (2010).

46. P. Leblanc & G. S. Frankel A study of corrosion and pitting of AA2024-T3 using Atomic Force Microscopy. *Journal of the Electrochemical Society* **149**, B239–B247 (2002).

47. Kiehl, H. B. Corrosion inhibited metal pigments. *Macromolecular Symposia* **187**, 109–120 (2002).

48. Kendig, M. W., Davenport, A. J. & Isaacs, H. S. The mechanism of corrosion inhibition by chromate conversion coatings from x-ray absorption near edge spectroscopy (Xanes). *Corrosion Science* **34**, 41–49 (1993).

49. Ali, S. A., Al-Muallem, H. A., Rahman, S. U. & Saeed, M. T. Bis-isoxazolidines: A new class of corrosion inhibitors of mild steel in acidic media. *Corrosion Science* **50**, 3070–3077 (2008).

50. Mennucci, M. M., Banczek, E. P., Rodrigues, P. R. P. & Costa, I. Evaluation of benzotriazole as corrosion inhibitor for carbon steel in simulated pore solution. *Cement and Concrete Composites* **31**, 418–424 (2009).

51. Moretti, G., Quartarone, G., Tassan, A. & Zlngales, A. 5-Amino- and 5-chloro-indole as mild steel corrosion inhibitors in 1 N sulphuric acid. *Electrochimica Acta* **41**, 1971–1980 (1996).

52. Refaey, S. A. M. Inhibition of steel pitting corrosion in HCl by some inorganic anions. *Applied Surface Science* **240**, 396–404 (2005).

53. Naderi, R., Mahdavian, M. & Attar, M. M. Electrochemical behavior of organic and inorganic complexes of Zn(II) as corrosion inhibitors for mild steel: Solution phase study. *Electrochimica Acta* **54**, 6892–6895 (2009).

54. Karlsson, P., Palmqvist, A. E. C. & Holmberg, K. Surface modification for aluminium pigment inhibition. *Advances in Colloid and Interface Science* **128-130**, 121–134 (2006).

55. Sherif, E. M. & Park, S.-M. Effects of 1,4-naphthoquinone on aluminum corrosion in 0.50 M sodium chloride solutions. *Electrochimica Acta* **51**, 1313–1321 (2006).

56. Kummert, R. & Stumm, W. The surface complexation of organic acids on hydrous [gamma]-Al2O3. *Journal of Colloid and Interface Science* **75**, 373–385 (1980).

57. Hidber, P. C., Graule, T. J. & Gauckler, L. J. Influence of the dispersant structure on properties of electrostatically stabilized aqueous alumina suspensions. *Journal of the European Ceramic Society* **17**, 239–249 (1997).

58. Muller, B., Shahid, M. & Kinet, G. Nitro- and aminophenols as corrosion inhibitors foraluminium and zinc pigments. *Corrosion Science* **41**, 1323–1331 (1999).

59. Alexander, M. R., Beamson, G., Blomfield, C. J., Leggett, G. & Duc, T. M. Interaction of carboxylic acids with the oxyhydroxide surface of aluminium: poly(acrylic acid), acetic acid and propionic acid on pseudoboehmite. *Journal of Electron Spectroscopy and Related Phenomena* **121**, 19–32 (2001).

60. Boisier, G., Lamure, A., Pebere, N., Portail, N. & Villatte, M. Corrosion protection of AA2024 sealed anodic layers using the hydrophobic properties of carboxylic acids. *Surface and Coatings Technology* **203**, 3420–3426 (2009).

61. Shulman, G. P. & Bauman, A. J. Organic acid sealants for anodized aluminum--A new method for corrosion protection. *Metal Finishing* **93**, 16 (1995).

62. Hu, J.-M., Liu, L., Zhang, J.-Q. & Cao, C.-N. Electrodeposition of silane films on aluminum alloys for corrosion protection. *Progress in Organic Coatings* **58**, 265–271 (2007).

63. Das, M. R. & Mahiuddin, S. Kinetics and adsorption behaviour of benzoate and phthalate at the [alpha]-alumina-water interface: Influence of functionality. *Colloids and Surfaces A: Physicochemical and Engineering Aspects* **264**, 90–100 (2005).

64. Muller, B., Kubitzki, G. & Kinet, G. Aromatic 2-Hydroxy-Oximes as corrosion inhibitors for aluminium and zinc pigments. *Corrosion Science* **40**, 1469–1477 (1998).

65. Zana, R. Dimeric and oligomeric surfactants. Behavior at interfaces and in aqueous solution: a review. *Advances in Colloid and Interface Science* **97**, 205–253 (2002).

66. Jurasin, D., Habus, I. & Filipovic-Vincekovic, N. Role of the alkyl chain number and head groups location on surfactants self-assembly in aqueous solutions. *Colloids and Surfaces A: Physicochemical and Engineering Aspects* **368**, 119–128 (2010).

67. Kiehl, A. & Greiwe, K. Encapsulated aluminium pigments. *Progress in Organic Coatings* **37**, 179–183 (1999).

68. Hamdy, A. S. Corrosion protection of aluminum composites by silicate/cerate conversion coating. *Surface and Coatings Technology* **200**, 3786–3792 (2006).

69. Mishra, A. K. & Balasubramaniam, R. Corrosion inhibition of aluminum alloy AA 2014 by rare earth chlorides. *Corrosion Science* **49**, 1027–1044 (2007).

70. Conde, A., Arenas, M. A., de Frutos, A. & de Damborenea, J. Effective corrosion protection of 8090 alloy by cerium conversion coatings. *Electrochimica Acta* **53**, 7760–7768 (2008).

71. Hamdy, A. S. A clean low cost anti-corrosion molybdate based nano-particles coating for aluminum alloys. *Progress in Organic Coatings* **56**, 146–150 (2006).

72. Lomakina, S. V., Shatova, T. S. & Kazansky, L. P. Heteropoly anions as corrosion inhibitors for aluminium in high temperature water. *Corrosion Science* **36**, 1645–1651 (1994).

73. Sun, X. *et al.* Some observations for effects of copper on zinc phosphate conversion coatings on aluminum surfaces. *Surface and Coatings Technology* **155**, 46–50 (2002).

74. Hamdy, A. S. Advanced nano-particles anti-corrosion ceria based sol gel coatings for aluminum alloys. *Materials Letters* **60**, 2633–2637 (2006).

75. Arnott, D. R., Ryan, N. E., Hinton, B. R. W., Sexton, B. A. & Hughes, A. E. Auger and XPS studies of cerium corrosion inhibition on 7075 aluminum alloy. *Applications of Surface Science* **22-23**, 236–251 (1985).

76. Bickmore, B. R., Nagy, K. L., Gray, A. K. & Brinkerhoff, A. R. The effect of Al(OH)4- on the dissolution rate of quartz. *Geochimica et Cosmochimica Acta* **70**, 290–305 (2006).

77. Franquet, A., Terryn, H. & Vereecken, J. IRSE study on effect of thermal curing on the chemistry and thickness of organosilane films coated on aluminium. *Applied Surface Science* **211**, 259–269 (2003).

78. Labbe, J. P. & Pagetti, J. Study of an inhibiting aluminosilicate interface by infrared reflection spectroscopy. *Thin Solid Films* **82**, 113–119 (1981).

79. J. Thompson, B. Scheetz, M. Schock, D. Lytle & P. Delaney Sodium Silicate corrosion inhibitors: issues of effectiveness and mechanism. *Industrial chemical division* (1997).

80. Joshua Du, Y. *et al.* Inorganic/organic hybrid coatings for aircraft aluminum alloy substrates. *Progress in Organic Coatings* **41**, 226–232 (2001).

81. Wahab, F. M. A. E., Khedr, M. G. A. & Din, A. M. S. E. Effect of anions on the dissolution of Al in acid solutions. *Journal of Electroanalytical Chemistry and Interfacial Electrochemistry* **86**, 383–393 (1978).

Chapter III

Basics of aluminum reactivity

3. Basics of aluminum reactivity

This work is focused on the reactivity of Al pigments for steel protection. In the present chapter the mechanisms of Al reactivity are reviewed.

3.1. Spontaneous reactivity of Al

Corrosion of Al as a function of pH

Studies of corrosion behavior of aluminum alloys are numerous [1, 2, 3, 4, 5]. Aluminum has a very low corrosion rate in neutral solutions due to the formation of an insoluble passive film; however its dissolution is very rapid in low and in high pH electrolytes [6]. The aluminum reactivity in alkaline solutions was reviewed recently by Zhang et al. [6]. The reactivity of Al follows closely the solubility of Al oxides and hydroxides. When the pH is between about 4.0 and 8.5, the solubility of the aluminum oxide is less than 10^{-6} mol/l [7]. It can be calculated from the data presented in [6] that the reaction rate is very near first order with hydroxide becoming significant at pH≥10. It is generally admitted that the key factor controlling the Al reactivity is its stable oxide film. The film stability is determined by the pH near the surface. The open circuit potential of pure Al in neutral aqueous solution (E_{oc} = -0.69 V vs. Ag/AgCl) is much higher than the equilibrium potential of the Al/Al^{3+} couple ($E^{\circ} = -1.873$ V vs. Ag/AgCl) [8]. This shift is interpreted as the presence of a poorly conducting oxide film that separates the metal from the environment (reactions 3.1 and 3.2 [1]) [7].

$$Al + 3OH^{-} \rightarrow Al(OH)_{3, \, surf} + 3e^{-} \qquad\qquad [3.1]$$

or

$$Al + 3OH^{-} \rightarrow AlO(OH) + H_2O + 3e^{-} \qquad\qquad [3.2]$$
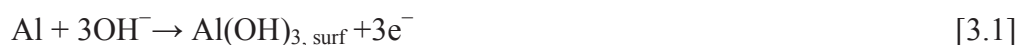
The passivity of Al is usually attributed to the AlOOH thin film formed under an Al$_2$O$_3$ layer [9]. The dissolution of this film will be explained below**.** As long as this film is intact, the Al metal is well protected from the environment and the corrosion rate is very low. This is the case in neutral solutions for which the solubility of Al^{3+} is minimal [3].

---

[1] Here and in future we will write the species and reactions as it was proposed in original papers.

High pH destabilizes the Al oxide film and leads to its thinning according to the reaction 3.4.

$$AlOOH_{surf} + OH^- + H_2O \rightarrow Al(OH)_4^-{}_{(aq)}$$ [3.3]
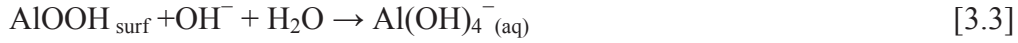
The low pH can also be destabilized according to the reaction:

$$AlOOH + 3H^+ \rightarrow Al^{3+}{}_{aq} + 3H_2O$$ [3.4]

Finally, the low or high pH is necessary to increase the dissolution rate of Al. These pH values can be achieved if any factor intensifies either the cathodic reaction rate (reactions 3.5 and 3.6) or the hydrolysis of Al^{3+} in the solution (see below).

1) Oxygen reduction, $O_2 + 2H_2O + 4e^- \rightarrow 4OH^-$ [3.5]

2) Water reduction, $2H_2O + 2e^- \rightarrow H_2 + 2OH^-$ [3.6]
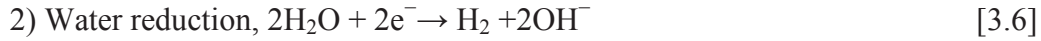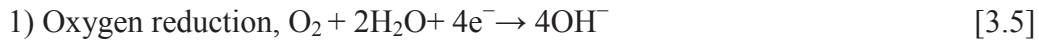
For example, the presence of noble phases (like Al_2Cu, for example) in Al alloys reacting as local cathodes leads to the increase of the chemical Al oxide film dissolution near cathodic sites [10, 11]. The cathodic activity of Al alloys strongly depends on the amount of noble phases as Cu, $Al_xFe_yMn_{1-y}Si$ in the structure [11, 12], due to the increase of the area, where cathodic reaction of water decomposition can take place [13].

> **The key factor for the Al reactivity is its stable oxide film. Its stability is controlled by the pH.**

Hydrolyses of Al^{3+}

As soon as the oxide-free surface of Al is exposed to an aqueous electrolyte, the ionization of Al takes place (equation 3.7), with a time constant smaller than 10^{-6} s [14]:

$$Al^0 \rightarrow Al^{3+} + 3e$$ [3.7]

Al^{3+} is not stable in aqueous solution. In an electrolyte with a pH above 3, the Al^{3+} ions are hydrated with the coordination number of aluminum equal 6. The equilibrium is achieved in about 1 µs [15]. The hydrated Al^{3+} ions undergo the very fast hydrolysis reaction (3.8)-(3.15) resulting in pH decrease. The most studied species are $Al(OH)_3$ and $Al(OH)_4^-$ [15, 6].

$$Al^{3+} + H_2O \leftrightarrow Al(OH)^{2+} + H^+$$ [3.8]

$$Al(OH)^{2+} + H_2O \leftrightarrow Al(OH)_2^+ + H^+ \tag{3.9}$$

$$Al(OH)_2^+ + H_2O \leftrightarrow Al(OH)_{3(aq)} + H^+ \tag{3.10}$$

$$Al(OH)_{3(aq)} + H_2O \leftrightarrow Al(OH)_4^- + H^+ \tag{3.11}$$

The formation mono-nuclear species ($AlOH^{2+}$, $Al(OH)_2^+$, $Al(OH)_3$, $Al(OH)_4^-$) is dominant at concentrations lower then 0.001 mol·l^{-1} [16, 17]. The formation of poly-nuclear species by the reactions (3.12)-(3.15) with x values up to 13 can also occur in concentrated aqueous solutions of Al at the appropriate intermediate pH conditions [15, 18, 19, 14].

$$2Al^{3+} + 2H_2O \leftrightarrow Al_2(OH)_2^{4+} + 2H^+ \tag{3.12}$$

$$3Al^{3+} + 4H_2O \leftrightarrow Al_3(OH)_4^{5+} + 4H^+ \tag{3.13}$$

$$13Al^{3+} + 28H_2O \leftrightarrow Al_{13}O_4(OH)_{24}^{7+} + 32H^+ \tag{3.14}$$

Or in a general form:

$$xAl^{3+} + yH_2O \leftrightarrow Al_x(OH)_y^{3x-y} + yH^+ \tag{3.15}$$

The small poly-nuclear species like $Al_2(OH)_2^{4+}$ are formed more rapidly than the others. For reaction (3.12), the forward reaction rate constant is about $10^{-2}\,M^{-1}\cdot s^{-1}$ in water at 25 °C [20]. The dimeric $Al_2(OH)_2^{4+}$ is present in the solution in measurable concentrations (about 1-2%). The concentration of the dimeric species becomes significant and even overcomes the concentration of the first monomeric species ($AlOH^{2+}$), when the total Al(III) concentrate increases. The presence of mono- or poly-nuclear complexes can be important factor for the controlled formation of oxide film.

Hydrolysis processes lead to the decrease of pH of solutions containing Al^{3+}.

Numerous mono- and poly- nuclear complexes are formed.

Role of chloride

Chloride ions are known to accelerate the pitting corrosion of Al [21]. The ratio of the equilibrium constants for (oxygen gas)-(chloride ion) adsorption on the Al oxide surface is

8000:1 [22]. This ratio indicated the extremely high affinity of Al oxide to molecular oxygen rather than chloride ion adsorption. It was shown using radioactive-labeled chloride [23] that chloride does not enter the oxide film but that it is chemisorbed onto the oxide surface and acts as a reaction partner, increasing Al dissolution due to the formation of oxide–chloride complexes. A mechanism, in which molecular oxygen is firstly chemisorbed onto the metal surface followed by chloride ion adsorption with a subsequent formation of oxide–chloride complex as a rate-determining step, was proposed [22, 9]

The presence of Cl^- ions in the solution does not influence the reaction 3.7. However, in the chloride solution, both Al^{3+} and $AlOH^{2+}$ can react with Cl^- ions according to the reactions:

$$Al^{3+} + Cl^- \leftrightarrow AlCl^{2+} \qquad\qquad [3.16]$$

$$AlOH^{2+} + Cl^- \leftrightarrow Al(OH)Cl^+ \qquad\qquad [3.17]$$

These reactions can take place because of electrostatic affinity or ion pair formation between Al^{3+} or $AlOH^{2+}$ and Cl^- [24]. Both species, $AlCl^{2+}$ and $Al(OH)Cl^+$, react further with water to form the relatively stable species $Al(OH)_2Cl$ [14]:

$$AlCl^{2+} + 2H_2O \rightarrow Al(OH)_2Cl + 2H^+ \qquad\qquad [3.18]$$

$$Al(OH)Cl^+ + H_2O \rightarrow Al(OH)_2Cl + H^+ \qquad\qquad [3.19]$$
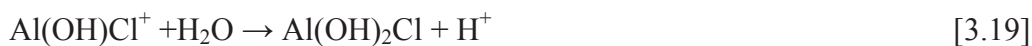
The dissolution process retards the formation of passivation film in reaction with water [25], because of formation of soluble Al~Cl complexes.

The predominant Al^{3+} containing species depend on the distance from the metal / oxide interface [26, 27]; near the interface only complexes with one Cl^- are detected.

The formation of complexes with more than one chloride-ion is possible at high distance from the oxide/metal interface. The formation of poly-nuclear complexes is possible only when the current density of Al dissolution is higher than 1 $A \cdot cm^{-2}$ [14].

At neutral pH, $Al(OH)_2Cl_2$ complex formation by the reaction 3.20 in place of the reactions (3.9) and (3.10) can result in the local oxide thinning [28].

$$Al^{3+} + 2Cl^- + 2OH^- \leftrightarrow Al(OH)_2Cl_2^- \qquad\qquad [3.20]$$

The oxide film is still very stable even in presence of Cl⁻ [29, 28]. Such passive films, however, are susceptible to localized breakdown, resulting in accelerated dissolution of the underlying metal. If the attack initiates on an open surface, it is called pitting corrosion [21]. The hydrolyses of Al salts occurs in pits leading to further pH decrease and increase of the corrosion rate [21, 30].

At low pH the Al dissolution in presence of Cl⁻ is supposed as (3.21 and 3.22):

$$Cl^-_{(solution)} \rightarrow Cl^-_{(adsorbed\ on\ aluminum\ oxides)} \qquad [3.21]$$

$$Al^{3+}_{(from\ the\ oxides)} + 4Cl^- \leftrightarrow AlCl_4^{\ -} \qquad [3.22]$$

The formation of $AlCl_4^-$ complexes is followed by the oxide thinning. It was suggested that when Al is immersed in chloride media and Cl⁻ ions adsorb on the surface, the reaction 3.39 passes without any intermediates is controlled by the Cl⁻ diffusion [28].

The presence of the Cl⁻ in the solution of the electrolyte causes the localized corrosion of Al due to the local oxide thinning by the formation of soluble complexes.

3.2. Point defect mechanism of aluminum reactivity

The porous Al oxide film is an ionic conductor [31, 32, 33] and its formation on the metal solution interface proceeds by the movement of oxygen vacancies or metal cations through the surface oxide film [34]. According to the point defect model [35], the electrochemical reaction involving oxygen vacancy generation at the metal/oxide film interface can be written as:

$$Al_{Al}(m) = Al_{Al}(ox) + 1.5V_O^{2+}(ox) + 3e, \qquad [3.23]$$
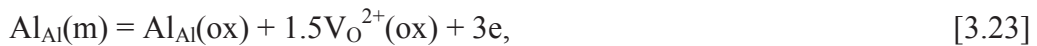
where $Al_{Al}(m)$ is the normal Al atom in the regular metal lattice; $Al_{Al}(ox)$ is the normal aluminum atom in the regular lattice of the oxide film; $V_O^{2+}(ox)$ is the positively charged oxygen vacancy; and *e* represents the electron. The generated oxygen vacancies are removed at the oxide/electrolyte interface:

$$H_2O + V_O^{2+}(ox) = O_O(ox) + 2H^+(aq), \qquad [3.24]$$

where $O_O(ox)$ is the normal oxygen ion in the regular lattice of the oxide film and $H^+(aq)$ represents the hydrogen ion in the aqueous solution.

From equations (3.8) and (3.9), the oxide film formation is given by:

$$2Al(m) + 3H_2O = Al_2O_3 + 6H^+(aq) + 6e \qquad [3.25]$$

The dissolution reaction of pure Al can be obtained by combining the electrochemical oxide formation, reaction (3.25), and the chemical dissolution reaction presented as reaction (3.26) [31]:

$$Al_2O_3 + 2OH^-_{ads} = 2AlO_2^-(aq) + H_2O, \qquad [3.26]$$

where OH^-_{ads} is the adsorbed hydroxide ion and $AlO_2^-(aq)$ is the aluminate-ion in the aqueous solution.

It gives the Al dissolution reaction as:

$$Al(m) + H_2O + OH^-(ad) = AlO_2^-(aq) + 3H^+(aq) + 3e. \qquad [3.27]$$
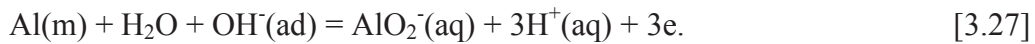
The short-circuited corrosion reaction of pure Al in de-aerated solution can be obtained by combining equations (3.3) and (3.26) representing anodic and cathodic partial reactions, respectively, as follows:

$$Al(m) + H_2O + OH^-(ad) = AlO_2^- + 1.5H_2. \qquad [3.28]$$
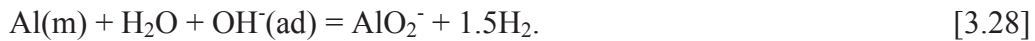
> **The point defect mechanism consists of a number of intermediate steps during Al dissolution. These steps include the migration of vacancies into the solid growing oxide layer. The modification of the ionic properties (conductivity) of the film by structure modification can be a useful strategy to control Al reactivity.**

3.4. Cathodic dissolution of aluminum

The Al dissolution during cathodic polarization is known as cathodic corrosion [36, 37]. It is a well known, but still not completely understood process. Relatively few publications have

addressed the quantitative analysis of this phenomenon. This is partially due to the difficulty of the simultaneous measurement of the cathodic electrical current and the Al dissolution rate.

As noted before, the native surface oxide film can grow during cathodic polarization even in acidic solution because of high local pH [37, 38, 39, 40]. This means that the cathodic corrosion mechanism for pure Al should include the simultaneous formation and dissolution of the surface oxide film [41]. At the same time as a result of a high local pH, the reactivity of Al under cathodic polarization can be considered as its reactivity in alkaline solutions. High pH destabilizes the Al oxide film and leads to its thinning according to the reaction 3.3. When oxide dissolution occurs, the underlying metal becomes exposed and oxidizes to replace the dissolved portion of the film by reaction 3.29 [9]:

$$Al + 3OH^- \rightarrow AlOOH_{surf} + H_2O + 3e^- \qquad [3.29]$$

The overall reaction will be:

$$Al + 4H_2O + e^- \rightarrow 2H_2 + Al(OH)_{4\ (aq)}^- \qquad [3.30]$$

It is important to remember, that in aqueous solutions the coordination number of aluminum is equal to 6 [14]. It corresponds to the $Al(OH)_4^- \cdot 2H_2O$ complex (see more details about solution chemistry of Al in **section 3.1**). However, in the chemical equations used in this work (**chapter 3**) we will respect the original position of authors and write the same species as they did.

The dissolution of the Al in the presence of hydroxides can be classified as an electrochemical or a chemical process. Since the electrochemical dissolution of Al includes the ejection of Al^{3+} into the solution, the electrochemical dissolution of Al is accelerated under anodic polarization. This acceleration hardly occurs under cathodic polarization. Thus, it can be said that before the Al^{3+} species go into the solution the surface oxide film occurs. This oxide dissolves chemically owing to the attack by OH⁻ in the cathodic domain[42, 41].

The cathodic polarization of passivated Al [2] and Al–Sn alloys [5] in a chloride solution is characterized by two regions of potentials with distinctly different phenomena: the range of low and high cathodic potentials (LCP and HCP). In the LCP range, the oxide film retains its properties and the electrochemical reaction between electrons in the metal and the species in solution is controlled by the transport of electrons through the oxide film. The Tafel slope at

this stage is relatively high. In this region the cathodic aluminum dissolution at a specific potential should depend on the cathodic current rather than the potential, therefore on the catalytic activity of the surface for cathodic reaction.

After the breakdown, in HCP the pH increases by cathodic reactions (3.5 and 3.6) leading to an enhanced solubility of aluminum oxide followed by the oxidation of the underlying metal to replace the dissolved portion of the film. At high cathodic potentials, the cathodic process occurring initially at the surface of the oxide is followed by oxide hydration and a transfer of the cathodic process to the metal-hydrated oxide interface, with a subsequent change of the properties of the metal surface by the possible formation of the metal hydride, which can react as an intermediate. The Tafel slope in HCP region decreases compared to LCP.

Some authors using classical electrochemical methods, suggested that the kinetics of Al cathodic dissolution in alkaline solutions is not very sensitive to the pH or applied electric field as would be expected if OH^- participated directly in the oxidation process as assumed in ref. [31, 1]. This was explained by either the growth of an Al_2O_3 layer on the surface or by the difference between bulk and surface pH making the rate determining step H diffusion. The hydrogen mechanism of corrosion for which the diffusion can be the rate limiting step can also explain these observations.

According to this mechanism the cathodic aluminum reactivity could be controlled by the structural modification in the oxide layer.

3.5. Hydride mechanism of aluminum reactivity

In the hydrogen mechanism of Al dissolution, the first electrochemical step is a formation of adsorbed hydrogen atom ($H^.$) and hydroxide ion (OH^-) from a molecule of water on the surface of Al [1]. The presence of three species – $H^.$ at the surface, an Al atom with 3p-electrons (or pair Al^+ + e) in the outer shell and a highly polar molecule H_2O – could stimulate the release of the electron from the Al atom on the proton in the molecule of water with the formation of the 2 covalent bond in the result. Thus AlOH species form on the surface:

$$H_2O_{ads} + e \rightarrow H^._{ads} + OH^- \qquad \text{(rate determining step)} \qquad [3.31]$$

$$H^{\cdot}_{ads} + Al + H_2O \rightarrow H_2 + AlOH \qquad\qquad [3.32]$$

The formation and the adsorption of the hydrogen atom [43, 14] is additionally stimulated by the possibility of creating an Al-OH bond with the release of an electron.

The presence of a hydrogen atom on the surface leads to the additional hydride AlH_3 formation (equation 3.18) [45]:

$$Al + 3H_{ads} \rightarrow AlH_3 \qquad\qquad [3.33]$$

The stoichiometry of AlH_3 oxidation to the $Al(OH)_4^-$ in presence of OH^- in aqueous solution is close to the reaction (3.34):

$$AlH_3 + 7OH^- \rightarrow Al(OH)_4^- + 3H_2O + 6e \qquad\qquad [3.34]$$

The overall spontaneous reaction obtained by balancing electrons through reactions (3.31)-(3.34) accounts for the formation of AlH_3 as a product:

$$2Al + OH^- + 3H_2O \rightarrow Al(OH)_4^- + AlH_3 \qquad\qquad [3.35]$$

According to the hydrogen mechanism of Al corrosion, one hydrogen molecule (H_2) is produced for each external electron and giving the hydrogen yield of the reaction as 2. The surface specie AlOH supposes the existence of Al(I) which could convert into Al^{3+} by one of the following reactions (3.36-3.38) [1, 45]:

1) $AlOH + H_2O \rightarrow AlOOH + H_2$ [3.36]
2) $AlOH + OH^- \rightarrow AlO_2^- + H_2$ [3.37]
3) $3AlOH \rightarrow Al + AlOOH + H_2O$ [3.38].
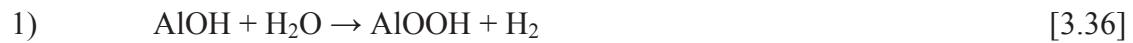
Both reactions (3.36) and (3.38) can be continued in alkaline solutions by the reaction AlOOH with hydroxides (3.39):

$$AlOOH + OH^- = AlO_2^- + H_2O \qquad\qquad [3.39],$$

The reaction (3.38) also leads to the continuous reaction (3.40):

$$Al + 4H_2O + 3e = 3H_2 + AlO_2^- + 2OH^- \qquad\qquad [3.40]$$
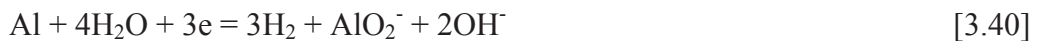
In the case of the side reaction (3.36)-(3.37) the hydrogen yield increases to greater than 2.

The hydride mechanism of Al corrosion should result in hydrogen yield of 2 (only reactions 3.31 and 3.32) or more (with aside reaction 3.36-3.37). If hydride is not present, the reaction 3.6 should result in a yield of 1. For HCP experimental hydrogen yield equal to 2 is observed at room temperature and more then 2 at high temperature [1]. This validates the hydride mechanism for HCP and indicates the necessity of thermal activation for reactions 3.36-3.37.

The hydrogen mechanism of Al corrosion consists of a number of intermediate steps and parallel reactions. These steps include the formation of the adsorbed hydrogen atom and unstable AlH$_3$, which is further oxidized to stable Al(OH)$_4^-$.

3.6. Conclusions

The Al dissolution is controlled by the stability and conductivity of the oxide film. The modification of solution chemistry (pH, Cl$^-$, etc.) can be used as a strategy to control Al reactivity via the modification of the film structure and stability.

3.7. References

1. Despic, A. R., Radosevic, J., Dabic, P. & Kliskic, M. Abnormal yields of hydrogen and the mechanism of its evolution during cathodic polarization of aluminium. *Electrochimica Acta* **35**, 1743–1746 (1990).

2. Despic, A. R., Drazic, D. M., Balakina, J., Gajic, L. J. & Stepanov, R. M. Investigation of oxidation potentials of substances accumulated during cathodic polarization of aluminium. *Electrochimica Acta* **35**, 1747–1755 (1990).

3. Ogle, K., Serdechnova, M., Mokaddem, M. & Volovitch, P. The cathodic dissolution of Al, Al2Cu, and Al alloys. *Electrochimica Acta* **56**, 1711–1718 (2011).

4. Volovitch, P., Serdechnova, M. & Ogle, K. Aqueous Corrosion of Mg-Al Binary Alloys: Roles of Al and Mg. *Corrosion* (2012).

5. Gudic, S., Radossevic, J., Smoljko, I. & Kliskic, M. Cathodic breakdown of anodic oxide film on Al and Al–Sn alloys in NaCl solution. *Electrochimica Acta* **50**, 5624 – 5632 (2005).

6. Zhang, J., Klasky, M. & Letellier, B. C. The aluminum chemistry and corrosion in alkaline solutions. *Journal of Nuclear Materials* **384**, 175–189 (2009).

7. Pourbaix, M. *Atlas d'Equilibres Electrochimiques à 25 °C*. (Paris, 1963).

8. Bard, A. J. & Faulkner, L. R. *Electrochemical Methods: Fundamentals and Applications*. (2001).

9. Bockris, J. O. & Minevski, L. V. On the mechanism of the passivity of aluminum and aluminum alloys. *Journal of Electroanalytical Chemistry* **349**, 375–414 (1993).

10. Takahashi, H., Fujiwara, K. & Seo, M. The cathodic polarization of aluminum covered with anodic oxide films in a neutral borate solution--II. Film breakdown and pit formation. *Corrosion Science* **36**, 689–705 (1994).

11. Y. Baek & G. S. Frankel Electrochemical Quartz Crystal Microbalance Study of Corrosion of Phases in AA2024. *Journal of the Electrochemical Society* **150**, B1–B9 (2003).

12. Muller, I. L. & Galvele, J. R. Pitting potential of high purity binary aluminium alloys--I. Al---Cu alloys. Pitting and intergranular corrosion. *Corrosion Science* **17**, 179–193 (1977).

13. Bethencourt, M. *et al.* Behaviour of the alloy AA2017 in aqueous solutions of NaCl. Part I: Corrosion mechanisms. *Corrosion Science* **51**, 518–524 (2009).

14. Guseva, O., Schmutz, P., Suter, T. & von Trzebiatowski, O. Modelling of anodic dissolution of pure aluminium in sodium chloride. *Electrochimica Acta* **54**, 4514–4524 (2009).

15. Benezeth, P., Palmer, D. A. & Wesolowski, D. J. The aqueous chemistry of aluminum. A new approach to high-temperature solubility measurements. *Geothermics* **26**, 465–481 (1997).

16. Couturier, Y., Michard, G. & Gerard Sarazin Constantes de formation des complexes hydroxydes de l'aluminium en solution aqueuse de 20 a 70°C. *Geochimica et Cosmochimica Acta* **48**, 649–659 (1984).

17. Akitt, J. W. & Elders, J. M. The hexa-aquo aluminum cation as reference in aluminum-27 NMR spectroscopy. Possible detection of second sphere effects. *Journal of Magnetic Resonance (1969)* **63**, 587–589 (1985).

18. Baes, J. & Mesmer, R. E. *The Hydrolysis of Cations*. (New York, 1976).

19. Ohman, L.-O. & Sjoberg, S. Complex formation in the Al3+---citrate system. *Inorganica Chimica Acta* **79**, 215–216 (1983).

20. Holmes, L., Cole, D. & Eyring, E. Kinetics of Aluminum Ion Hydrolysis in Dilute Solutions. *J. Phys. Chem.* **72**, 301–304 (1968).

21. Frankel, G. S. Pitting Corrosion. *Metals Handbook* **13A**, 236–241 (2003).

22. Abdel-Gaber, A. M., Abd-El-Nabey, B. A., Sidahmed, I. M., El-Zayady, A. M. & Saadawy, M. Kinetics and thermodynamics of aluminium dissolution in 1.0 M sulphuric acid containing chloride ions. *Materials Chemistry and Physics* **98**, 291–297 (2006).

23. Garrigues, L., Pebere, N. & Dabosi, F. An investigation of the corrosion inhibition of pure aluminum in neutral and acidic chloride solutions. *Electrochimica Acta* **41**, 1209–1215 (Mai).

24. Dietzel, M. & Bohme, G. The dissolution rates of gibbsite in the presence of chloride, nitrate, silica, sulfate, and citrate in open and closed systems at 20 °C. *Geochimica et Cosmochimica Acta* **69**, 1199–1211 (2005).

25. Nguyen, T. N. & Foley, R. T. The Chemical Nature of Aluminum Corrosion II. The Initial Dissolution Step. *J. Electrochem. Soc.* **129**, 27–32 (2005).

26. Suter, T. & Bohni, H. Microelectrodes for corrosion studies in microsystems. *Electrochimica Acta* **47**, 191–199 (2001).

27. Suter, T. & Alkire, R. Microelectrochemical studies of pit initiation at single inclusion in Al 2024-T3. *Journal of the Electrochemical Society* **148**, B36–B42 (2001).

28. Mazhar, A. A., Badawy, W. A. & Abou-Romia, M. M. Impedance studies of corrosion resistance of aluminium in chloride media. *Surface and Coatings Technology* **29**, 335–345 (1986).

29. Mishra, A. K. & Balasubramaniam, R. Corrosion inhibition of aluminum alloy AA 2014 by rare earth chlorides. *Corrosion Science* **49**, 1027–1044 (2007).

30. Szklarska-Smialowska, Z. Pitting corrosion of aluminum. *Corrosion science* **41**, 1743–1767 (1999).

31. Moon, S.-M. & Pyun, S.-I. The formation and dissolution of anodic oxide films on pure aluminium in alkaline solution. *Electrochimica Acta* **44**, 2445–2454 (1999).

32. Randall Jr., J. J. & Bernard, W. J. A radiotracer study of the anodization of aluminum in aqueous phosphate solutions. *Electrochimica Acta* **20**, 653–661 (1975).

33. Khalil, N. & Leach, J. S. L. The anodic oxidation of valve metals--I. Determination of ionic transport numbers by [alpha]-spectrometry. *Electrochimica Acta* **31**, 1279–1285 (1986).

34. Pyun, S.-I. & Hong, M.-H. A model describing the growth kinetics of passivating oxide film prepared under potentiostatic conditions. *Electrochimica Acta* **37**, 327–332 (1992).

35. Chao, C. Y., Lin, L. F. & Macdonald, D. D. POINT DEFECT MODEL FOR ANODIC PASSIVE FILMS. *Journal of the Electrochemical Society* **128**, 1187–1194 (1981).

36. Caldwell, B. P. & Albano, V. J. Rate of Solution of Zinc and Aluminum while Cathodic. *Transactions of the Electrochemical Society* **76**, 271–285 (1939).

37. Moon, S.-M. & Pyun, S.-I. The corrosion of pure aluminium during cathodic polarization in aqueous solutions. *Corrosion Science* **39**, 399–408 (1997).

38. Lin, C.-F. & Hebert, K. R. Changes Produced by Cathodic Polarization in the Electrical Conduction Behavior of Surface Films on Aluminum. *J. Electrochem. Soc.* **141**, 104–110 (1994).

39. E.P.G.T. van de Ven & Koelman, H. The cathodic corrosion of aluminum. *J. Electrochem. Soc.* **123**, 143–144 (1976).

40. S. Szabó & I. Bakos Catalytic aspects of oxygen reduction in metal corrosion. *Corrosion reviews* **26**, 51–71 (2010).

41. Kim, Y.-S., Pyun, S.-I., Moon, S.-M. & Kim, J.-D. The effects of applied potential and pH on the electrochemical dissolution of barrier layer in porous anodic oxide film on pure aluminium. *Corrosion Science* **38**, 329–336 (1996).

42. Diggle, J. W., Downie, T. C. & Goulding, C. W. The dissolution of porous oxide films on aluminium. *Electrochimica Acta* **15**, 1079–1093 (1970).

43. Skulason,, E., Karlberg, G. S. & Rossmeisl, J. Density functional theory calculations for the hydrogen evolution reaction in an electrochemical double layer on the Pt(111) electrode. *Phys. Chem. Chem. Phys.* **9**, 3241–3250 (2007).

44. E. Skulason,, Tripkovic, V. & Bjorketun, M. E. Modeling the Electrochemical Hydrogen Oxidation and Evolution Reactions on the Basis of Density Functional Theory Calculations. *J. Phys. Chem. C* **114**, 18182–18197 (2010).

45. Adhikari, S. & Hebert, K. R. Factors controlling the time evolution of the corrosion potential of aluminum in alkaline solutions. *Corrosion Science* **50**, 1414–1421 (2008).

Chapter IV

Atomic emission spectroelectrochemistry (AESEC) technique

4. Atomic emission spectoelectrochemistry (AESEC) technique

4.1. Introduction

Atomic emission spectroelectrochemistry (AESEC) directly measures the release rate from a material into an aggressive electrolyte allowing an *in-situ* analysis of degradation phenomena. In this work, this will be the principal methodology used to characterize the degradation mechanism of pure Al, Al alloys, Al intermetallics and model anticorrosion high temperature coatings based on metallic Al particles in a siloxane binder. In this chapter general principles of ICP spectrometry and the AESEC technique will be presented explaining the choice of operating parameters and quantification procedure. Improvements proposed in this PhD work (pH monitoring, quantification of released particles and the improvement of convolution procedure) are also described **(section 4.8)**

4.2 Overview of AESEC

Figure 4.1 gives a simplified schematic diagram of the AESEC method. Briefly, the reaction between a sample and an electrolyte occurs in the flow cell (**figure 4.1(I)**) leading to the production of dissolved ions. From the flow-cell the electrolyte containing the ions is transported to the inductively coupled plasma optical emission spectrometer (ICP-OES) where its composition is continually analyzed (**figure 4.1 (II)**). The concentration of the each element M in the solution is measured from the emission intensity at a specific wavelength using normal quantitative procedures for ICP spectrometry.

The instantaneous dissolution rate in the cell is directly related to the instantaneous concentration downstream from the cell (see calculation in **sections 4.4-4.5**). The dissolution rate of each element as a function of time shows the real time kinetics of the material degradation and performs the direct measurement of releasing elements.

The flow-cell for AESEC experiments is configured as a three electrode electrochemical cell. In this way the potential can be monitored and controlled for the acceleration of the reaction during the experiment as well as the total electrochemical current can be either monitored under applied potential or controlled for galvanostatic experiment. Also the dissolution rate can be recalculated into units of the elemental dissolution current, according to the Faraday

law, and thus, the total electrochemical current can be decomposed into the contribution of elementary reactions so that the electrochemical current may be quantitatively compared with the elemental dissolution rates.
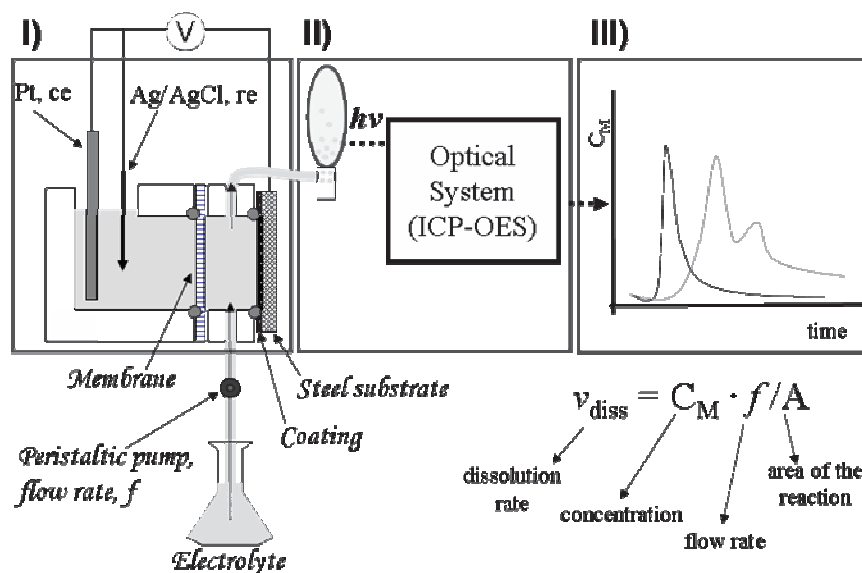
Figure 4.1. The simplified diagram of the AESEC experiment: I) three electrode cell for the reaction; II) analytical ICP-OES system; III) monitoring result.

4.3. Schematic Diagram of ICP-OES

The electrolyte is removed from the electrochemical flow-cell by a peristaltic pump and aspirated into the torch of an inductively coupled plasma atomic emission spectrometer. Photons emitted from the plasma may be analyzed to determine the specific composition of the electrolyte both qualitatively and quantitatively. Data from the phototubes are recorded simultaneously along with signals from the electrochemical experiments; in this way electrochemical experiment is combined with elemental quantification analysis.

The ICP spectrometer used in this work (Horiba JobynYvon Ultimata2C[TM]) consists of an 40.68 MHz inductively coupled argon plasma, which is an electrically neutral, highly ionized gas that consists of ions, electrons, and atoms, as the atomization and excitation source. **Figure 4.2** gives a schematic of an ICP torch. The circular quartz tube (12–30 mm OD) has three separate gas inlets. The only gas routinely used is argon as it has high ionization energy

(15.6 eV) and a good capacity to atomize, ionize and excite most of the elements. The plasmagene gas enters the plasma through the outer channel with a tangential flow pattern at a rate of 8 – 20 L min^{-1}. This rate is optimized in function of solution composition and viscosity. Due to this optimization a very large range of solutions may used (from aqueous solutions with high ionic force to organic liquids). The auxiliary gas, which travels up the centre channel, also has a tangential flow (0.5 – 3 L min^{-1}) pattern. The nebulizer gas has a laminar flow pattern (0.1 to 1.0 L min^{-1}) and injects the sample into the plasma. The analytical zone is approximately 1 cm above the coils and offers the best optical viewing area for maximum sensitivity. Both atomic and some ionic emission lines can be analyzed. The plasma temperature in the analytical zone ranges from 5000–8000 K (the temperature varies with power, flow rate, etc.). The high temperature assures that the sample is completely atomized.

As a disadvantage, the complete species atomization in the plasma leads to the **loss of any information about oxidation state or molecular form of the measured species**. On the other hand, the complete atomization leads to **very low matrix effects** and makes possible working in most liquid solutions.
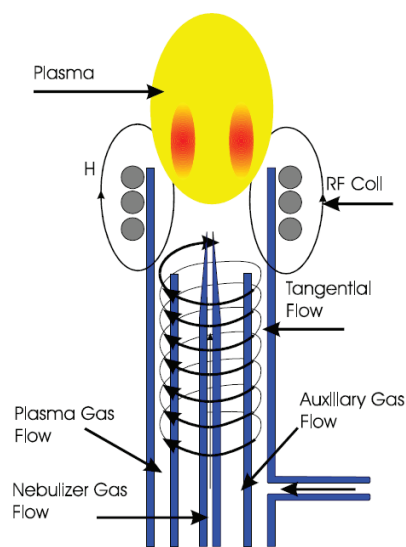
Figure 4.2. A schematic diagram of an ICP torch.

The species concentration varies at different positions in plasma leading to the influence of plasma instability on the noise of the signal. The Ultima2C^{TM} system contains polychromator (poly) and monochromator (mono) optical modules. Radiation emitted from the plasma (hν)

was collected in the radial direction and collected by a polychromator for the simultaneous detection of 30 predetermined wavelengths and a monochromator that could be used for the detection of an adjustable wavelength. The polychromator used a Paschen–Runge configuration with a 0.5 M focal plane and was equipped with a holographic grating of 3600 grooves/mm and **30 independent photomultiplier tubes** (PMT, **Figure 4.3**).

The theoretical resolution of the polychromator in Ultima2C^{TM} is 0.025 nm in the first order and 0.015 nm in the second order covering a spectral range from 165 to 408 nm. The monochromator using Czerny–Turner configuration with a 1.0 m focal plane, equipped with a holographic grating of 2400 grooves / mm and a practical resolution of 0.005 nm in a spectral range from 120 to 320 nm and a resolution of 0.010 nm in a range from 320 to 800 nm. Both polychromator and monochromator were nitrogen purged.
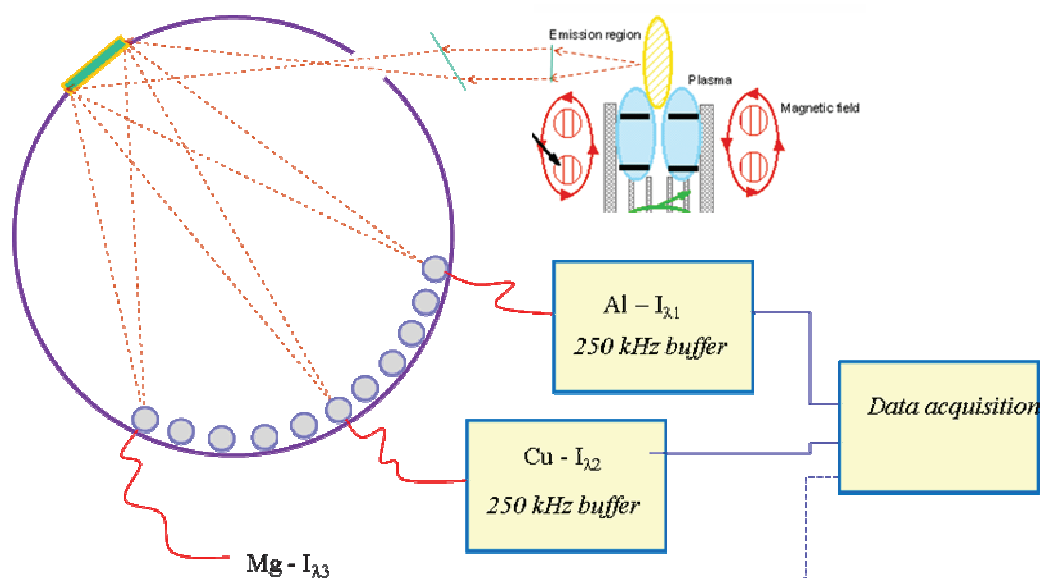
Figure 4.3 Simplified schematic of the data acquisition system from optical system with simultaneous measurement [1]

The utilization of 30 independent photomultiplier tubes in polychromator allows collecting emission signals of 30 wavelengths simultaneously. The time resolution during the experiment may be changed without losing the emission signal for each element: with the increase of the time per point, the signal to ratio will proportionally increase.

4.4. Quantification principles of AESEC

Inductively coupled plasma-atomic emission spectrometry is designed to determine the amount (concentration) of one or several test elements from a liquid sample, by atomizing and

exciting the element in the inductively coupled plasma (ICP), and determining the intensity of atomic emission spectral line. Each element has a number of specific atomic and ionic emission wavelengths. The emission spectrum is produced by an electronic transition from a high energy level E_n to a lower energy level E_m (**Figure 4.4**). The emitted radiation can be easily detected when it is in the vacuum ultraviolet (VUV, 120–185 nm), ultraviolet (UV, 185–400 nm), visible (VIS, 400–700 nm), and near infrared regions (NIR, 700–850 nm) [2].
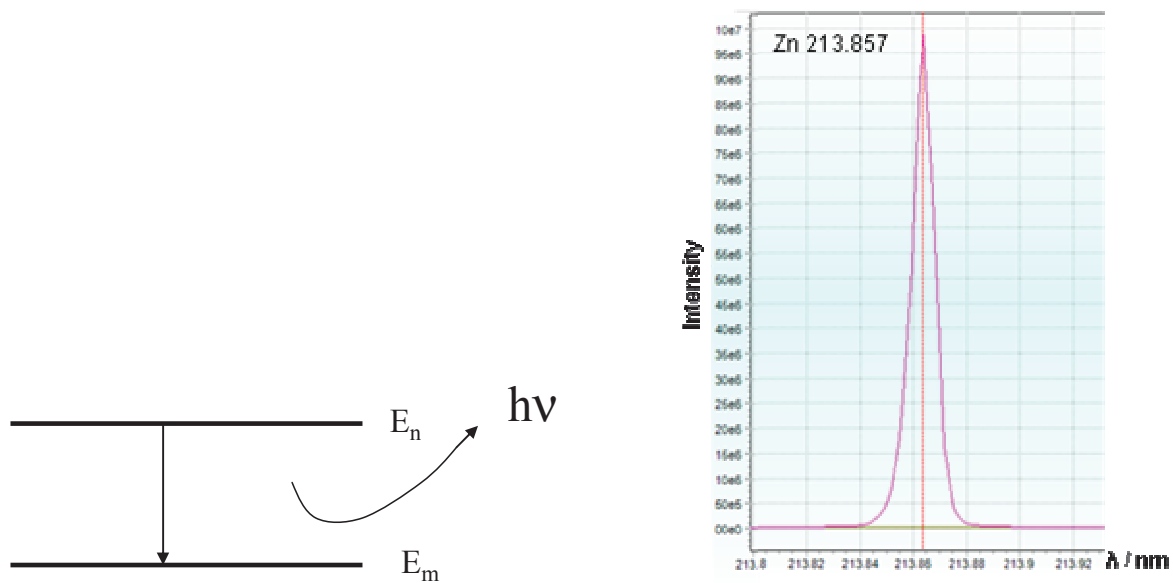
Figure 4.4. Schematic diagram of emission of radiation upon relaxation from high energy level (left) [2] and the spectra measured by ICP (right).

The basic quantification principle of ICP-OES is that the emission intensity (I_λ) of a given element, M, at its spectral line, λ, is proportional to the concentration of that element (C_M, ppm) in the electrolyte:

$$C_M = (1/k) \ (I_\lambda - I_\lambda^\circ) \hspace{5cm} [4.1]$$

where k is the constant of the proportionality, depending on the flow rate of the electrolyte, the pressure in the system, the temperature of the plasma, etc. and I_λ° is the background intensity.

Figure 4.5 gives an example of Al detection in 3 % NaCl at 167.081 nm from polychromator. According the equation 4.1 the different concentration will have different response intensity (I); the higher the concentration is, the higher intensity will be (**figure 4.5**).The experiment

was performed in two ways: solutions go directly to the plasma and solution passes through the cell with inert material in place of a sample. The relationship between the concentration of Al and Mg and corrected ICP response atomic emission signal intensity $(I - I_0)$ is shown in **figure 4.6**. This result demonstrates the good efficiency of the ionic transport to the plasma. However, at very high concentration of released ions (around 10 ppm) and long time of the experiment (more than 10 hours) the loss of elements (Al and Fe during this PhD work) through the membrane was still detected.
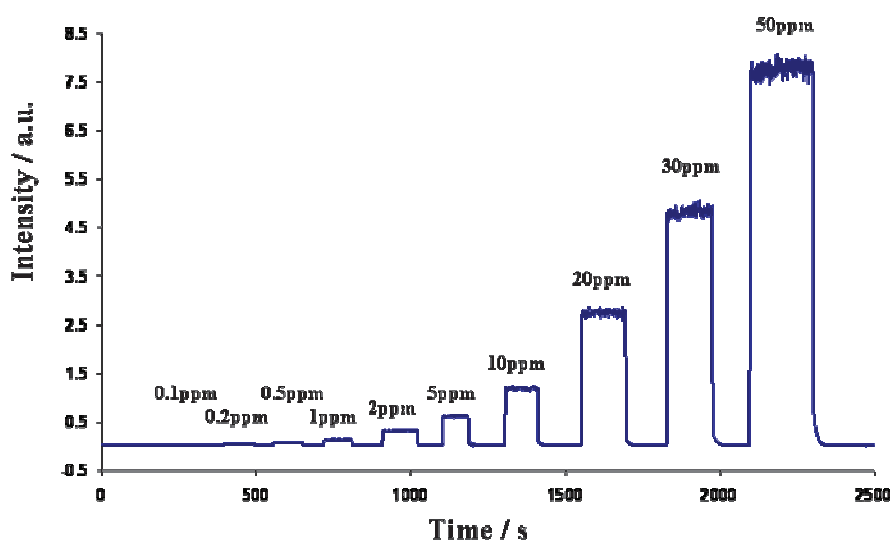
Figure 4.5. The Al detection at 167.081 nm from polychromator under different concentration

The concentration equivalent to the detection limit of the reaction was determined as $C_{2\sigma}$ and was calculated as

$$C_{2\sigma} = (2\sigma/(I-I_0)) \, C_M \qquad\qquad [4.2]$$

where σ is the standard deviation of the background intensity; I_0 is the absolute value of the background signal intensity, and I is the intensity measured for a standard solution concentration of an element M, C_M.

Typical $C_{2\sigma}$ values for the elements used in this work (3% NaCl solution, 3 ml/min flow-rate) are given in table 4.2.

Table 4.2. The $C_{2\sigma}$ of each element used in this work

	Al	**Fe**	**Zn**	**Si**	**Mn**	**Cr**
Wavelength / nm	231.60	259.94	213.84	251.11	257.61	257.61
$C_{2\sigma}$ / ppb	1.20	1.40	48.62	69.85	1.64	15.71

4.5 AESEC Rate Measurements

A typical example of a transient AESEC measurement for pure Al reactivity is shown in **Figure 4.7**.
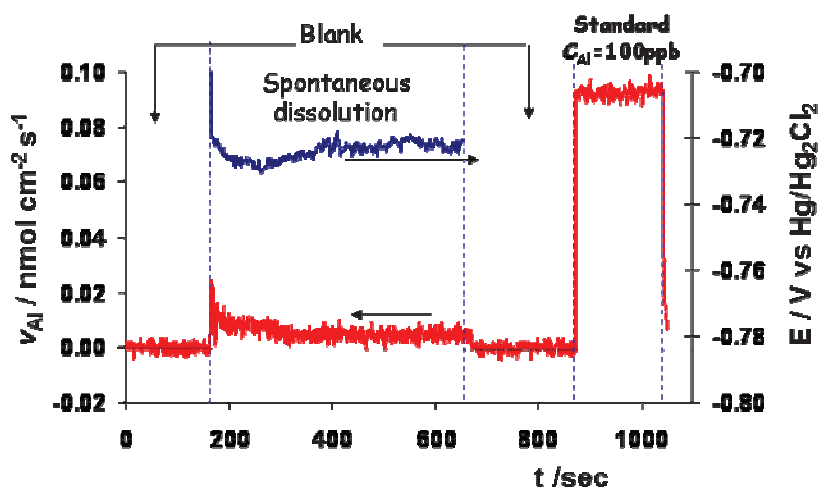
Figure 4.7. A typical example of a transient AESEC measurement of pure Al reactivity.

The instantaneous dissolution rate of an element M in the cell, v_M, in nmol s^{-1} cm^{-2}, is directly related to the instantaneous downstream concentration as:

$$v_M = C_M f / (A\ M_M) \hspace{4cm} [4.3]$$

where f is the flow rate of electrolyte (in this work, 3.02 cm^3 min^{-1}), C_M is a concentration of element M (in mol l^{-1}), and A is the exposed surface area (0.51 cm^2) and M_M is an atomic mass of the element M [3]. Equation 4.1 demonstrates the importance of the background signal measurement, which is very sensitive to the experiment conditions (temperature, flow rate, nebulization, etc.). For the correct quantification it is important to control that background signal does not change during the experiment, so that the blank solution is analyzed before and after the experiment using the valve bypass system showing in **Figure 4.7**.

If the experiment involves a high concentration of an element for a sufficiently long, time the background signal will be more intense after the experiment due to contaminations of the system (by Al for example). For these special cases the value $I_\lambda°$ after the experiment was used to calculate the concentration at the quasi steady state conditions.

4.6. Correlation of electrochemical data and dissolution rates

With the assumption that the dissolution of the element M is described as:

$$M + n\ e \rightarrow M^{n+} \hspace{4cm} [4.4]$$

where M is the dissolved element and n is the number of electrons, the dissolution rate can be expressed as elementary dissolution current according the Faraday low as:

$$j_M = n\ F\ v_M \hspace{4cm} [4.5]$$

where F is the Faraday constant, n is the number of electrons in the reaction 4.4.

The total electrical current density between working and counter electrodes, i_e, is measured by AESEC method. The total current density is the sum of the cathodic current density, j_c, and

the anodic current density, j_a (equation 4.6) in the assumption of the same areas of the cathodic and anodic reactions respectively (A cm^{-2}):

$$j_e = j_c + j_a \hspace{4cm} [4.6]$$

According equations 4.5 and 4.6 the difference between total electron current, j_e, measured by potentiostat, and total elemental dissolution, j_M, can give the access to the indirect measurement of the cathodic current of the reaction, j_c, and rate of insoluble species formation, j_{ins}.

Under anodic polarization, it is often possible to ignore the contribution of j_c. If, under these circumstances, all anodic current leads to the formation of soluble species, the comparison of the electrochemical currents and the dissolution rates of the component elements may be used to determine the stoichiometry of anodic dissolution. A recent example of this type of analysis for Mg dissolution is given in [4] where a clear $n = 2$ stoichiometry was observed in contradiction with previous reports of an $n = 1$ stoichiometry.

If the insoluble species such as oxides and hydroxides make an important contribution to the anodic reaction, the insoluble, j_{ins}, components may be determined by the difference between the anodic current and the sum of the elemental dissolution currents, Σj_M.

$$j_{ins} \hspace{1cm} = j_a - \Sigma j_M \hspace{4cm} [4.7]$$

More details about these calculations are presented in the result chapters, where they are used and discussed with all the proposed assumptions.

4.7. Technical characteristics of the instrumentation

4.7.1. Electrochemical flow cell and potentiostat M273A

The cell is composed of a two-compartment system in which the working electrode (we) is exposed to a flowing electrolyte in a small volume of flow cell. The geometrical area of the sample exposed to the electrolyte was 0.51 cm^2 defined by the contour of the o-ring (j). The flow channel has an entrance at the bottom and exit at the top so that the electrolyte passes

through the cell from bottom to top such that cathodically generated hydrogen during the experiment flows out of the cell.

A 10 ml cylindrical secondary compartment of stagnant electrolyte is separated from the working electrode compartment by a porous membrane. This membrane allows ionic current to pass from one compartment to the other while preventing bulk mixing of the two electrolytes. A Pt counter electrode and an Ag/AgCl or Hg/Hg_2Cl_2 reference electrodes were placed in the secondary compartment.

An EG&G PAR M273A potentiostat was used for all electrochemical experiments. This potentiostat has analog out-put and the signals were specially adapted so that they could be channeled into the ICP-OES spectrometer and collected simultaneously by the ICP-OES software as described below. This allows comparison between total current of the corrosion processes (measured by potentiostat) and elemental dissolution curve (measured by ICP-OES, see description below). The working mode of the potentiostat is defined on the front-panel of the technique, allowing its easy application.

4.7.2. Transport of the electrolyte

The pump served to transfer the electrolyte into the electrochemical flow-cell and then into a ICP detection system. The flow-rate is optimized in order to find a compromise between the analytical parameters of ICP (plasma is more stable at low flow-rates, standard systems are optimized for 1 ml/min) and the time resolution of the kinetic measurement. For the most part the experiments in this PhD work used a flow-rate of approximately 3 ml/min.

For slow dissolution reactions, and hence low concentration of released ions, it can be interesting to decrease the flow-rate and to concentrate the species for the sensitivity improvement during the measurement. It allows making a more precise elemental quantification but the information about quick corrosion processes is lost.

The *Meinhard K3* nebulizer is chosen to be used with the electrolyte flow-rate around 3 ml/min and *Conical* nebulizer for flow-rate equal to 1 ml/min.

The electrolyte flow can be disturbed by several factors:

   1. The presence of non-soluble species blocking the nebulizer,

2. The formation of zones where the solution is stagnant because of connection or folds,

3. The gas formation which leads to the bubbles and variation of density and viscosity of the electrolyte.

The effect of insoluble species formation is partly compensated by the choice of the *Meinhard K3* nebulizer with relatively large diameter of internal capillary.

4.7.3. Role of oxygen for the Al quantification

The most sensitive lines of Al and phosphorus analyzed in this work are located in the UV region (167.081 nm and 178.291 nm respectively). As only a very small number of elements emit radiation in the UV region decreasing the possibility of interferences. However, oxygen and nitrogen present in air can reduce the measured emission radiation in the UV region of the spectrum.

The absorption of the N_2 in the domain between 160 and 250 nm is really negligible and may be ignored [5]. The poly- and monochromator of the ICP technique used in this work are purged with nitrogen. However, the small amount of other gases (O_2, CO_2, H_2O vapor) can penetrate into the system and absorb the emission radiation in the domain of wavelengths shorter then 190 nm. This absorption follows the Beer–Lambert–Bouguer law:

$$I = I° \exp(-k \, C \, l), \qquad\qquad [4.8]$$

where $I°$ and I are the intensity (or power) of the incident light and the transmitted light, respectively; C is the absorbent gas concentration, k is the absorption coefficient for each gas, l is the distance between plasma and detector.

The absorption coefficients of these gases decrease rapidly for wavelengths higher than 160-200 nm (**figure 4.8**) and irradiation with the wavelengths more than 200 nm pass through them easily. The concentration of oxygen is 100 times higher than either carbon dioxide or water. Therefore, oxygen plays the main role and has highest influence on the absorption spectra during ICP analysis in the domain with wavelengths shorter then 200 nm. In our system the maximal O_2 concentration allowed is 3 ppm.
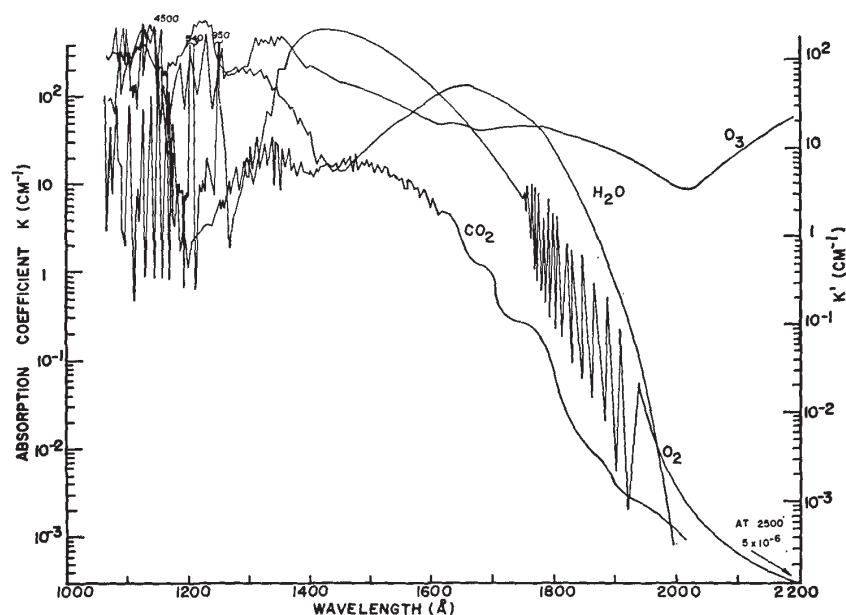
Figure 4.8. The extinction coefficients of the oxygen, water and carbon dioxide in between 100 and 220 nm [6].

4.8. Improvements of AESEC

4.8.1. Analysis of the residual solution

The specificity of the ICP analysis is that only about 5% of the solution is aspirated into the plasma, 95 % of the solution is removed from the cyclonic chamber by a second channel of the peristaltic pump. This removed solution may be collected and used for further analysis.

During the spontaneous reaction and under potentiostatic conditions, the solution was collected in 9 cm^3 portions (during each 3 minutes) and the pH of the electrolyte after the contact was measured. During the work with coated materials based on particles, the evolution of the shape, the size and elemental composition of the released species in collected after the experiment solution were also analyzed by the scanning electron microscopy (SEM-FEG-EDS).

4.8.2. Convolution

Using the AESEC method, it is impossible to compare directly the electrochemical current and the elemental dissolution current because of the significantly smaller time constant associated with current measurements. A number of complex physical processes contribute to the broadening of the elemental dissolution current: (1) the diffusion from the surface into the flowing electrolyte stream, (2) mixing in the channel flow cell, (3) spreading out during the laminar flow in the capillaries between the cell and the spectrometer, (4) the complicated nebulization system, etc.

In this work the time constant distribution for the cell is determined experimentally using a copper pulse experiment. A copper electrode is placed in contact with 1 M HCl under open circuit potential, followed by a 1 s potentiostatic pulse, and then return to the open circuit potential, measuring the concentration-time response to a "delta" function of dissolution (time resolution is 1 s).

A typical time constant distribution is shown in **Figure 4.9**, for a 100 mV anodic potential applied for 1 s (upper curve) and the broadened dissolution of copper (lower curve). The shift time, t_0, is the time between the current response and the first point of data which rises above the background, which is associated with the time necessary for the copper ions to travel between the dissolution cell and the plasma.
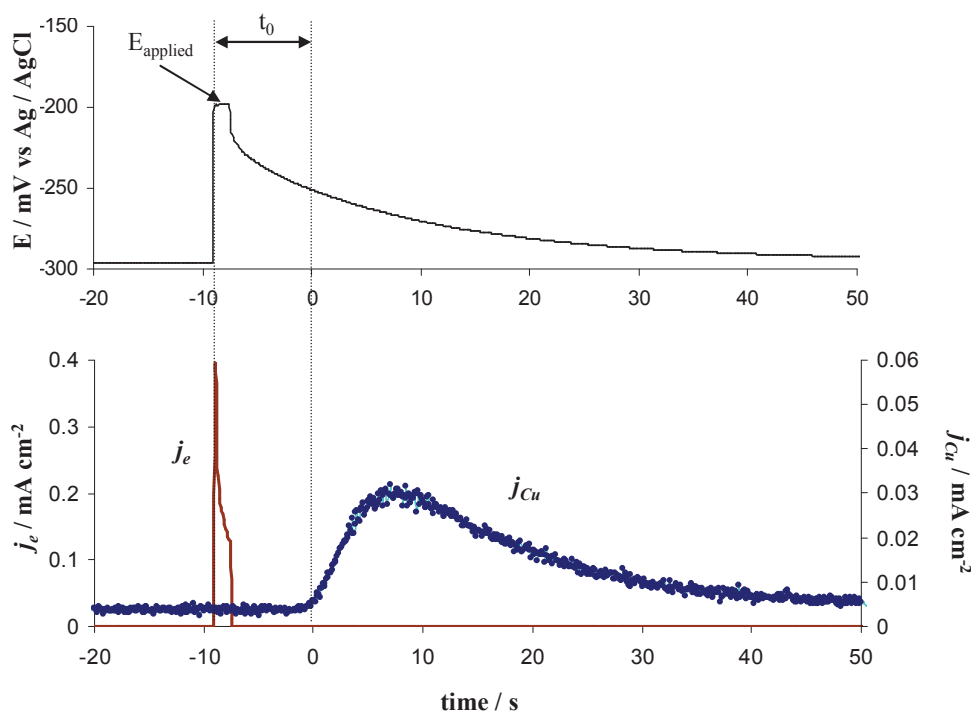
Figure 4.9. Residence time distribution of the flow cell.

Under the conditions of the experiment, the yields of the Cu dissolution reaction should be near 100%, so the measured dissolution rate vs time will be given by the convolution integral:

$$H(t) = (I-I°) / Q \qquad [4.9]$$

where H(t) is the distribution of time constants in the flow cell, I is the total current of the Cu dissolution reaction, corresponded to the applied anodic potential (/ mA cm^{-2}), $I°$ is the background current signal (/ mA cm^{-2}), Q is the total amount of charge (C passed into the system).

An empirical model is proposed to simulate the time constant distribution with a *log-normal* function:

$$H(t) = \frac{I - I°}{Q} = \sqrt{\frac{\beta}{\pi \tau^2}}\, e^{-\frac{1}{4\beta}}\, e^{-\beta \ln^2\left(\frac{t}{\tau}\right)}$$

$$[4.10]$$

where β and τ are characteristic constants for the log-normal distribution.

Figure 4.10 shows the data from **Figure 4.9** using simulated by equation 4.10 as a function of time on a logarithmic scale. This equation is used as an approximation of the experimental residence time distribution. The time constants β and τ are determined to be 1.01 s and 9.8 s respectively.
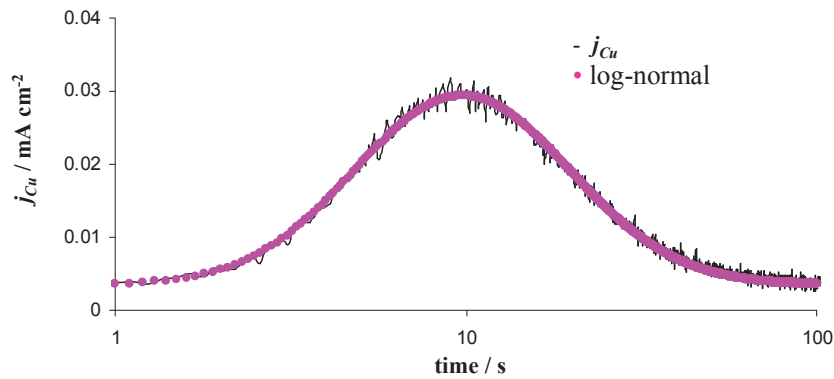
Figure 4.10. The Cu dissolution curve and convoluted total current from Figure 4.9.

4.8.3. Application of AESEC for particles release

The quantification of released particles can provide important information about the corrosion mechanisms of some materials such as aluminum alloys containing precipitated copper intermetallics [7] or the degradation of particle rich paint systems. The most common method of sample introduction into plasmas is the nebulization of a homogeneous liquid into which the elements of interest have been dissolved. The release of metallic particles in the corrosion mechanism, may however lead to the introduction of these metallic particles directly into the plasma. It has been noted that emission spectroscopic monitoring by ICP can provide the quantitative information concerning the mass and composition of the individual particles if the particles are not too small (diameter $\gtrsim 250$ nm) or not too big to be fully atomized in the ICP [8].

It is well known that the particle size distribution is the limiting factor to control their analytical transfer into the plasma [9]. Particles nebulization requires that both, the transport efficiency of the particle through the sample introduction system and the atomization efficiency of these particles in the plasma, must be identical for all particles in the solution [9]. Only if these criteria are met, the simple aqueous calibration may be used and precise analytical results attained. However, these criteria are rarely met. The transport and atomization efficiencies for the kaolin particles (chemical composition is $Al_4[Si_4O_{10}](OH)_8$, contains 39,5% Al_2O_3, 46,5% SiO_2 and 14% H_2O) directly from emission intensity data was measured [10]. It was shown that the transport efficiency for particles of 10 µm diameter is about 3–4%. This transport efficiency improved to 14–15% when the particle size decreases up to 5 µm. The transport efficiency of the particles changes when the material of the particles and nebulization system changes [11].

During the degradation of the coating, the detachment of Al particles and their dissolution take place simultaneously. In order to distinguish these phenomena the behavior of the particles in the plasma was analyzed during this PhD work (see **chapter 6**). The frequency of the Al particles release from the coating was determined by a home-made peak detection software. The program works with the original data files, obtained by Quantum XP software in the AESEC technique.

4.9. Conclusions

In this chapter, there is a detailed introduction about AESEC technique, its principles and quantification procedure.

The aim of this work is to measure *in-situ* the complex degradation phenomena for complex systems such as metals, alloys and intermetallics and model high temperature coated system. The novelty of this work is the use of atomic emission spectroelectrochemistry (AESEC), which allows us to determine the individual rates of each elemental phenomena in real time and compare them with total current of the reaction due to the couple between ICP and electrochemical cell. The degradation is investigated both at open circuit and under electrochemical control to simulate the conditions that might occur during a galvanic couple between steel and Al when both anode and cathode are in close proximity.

The main advantages of the ICP-OES for this application are:
- Measurement of elemental concentrations as a function of time(mainly Al, Si, Mg, Cu and Fe are investigated in this work);
- Linearity up to 5 orders of magnitude (from µg/L to g/L during the same experiment);
- Simultaneous quantification of up to 30 elements;
- Low detection limits (1.5 µg/L for Al and Fe, 4 µg/L for Cr, etc.);
- Low matrix effect;
- Simple operation processes.

The main improvements of the AESEC method presented in this work include:
- The measurement of the pH after the contact of the aggressive electrolyte with reactive surface;
- The analyses of the released particles and quantification procedure for them;
- The convolution procedure for short transient calculations.

4.10. References

1. Ogle, K. The Cathodic Dissolution of Al and Al Alloys_and Al-Rich Silane Based Paints. (2010).
2. Manning, T. J. & Grow, W. R. Inductively coupled plasma – atomic emission spectrometry. *THE C H E M I C A L EDUCATOR* **2**, (1997).
3. Ogle, K., Baeyens, J., Swiatowska, J. & Volovitch, P. Atomic emission spectroelectrochemistry applied to dealloying phenomena: I. The formation and dissolution of residual copper films on stainless steel. *Electrochimica Acta* **54**, 5163–5170 (2009).
4. Światowska, J., Volovitch, P. & Ogle, K. The anodic dissolution of Mg in NaCl and Na2SO4 electrolytes by atomic emission spectroelectrochemistry. *Corrosion Science* **52**, 2372–2378 (2010).
5. Мосин, О. В. ПОГЛОЩЕНИЕ СОЛНЕЧНОГО ИЗЛУЧЕНИЯ АТМОСФЕРОЙ И ГИДРОСФЕРОЙ ЗЕМЛИ И ПРОИСХОЖДЕНИЕ ЖИЗНИ. *Самиздат* (2007).at <http://zhurnal.lib.ru/o/oleg_w_m/cdocumentsandsettingsolegmosinmoidokumentypoglosh eniesolnechnogoizluchenijaatmosferojigidrosferojzemrtf.shtml>
6. Berkner, L. V. & Marshall, L. C. On the Origin and Rise of Oxygen Concentration in the Earth's Atmosphere. *J. Atmos. Sci.* **22**, 225–261 (1965).
7. Mokaddem, M., Volovitch, P., Rechou, F., Oltra, R. & Ogle, K. The anodic and cathodic dissolution of Al and Al-Cu-Mg alloy. *Electrochimica Acta* **55**, 3779–3786 (2010).
8. Miclea, M., Garcia, C. C., Exius, I., Lindner, H. & Niemax, K. Emission spectroscopic monitoring of particle composition, size and transport in laser ablation inductively coupled plasma spectrometry. *Spectrochimica Acta Part B: Atomic Spectroscopy* **61**, 361–367 (2006).
9. Goodall, P., Foulkes, M. E. & Ebdon, L. Slurry nebulization inductively coupled plasma spectrometry-the fundamental parameters discussed. *Spectrochimica Acta Part B: Atomic Spectroscopy* **48**, 1563–1577 (1993).
10. Ebdon, L. & Collier, A. R. Particle size effects on kaolin slurry analysis by inductively coupled plasma-atomic emission spectrometry. *Spectrochimica Acta Part B: Atomic Spectroscopy* **43**, 355–369 (1988).
11. Fernandez-Sanches, M. L., Fairman, B. & Sanz-Medel, A. Direct Analysis of Slags by Inductively Coupled Plasma Atomic Emission Spectrometry Using Slurry Sample Introduction Techniques. *Journal of analytical atomic spectrometry* **6**, 397–401 (1991).

Chapter V

Atomic Emission Spectroelectrochemistry study of the degradation mechanism of model high-temperature paint containing sacrificial aluminum particles

Maria Serdechnova, Polina Volovitch, Kevin Ogle

Atomic Emission Spectroelectrochemistry study of the degradation mechanism of model high-temperature paint containing sacrificial aluminum particles

The atomic emission spectroelectrochemistry (AESEC) technique was used to monitor the degradation of a model high temperature coating in 30 g/l NaCl electrolyte during spontaneous reaction and under polarization. The kinetics of the dissolution of the binder, the detachment and the dissolution of metallic pigment particles and the corrosion of the substrate were measured simultaneously. Sharp peaks and a continuous increase of the background level under the peaks were observed on the Al dissolution profile (concentration vs. time) under applied cathodic potential. By comparing of the real coating with the model particle suspension, it was demonstrated that the peaks correspond to the release of Al particles from the coating due to the destruction of the binder. The continuous increase of the background level under the peaks during the coating degradation was related to the Al dissolution reaction due to the local pH increase near the surface. High Si dissolution coming from the binder was observed under cathodic polarization, accompanied by the decrease of Al dissolution rate. These results strongly suggest that the dissolution of the Al particles and the Si binder under cathodic polarization are related competitive reactions. Specific calibration was made to quantify the amount of the released particles at different applied potentials and recalculate it as a thickness of the degraded coating. It was demonstrated that the coating can be completely destroyed under applied cathodic potential.

5.1. Introduction

Sacrificial metallic pigments are widely used in high temperature paints (Al – [1-3], Mg – [4-6], Zn – [7, 8]). In existing formulations sacrificial particles are suspended in an inorganic matrix [9, 10] and combined with a Cr (VI)-based inhibitor [11]. Silicate-containing binders are widely used for high temperature applications [9, 12]. All coating components mutually influence the coating performance. For instance, the presence of soluble silicates released from the binder can influence the behavior of the Al particles. Rahman at al. [13-15] noted the increase of the open circuit potential and of the Al corrosion rate in the presence of silicates. The accelerating effect of silicates is explained by a structural modification of the aluminum oxide layer (the formation of alkali metal aluminosilicate) in the presence of soluble silicates in NaOH solution [16].

The replacement of chromate due to the toxicity of chromium (VI) [17] necessitates the reformulation of older systems. A large number of simultaneous phenomena occurring during coating degradation makes it difficult to interpret the influence of the formulation changes on the coating performance by classical electrochemical measurements or by corrosion tests. For example, for steel covered with a coating containing a sacrificial metallic pigment, degradation phenomena may include: (i) the dissolution of the binder, (ii) the dissolution of the metallic pigment, (iii) the release of the pigment particles, and (iv) the leaching of the inhibitor. The steel substrate can also react with the electrolyte through the pores in the coating. Electron transfer or chemical interaction between dissolved ions can further complicate the degradation mechanisms.

The aim of this work is to measure *in situ* the complex degradation phenomena for a model high temperature coated system. The novelty of this work is the use of atomic emission spectroelectrochemistry (AESEC), which allows us to determine the individual rates of each of the previously mentioned elemental phenomena in real time. The degradation is investigated both at open circuit and under electrochemical control to simulate the conditions that might occur during a galvanic couple between steel and Al when both anode and cathode are in close proximity.

5.2. Materials

All samples used in this work were model samples - they were prepared in the laboratory with the intention of reproducing phenomena that might be observed with commercial materials. However, they should not be considered representative of any existing commercial product or products in development.

The model system consists of a 15CDV6 steel substrate (elemental composition in table 5.1) with an Al-particle rich silicone based coating of 25 to 35 µm thickness. Before application of the coating, the steel substrate was sand blasted with silica particles (diameter 80–150 µm, air pressure 4 bar).

Table 5.1. Elemental composition of 15CDV6 steel

Metal	Fe	C	Si	Mn	Cr	Mo	V	S	P
Wt. %	Base	0.16	0.18	0.86	1.60	0.85	0.220	0.001	0.006

Commercial 99.8% Al powder with 13.1 µm average particle diameter was mixed with a Si binder and applied by spray to the surface. The coated samples were kept for 15 minutes at room temperature, 1 hour at 250 °C corresponding to the typical conditions for reticulation of the binder, used in this work. They were subsequently stored at room temperature under air for about 4 months.

A cross-section SEM image of the steel/coating interface is shown in **figure 5.1A** obtained with a Zeiss Supra 55 VP scanning electron microscope_operating with an accelerating voltage of 5 kV. The particle size distribution for the 13.1 µm Al particles, used for the preparation of model high temperature coating, and are presented in **figure 5.1B**. Also shown, are the particle size distributions of two other samples of Al particles used in the particle calibration experiments. The particle size distributions were obtained with a laser scattering analyzer Horiba LA-950. The experiment was done in isopropanol.
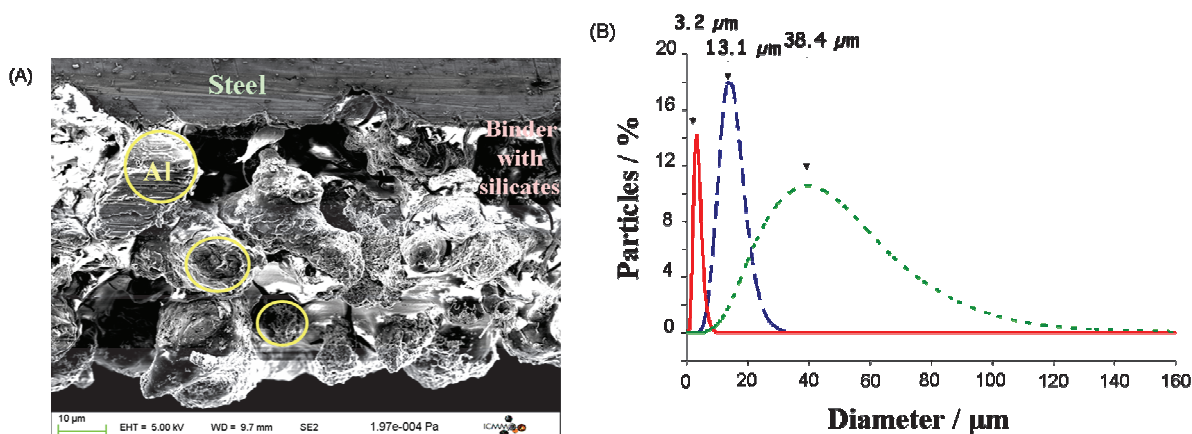
Figure 5.1. Cross-section image of the steel/coating interface of the model sample obtained by scanning electron microscopy (A) and and the size distributions of three different types of Al pigments, used in this work (B).

Before the experiment, the samples were rinsed in purified water obtained with a Millipore[TM] system (resistivity of 18.2 MΩ cm). Dissolution rates of the coating elements were measured in a 3 % NaCl electrolyte. All reagents were of analytical purity grade and produced by Analar Normapur VWR[®] BDH Prolabo[®].

5.3. Technique

The atomic emission spectroelectrochemistry (AESEC) technique has been previously described in detail [18] and a simplified schematic diagram is shown in **figure 5.2**. Briefly, the reaction between the steel/paint system and the electrolyte occurs in the flow cell (**figure 5.2.I**) and leads to the production of dissolved ions and released particles. The flow-cell for AESEC experiments is configured as a three electrode electrochemical cell. In this way the potential can be monitored and controlled for the acceleration of the reaction during the experiment. All potentials are given relative to an Ag/AgCl electrode. The area of the contact between coated sample and the electrolyte during the reaction is $A = 0.51$ cm^2.
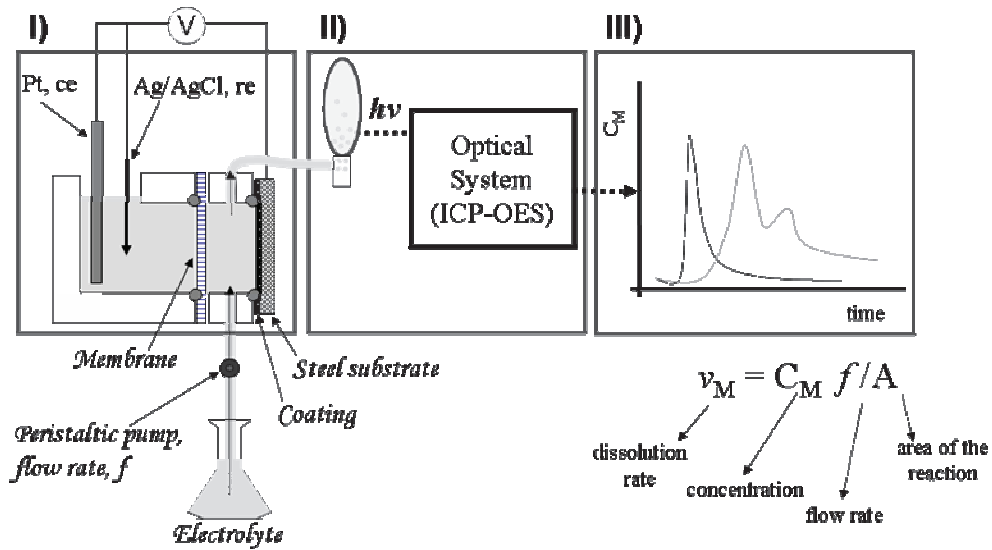
Figure 5.2. Simplified diagram of the AESEC experiment: I) reaction three electrode cell; II) analytical ICP-OES system; III) monitoring result.

The electrolyte is transported to the inductively coupled plasma optical emission spectrometer (ICP-OES) where its composition is continually analyzed (**figure 5.2.II**). The instantaneous rate of dissolution in the cell, v_M, is directly related to the instantaneous concentration downstream from the cell by the equation 5.1 (**figure 5.2.III**):

$$v_M = f\,C_M/A \qquad\qquad\qquad [5.1]$$

where f is the flow-rate (3.0 ± 0.1 cm^3/min in our experiments), C_M is the concentration of the element M in the solution, and A is the area of the exposed surface . C_M is measured from the emission intensity at a specific wavelength using normal quantitative procedures in ICP experiment.

The dissolution rate can be recalculated into units of the elemental dissolution current, according to the Faraday law (equation 5.2):

$$j_M = n\,f\,F\,C_M/A = n\,F\,v_M \qquad\qquad\qquad [5.2]$$

where j_M is the effective elemental current in A cm^{-2}, n is number of electrons, F is the Faraday constant. Thus, the total electrochemical current (J) can be decomposed into the contribution of elementary reactions.

ICP measurements were made with an ICP-OES Ultima2C (produced by Horiba JobinYvon), which uses a polychromator to allow simultaneous measurement of 30 spectral lines of different elements. The focal distance of the polychromator is 50 cm. The nebulizer *Meinhard K3*, produced by Horiba JobinYvon, was used to aspirate the solution after the reaction into the plasma. The wavelengths and standard deviations of the signal (2σ) [18] during the experiment, studied in this work, are listed in table 5.2.

Table 5.2. The detection limits of the AESEC technique under the conditions of the experiment.

	Al	Fe	Si
λ / nm	167.021	259.940	251.610
$C_{2\sigma}$ / ng cm^{-3}	2.0	2.2	9.0
$i_{2\sigma}$ / μA cm^{-2}	1.2	1.1	4.0

One advantage of the ICP analysis is that only a fraction of the solution (about 5%) is aspirated into the plasma, the remaining 95 % of the solution is retained. Therefore it is possible to analyze the pH of this residual solution. During the applied potential experiment, the solution was collected by aliquots of 9 cm^3 (during each 3 minutes) and the pH was measured.

The frequency of Al particle release from the coating was determined using a peak detection software developed in-house for this application.

5.4. Results

5.4.1. ICP-OES detection of released particles

During the degradation of the coating, the detachment of the Al particles and their dissolution take place simultaneously. In order to distinguish these phenomena, a simulation experiment was done. Suspensions with different concentrations of Al particles in 3 % NaCl were prepared and aspirated into the plasma.

Figure 5.3 presents the ICP signal as a function of time during the aspiration of a suspension of $8.5 \cdot 10^{-4}$ g cm^{-3} Al particles, in 3 % NaCl (initial pH 6.3). The average size was 13.1 µm as used in the model coating. The first time period, I, shows the 3 % NaCl electrolyte without particles. The second time period, II, shows the effect of the Al particles on the signal. The aspiration of individual particles into the plasma leads to the appearance of narrow peaks in the intensity versus time profile. In neutral pH (time from 0 to 400 sec) the reactivity of

aluminum is low and only isolated particles are transferred to the plasma and no significant background increase in Al concentration is observed.
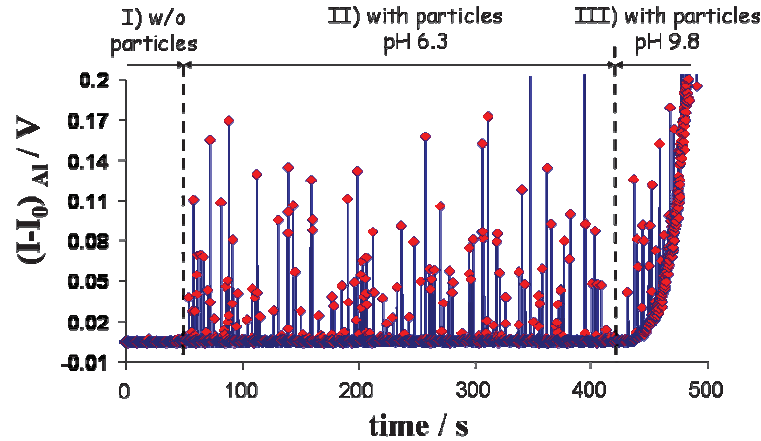
Figure 5.3. Measured by AESEC Al signal (I-I$_0$) form the Al particles suspension (concentration 8.5·10^{-4} g/cm^3) at neutral pH and after the injection of NaOH.

Period III shows the effect of adding a drop of NaOH into the solution with Al particles. The pH increased continuously up-to 9.8 with a simultaneous increase in the Al dissolution. A marked and steady increase in the background Al concentration is observed which we attribute to an increase in the Al dissolution rate due to the increase of the solution pH.

To estimate the number of particles released from the coating, a calibration in 3 % NaCl at neutral pH was done. **Figure 5.4A** gives the resulting calibration curves obtained from dissolved Al standards (0 μm particle size) and the 3.2 μm, 13.1 μm and 38.4 μm particle systems. The total number of peaks (N_{pi}), which are higher then detection limit (2σ) during the calibration experiments, was determined using a special software developed for this purpose. The number of Al particles in the solution (N_{pa}) was estimated from the total Al weight in the suspension divided by the average weight of 1 particle. The average ratio of these two values (N_{pi}/N_{pa}) gives the percentage of particles transferred to the plasma – 87 % for 3.2 μm, 4 % for 13.1 μm, about 0.1 % for 38.4 μm particles (**figure 5.4B**). The particle size distribution analysis shows that these percentage values correspond to the fraction of the particles less than 7 μm diameters (5.0 μm for 3.2μm particles, 7.0 μm for 13.1 μm particles and 6.9 μm for 38.4 μm particles).
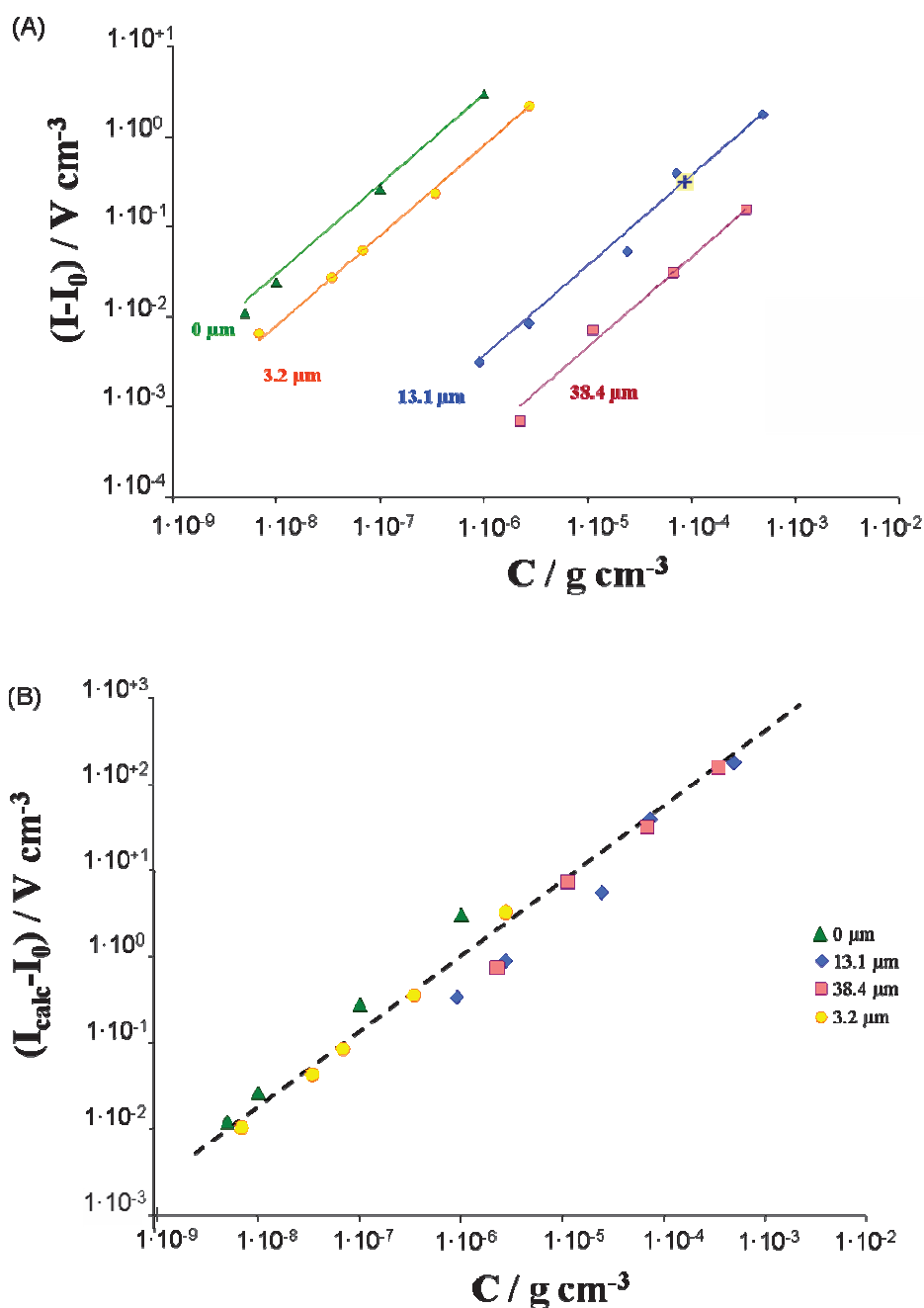
Figure 5.4. Calibration curves for suspension with different average particles diameter (3.2 nm, 13.1 nm and 38.4 μm) and solution. a) Measured ICP signal intensities (I-I_0) as function of concentration; b) theoretical intensity of the ICP signal (I_{calc}-I_0), calculated in assumption that 100 % of the particles could be injected to the plasma. The big point on the 13.1 μm suspension corresponds to the detached particles from model sample (see section 5.2).

The results presented in **figure 5.4A**, demonstrate that the AESEC technique is more sensitive to those particles with smaller diameter, corresponding with literature data [19]. However, for each series of solutions, there is a linear dependence between the Al particle concentration in the solution and the total peak intensity per cm³ of solution (obtained by the integration of the

curve), **figure 5.4A**. This linear dependence allows us to calculate the concentration of Al in the solution. The theoretical intensity of ICP signal (I_{calc}), calculated by assumption that 100 % of the particles could be injected to the plasma, is shown on **figure 5.4B**. All curves for different size distributions coincide well in this normalization.

5.4.2. Coating degradation in 3% NaCl: spontaneous reaction and polarization experiment

Figure 5.5 shows typical dissolution profiles of Fe, Si, Al and open circuit potential in 3% NaCl as a function of time. The background level (**figure 5.5**, region I) is measured prior to contact between the sample and the electrolyte (t < 0).
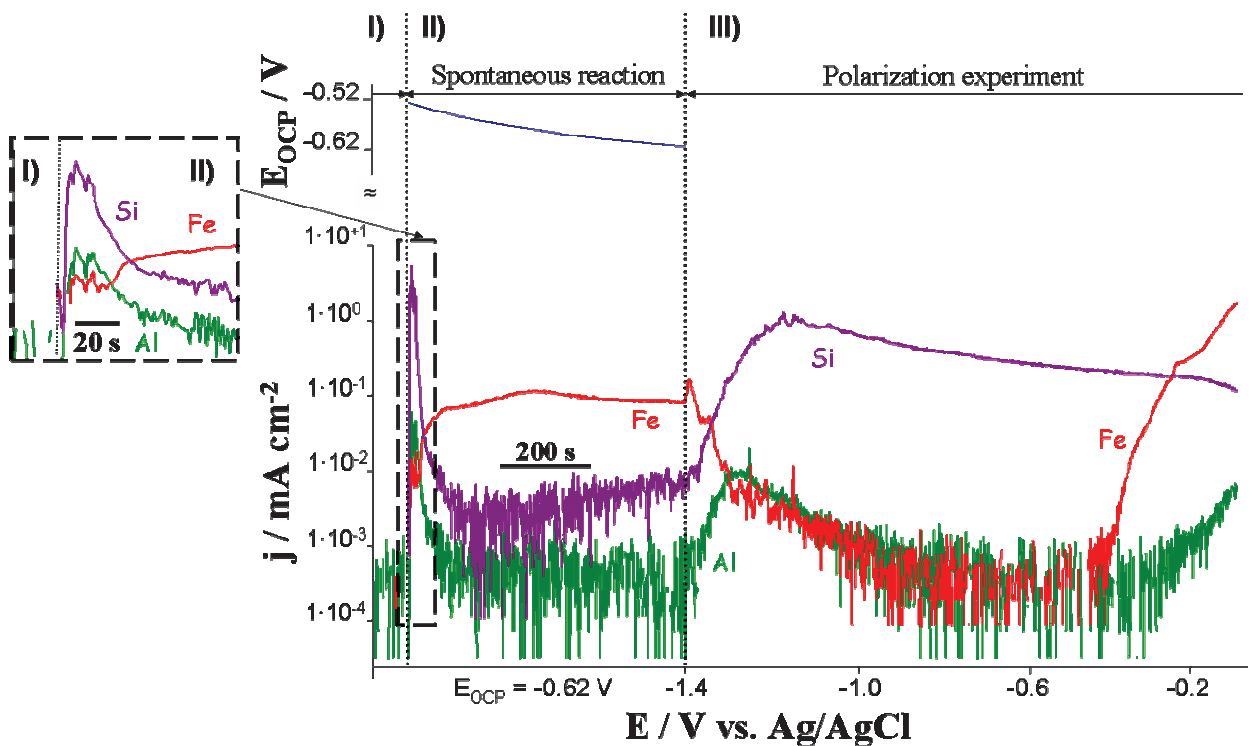
Figure 5.5. Dissolution rates of Fe, Si and Al during spontaneous reaction (region II) and under

At time t = 0 the electrolyte contacts the surface (**figure 5.5**, region II) and Si dissolution is observed. Due to the high dissolution rate of unstable Si impurities on the surface, several particles of Al from the coating are also removed. However the dissolution rate of Al and Si decrease rapidly after the initial surface reaction because of the formation of a protective Al oxide layer in neutral pH.

The Fe dissolution rate increases significantly as soon as Al particles are released, probably due to the formation of pores in the coating and the consequent contact of the steel substrate with the electrolyte. The value of the open circuit potential (-0.62 V vs. Ag/AgCl) corresponds to the corrosion potential of the steel substrate in the absence of the coating.

After 600 s the sample is polarized (**figure 5.5**, region III). Under cathodic potential the dissolution rates of Si and Al pass through a maximum and decrease. The Fe dissolution rate decreases at the same time. In the anodic region, intense dissolution of Fe is observed. This indicates that the destroyed coating no longer protects the steel substrate and no galvanic protection effect is observed.

5.4.3. The coating degradation under constant applied potential

To understand the change of the Al, Si and Fe dissolution rates during polarization, a series of experiments was performed with a constant imposed potential. Cathodic potentials (-1.4 V, -1.3 V, -1.2 V, -1.1 V vs Ag/AgCl) were applied in separate experiments using a fresh sample.

Figure 5.6 shows the typical form of the dissolution rates of Fe, Si, Al and the total electrochemical current as a function of time for the model sample at one of the applied cathodic potential (-1.3 V); t = 0 corresponds to the beginning of the applied potential; t < 0 – the sample is in contact with the electrolyte at the open circuit potential.

Figure 5.6. Total electrochemical current J and the elemental dissolution currents j_{Si4+}, j_{Al3+}, j_{Fe3+} measured by AESEC during spontaneous reaction and under applied cathodic potential ($E_{applied}$) -1.3 V vs. Ag/AgCl as indicated. See text for more details.

It is possible to distinguish 5 periods in the dissolution profile at applied potential.

First period (I): A low level of Fe and Al dissolution is observed. Several peaks are seen for Al dissolution in both Al emission lines (167.020 nm and 396.152 nm). These we attribute to particle detachment as described in section 4.1

Second period (II): The Fe dissolution rate decreases, while the Al and Si dissolution rates increase and the frequency of the Al peaks increases.

Third period (III): The Fe dissolution rate increases. The Si dissolution rate increases and at the end of third period reaches its maximum. The Al dissolution rate decreases. The frequency of the Al peaks is practically the same as in the second period.

Fourth period (IV): The Fe dissolution rate is maximal and the Al dissolution rate is minimal. The Si dissolution rate decreases. The frequency of the Al peaks increases dramatically.

Fifth period (V): The Fe and Si dissolution rates decrease. The Al dissolution rate increases and the frequency of the Al peaks is very high.

The pH of the solution increases from 6.3 during spontaneous reaction to 9.3 during cathodic polarization (table 5.3).

Table 5.3. pH of the solution during the applied potential experiment

Time / s	Initial	0-180	180-360	360-540	540-720	720-900	900-1080
Average pH	6.3	6.6	7.3	7.8	8.7	9.1	9.3

The kinetics of degradation under an applied anodic potential are very different (**figures 5.7**, the applied potential -0.3 V vs. Ag/AgCl). The Si dissolution rate is negligible. Both Al and Fe dissolve under these conditions and the Fe dissolution rate is much higher than the Al dissolution rate. This result demonstrates the absence of a galvanic coupling effect between steel and Al due to the absence of the electrical contact between them. The absence of this contact is probably due to a layer of passive Al oxide.
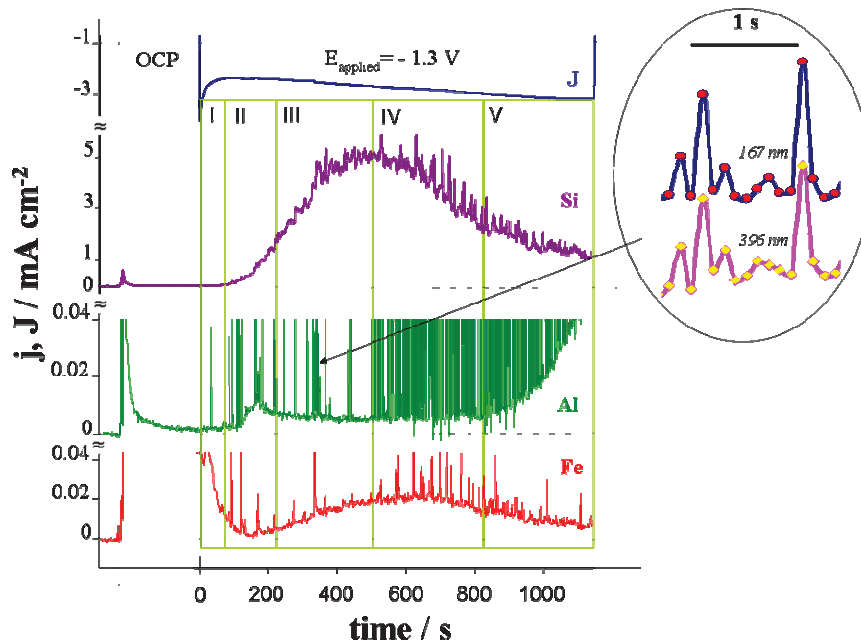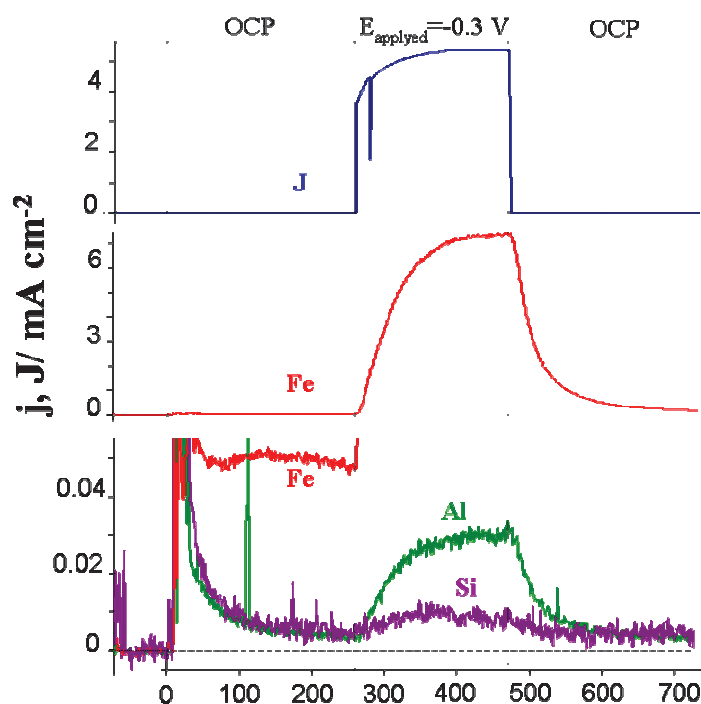
Figure 5.7. Total electrochemical current J and the elemental dissolution currents j_{Si4+}, j_{Al3+}, j_{Fe3+} measured by AESEC during spontaneous reaction and under applied anodic potential - 0.3 V vs. Ag/AgCl. See text for more details.

5.4.4. Level of Si dissolution

During the constant potential experiment, the absolute value of the Si dissolution rate depends on the applied potential (**figure 5.8A**). However, trends are similar for all applied cathodic potentials.

First of all, there is a maximum of Si dissolution. The shaded regions for each potential curve have the same area showing that the amount of dissolved Si prior to the maximum is the same in each case: $(15 - 18$ g m$^{-2})$. Assuming that the Si is present in the coating as SiO_2 with density – 2.2 g cm^{-3}, the thickness of dissolved Si can be approximated as 7-8 μm This value is approximately equal to the amount of Si used. The maximum on the Si dissolution rate corresponds to the quick increase of Al particle release: the average frequency of peaks in the Al dissolution profile increases considerably (**figure 5.8B**). The logical interpretation is that when the binder from the coating dissolves, the metallic particles detach from the surface more easily.
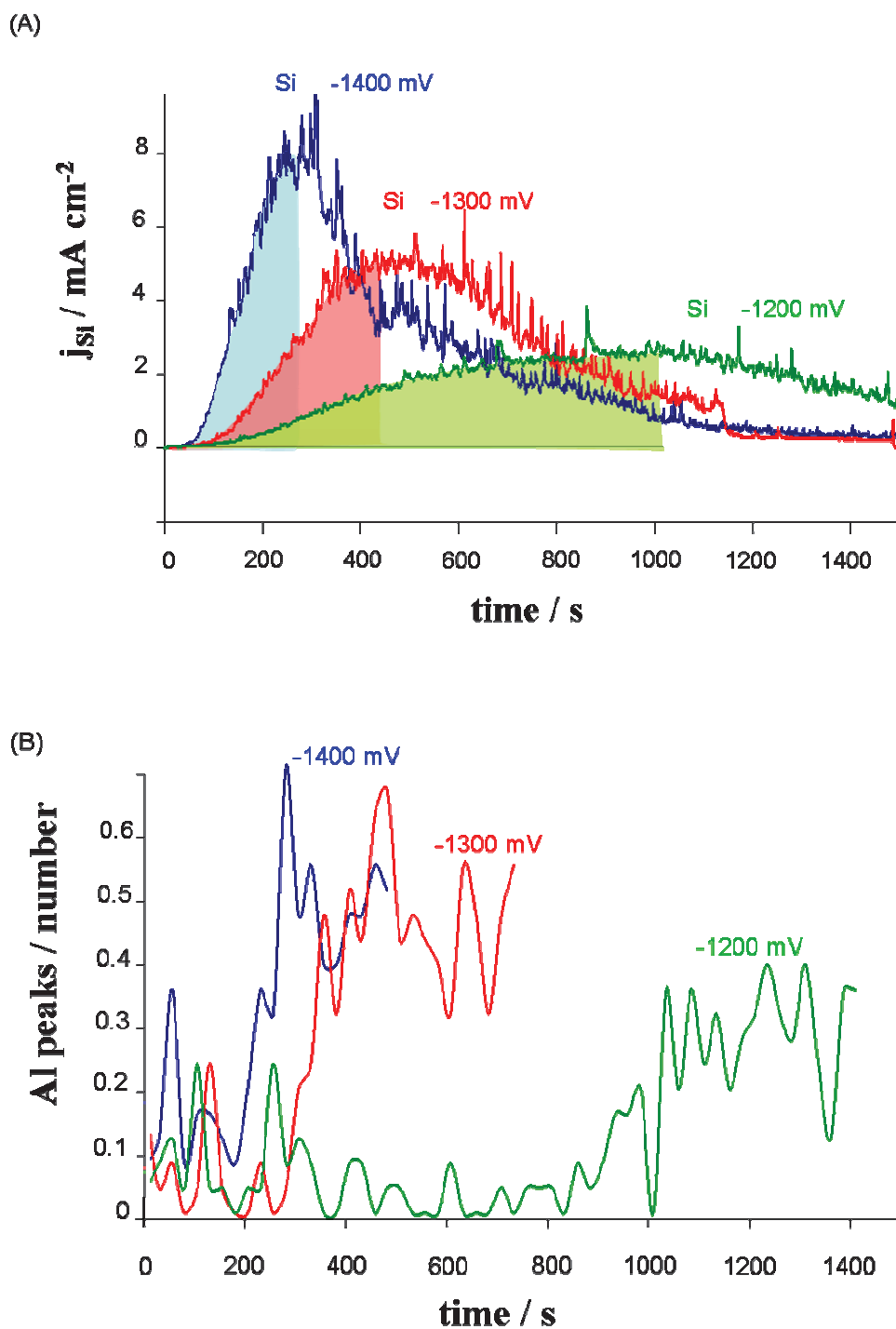
Figure 5.8. Dissolution rates of the siloxane binder, j_{Si4+} (A) and the average number of peaks on aluminum dissolution rate (peaks in second) (B) as a function of time under different applied potential.

Secondly, when the dissolution rate of Si is high, the dissolution rate of Al is low. The dependence of Al and Si dissolution rate as a function of the total current of the reaction is shown in the **figure 5.9**. The Al peaks due to detached particles have been removed for this figure by simply deleting the point (the width of the particle peaks is well below the

integration time for data acquisition, so each peak represents a single point. This was done because the detached Al particles do not transfer electrical charge and could not be compared with total current of the reaction.
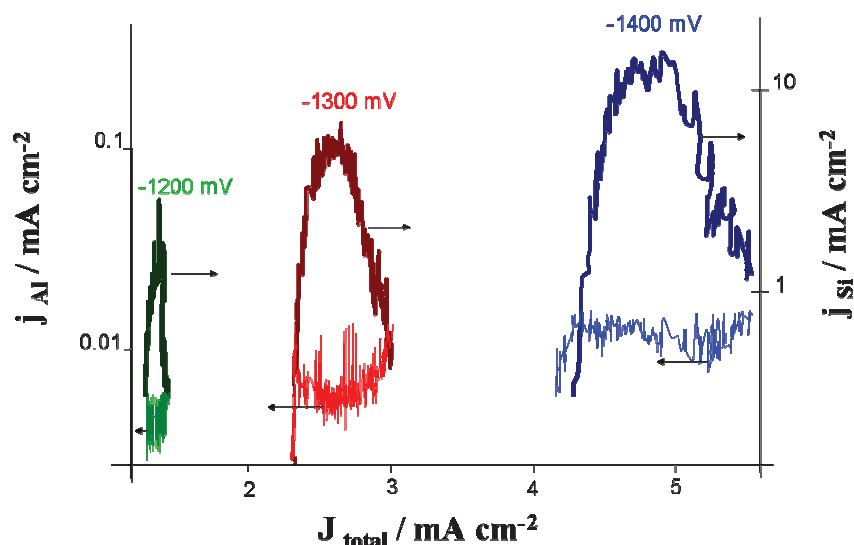
Figure 5.9. Dissolution rates of the siloxane binder (j_{Si4+}) and of Al pigment (j_{Al3+}) as a function of the total electrochemical current (J).

5.5. Discussion

5.5.1. The ratio between the siloxane dissolution rate and Al reactivity

The results presented in this article may be interpreted in terms of the competitive dissolution reactions. Under cathodic polarization, water decomposition leads to the formation of OH^- on the surface according to reaction (5.3) [20, p.16-23]:

$$2H_2O + 2e \rightarrow H_2 + 2OH^- \qquad (E = - 0.83 \text{ V vs NHE or } E = -1.03 \text{ vs Ag/AgCl}) \qquad [5.3]$$

In the previous studies it was shown that OH^- ions can react with both the siloxane in the binder (by reaction 5.4) [20, p. 105-154] and the Al particles (by reactions 5.5 and 5.6) [21].

$$(k_1) \qquad [5.4]$$

$$Al + 4OH^- -3e \rightarrow Al(OH)_3 + OH^- \rightarrow Al(OH)_4^- \qquad (k_2) \qquad [5.5]$$

81

$$Al_2O_3 + 3H_2O + 2OH^- \rightarrow 2Al(OH)_4^- \qquad\qquad [5.6]$$
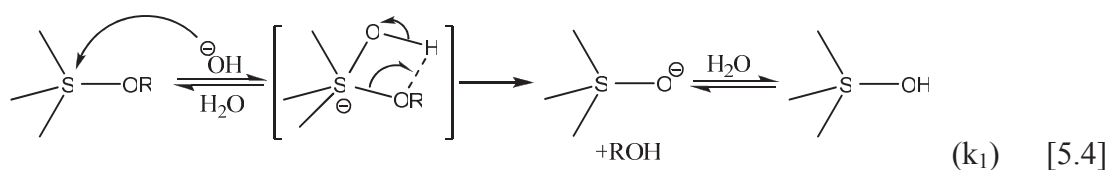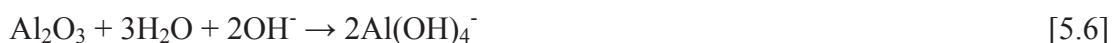
Our results suggest that the binder reacts first with OH^-, probably because the Al particles are covered by the siloxane binder. When the siloxane binder dissolves actively, the amount of OH^-, available for the Al dissolution, decreases. During this time Al can be reached only through the porosities formed in the destroyed binder by OH^- that has not reacted with the binder.

At the beginning of the degradation (periods I and II, **figure 5.6**), the active surface of Al is smaller than the active surface of the siloxane binder; however the effective rate constant is considerably higher for reaction (5.5) [22] than for reaction (5.4) [23]. This leads to comparable dissolution rates of Al and Si at the beginning of the reaction.

With time (periods II and III, **figure 5.6**) the binder is partly destroyed and its active surface increases due to the penetration of the solution into the binder. It leads to the continuous increase of the siloxane dissolution rate.

This mechanism is consistent with the behavior of Al particles observed during the applied potential experiment. The five periods which observed in **figure 5.6** are summarized in **figure 5.10**.
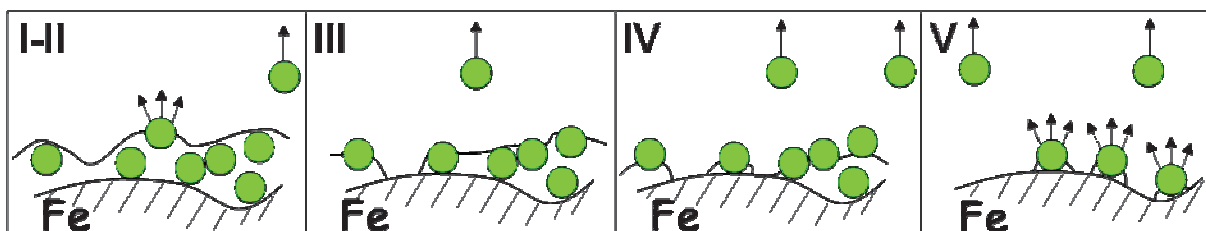
Figure 5.10. Proposed mechanism of the coating degradation under applied cathodic potential.

First period (I): The steel substrate is partially protected by a barrier effect, but the siloxane binder dissolves slowly with increasing dissolution rate because of the increase of the active surface. Only those particles, which are poorly attached, will be removed.

Second period (II): The number of pores in the siloxane binder increases and Al can dissolve through the micropores in the siloxane binder by reaction (5.5). The rate of reaction (5.5) is four orders of magnitude higher than the rate of reaction (5.4) [22, 23], allowing us to detect

the dissolved Al by AESEC. The electrolyte has not come into contact with the Fe substrate at this stage.

Third period (III): The rate of Si dissolution is very high and nearly all OH⁻ ions produced by reaction (5.3) are consumed by reaction (5.4). The frequency of the Al particle release is practically the same as in the first and second periods. At the end of the third period the Si dissolution passes through a maximum. We attribute this decrease to the fact that the siloxane layer is mostly consumed.

Fourth period (IV): The binder is mostly consumed leading to a dramatic increase in the frequency of Al particle release. However, Al dissolution is still blocked by siloxane dissolution (reaction (5.4)).

Fifth period (V): All binder is consumed. The decrease of the siloxane dissolution rate is accompanied by the increase in the Al dissolution rate; OH⁻ ions formed during the cathodic reaction are available and can react with Al, leading to its dissolution. The slow decrease of the siloxane dissolution rate is due to its build up in the capillaries between the reaction cell and the plasma.

5.5.2. Particle detachment during the experiment

Particle detachment occurs during the periods IV and V (**figure 5.6**). Using the calibration curve it is easy to calculate the number of the Al particles in the solution. The sum of the peak intensities of the ICP signal during the reference period can be transformed into the average peak intensity per cm^3 of the solution in V cm^{-3}:

$$I_{a,\,cm3} = \Sigma_{time}(I - I_0) \,/\, (\Delta t\, f),\qquad\qquad\qquad [5.7]$$

where I is the output intensity of the photomultiplier at 167.020 nm in V, I_0 is the average background intensity in V, Δt is the time of the reference period in s.

Calculated by equation (5.7), the average peak intensity for the period of particle release (500-800 sec on **figure 5.6**, period 4) corresponds to the concentration $c_0 = 1.2 \cdot 10^{-4}$ g cm^{-3} (**figure 4a**).

In the approach of ratio between volumes occupied by aluminum in the spherical particle layer (which were used for coating production) and dense Al layer as ¾ (the average atomic

packing factor for a close-packed structure), the thickness of the detached aluminum layer during the time period from 500 to 1400 sec can be shown to be:

$$d = c_0 f t / (\rho A \, {}^3/_4) \qquad\qquad [5.8],$$

where t is time of the reference period in s, ρ is density of aluminum 2.7 g cm^{-3}, c_0 is the concentration of detached particles.

For the period of intensive particle detachment in **figure 5.6** (from 500 to 1400 s approximately) d is estimated to be about 35 µm. This agrees well with the thickness of the coating measured by SEM (in the range 23-36 µm).

5.6. Conclusions

- The AESEC method allows us to distinguish and to quantify elementary degradation phenomena such as dissolution of metallic pigment, detachment of the pigment particles, the dissolution of the siloxane binder and the corrosion of the steel substrate in a model high temperature paint system.
- The detachment of Al particles during the polarization experiment is observed by ICP and confirmed by SEM. It was shown, that the ICP-OES technique detects only particles with diameter less then 7 µm under the conditions of these experiments.
- Under cathodic polarization, the intensive dissolution of the Si binder blocks the dissolution of Al pigment due to the competitive dissolution reactions (see reactions 5.4 and 5.5), but enhances particle detachment.
- No galvanic protection is observed during the anodic polarization. It can be interpreted by the presence of a passive Al oxide layer on the particles.

5.7. Acknowledgements

(Institute of bioorganic chemistry of the Russian Academy of Sciences, Russia) for developing the peak analyses soft-ware.

5.8. References

1. M.F. Mosser, "Spherical aluminum particles in coatings", United States Patent 4537632, (1985).

2. A.R. Parks, Aluminum sprayed coatings on board U.S. Navy Ships. A ten year overview, United States Navy, Naval Sea Systems Command, Washington, DC http://www.intmetl.com/us_navy.htm

3. Naval Ships Technical Manual, Preservation of Ships in Service, Chapter 631, NAVSEA S9086-D-STM-00, (April 1987).

4. G. Bierwagen, R. Brown, D. Battocchi, S. Hayes, "Active metal-based corrosion protective coating systems for aircraft requiring no-chromate pretreatment" *Progress in Organic Coatings*, **67** (2010) 195–208.

5. M. Nanna, G. Bierwagen, "Mg-rich coatings: A new paradigm for Cr-free corrosion protection of Al aerospace alloys" *Journal of Coatings Technology and Research*, **1,** 2 (2004) 69-80.

6. D. Battocchi, A. M. Simoes, D. E. Tallman, G. P. Bierwagen, "Electrochemical behaviour of a Mg-rich primer in the protection of Al alloys" *Corrosion Science*, **48** (2006) 1292-1306.

7. S. A. Lindquist, L. Més-saros, L. Svenson, "Aspects of Galvanic Action of Zinc-Rich Paints Electrochemical Investigation of Eight Commercial Primers" *Journal of Oil & Colour Chemists Association*, **68** (1985) p. 10.

8. D. Pereira, J. D. Scantlebury, M. G. S. Ferreira, M. C. Almeida, "The Application of Electrochemical Measurements to the Study and Behaviour of Zinc–Rich Coatings" *Corrosion Science*, **30**, 11 (1990) 1135-1147.

9. F. Hoshyargar, S. A. Sherafati, M.M. Hashemi "A new study on binder performance and formulation modification of anti-corrosive primer based on ethyl silicate resin**"** *Progress in Organic Coatings*, **65** (2009) 410–413.

10. X. R. Novoa, M. Izquierdo, P. Merino and L. Espada, "Electrochemical Impedance Spectroscopy and Zero Resistance Ammetres (ZRA) as Tools for Studying the Behaviour of Zinc-Rich Inorganic Coatings" *Material Science Forum*, **44-45** (1989) 223-234.

11. M. Kendig, A. Davenport, H. Isaacs, "The mechanism of corrosion inhibition by chromate conversion coatings from x-ray absorption near edge spectroscopy (Xanes)" *Corrosion Science*, **34** (1993) 41-49.

12. G. Parashar, D. Srivastava, P. Kumar, "Ethyl silicate binders for high performance coatings" *Progress in Organic Coatings*, **42** (2001) 1–14.

13. A.B.M. Rahman, S. Kumar, A.R. Gerson, "The role of silicon in the corrosion of AA6061 aluminum alloy laser weldment" *Corrosion Science*, **52** (2010) 1969-1975.

14. A.B.M. Rahman, S. Kumar, A.R. Gerson, "The specification of Si and other alloying elements in the oxide surface film of galvanically corroded weld fusion zone of laser welded AA6061 aluminum alloy" *Corrosion Science,* **50** (2008) 1267-1273.

15. E.H. Oelkers, "General kinetic description of multioxide silicate mineral and glass dissolution" *Geochimica et Cosmochimica Acta*, **65** (2001) 3703–3719.

16. J. P. Labbe, J. Pagetti, "Study of an inhibiting aluminosilicate interface by infrared reflection spectroscopy" *Thin Solid Films*, **82** (1981) 113-119.

17. http://www.serdp.org (e.g., SERDP Fact Sheet 1119: "Critical Factors for the Transition from Chromate to Chromate-Free Corrosion Protection").

18. K. Ogle, J. Baeyens, J. Swiatowska, P. Volovitch, "Atomic emission spectroelectrochemistry applied to dealloying phenomena: I. The formation and dissolution of residual copper films on stainless steel" *Electrochimica Acta*, **54** (2009) 5163–5170.

19. P. Goodall, M.E. Foijlkes, L. Ebdon, "Slurry nebulization inductively coupled plasma spectrometry-the fundamental parameters discussed" *Spectrochimica Acta* **48B,** 13 (1993) 1563-1577.

20. Неорганическая химия в трех томах, под ред. Ю.Д. Третьякова, Москва *ACADEMIA*, т.2 (2004) (in Russian).

21. K. Ogle, M. Serdechnova, M. Mokaddem, P. Volovitch, "The cathodic dissolution of Al, Al$_2$Cu and Al alloys" *Electrochimica Acta*, **56** (2011) 1711–1718.

22. M. Fertani-Gmati, M. Jemal, "Thermochemistry and kinetics of silica dissolution in NaOH aqueous solution" *Thermochimica Acta*, **513** (2011) 43–48.

23. A.M. Abdel-Gaber, B.A. Abd-El-Nabey, I.M. Sidahmed, A.M. El-Zayady, M. Saadawy, "Kinetics and thermodynamics of aluminum dissolution in 1.0 M sulphuric acid containing chloride ions"*, Materials Chemistry and Physics*, **98** (2006) 291–297.

Chapter VI

The cathodic dissolution of Al, Al$_2$Cu and Al alloys

K.Ogle, M. Serdechnova, M. Mokaddem, P. Volovitch

The Cathodic Dissolution of Al, Al$_2$Cu and Al Alloys

The cathodic dissolution of aluminum has been investigated for 99.99% Al, synthetic Al$_2$Cu, and three Al-Cu –Mg alloys: AA2024, AA7050, and AA2214 offering a range of over two orders of magnitude in hydrogen reduction activity. Atomic emission spectroelectrochemistry (AESEC) was used to directly measure the dissolution rate of the alloy components as a function of the cathodic current during potential sweep and potential step experiments. It was found that for all samples, regardless of the cathodic current density, the stoichiometric ratio of OH produced to Al dissolved varied between 1.4 and 1.8. This value is interpreted in terms of a simple model in which hydroxide generation, Al(OH)$_3$ formation / dissolution, and Al(OH)$_4^-$ diffusion are kinetically coupled together. The selective dissolution of Mg and Cu is also measured and discussed.

6.1. Introduction

Aluminum dissolution occurs even when the aluminum is polarized cathodically, a phenomenon also referred to as "chemical dissolution" or "cathodic corrosion". It was first reported by Caldwell et al. [1] and further investigated by several researchers [2-5]. It may be rate determining for the corrosion of aluminum in neutral solution or under atmospheric conditions due to the local pH increase resulting from a cathodic reaction on the aluminum surface; on the surface of cathodic intermetallic phases such as the Θ phase, Al_2Cu, or the S phase, Al_2CuMg, among others [7-10]; or when the aluminum is in contact with active metals such as Mg [11]. The mechanism by which the cathodic dissolution of aluminum occurs is fairly well understood qualitatively, however little work has addressed the question quantitatively. This is partially due to the difficulty of simultaneously measuring the cathodic electrical current and the Al dissolution rate. This paper addresses this problem using atomic emission spectroelectrochemistry (AESEC) [12-17] to directly measure the dissolution rate of Al and the cathodic current in real time.

The open circuit potential of pure aluminum in neutral pH (determined in this work as E_{oc} = -0.69 vs. Ag/AgCl / V is much more positive than the equilibrium potential of the Al/Al^{3+} couple ($E°$ = -1.873 vs. Ag/AgCl / V) [18]. This is due to the presence of a non conducting oxide film that separates the metal from the environment [19]. As long as this film is intact, the aluminum metal is well protected from the environment and the corrosion rate is very low. This is the case in neutral solution since the $Al(OH)_3$ and other aluminum oxides have a minimum solubility around pH = 6 to 7. If, however, the aluminum is polarized cathodically in a neutral unbuffered solution, hydrogen formation will occur giving rise to a pH increase near the surface. The increased pH leads to an increased solubility of the aluminum oxide film. When oxide dissolution occurs, the underlying metal is exposed and oxidized to replace the dissolved portion of the film.

The overall reactions may be written as:

$$2H_2O + 2e^- \rightarrow H_2 + 2OH^- \qquad\qquad [6.1]$$

$$Al + 3OH^- \rightarrow Al(OH)_3 + 3e^- \qquad\qquad [6.2]$$

$$Al(OH)_3 + OH^- \rightarrow Al(OH)_4^- \qquad\qquad [6.3]$$

The overall reaction is thus

$$Al + 4H_2O + e^- \rightarrow 2H_2 + Al(OH)_4^-$$ [6.4]
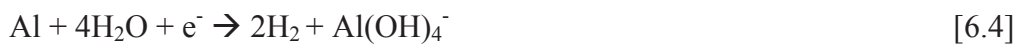
Oxygen reduction may also occur in the solutions exposed to the atmosphere. The diffusion limited oxygen reduction current should be much less than the hydrogen reduction currents observed in this work. Despic *et al.* [2] investigated the stoichiometry between the amount of hydrogen generated and the cathodic current. The H/e ratio varied from 2 at low temperature to 4 at higher temperature. Deviations from 4 at higher temperature were attributed to an increasing fraction of hydroxide escaping by diffusion while the value of 2 obtained at low temperature was attributed to the formation of monovalent Al species on the surface. By combining gravimetric and volumetric analysis with a continuous abrading methodology, Moon and Pyun [3] demonstrated that an oxide film is present on the surface at all applied potentials. The difficulty with these experiments was that the volumetric and gravimetric analysis required rather extreme cathodic conditions for long time periods to collect a significant volume of hydrogen. As an improvement in time resolution and sensitivity, Frankel *et al.* [4] performed time resolved rate measurements using a quartz crystal microbalance on Al and Al-Cu mixtures vapor deposited on the quartz crystal. The authors were able to measure the relationship between the cathodic current although the focus of that work was the effect of chromate and not the mechanism of cathodic dissolution.

In recent work, we applied *atomic emission spectroelectrochemistry* (AESEC) to investigate the dissolution of 99.99 % Al (AA1199) and AA2024 alloy [12]. The AESEC technique, explained in detail in previous publications [12-17] allows us to follow partial elemental dissolution rates *in situ* during a conventional electrochemical experiment. With this technique we demonstrated that we could quantitatively follow reaction processes that cannot be measured with either conventional electrochemical methods or gravimetric and volumetric methods. Examples from reference [12] include the selective dissolution of Mg from AA2024, the release of Cu rich particles from AA2024, and the cathodic dissolution of Al from both Al and AA2024.

The AESEC technique is particularly well adapted for the characterization of the cathodic dissolution of aluminum alloys in that it alloys a direct measurement of the rate of reaction 6.3, v_{Al}, in real time with much higher sensitivity and time resolution than is possible with volumetric or gravimetric techniques. v_{Al} is calculated from the (molar) concentration of Al downstream from the dissolution cell.

$$v_{Al} = f\,C_{Al} / A = f\,(I_\lambda - I_\lambda^\circ)/k_\lambda A$$ [6.5]

Where f is the flow rate of electrolyte in the cell, A is the exposed surface area of the working electrode, I_λ is the emission intensity at λ, I_λ° is the background emission at l in the absence of Al, k_λ is the emission sensitivity expressed in molarity. To facilitate comparison with the measured electrochemical current density, j, it is convenient to express the dissolution rate as an effective current assuming n= 3, therefore,

$$j_{Al} = 3 \; F \nu_{Al} \qquad\qquad\qquad [6.6]$$

Likewise, the total current, j, as measured by the potentiostat is

$$j = j_{cat} + j_{Al} \qquad\qquad\qquad [6.7]$$

where j_{cat} is the total cathodic current. It is important to recognize that we do not measure j_{cat} in this experiment, only the cathodic current *in excess* of that necessary to balance Al oxidation. A simultaneous volumetric measurement of hydrogen would correct this problem to the extent that hydrogen reduction (j_{H_2}, reaction 6.1) is certainly the major contribution to j_{cat}. At the present time however we have no system for this.

The objective of this paper is to use the AESEC method to demonstrate the stoichiometry between j and j_{Al} and to measure the true cathodic polarization curve, j_{cat} as a function of potential. Both measurements requiring the simultaneous measurement of j and j_{Al}. The above hypothesis predicts that the rate of aluminum dissolution at a specific cathodic potential should depend directly on the hydrogen reduction current which is in turn a function of potential and the nature of the oxide/hydroxide film and/or the presence of copper. Therefore the sensitivity of a specific alloy will depend on the catalytic activity of the aluminum surface for hydrogen reduction. This of course is very low for pure Al with an intact oxide / hydroxide film, but is much higher when Cu is present in the alloy. In this work we use a variety of alloys (99.99% Al, pure Al_2Cu, and three commercial Al-Cu alloys) so as to confirm that the j / j_{Al} stoichiometry is independent of the catalytic activity for hydrogen reduction for over several orders of magnitude of cathodic activity.

6.2. Experimental

6.2.1 Materials

The elemental analysis of the commercial aluminum alloys used in this work is given in Table 6.1. The Al metal reference was 99.99% Al (AA1199). The Al_2Cu (θ) phase was synthesized from the elements Al (99.9% purity) and Cu (99.99% purity) by melting small pieces (3-

8 mm) under argon gas in a high frequency inductive furnace, carried out at the University of Nancy (see acknowledgements). A future publication will give the details of the synthesis. All specimens were ground with 1000, 2400 and 4000 grit SiC paper and cleaned with ethanol and deionized water.

Table 6.1: Elemental analysis of the commercial aluminum alloys used in this work. Results are given in mass percent

	Al	Si	Fe	Cu	Mn	Mg	Cr	Zn	Ti	Zr
AA7050	rest	0.04	0.09	2.2	0.01	2.2	0.01	6.3	0.04	0.10
AA2214	rest	0.72	0.17	4.5	0.89	0.54	0.02	0.03	0.03	-
AA2024	rest	0.083	0.162	4.47	0.48	1.51	0.006	0.195	0.022	0.0061
AA1199	99.99	-	-	-	-	-	-	-	-	-

2.2 Instrumentation

The AESEC method has been described in detail in a recent article including a schematic of the electrochemical flow cell and a detailed description of the data acquisition module and the calibration procedure [13]. Briefly, the system consists of an Horiba- JobinYvon inductively coupled plasma optical emission spectrometer (ICP-OES) coupled with an EG&G PAR M273A potentiostat/galvanostat and a home made electrochemical flow cell. The working electrode is exposed to a flowing electrolyte (f = 3 ml/min) in a small volume (0.2 ml) flow cell. The geometrical area of the sample exposed to the electrolyte was 0.5 cm^2 defined by the contour of the *o*-ring. The flow channel has an entrance at the bottom and exit at the top so that electrolyte passes through the cell from bottom to top such that any gas generated during the experiment flows out of the cell. The electrolyte from the electrochemical flow cell was continuously fed into the plasma using a peristaltic pump. The electrolyte is atomized in the plasma and the elemental components are monitored in real time by following the emission at specific wavelengths using an array of photomultipliers in a polychromator.A Pt wire counter electrode and 3 mol dm^{-3} Ag/AgCl reference electrode (E = +208 mV versus SHE at 25°C) were used. In the electrochemical flow cell they are positioned in a 10 ml cylindrical secondary compartment of stagnant electrolyte. This compartment is separated from the working electrode compartment by a porous membrane which allows ionic current to pass from one compartment to the other while preventing bulk mixing of the two electrolytes. All experiments were performed at ambient temperature, approximately 24 ± 1 °C.

In this work, the emission intensity of Al (167.081 nm), Mg (279.553 nm), Mn (257.610 nm), Fe (259.940 nm), Si (251.611 nm) and Cu (325.754 nm) were recorded simultaneously as a function of time along with the electrochemical potential and current. Calibration of intensity vs. concentration was performed using standard ICP-OES methods and normalized calibration standards purchased from *SPC Science*, France. Table 6.2 gives the operating conditions of the plasma defined as $C_{2\sigma}$ the concentration equivalent of the standard deviation (σ) of the background signal at a given wavelength. the as described previously.

Table 6.2: Typical analytical characteristics of the ICP-OES spectrometer with the 2s equivalent concentration and equivalent current assuming n=3 for Al, n=4 for Si and n=2 for the other elements.

	Al*	Al	Zn	Si	Mn	Fe	Mg	Cu
$C_{2\sigma}$ (ng cm^{-3})	1.72	5.8	3.9	9.7	0.57	3.0	1.3	1.1
$j_{2\sigma}$ (μA cm^{-2})	1.85	6.22	1.15	14.4	0.20	1.04	1.03	0.33

* Conditions used for the experiments with AA1199 in which a better detection limit was necessary.

The transfer time between the electrochemical cell and the spectrometer was approximately 22 s under the conditions of these experiments. Note that the spectrometric data has been off-set with respect to the current and potential data sets to correct for this time lag. Details of the procedure are given in [20].

6.3. Results

6.3.1 AESEC Polarization Curves

To demonstrate the cathodic dissolution phenomenon quantitatively over a wide range of cathodic current densities, polarization experiments were performed for the different Al alloy materials in **Figure 6.1-6.4.** The *AESEC polarization curve* consists of the electrical current density, j, measured with the potentiostat, and the elemental dissolution currents, j_M, for M = Al, Cu, Mg, Mn, Fe, and Si. The polarization experiments were performed in a three step sequence: (a) An open circuit exposure of the sample to the electrolyte for several minutes; (b) An applied potential of -1.4 vs. Ag/AgCl /V for 120 s; (c) A potential sweep to -0.5 V at

0.5 mV/s. The data is shown as a function of time, however, for clarity, a potential axis is shown for the data in period (c). As this paper is focused on the cathodic dissolution of aluminum, the dissolution of other elements will be postponed until Section 3.4.

The AESEC polarization curves for Al and Al$_2$Cu phase are shown in **Figure 6.1** and **6.2** and for AA7050 alloy and AA2214 in **Figure 6.3** and **6.4**. The polarization curve for AA2024 was given in reference [12]. Regardless of the sample, the AESEC polarization curve may be divided into three domains: (1) a cathodic domain in which the j and j$_{Al}$ either decrease monotonically from the current obtained at the end of the potentiostatic period or in the case of pure Al, increase and pass through a maximum; (2) a "passive" domain were j$_{Al}$ is very low and not detectable above background; and (3) a transpassive domain where the j$_{Al}$ and j increase rapidly as do the partial elemental currents for other components of the alloy such as Mg, Zn, Fe, etc. according to the alloy composition.

Figure 6.1. 99.99% Al (AA1199): AESEC polarization curves in 30 g/l NaCl solution at pH = 6.1. The curve is divided into period (a) open circuit exposure to electrolyte; (b) imposed potential of -1400 mV vs. Ag/AgCl; (c) anodic potential sweep at 0.5 mV/s. Prior to (a) a blank solution was pumped into the plasma, bypassing the flow cell, to define the background intensity level.
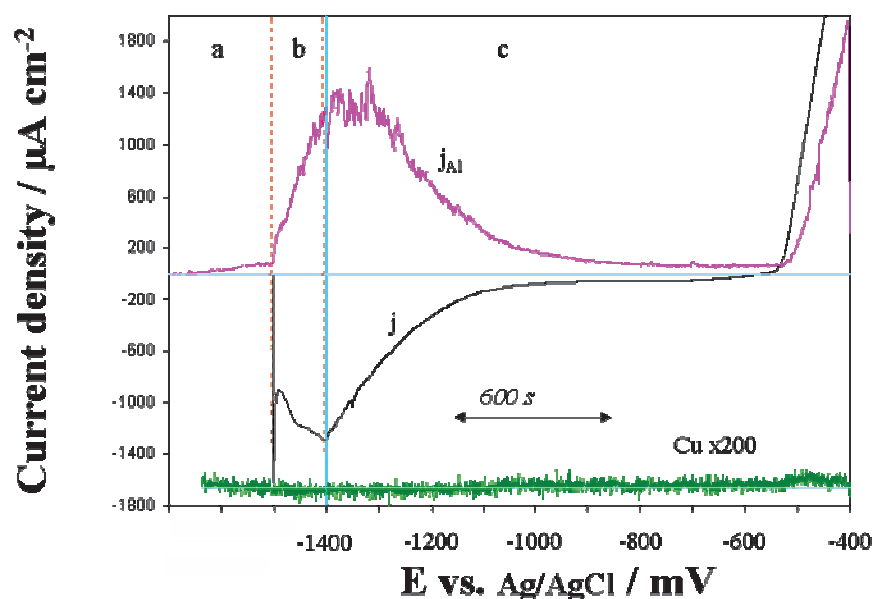
Figure 6.2. Synthetic Al₂Cu: AESEC polarization curve in 30 g/l NaCl solution at pH = 6.1. The curve is divided into period (a) open circuit exposure to electrolyte; (b) imposed potential of -1400 mV vs. Ag/AgCl; (c) anodic potential sweep at 0.5 mV/s.
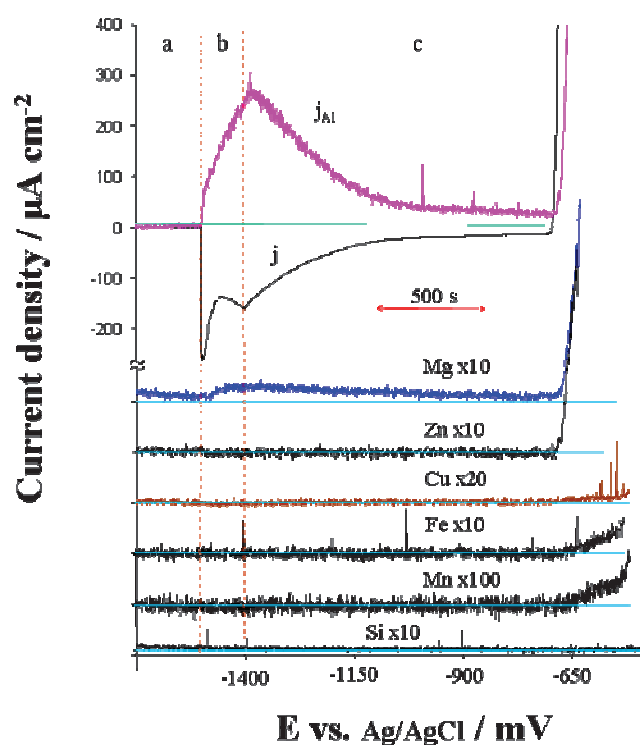
Figure 6.3 AA7050: AESEC polarization curves in 30 g/l NaCl solution at pH = 6.1. The curve is divided into period (a) open circuit exposure to electrolyte; (b) imposed potential of -1400 mV vs. Ag/AgCl; (c) anodic potential sweep at 0.5 mV/s.
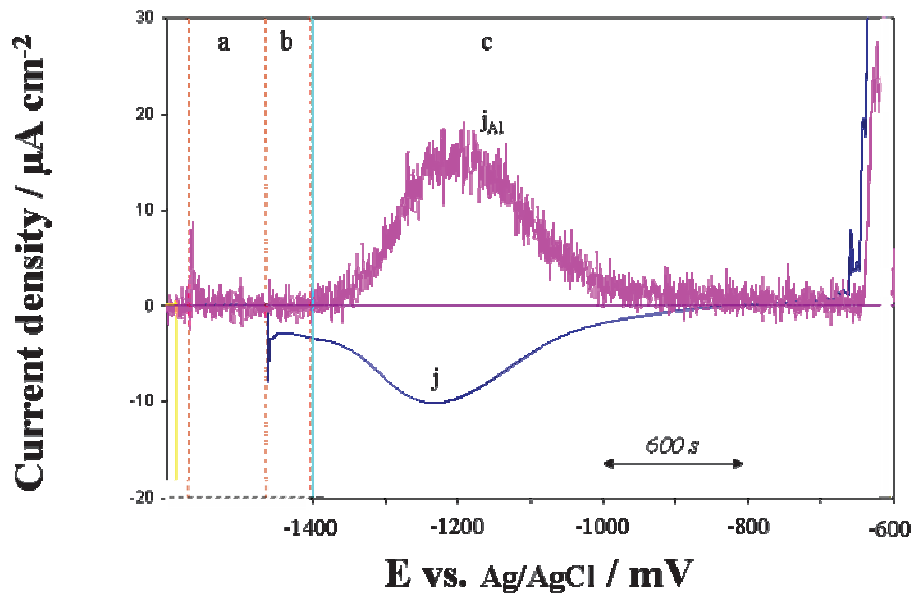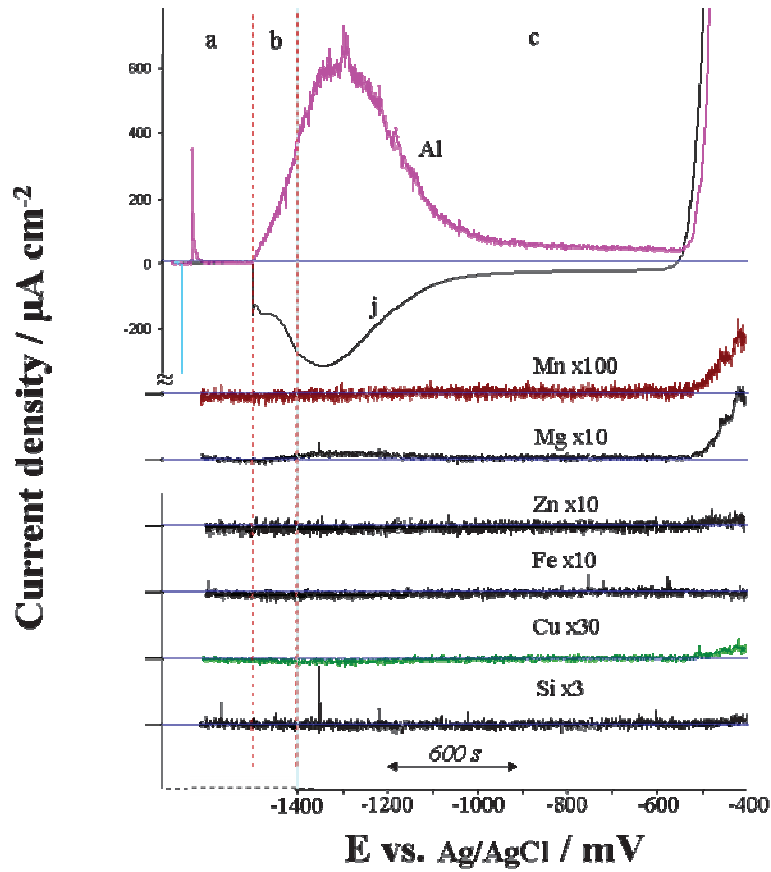
Figure 6.4 AA2214: AESEC polarization curves in 30 g/l NaCl solution at pH = 6.1. The curve is divided into period (a) open circuit exposure to electrolyte; (b) imposed potential of -1400 mV vs. Ag/AgCl; (c) anodic potential sweep at 0.5 mV/s.

The values of j_{Al} and j at the beginning of the potential sweep depend upon the exposure time at -1.4 V vs. Ag/AgCl. During this potentiostatic period, the current increases monotonically with time and then decreases during the potential sweep. In our previous publication, a much higher dissolution rate was obtained for pure Al as compared to **Figure 6.1** and for AA2024 as compared with AA7050 in **Figure 6.3**. These higher dissolution rates may be attributed to the use of a longer period of activation at -1.4 V vs. Ag/AgCl than was used here. In this work the four specimens investigated cover nearly three orders of magnitude of hydrogen reduction activity and Al dissolution rate ranging from 99.99% Al with $j_{Al} = 15 \ \mu A \ cm^{-2}$ to the pure Al_2Cu with $j_{Al} = 1300 \ \mu A \ cm^{-2}$. AA7050 and AA2214 show an intermediate activity with 270 $\mu A \ cm^{-2}$ and 620 $\mu A \ cm^{-2}$.

The obvious interpretation of this result is that the potentiostatic period at -1.4 V vs. Ag/AgCl is necessary to activate the surface presumably by generating hydroxide that in turn dissolves the surface oxide film. The counter example is 99.99% Al, **Figure 6.1,** were no Al dissolution

is observed during the potentiostatic period despite a cathodic current of approximately -3 $\mu A\ cm^{-2}$. For this specimen, the potentiostatic period was not sufficient to activate the surface under the conditions of this experiment. As pointed out in our previous publication [12], the form and intensity of the cathodic polarization curve depends markedly on surface preparation.

The difference in the catalytic activity of the different materials for hydrogen reduction is also seen in the steady state cathodic current observed during the passive domain. For the copper containing samples, a steady state cathodic current and an aluminum dissolution current are observed in the passive domain until about E = -800 mV vs. Ag/AgCl (steady state values for Al_2Cu, j = -23.7 $\mu A\ cm^{-2}$ and j_{Al} = 45.2 $\mu A\ cm^{-2}$; for AA7050, j = -15.9 $\mu A\ cm^{-2}$ and j_{Al} = 28.7 $\mu A\ cm^{-2}$; for AA2214, j = -21.8 $\mu A\ cm^{-2}$ and j_{Al} = 46.5 $\mu A\ cm^{-2}$) where presumably the anodic dissolution of aluminum in neutral solution begins as indicated by the steady increase in j. For Al, both j and j_{Al} decrease to zero in this domain with no measurable steady state current.

Despite the large variability in the cathodic current between the samples, in all cases, the aluminum dissolution rate is an approximate mirror image of the cathodic current. Quantitatively we can approximate this relationship as:

$$j_{Al} = -(3\ /\ m)\ j \qquad\qquad\qquad [6.8]$$

Where *m* is the stoichiometric number of hydroxides produced per Al dissolved assuming every electron leads to formation of one hydroxide. The factor 3 is the charge of the Al cation used in the calculation of j_{Al} by equation 6. Analysis of the steady state data j_{Al} and j values in the previous paragraph gives m=1.57 (Al_2Cu), m=1.66 (AA7050), and m=1.40 AA2214). The suggestion is that the ratio m is nearly independent of the matrix upon which the cathodic dissolution of aluminum is occurring.

Figure 6.5 shows j_{Al} as a function of j from the entire cathodic region for **Figures 6.1 – 6.4** and also the AA2024 alloy from our previous publication [12]. The five curves have been offset on the vertical scale for clarity. A net linear relationship is observed for currents up to j = -200 μA with m = 1.44 to 1.70 nearly independent of the alloy material. At higher currents, j_{Al} is lower than predicted indicating that the efficiency of OH^-/Al decreases. This is especially true for the Al_2Cu sample. A possible explanation would be if the selective dissolution of Al led to the formation of copper rich islands. In this situation, hydroxide

²produced in the center of the islands would be less efficient for dissolving Al than the hydroxide produced on the edge. The insert shows the determination of m for the 99.9% Al on an expanded scale. This curve shows a cycle because j and j_{Al} increased during the first part of the potential sweep.
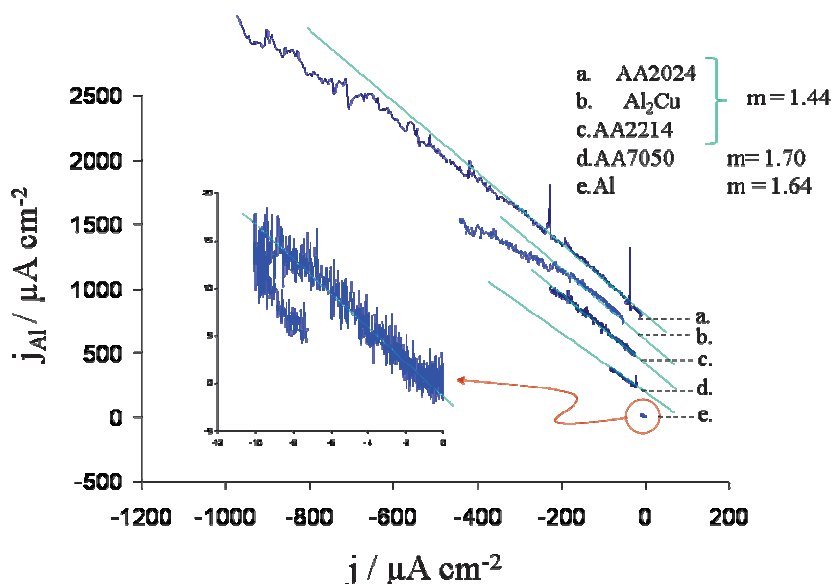
Figure 6.5 *j_{Al} as a function of j from the cathodic region of the AESEC polarization curves (Figures 1 – 4). Also shown is the data for AA2024 from reference [12]. A linear relationship is observed over a wide range of current density with a slope varying from 1.44 to 1.70.*

6.3.2 Transient Analysis of the Cathodic Dissolution Rate

The above results confirm an apparently simple stoichiometric relationship between j and j_{Al} under conditions in which a steady state between film formation and film dissolution might be supposed. However since the relationship between reduction and dissolution is indirect, it is of interest to determine the time necessary for the steady state to be obtained. In order to measure the time required, transient potential step experiments were performed. **Figure 6.6** shows a series of typical j_{Al} and j transients for pure Al when the potential was stepped from the spontaneous open circuit value (approximately -0.73 V vs. Ag/AgCl) to an applied potential between -1.0 V and -1.5 V vs. Ag/AgCl, and then allowed to return to the open circuit potential (E_{oc}) to achieve a final value. When the potential step is applied (t=0), j shows a very sharp intense cathodic peak and then decreases progressively at low potential steps. For more negative potentials, the intense cathodic peak (labeled α) is observed followed by a minimum and then a slow rise to pass through a maximum (labeled β). In all

cases, j_{Al} increases more slowly, passing through maximum and then decreasing progressively in synch with j.
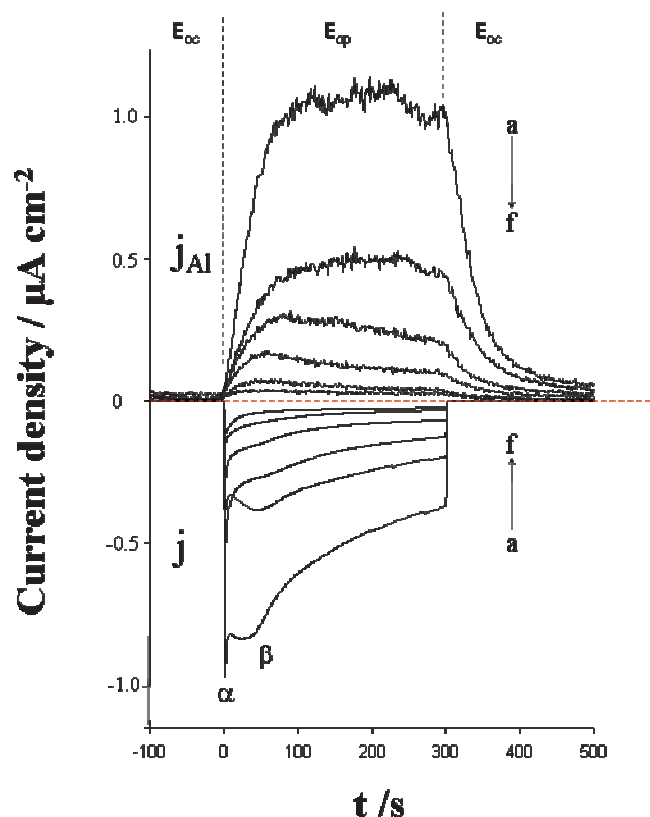
Figure 6.6. *Potential step transients for pure Al, from open circuit to variable cathodic potential. The cell is at open circuit (Eoc) for t<0 and t > 300. The potential step begins at t = 0 for a duration of 300 s. Potential steps were a) -1.6, b) -1.55, c) -1.45, d) -1.4, e) -1.3, f) -1.2 V vs. Ag/AgCl.*

The form of these curves suggests that the transient experiments may be interpreted in terms of (at least) three different time constants: (a) equilibration between hydrogen reduction and the applied potential, (b) equilibration of the cathodic current with aluminum dissolution, and (c) an ultimate steady state between hydrogen reduction / aluminum dissolution rate which involves the reformation and modification of the aluminum oxide film. (Note the word "equilibration" is used above to mean arrival at a steady state condition; thermodynamic equilibrium is not implied.) Surprisingly, when the potential step is applied, the cathodic current intensity jumps to a large value and then decreases with time. This suggests that the equilibration between hydrogen reduction and applied potential is very rapid on the time scale of these experiments.

Equilibration between the cathodic current and aluminum dissolution is investigated in **Figure 6.7**. In this case, the transients of **Figure 6.6** are presented as m = $3j/j_{Al}$ (from equation 8) as a function of time. It is observed that during the first 50 to 80 s the m value passes through a sharp maximum (high j, low j_{Al}) indicating that initially a large excess of current is necessary to dissolve the initially present passive film. The value of "m" then drops down to a nearly steady state value despite the fact that a steady state was not obtained in the total current. The steady state value varies between 1 and 3 consistent with the results of **Figure 6.5** despite a large apparent variation in m. This result demonstrates that the steady state between cathodic current and Al dissolution occurs rapidly on the time scale of this experiment. Some caution must be used in interpreting this result as we have not corrected the current data for the time constant distribution of the electrochemical flow cell so that it is truly comparable with j_{Al}. In previous work we were able to perform this correction, which involves solving a convolution integral, for pure Zn and thereby calculate the quantity of oxide formed on the surface at any time by a difference of j and j_{Zn} [17]. This will be attempted for the Al system in future experiments. (Note that the data has been corrected for the time offset due to the transfer from the electrochemical cell to the spectrometer.)
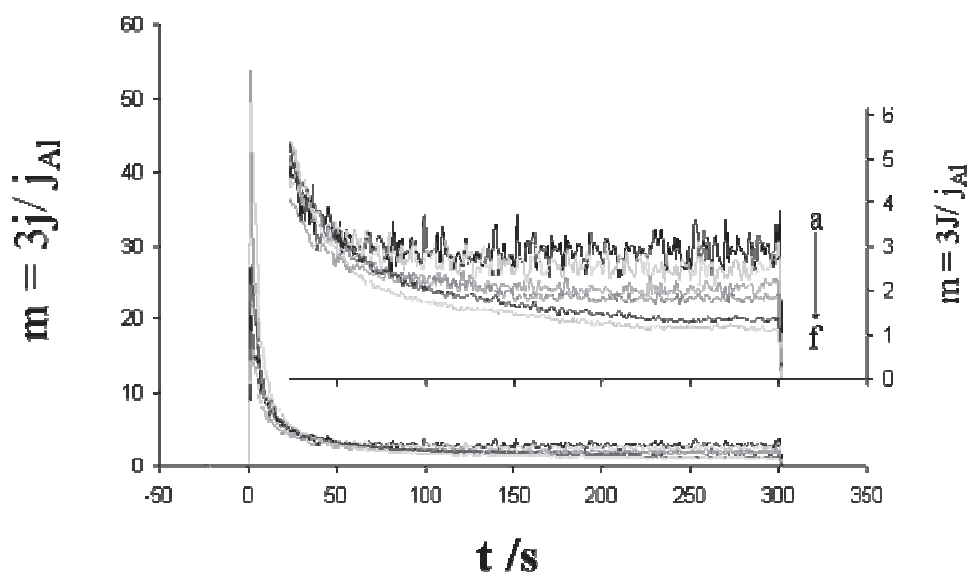
Figure 6.7. *The stoichiometric factor m = $3j/j_{Al}$ calculated from the data of Fig. 7. The potential step begins at t = 0 for a duration of 300 s. The working electrode is at open circuit (Eoc) for t<0 and t > 300.Potential steps were a) -1.6, b) -1.55, c) -1.45, d) -1.4, e) -1.3, f) -1.2 V vs. Ag/AgCl.*

6.3.3 Steady State Stoichiometry and Cathodic Polarization Curves

In addition to the transient experiments of **Figure 6.6**, further experiments were performed by first stepping the potential from open circuit to -1.6 V vs. Ag/AgCl for 200s so as to activate the surface and then stepping to a potential between -1.0 V vs. Ag/AgCl and -1.55 V vs. Ag/AgCl. In this way, the transient corresponds to a jump from more active to less active as compared with the transients of **Figures 6.6 and 6.7** which correspond to a jump from less active to more active. Further, both sets of experiments were repeated with the Al_2Cu sample. A detailed treatment of the transients is outside the scope of this article; however a number of interesting conclusions may be reached by consideration of the average values of j and j_{Al} obtained during the final part of the experiment.

Figure 6.8 gives j_{Al} as a function of j, measured during the final 100 seconds of the transient experiment for all the transient experiments performed including Al_2Cu and Al and for both the cathodic step and anodic step experiments. The overall value of m determined from this data is 1.83, consistent with the value obtained from **Figure 6.5**. However, the transient analysis given above demonstrates that this value varies within a range of 1 to 2 depending on the history of the sample and a large scatter is presented in the data.
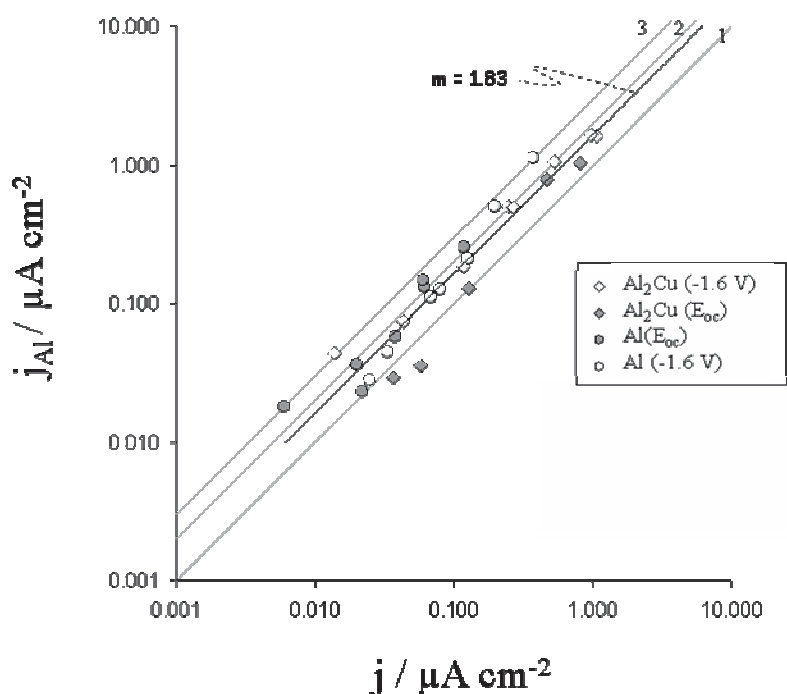
Figure 6.8. *j_{Al} as a function of j, integrated during the final 100 s of the potential step experiments for 99.99% Al (circles) and Al_2Cu (diamonds). Potential step experiments were performed in both the anodic (empty) and cathodic (filled) directions. Straight lines indicate m=1, m=2, and m=3 as indicated. A least squares fit to the entire data set is also shown indicating a slope of 1.83.*

Figure 6.9 shows a cathodic polarization curve for Al_2Cu and Al obtained by determining the total cathodic current by the relationship

$$j_{cat} = j - j_{Al} \qquad\qquad [6.9]$$

Although this is not a true steady state cathodic polarization curve, it does clearly show the differences in hydrogen reduction behavior of Al and Al_2Cu. The high values of the Tafel slopes suggest that an oxide film is present on the surface throughout the polarization experiment.
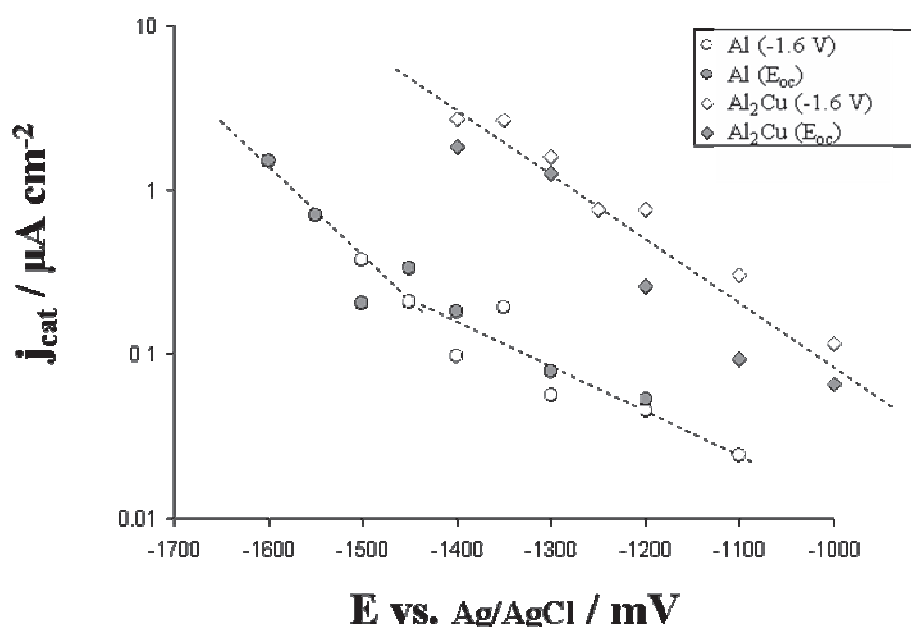
Figure 6.9 *The total cathodic current as a function of applied potential for cathodic polarization curve for 99.99% Al (circles) and Al_2Cu (diamonds). Potential step experiments were performed in both the anodic (empty, from -1.6 V vs. Ag/AgCl) and cathodic (filled, from E_{oc}) directions.*

6.3.4 Selective Dissolution of Alloying Elements

Table 6.3 gives the relative proportions of different elements dissolving in different regions of the AESEC polarization curves of AA7050 and AA2214. The data is presented as a % solution (%soln) and as a selective dissolution factor γ = %soln/ %bulk, where % bulk is taken from Table 6.1. The remainder of the solution composition is Al which is not given. The

anodic zone was integrated over a 70 s (35 mV) period after the beginning of the transpassive region. Note that this corresponds to a different potential range for the two samples.

Table 6.3: Solution composition for the anodic and cathodic domains of the polarization curves of AA7050 (Fig. 3) and AA2214 (Fig.4). The %soln expresses the solution composition as a mass percentage with the remainder being Al. γ is the selective dissolution factor defined as %soln/ %solid from the elemental analysis of Table 6.1. Data for the anodic domain was integrated over 70s (35 mV) interval during the initial rise of the transpassive dissolution. Note that the potential in this domain varied between the two samples. The data for the cathodic domain was integrated over the entire cathodic dissolution peak.

		Zn	Si	Mn	Fe	Mg	Cu
AA7050	%soln	14.0	-	-	-	0.091	0.0051
Anodic (-668 mV vs. Ag/AgCl)	γ	2.2				0.045	0.0022
cathodic	%soln	-	-	-	-	3.6	-
	γ					1.6	
AA2214	%soln	0.10	-	0.13	0.077	0.65	0.108
Anodic (-418 mV vs. Ag/AgCl)	γ	3.3		0.14	0.45	1.2	0.024
cathodic	%soln		-	-	-	0.42	
	γ	-				0.78	

Mg dissolution occurs in both the anodic and cathodic domain for the two alloys. In the cathodic domain, Mg dissolution occurs in a similar fashion to what was observed previously for the AA2024 alloy [12]. However in the AA2024 alloy, the Mg dissolution maximum was shifted to higher potential with respect to the Al dissolution maximum. Fig. 3 and 4 show that for AA7050 and AA2214 Al and Mg closely follow each other throughout the cathodic domain. This result may be interpreted in terms of the interfacial pH that is produced during cathodic polarization on the different samples. In an unbuffered neutral solution, the hydroxide ion concentration at the surface will increase in proportion to the cathodic current. The polarization curve of AA2024 in reference [12], the cathodic current at low potential is an order of magnitude larger than for the AA7050 and AA2214. Consequently the hydroxide ion concentration must be an order of magnitude larger as well, leading to the formation of insoluble $Mg(OH)_2$.

The Mg dissolution rate observed for AA2214 is very close (within 20%) to that predicted from the elemental analysis in both the cathodic and anodic domains. For AA7050 however, the cathodic domain shows a significant enrichment of Mg in solution (γ =1.6) while the anodic domain shows a marked depletion in solution (γ =0.045).

Copper dissolution is only observed in the transpassive domain for the alloys and the Al_2Cu intermetallic. All showed significantly less copper than would be predicted from the bulk analysis, with γ =0.0022 and 0.024 for AA7050 and AA2214. The difference probably results from the difference in the potential range since AA7050 occurs at -0.67 V vs. Ag/AgCl against -0.42 V vs. Ag/AgCl for AA2214. A major difference is the appearance of sharp transient peaks in the copper signal for AA7050. In our previous work identical transients were definitively associated with the release of copper rich particles [12]. Neither the AA2214 or the Al_2Cu phase demonstrate this phenomenon. For Al_2Cu this is logical since this specimen does not contain copper rich particles. AA2214 does contain copper rich particles and it is not clear why they are not observed in these curves.

The AA2214 and AA7050 alloys differ markedly in their Zn content, 0.03% and 6.3% respectively. Zn dissolution is clearly detected in the AESEC polarization curve of both materials with a selective dissolution of γ =2.2 and 3.3 respectively. Mn dissolution is observed for AA2214 but not AA7050 although well below the predicted value (γ =0.14). Fe was detected for AA7050 (γ =0.45) but not AA2214 probably due to the very low concentration in the latter.

These results demonstrate that the anodic dissolution of the alloys is complex with a highly enriched dissolution of Zn and a depletion of the other alloying elements.

6.4. Discussion

The results presented here demonstrate that an excess of hydroxide is necessary to drive reaction 3 to the right. Within the framework of reaction 1-3, the dissolution of the $Al(OH)_3$ exposes the underlying metallic Al substrate so that it can react with the electrolyte replenishing the $Al(OH)_3$ film. **Figure 6.10** gives the calculated solubility of $Al(OH)_3$ as a function of pH in pure water. The initial pH of the solution is 6.1, corresponding to the minimum solubility of $Al(OH)_3$. However, the solution is unbuffered so that the pH will increase rapidly when hydrogen reduction occurs at the surface.

The cathodic dissolution of Al may be understood in terms of the reactions $1 - 3$. The concentration of hydroxide at the interface $[OH^-]°$ may be simply related to the cathodic current by consideration of a mass balance between hydroxide formation at the surface and diffusion away from the surface :

$$d[OH^-]/dt = (-j-j_{Al}/3) - (D_{OH}/\delta)([OH^-]^\circ - [OH^-]^\infty) \qquad [6.10]$$

where $[OH^-]^\infty$ is the concentration in the flowing electrolyte far from the surface and D_{OH} and δ are the diffusion coefficient for hydroxide and the length of the diffusion layer at the metal / flowing electrolyte interface respectively. At least for low cathodic current densities, we can assume that $[OH^-]^\infty << [OH^-]^\circ$ since pH = 6.1 far from the electrode. The steady state condition for hydroxide formation gives

$$[OH^-]^\circ = -(\delta / D_{OH}) (j + j_{Al}/3) \qquad [6.11]$$
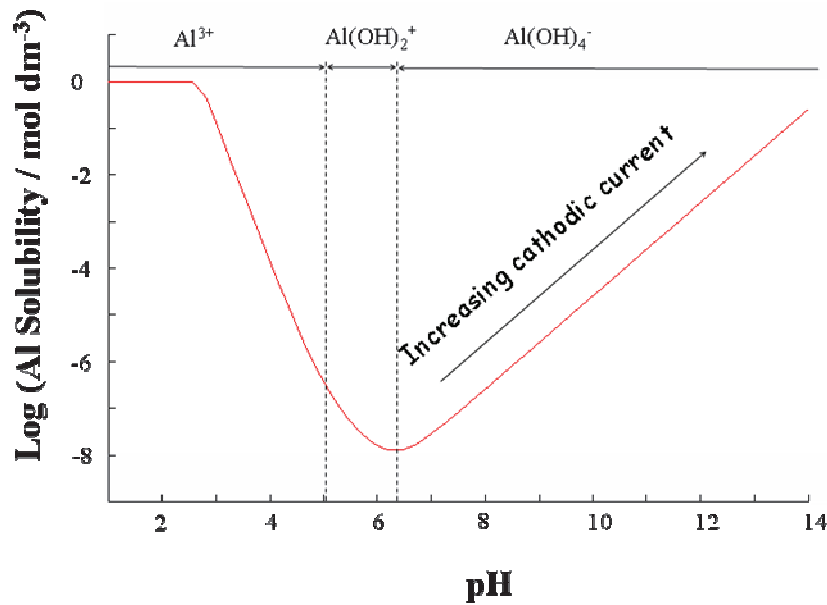
Figure 6.10 *Predicted solubility of Al^{3+} in pure water as a function of pH calculated with Hydra – Medusa™ software for a total concentration of $[Al^{3+}] = 1$ mol dm^{-3}. The following Al species were used in the calculation : Soluble species : $Al(OH)_2^+$, $Al(OH)_3$ (aq), $Al(OH)_4^-$, $Al_2(OH)_4^{4+}$, $Al_3(OH)_4^{5+}$, $AlOH^{2+}$; insoluble species : $Al(OH)_3$ (am), $Al(OH)_3$ (cr), $AlOOH$ (cr). The predominant solution species are shown above. For pH > 7, only $Al(OH)_3$ (cr) and $Al(OH)_4^-$ make a significant contribution.*

The equilibrium concentration of dissolved aluminum is directly proportional to the hydroxide concentration.

$$[Al(OH)_4^-] = K[OH^-]^\circ \qquad [6.12]$$

Where K is the equilibrium constant for reaction 3. If we assume that the equilibrium concentration is determined by a mass balance between the Al dissolution rate and the diffusion of $[Al(OH)_4^-]$ away from the interface with diffusion coefficient, D_{Al}), we can write:

$$d[Al(OH)_4^-]/dt = j_{Al} /3 - (D_{Al}/ \delta)([Al(OH)_4^-]^\circ - [Al(OH)_4^-]^\infty) \qquad [6.13]$$

Assuming $[Al(OH)_4^-]^\infty = 0$ and steady state and substituting (11) and (12) :

$$j_{Al} /3 = (D_{Al}/ \delta) K[OH^-]^\circ = -(KD_{Al}/ D_{OH}) (j + j_{Al}/3) \qquad [6.14]$$

$$(1+ D_{OH} / KD_{Al}) j_{Al} = - 3 j \qquad [6.15]$$

This model, although very simple, does predict that the rate of Al dissolution is related to the total current by a constant factor as seen in the experimental data. The factor m, defined in Equation 8 will be given by

$$m = (1+ D_{OH} / KD_{Al}) \qquad [6.16]$$

Further, m is predicted to be independent of the magnitude of the total current and total dissolution rate within the limits implied by the assumption that δ is constant for all species (determined by flow characteristics of the cell) and that the concentration of each species is negligible far from the electrode surface. The first assumption is probably valid since a flow cell is used and δ should be determined by the hydrodynamic characteristics of the cell. The second assumption should be valid for low dissolution rates and is consistent with the experimental results of **Figure 6.5** with only slight deviations from linearity above j = -250 μA cm^{-2}. Other assumptions include a linear diffusion gradient and that the j and j_{Al} have an identical distribution on the surface. The first assumption probably fails close to the surface as the $Al(OH)_3$ film is most likely porous and much of the dissolution may occur within the pores. The assumption that j and j_{Al} have identical distributions is probably valid at least Al dissolution requires hydroxide and thus must occur in proximity to the cathodic sites on the surface. For pure Al and for Al_2Cu at early times, all hydroxide generation must occur in the vicinity of Al; therefore Al dissolution should have the same distribution as the cathodic reaction. For Cu containing alloys after significant dissolution, it is possible that copper rich islands may form on the surface such that the cathodic reaction may occur such that the hydroxide generated is not available to react with the $Al(OH)_3$ film. This would result in an increase of m.

It is of interest to compare the experimental value of m obtained here with the value predicted by Eqn. 6.16. Unfortunately, to our knowledge, the diffusion coefficients and effective equilibrium constant are not known under the conditions of these experiments. An order of magnitude approximation may be made by comparison with data obtained in other conditions. The infinite diffusion coefficient for $Al(OH)_4^-$ has been determined as $1.04 \pm 0.02 \cdot 10^{-5}$ cm^2 s^{-1} using the diaphragm cell method [21] while the estimated diffusion coefficients for hydroxide is $2.19 \cdot 10^{-5}$ cm^2/s in 0.5 mol dm^{-3} to 5 mol dm^{-3} LiOH [22]. A value of K = 0.25 may be determined from the linear relationship between $[Al(OH)_4^-]$ and pH, above pH = 7. These values predict m = 9 as compared to the experimental m=1.8. Nevertheless, the value is certainly overestimated as the effective value of K is probably much larger than the thermodynamic value due to the presence of chloride ions in the electrolyte and the fact that the surface film is probably not crystalline $Al(OH)_3$ used in the calculation of **Figure 6.10**.

6.5. Conclusions

(1) We have demonstrated the use of atomic emission spectroelectrochemistry to measure the cathodic dissolution reaction of Al with high sensitivity and in real time for pure Al, pure Al_2Cu, AA7050 and AA2214 as a function of potential. The elementary dissolution rates of Al, Cu, Mg, Zn, Fe and Si were measurable.

(2) Cathodic aluminum dissolution was observed for all materials investigated. Under near steady state conditions, the Al dissolution was directly related to the cathodic current with an e/Al ratio of approximately 1.8, surprisingly constant for over two orders of magnitude of cathodic current density (10 µA → 2 mA) and independent of the substrate material.

(3) The results are interpreted in terms of a cathodic dissolution rate controlled by the chemical dissolution of a passivating aluminum oxide / hydroxide film by reaction with cathodically generated hydroxide followed by oxidation of the aluminum to rebuild the passive film. The overall reaction stoichiometry is $Al + 4H_2O + e^- \rightarrow 2H_2 + Al(OH)_4^-$. The measured e/Al ratio is greater than 1 because a certain excess of hydroxide is required to compensate for diffusion of hydroxide away from the interfacial region.

6.6. Acknowledgements

6.7. References

1. B. P. Caldwell, V. J. Albano, *Trans., J. Electrochem. Soc.* **76** (1939) 271.

2. A. R. Despic, J. Radosevic, P. Dabic, M. Kliski, *Electrochimica Acta* **35** (1990) 1743.

3. S. -M. Moon and S. -I. Pyun, *Corros. Sci.* **39** (1997) 399.

4 Y. Baek, G. S. Frankel, *J. Electrochem. Soc.* **150** (2003) B1.

5. E. P. G. T. van der Ven, H. Koelmans, *J. Electrochem. Soc.* **123** (1976) 143.

6. H. Takahashi, K. Fujiwara, M. Seo, *Corros. Sci.* **36** (1994) 689.

7. P. Schmutz, G. S. Frankel, *J. Electrochem. Soc.* **145** (1998) 2285.

8. R. G. Buchheit, *J. Electrochem. Soc.* **142** (1995) 3994.

9. N. Dimitrov, J. A. Mann, M. Vukmirovic, K. Sieradzki, *J. Electrochem. Soc.* **147** (2000) 3283.

10. R. G. Buchheit, R. P. Grant, P. F. Hlava, B. McKenzie, G. L. Zender, *J. Electrochem. Soc.* **144** (1997) 2621.

11. H. P. Godaro, W. P. Jepson, M. R. Bothwell, R. L. Kane, *The Corrosion of Light Metals*, pp. 42, 268. John Wiley, New York (1967).

12. M. Mokaddem, P. Volovitch, F. Rechou, R. Oltra, K. Ogle, *Electrochim. Acta* **55** (2010) 3779–3786.

13. K. Ogle, J. Bayens, J. Swiatowska, P. Volovitch, *Electrochim. Acta* **54** (2009) 5163.

14. K. Ogle, J. Bayens, J. Swiatowska, P. Volovitch, *Electrochim. Acta* **54** (2009) 5163.

15. K. Ogle, P. Volovitch, M. Mokaddem, *Electrochim. Acta* **55** (2010) 913.

16. J. Światowska, P. Volovitch, K. Ogle, *Corros. Sci.* **52** (2010) 2372

17. M. Mokaddem, P. Volovitch, K. Ogle, *Electrochim. Acta* (2010) - doi:10.1016/j.electacta.2010.02.020.

18. A. J. Bard, L. R. Faulkner, "*Electrochemical Methods: Fundamentals and Applications, 2nd edition*", John Wiley & Sons, Inc., 2001, p808.

19. M. Pourbaix "*Atlas d'Equilibres Electrochimiques à 25 °C*", Gauthier-Villars & Cie, Paris, 1963, p171.

20. K. Ogle, S. Weber, *J. Electrochem. Soc.* **147** (2000) 1770.

21. J. E. Mackin, R. C. Aller, *Geochim. Cosmochim. Acta* **47** (1983) 959-961.

22. E. L. Littauer, K. C. Tsai, *Electrochim. Acta* **24** (1979) 351.

Chapter VII

The cathodic dissolution of the AA6061 aluminum alloy

M. Serdechnova, P. Volovitch, Fr. Brisset, K.Ogle

The cathodic dissolution of the AA6061 aluminum alloy

M. Serdechnova, P. Volovitch, Fr. Brisset, K. Ogle

The dissolution of an AA6061 aluminum alloy under cathodic polarizations was investigated. The dissolution of the base metal and the minor alloying elements was measured in real time using atomic emission spectroelectrochemistry. These data were used to verify the stoichiometry of 4.6 hydroxides per dissolved Al ion. It was found that at high cathodic currents, insoluble Mg^{2+} hydroxides /oxides precipitate on the surface. This quantity of $Mg(OH)_2$ did not effect the OH/Al stoichiometry.

7.1. Introduction

It is well known that the rate of anodic dissolution of Al increases with an increasing cathodic polarization, referred to as cathodic dissolution or cathodic corrosion [1,4,5]. This phenomenon may play an important role during the corrosion of Al in situations in which Al becomes the cathode when coupled to other materials such as galvanized steel [2]. Recent efforts to model Al corrosion include only a simple Tafel relationship for Al dissolution, the cathodic dissolution mechanism being taken into account by assuming a first order relationship between the exchange current and the hydroxide ion concentration [3].

In the recent work we investigated the cathodic dissolution of Al, Al_2Cu and Al alloys in an initially neutral 3% NaCl electrolyte [4,5]. The goal was to determine the stoichiometry of dissolution and to establish an empirical rate law between Al dissolution and hydroxide formation. The results were consistent with an overall reaction stoichiometry of

$$Al + 3OH^- \rightarrow Al(OH)_3 + 3e \qquad\qquad [7.1]$$

$$Al(OH)_3 + OH^- \rightarrow Al(OH)_4^- \qquad\qquad [7.2]$$

With however a total stoichiometry of approximately 4.7 were the excess hydroxide was lost to diffusion.

In this work we investigate the dissolution of Mg and Si that occurs simultaneously with Al dissolution and in particular, the effect of precipitated Mg^{2+} oxidation products on the cathodic Al dissolution rate. The AA6061 aluminum alloy used in this work is increasingly favored in vehicle design. This alloy includes Mg, Si, Fe and other additives including Mg_2Si phase [6,7]. The formation of mixed Al-Mg oxidized species often detected in corrosion products on Al-Mg compounds and on the Al alloys corroded in the presence of Mg^{2+} complicate the behavior of the system [8, 9, 10].

The solubility of Al^{3+} and Mg^{2+} species with pH are quite different. Al^{3+} is relatively insoluble at neutral and slightly acid pH [4] resulting in the passivation of Al metal over this pH range. At higher pH, Al^{3+} is soluble as $Al(OH)_4^-$ [12]. Mg^{2+} however is highly soluble in acid and neutral solution but becomes insoluble at higher pH [11]. Moreover, the presence of Cu in the alloy or intermetallic [13,14] is also important for Al dissolution because of the acceleration

of the cathodic water decomposition to hydroxide [15]. In our previous work, it was found that the addition of Cu to the alloy did not influence the stoichiometry of Al dissolution; however, it did significantly increase the cathodic activity of the surface [5]. As a result, the corrosion and pitting potential values could not satisfactorily predict the current densities of Al, Mg and other elements of the alloy or other more complex systems [16,17].

In this work the simultaneous measurement of Mg, Si and Al dissolution rates, v_M, together with the potential and the total electrochemical current density were performed simultaneously with atomic emission spectroelectochemistry (AESEC) [18]. The pH evolution of the electrolyte was also monitored downstream from the flow cell. The aim of this study is to distinguish the role of Al and alloying elements (such as Si, Mg, Fe, Cu) on the elementary corrosion phenomena (dissolution, surface oxide formation, precipitation) by simultaneous, *in-situ* measurement of the elementary dissolution rates for AA6061 alloys.

7.1.1. Measurement principles

The principle of the AESEC measurement has been previously described in detail [18, 19]. Briefly, it consists of an electrochemical flow cell combined with an inductively coupled plasma optical emission spectrometer (ICP-OES). In the cell, reactions between a sample and an aggressive electrolyte occur, leading to the production of dissolved ions. The concentrations of these ions are measured in real time downstream from the cell with the ICP-OES.

The instantaneous dissolution rate of an element M in the cell, v_M, is directly related to the downstream concentration (in nmol s^{-1} cm^{-2}) by (equation 7.3):

$$v_M = C_M f / A \qquad [7.3]$$

where f is the flow rate of electrolyte (in this work, 3.02 cm^3 min^{-1}), C_M is the instantaneous concentration of element M (mol cm^{-3}), and A is the exposed surface area (0.51 cm^2). C_M is measured from the emission intensity at a specific wavelength using normal quantitative procedures for ICP-OES spectrometry [4].

The total electrical current between working and counter electrodes, i_e (measured by the electrometer of potentiostat), is the sum of the cathodic current, i_c, and the anodic current, i_a (equation 7.4):

$$i_e = i_c + i_a \qquad [7.4]$$

The major cathodic reactions in neutral electrolyte are H_2O and O_2 reduction. Each of these reactions leads to the formation of one electron per OH^-. It is of interest to estimate the total cathodic reaction rate (v_{OH}) and the extent of formation of precipitated corrosion product films. This can be done considering the steady state values of the total current, j_e and the steady state elemental dissolution rates (v_M) with m = Al, Mg, Si, (combined with our knowledge of the bulk composition of the alloy) using two important assumptions:

1. We assume that aluminum oxide film growth is at steady state and the total instantaneous Al oxidation rate, $v°_{Al}$, is equal to the instantaneous dissolution rate, v_{Al}.

$$v°_{Al} = v_{Al} \qquad [7.5]$$

Clearly this assumption may not be valid during the early stages of a transient experiment when the aluminum oxide film is either growing or dissolving and is probably never valid during linear scan experiments.

2. We assume that Mg and Si are oxidized as rapidly as they are exposed. Under this condition, their exposure will be limited by the dissolution of Al, the total rate of Mg and Si oxidation, $v°_{Mg}$, and $v°_{Si}$, will be

$$v°_{Mg} = \alpha_{Mg} \, v_{Al} \qquad [7.6]$$

$$v°_{Si} = \alpha_{Si} \, v_{Al} \qquad [7.7]$$

where α_{Mg} = (mol.% Mg / mol.% Al) and α_{Si} = (mol.% Si / mol.% Al) in the bulk alloy. Obviously this assumption will also only be valid if $v°_{Al} = v_{Al}$.

Combining with exposed surface area, A, and Faraday constant, F, above

$$i_a = 3 \, A \, F \, v_{Al} + 2 \, A \, F\alpha_{Mg} \, v_{Al} + 4AF \, \alpha_{Si} \, v_{Al} \qquad [7.8]$$

Equation 7.8 is approximate because the stoichiometry of dissolved Si^{4+} is unknown. However, Mg and Si are present so the error is very small.

Combining Equation 7.8 and 7.4 we can estimate the total cathodic current from the measured electrical dissolution currents

$$i_c = i_e - 3\,A\,F\,\nu_{Al} - 2\,A\,F\,\alpha_{Mg}\,\nu_{Al} - 4AF\,\alpha_{Si}\,\nu_{Al} \qquad [7.9]$$

Dividing by (A F) and combining with Equation 7.9 gives

$$\nu_{OH} = -j_c / F = -j_e / F + (3 + 2\alpha_{Mg} + 4\alpha_{Si})\nu_{Al} \qquad [7.10]$$

7.1.2. Residual Mg oxidation products

As Mg oxidation products are insoluble over a large range of potential in these experiments, it is of interest to calculate the quantity of oxide on the surface. The rate at which insoluble products are formed, $\nu^i_{Mg,}$, is determined by:

$$\nu^i_{Mg,} = \nu^o_{Mg} - \nu_{Mg} = \alpha_{Mg}\,\nu_{Al} - \nu_{Mg} \qquad [7.11]$$

An estimate of the total quantity of Mg oxidation products formed between t1 and t2 will be given by the integral of $\nu^i_{Mg,}$ over this time period (equation 7.12). Note that there is an error in this calculation due to integration over transient periods prior to steady state.

$$Q_{Mg} = \int_{t1}^{t2} (\alpha_{Mg}\nu_{Al} - \nu_{Mg})\,dt \qquad [7.12]$$

7.1.3. Stoichiometry of Al dissolution

The stoichiometry of Al dissolution, χ, is defined as the ratio of the instantaneous hydroxide formation rate after removing hydroxide reacts with Mg and Si. We define the free hydroxide formation rate as:

$$\nu_{OH,Al} = \nu_{OH} - 2\nu^o_{Mg} - 4\nu^o_{Si} \qquad [7.13]$$

$$\chi = \nu_{OH,Al} / \nu_{Al} = (\nu_{OH} - 2\alpha_{Mg}\nu_{Al} - 4\alpha_{Si}\nu_{Al}) / \nu_{Al} \qquad [7.14]$$

Of course, $\chi > 4$ is expected due to the removal of hydroxide by mass transfer / diffusion and the precipitation of insoluble corrosion products on the surface as shown in our previous publications [4,5].

7.2. Experimental

7.2.1 Materials

A commercially available Al alloy AA6061 (elemental composition in table 7.1) was used during this work and compared with 99.99% Al (Al alloy AA1199 [5]). Before the ICP experiment the sample was mechanically polished with SiC paper up to grit 4000, rinsed twice with ethanol and de-ionized water and dried under nitrogen. For the XRD observation of the original AA6061 structure, the sample was polished up to 4000 grit SiC under dry conditions and cleaned with compressed nitrogen.

Table 7.1. The elemental microanalysis of AA6061 composition

	Al	Si	Fe	Cu	Mn	Mg	Zn	Cr	Ti
Mol.%	base	1.17%	0.72%	0.41%	0.1%	0.68%	<0.1%	<0.1%	<0.1%

The dissolution rates of the coating elements were measured in a 3 % NaCl electrolyte. Purified water (resistivity of 18.2 MΩ cm) obtained with a Millipore[TM] system was used to rinse the samples and prepare the solutions. All reagents were of analytical purity grade and produced by Analar Normapur VWR[®] BDH Prolabo[®].

7.2.2. Materials Characterization

The crystalline phases were determined by X-ray diffraction (XRD) using Cu Kα radiation (λ = 1.5406 Å) with a *PANalytical diffractometer* operating at 45 kV and 40 mA equipped with an incident beam Ge (111) monochromator and a linear PixCell detector (active length 14 mm). The XRD spectra were collected with an angular resolution of 0.02° and a scanning rate of 0.6 s per point. The phase identification was carried out by referencing the X'Pert HighScore software using PCPDFWIN version 2.02 containing the JCPDS (ICDD) database files.

The shape of intermetallic particles, which appeared on the surface during applied potential experiment, was observed by *scanning electron microscope* Zeiss Supra 55 VP, equipped with elemental microanalysis system (accelerating voltage is 5 keV). The particle observation was performed with an accelerating voltage of 15 keV.

7.2.3. Atomic emission spectroelectrochemistry

Electrolytes were prepared from analytical grade NaOH and deionized water (18.2 MΩ cm) prepared with a Millipore™ system. A saturated calomel reference electrode and a Pt wire counter electrode were placed in the counter electrode compartment of the electrochemical flow cell. The potentiostat was an EG&G Princeton Applied Electronics M273A functioning in the potentiostatic mode. The potentiostat was controlled manually from the front panel with the output analog signals current and potential signals being routed into the measuring circuit of the ICP-OES spectrometer (Ultimata 2C manufactured by Horiba JobinYvon). This circuit relies on a 16 bit A/D converter operating at 250 kHz simultaneously scanning the analog electrochemical signals and the output from the array of photomultipliers. The data is stored in a buffer and an average value over the integration period is then transferred to the computer for storage and presentation. All of the polarization measurements in this work were recorded with an integration time of 1 point/second corresponding to an average value of at least 10 000 individual 16 bit measurements. In this way, even if the integration period is long, the real data acquisition rate is well superior to the time constant of the circuit and a uniform measurement rate is assured throughout the integration period.

During applied potential experiments, the residual electrolyte (only 5 % of the electrolyte is actually aspirated into the plasma, 95% is removed as residual) was collected in 9 cm^3 portions (during each 3 minutes) and the pH was measured.

7.3. Results

7.3.1. Potentiostatic and potentiodynamic experiments

Potentiostatic step experiments were performed to investigate the steady state and transient variations of elemental dissolution rate with potential. A difficulty with these experiments is that the alloy surface composition (and thus, its relative activity or passivity) depends on the history of the sample. Therefore two different potential programs were applied: (1) Direct potential step from the open circuit potential (passive, 1800 s at approximately Eoc = -0.72 V) to the test potential, and (2) Pre-activation potential step in which a cathodic potential of -1.8 V was applied for 900 s followed by a step to the test potential. In light of the importance of the steady state approximation developed in **Section 7.1.2**, the dissolution experiments were continued for significantly longer times than in our previous publication [5].

A typical pre-activation potentiostatic step experiment is shown in **figure 7.1**, illustrating the dissolution reactions for Al, Mg, and Si that are investigated in this article. At the beginning, the sample was exposed to the electrolyte for 1800 s at open circuit (Eoc = -0.72 V) until a steady state dissolution rate was obtained. Following this, the potential was stepped to -1.8 V for 900 s and then stepped to the test potential (in this case, -1.5 V) for the duration of the experiment (around 3000 s). During the open circuit exposure of AA6061, there is a rather low spontaneous dissolution of Al, Mg and Si. When the potential is stepped to -1.8 V, an intense cathodic current is observed coupled with a dramatic increase in the Al dissolution rate. The dissolution rate of Mg however drops below the detection limit while the dissolution of Si increases. Following the pre-activation period, the step to the tested potential was performed (-1.5 V). Under this applied potential, the ν_e, ν_{Al} and ν_{Si} decrease. In contrast, ν_{Mg} increases. The dissolution rates of elements, ν_M, and the total current of the reaction, j_e, were measured as average values during the final 200 s of the applied potential period.

The direct potential step experiment (not shown) was identical except that the 900 s at -1.8 V was omitted such that the surface was initially passive when brought to the test potential.

The steady state polarization curve is given in **figure 7.2** showing $-j_e/F$ and ν_M for M = Al, Mg, and Si. The dissolution of Cu, Fe and Mn was not detected in the potential range of these experiments. The pH of the solution after contact with the sample is also shown. The empty circles represent the pre-activation (marked: "activated") experiment, the filled circles represent the direct application experiment (marked: "direct"). The continuous curve is a potentiodynamic polarization curve with a scan from -1.8 V to -0.7 V at 1 mV s^{-1}.
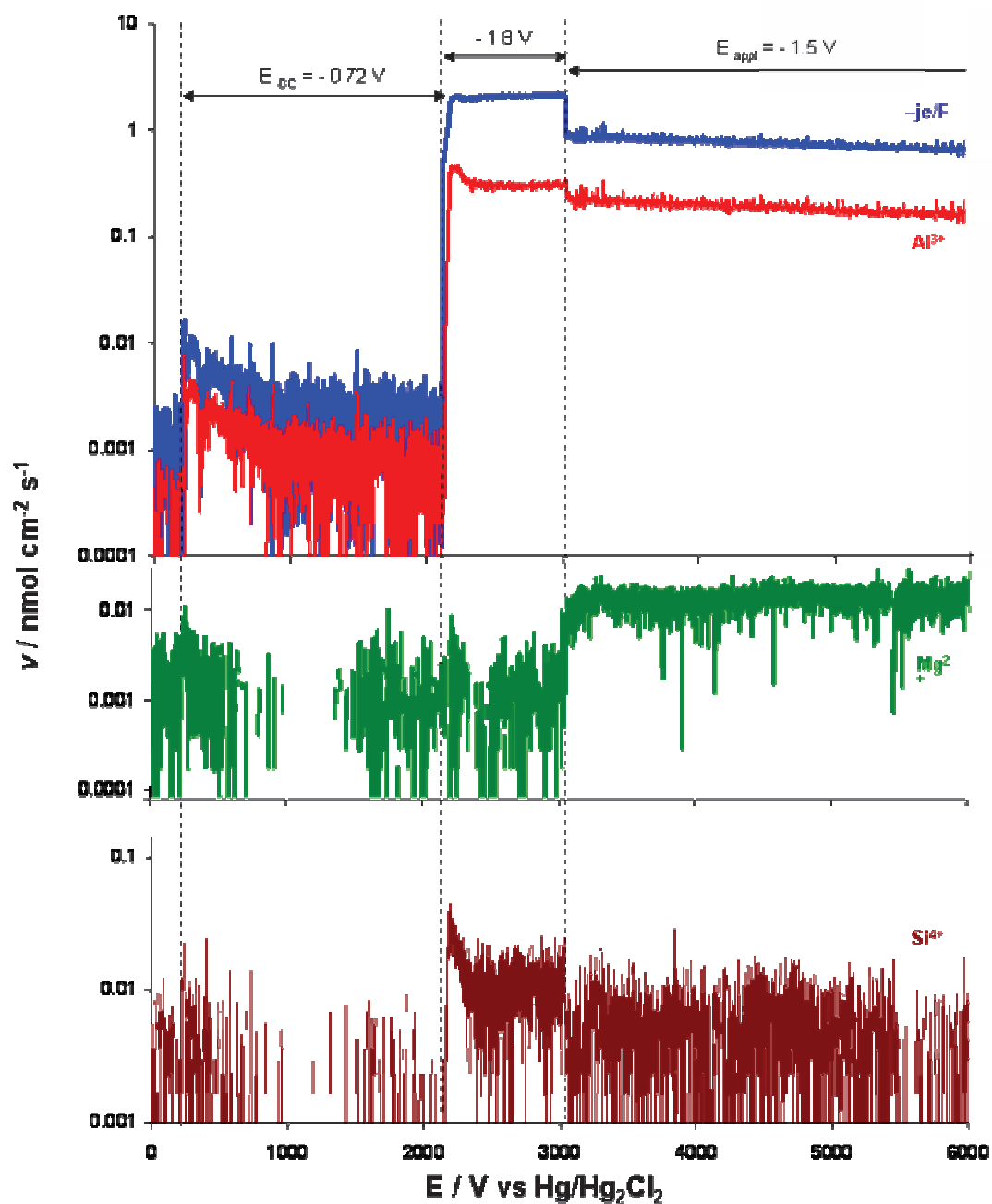
Figure 7.1. *The typical elemental dissolution profile during applied cathodic potential followed by activation of the surface by -1.8 V during 900 seconds.*
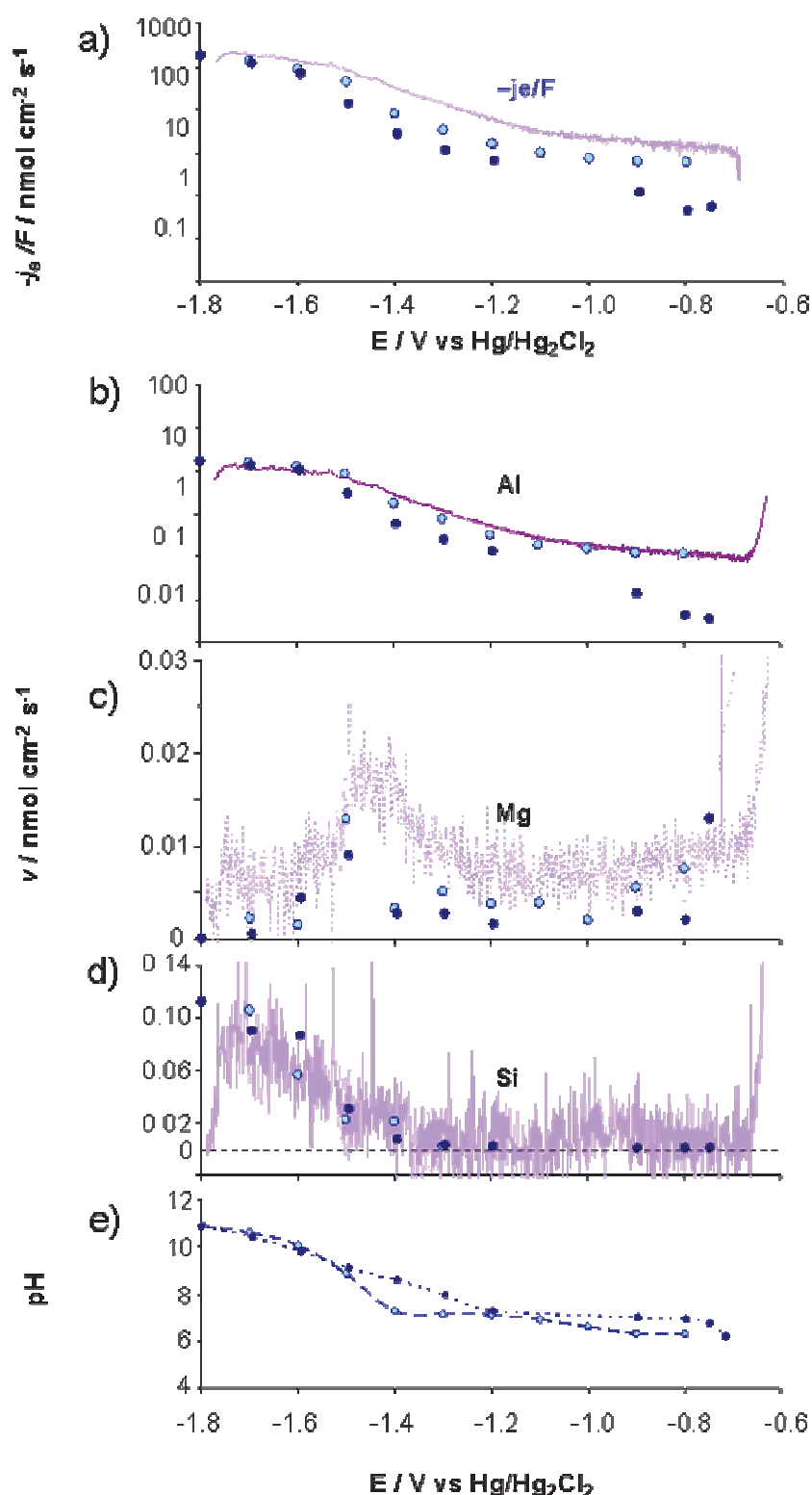
Figure 7.2. *Typical AESEC polarization curves for AA6061 alloy in 3% NaCl, initially neutral, electrolyte. Dissolution profiles are shown for the hydroxide formation rate, $v_{OH} = i_c/(A\ F)$ (a), Al (b), Mg (c) and Si (d). Continuous lines represent potentiodynamic curves obtained at 1 mV s^{-1}. Discrete points represent potentiostatic measurements obtained by direct potential step (filled circles) and with preactivation (empty circles); (e) gives the pH of the electrolyte measured downstream from the flow cell, obtained during the potentiostatic experiments.*

Regardless of the potential program used, certain features of the polarization behavior of AA6061 are clear. **Figure 7.2a** shows the current expressed as a hydroxide generation rate, ν_{OH}, according to equation 7.9. The total current remains cathodic throughout the potential range investigated here. Initially the cathodic reaction is very intense, approaching -13.5 mA cm^{-2} at -1.8 V but decreasing by several orders of magnitude as the potential becomes positive. This variation is also reflected in the electrolyte pH measured downstream from the electrochemical flow cell (**figure 7.2e**).

The ν_{Si} and ν_{Al} decrease with increasing potential and show good agreement between the two steady state modes as well as the potentiodynamic experiment. Mg dissolution however shows a more complex behavior. In the potentiodynamic curve, ν_{Mg} shows a peak centered around -1.5 V. These data are obviously affected by the transient formation of insoluble Mg oxidation products as the width of the dissolution peak is larger in the potentiodynamic experiment than in the potentiostatic experiment.

Similar experiments were performed for AA1199 (99.99% Al). The results were in good agreement with the results in our previous publication [5] and are not presented here.

7.3.2. Stoichiometry of Al dissolution

The fact that ν_{Mg} is very close to zero at the more negative cathodic potentials indicates that oxidized Mg corrosion products are building up on the surface in the form of a residual film. The quantity of residual Mg film formation may be estimated as Q_{Mg} (equation 7.12) and is presented in **figure 7.3a** as function of potential for AA6061. This calculation includes the build-up of Mg oxidation film during the preactivation step and during the applied test potential prior to the steady state rate measurement. The major difference between the direct experiment and the experiment with pre-activation step is the formation of a significant Mg oxidation film during the preactivation step at -1.8 V. In the domain more negative than -1.4 V the amount of Mg^{2+} increases when the potential decreases for both experimental modes. In the domain more positive than -1.4 V, no residual film formation occurs.

The stoichiometric ratio, $\chi = \nu_{OH,Al} / \nu_{Al}$ (equation 7.14) is presented in **figure 3b**. The results demonstrate that χ varies from 4 to 6 in the potential range more anodic than -1.7 V for

99.99% Al (AA1199) consistent with our previous work [5]. For AA6061, a similar result is observed only in a narrow potential range between -1.5 V and -1.2 V. For $E_{ap} <$ -1.5 V, χ increases, approaching 9 at -1.8 V for both the direct and the pre-activated potentiostatic experiments. In the more positive potential range, the direct potentiostatic experiment also yields approximately χ = 4 to 5. However following pre-activation, χ increases with increasing potential as in the cathodic domain.
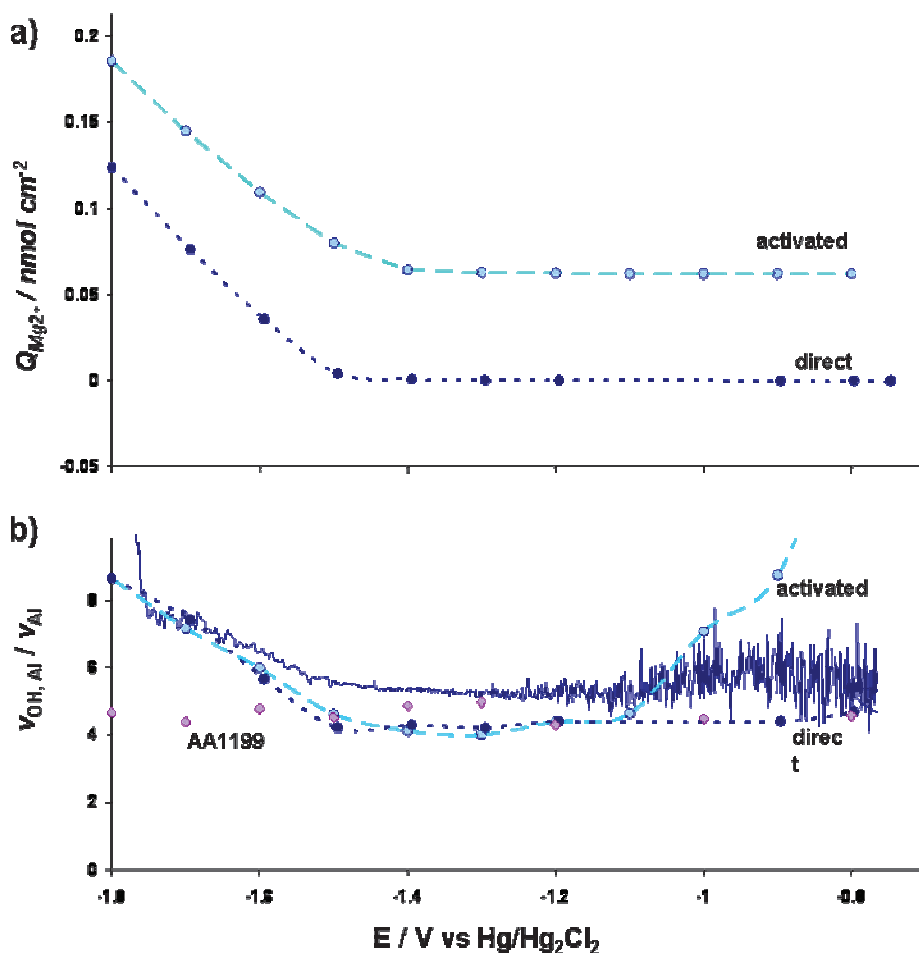
Figure 7.3. (a) - Amount of Mg(OH)$_2$ formed on the surface of AA6061 during potentiostatic experiment, (b) - $\nu_{OH,Al}$ / ν_{Al} as a function of potential in the cathodic domain for AA6061 (direct potential step is represented by filled circles and with preactivation is represented by empty circles) and 99.99% Al (AA1199 alloy) for both the direct and pre-activated experiment. For pure Al only the direct program was used.

Figure 7.4 gives ν_{Al} as a function of ν_{OH}. In this figure, the dissolution rate seems to depend only upon the magnitude of the cathodic current as the pre-activation and direct mode potential programs give identical results. This demonstrates that the quantity of Mg oxidation products on the surface does not significantly affect the stoichiometry of Al dissolution.

125
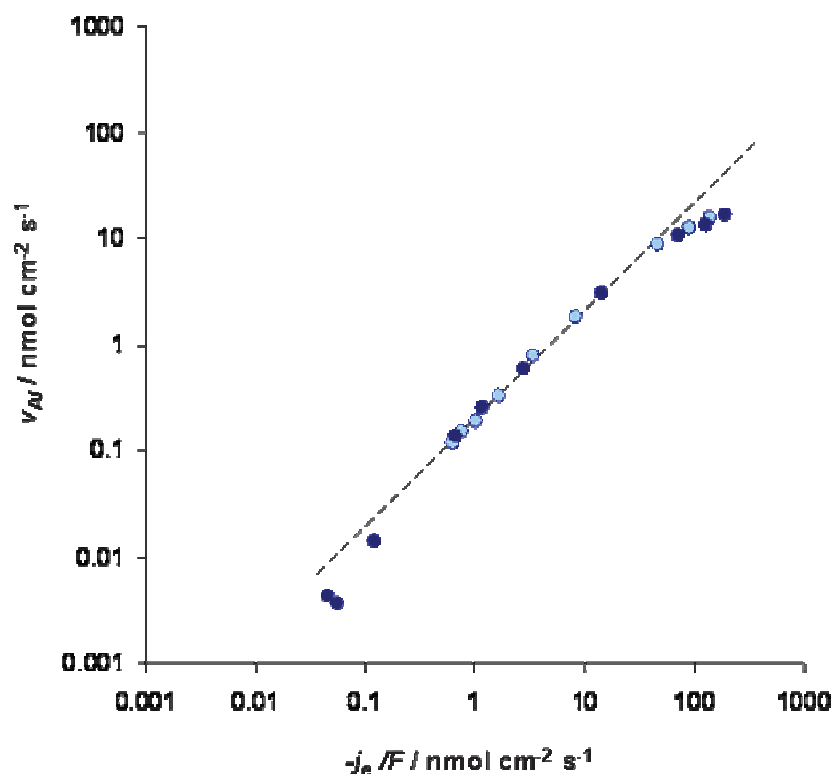
Figure 7.4. *The dissolution rate of Al as function of cathodic current (direct potential step is represented by filled circles and with preactivation is represented by empty circles).*

7.3.3. SEM and XRD characterization

Figure 7.5 shows scanning electron micrographs and elemental cartographies after 1 min and 90 min of applied constant cathodic potential (-1.5 V). The high selective Al dissolution in the strong cathodic domain leads to the appearance of visible by SEM Al, Fe, Mn and Si enriched particles on the surface and to the increase of Cu and Mg concentrations on the surrounding surface (see table 7.2). The visible size of the particles increases with increasing exposure time because of the dissolution of surrounding Al matrix. The SEM analysis did not reveal the increase of oxygen signal in particles indicating that the intermetallic stays in inoxydized form.
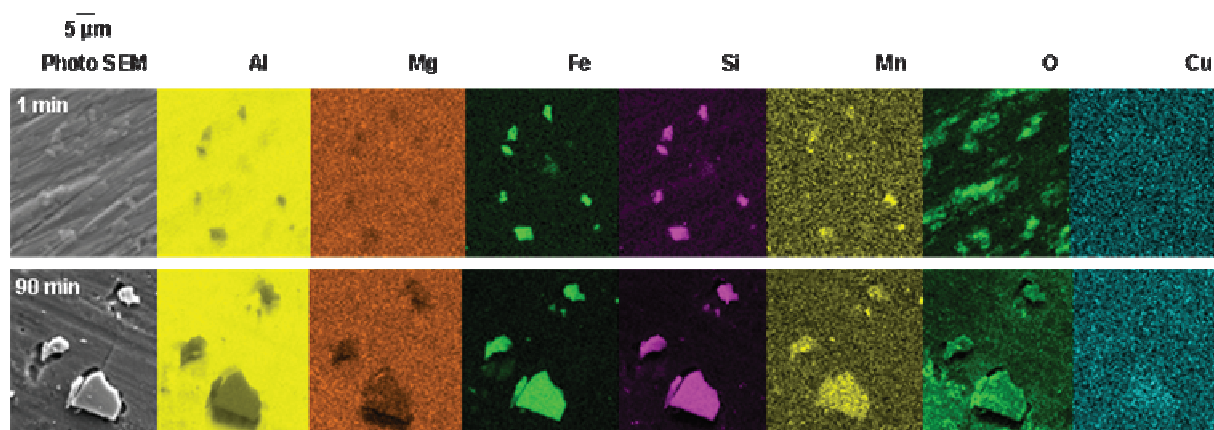
Figure 7.5. *The scanning electron micrograph and elemental cartography of the surface after 1 minute and 90 minutes of applied potential (-1.5 V) in 3% NaCl solution.*

Table 7.2. The elemental surface composition after applied cathodic potential (mol.%)				
	Element	% in particles	% out of particles	
-1.5 V (90 min)	Al	58.6	97	
	Mg	0.16	0.68	
	Si	11.16	1.13	
	Fe	26.4	0.31	
	Cu	0.5	0.43	
-1.8 V(15 min) and -1.5 V (90 min)	Al	30.5	91.9	
	Mg	2.3	2.3	
	Si	8.4	3.8	
	Fe	39.6	0.3	
	Cu	2.0	1.0	

Figure 7.6 shows XRD analysis of the original sample, polished under dry conditions, and after 90 minutes of applied cathodic potential -1.5 V. Both diffractograms show the presence of Al (labeled as "a"), SiO_2 (b), $MgSiO_3$ (c) and different intermetallics close to $Al_n[Fe_m,Mn_{1-m}]Si$ composition (d) [7] peaks (**figure 7.6**). The difference in the two diffraction patterns is the presence of Mg_2Si (β) which was detected in the original sample but not after the contact with aqueous electrolyte.
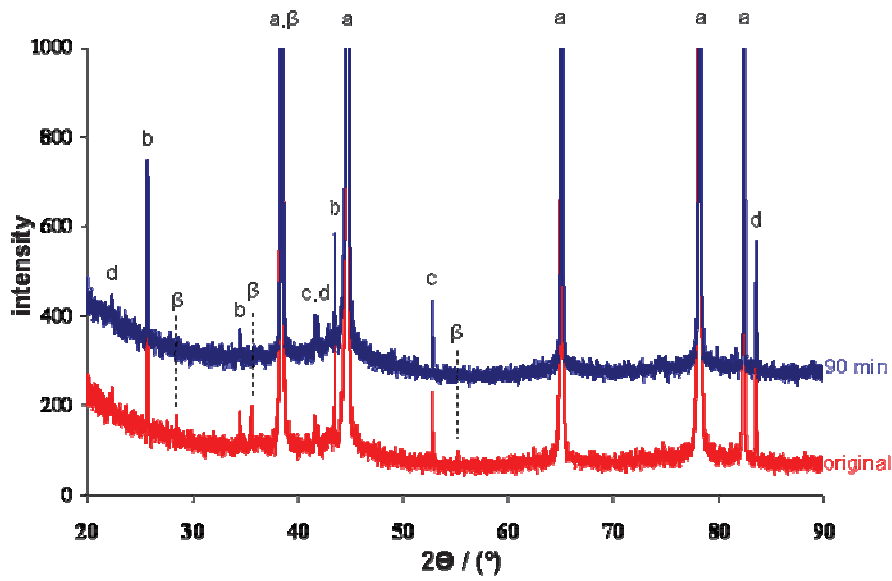
Figure 7.6. *The XRD spectra of the AA6061 original surface and after 90 min of the applied cathodic potential -1.5 V: (a) – Al, (b) – MgSiO3, (β) – Mg₂Si, (c) –SiO₂, (d) –* Al$_n$[Fe$_m$,Mn$_{1-m}$]Si.

7.4. Discussion

The results of this work can be interpreted in terms of Al, Si and Mg dissolution in presence of cathodically generated hydroxide. In a previous publication [20] a model was proposed to estimate the interfacial pH taking into account the amount of OH⁻ which is necessary for elemental dissolution (Al, Mg and Si in this work) and diffusion away from the surface in the assumption of a steady state reaction and stationary conditions on the interface according the equation:

$$-\log(C_i) = -\log(D_{OH} / \delta \, (\, v_{OH} - 4 \, v_{Al} - 2 \, v_{Mg} - 4 \, v_{Si}) + C^{\infty}) \qquad [7.15]$$

where C_i – the concentration of OH⁻ near the interface, C^{∞} is the concentration on the OH⁻ far from the surface, δ is the Nernst diffusion layer thickness estimated as 0.03 mm [21]. Following this model, the interfacial pH on the AA6061 was calculated for all potentiostatic experiments. The measured by AESEC magnesium concentration, C_{Mg}, as a function of the interfacial pH is presented in **figure 7.7**.
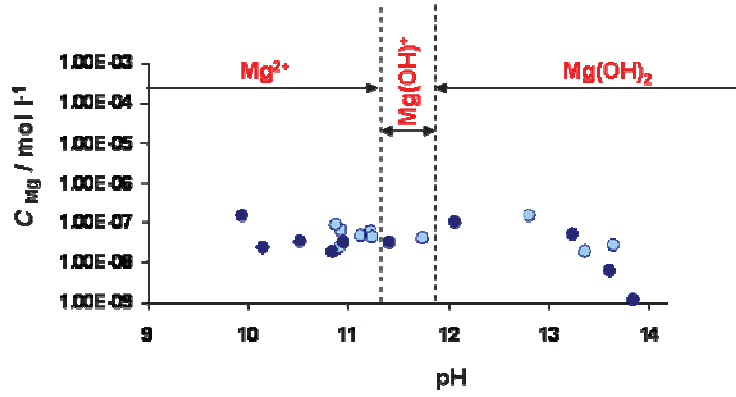
Figure 7.7. *Mg concentration, C_{Mg}, as a function of near surface pH. The dominant species are marked.*

Up to an interfacial pH of around 13.3, Mg dissolution is practically independent of interfacial pH. For pH > 13.3 the ν_{Mg} decreases. This pH corresponds to the -1.5 V applied potential (**figure 7.7**) [22].

The presence of Mg_2Si in the original structure [23, 24] of AA6061 alloy and its absence after the applied cathodic experiment (according to the XRD data) is consistent with literature data [25, 23]. This can be interpreted in terms of the Al corrosion mechanism, associated with the presence of Mg_2Si and $Al_n[Fe_m,Mn_{1-m}]Si$ in the alloy [26, 6]. As soon as the electrolyte contacts the surface, the decomposition of Mg_2Si begins (according to reaction 12) due to the more negative corrosion potential of Mg_2Si (-1.16 V vs SCE) in comparison with Al and other intermetallics [6, 26, 29]. Therefore we attribute the increase in χ at high cathodic currents to the increase in the formation rate of hydroxide ultimately becoming more rapid than the regeneration of the oxide film. The nature of the oxide film can be also different in case of transition from low to high cathodic potential reactivity type [20].

$$Mg_2Si + 6H_2O \rightarrow 2Mg^{2+} + SiO_2 + 4OH^- + 4H_2 \qquad [7.16]$$
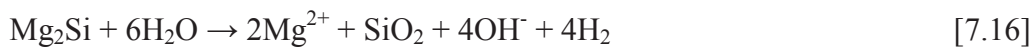
The XRD spectra of AA6061 alloy after either spontaneous dissolution during polishing in aqueous solution or applied potential do not contain peaks of Mg_2Si. The combination of XRD data with SEM analysis of the surface after the applied cathodic potential shows the growth of particles with composition close to $Al_n[Fe_m,Mn_{1-m}]Si$ with a hole in the substrate around them. These intermetallics are known to be cathodic activators of Al reactivity [29]. They may serve as local cathodes leading to the acceleration of water reduction in both the spontaneous and the cathodic potential domain. The increases rate of local pH formation

according to the equations 7.7 or 7.8 may accelerate the Mg_2Si decomposition. A simplified schematic diagram of the decomposition of AA6061 is presented in **figure 7.8**.
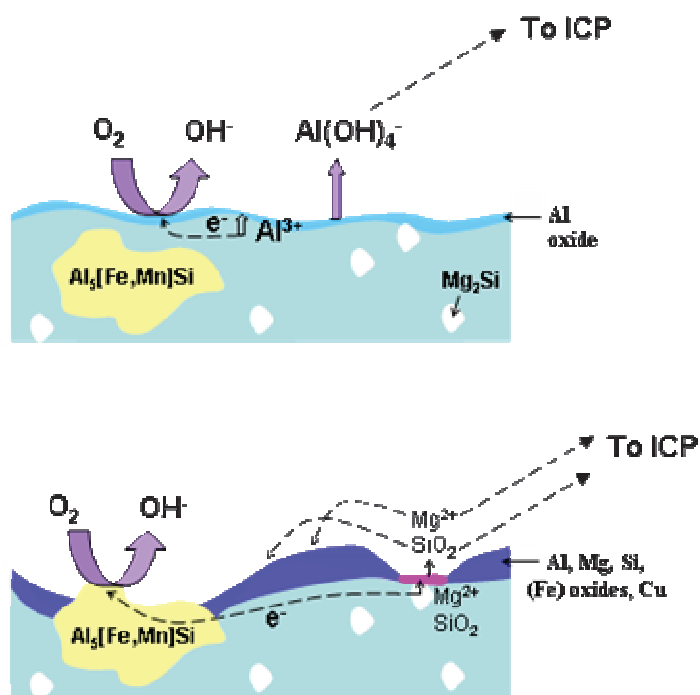
Figure 7.8. *The proposed mechanism of AA6061 corrosion.*

Hydroxides, formed during water reduction can participate in different processes. First, they react with Al in the substrate, leading to its dissolution. The results of the stoichiometry of Al dissolution follow the simple model in which hydroxide generation, $Al(OH)_3$ formation/dissolution (according to the reactions 7.1 and 7.2), and $Al(OH)_4^-$ diffusion are kinetically coupled [5]. The ratio between v_{OH} and v_{Al} (measured by AESEC) is independent of the cathodic current in the domain where Mg dissolves and does not block the surface.

The increase of the oxide formation rate at high cathodic currents (and hence high OH^- generation rate) can be interpreted in terms of the Mg hydroxide precipitation on the surface. The elemental microanalysis of the surface after an applied cathodic potential confirms the increase of Mg and O concentration on the surface after the experiment (see Table 7.2 and **figure 7.5**).

The formation of Mg residual film on the surface interrupts the access of the hydroxides to the Al and increases the stoichiometry between v_{Al} and v_{OH} in the strong cathodic domain

130

(**figure 7.2**). When the cathodic current decreases (the potential becomes more positive) the amount of Mg^{2+} combined with OH^- decreases. Mg^{2+} goes into the solution (maximum on the Mg dissolution curve in **figure 7.2**) and does not block the surface anymore: the stoichiometry of Al dissolution reaction returns to the stoichiometry observed on pure Al. As demonstrated in 3.2 the amount of Mg oxide deposited on the surface does not significantly affect the stoichiometry of Al dissolution.

The elemental analysis of the surface after the applied cathodic potential shows the enrichment by Cu. It was previously shown that such noble elements stay in their metallic form on the surface because their oxides are significantly less stable than Al oxide [27]. However in this case, the copper seems to be uniformly distributed on the surface while for many Cu containing Al alloys, the Cu is localized in discrete particles.

Hydroxide is also consumed by the dissolution of Si from the $Al_n[Fe_m,Mn_{1-m}]Si/SiO_2$ particles. It is known that both Al and Si dissolution reactions require OH^- (reaction 7.1-7.2 and 7.17) [19, 28].

$$SiO_2 + 2NaOH \rightarrow Na_2SiO_3 + H_2O \qquad\qquad [7.17]$$

For the alloy AA6061 Si dissolution is similar to Al dissolution: in the more cathodic domain the dissolution of Si is higher, while close to the corrosion potential Si dissolution decreases below the detection limit. Some uncomplexed hydroxides diffuse into the electrolyte and increase the pH of the solution.

7.5. Conclusion

The mechanism of AA6061 corrosion is proposed in this work using the AESEC method. The Al dissolution rate was interpreted in terms of the simple model in which hydroxide generation, $Al(OH)_3$ formation/dissolution and $Al(OH)_4^-$ diffusion are kinetically coupled. $Al_n[Fe_m,Mn_{1-m}]Si$ phases in the structure were explained as the local cathode which accelerates the Al dissolution rate; in contrast Mg precipitation on the surface occurs at high cathodic currents. This however has no apparent effect on the stoichiometry of the cathodic dissolution of Al.

7.6. References

1.   S.-M. Moon, S.-I. Pyun "The corrosion of pure aluminium during cathodic polarization in aqueous solutions" *Corrosion Science* **39** (1997) 399–408.

2.   A.P. Yadava, H. Katayama, K. Noda, H. Masuda, A. Nishikata, T. Tsuru "Effect of Al on the galvanic ability of Zn–Al coating under thin layer of electrolyte" *Electrochimica Acta* **52** (2007) 2411–2422.

3.   R. Oltra, A. Zimmer, C. Sorriano, F. Rechou, C. Borkowski "Simulation of pH-controlled dissolution of aluminum based on a modified Scanning Electrochemical Microscope experiment to mimic localized trenching on aluminum alloys" *Electrochimica Acta* **56** (2011) 7038-7044.

4.   M. Mokaddem, P. Volovitch, F. Rechou, R. Oltra, K. Ogle "The anodic and cathodic dissolution of Al and Al-Cu-Mg alloy" *Electrochimica Acta* **55** (2010) 3779–3786.

5.   K. Ogle, M. Serdechnova, M. Mokaddem, P. Volovitch, "The cathodic dissolution of Al, Al_2Cu, and Al alloys" *Electrochimica Acta* **56** (2011) 1711–1718.

6.   F. Zeng, Z. Wei, J. Li, C. Li, X. Tan,Z. Zhang, Z. Zheng "Corrosion mechanism associated with Mg2Si and Si particles in Al–Mg–Si alloys" *Transactions of Nonferrous Metals Society of China* **21** (2011) 2559–2567.

7.   A. Hekmat-Ardakan, X. Liu, F. Ajersch, X.-G. Chen "Wear behaviour of hypereutectic Al–Si–Cu–Mg casting alloys with variable Mg contents" *Wear* **269** (2010) 684–692.

8.   N. Birbilis, R.G. Buchheit "Electrochemical Characteristics of Intermetallic Phases in Aluminum Alloys An Experimental Survey and Discussion" *J. Electrochem. Soc.* **152** (2005) B140–B151.

9.   A. Pardoa, M.C. Merino, A.E. Coy, F. Viejo, R. Arrabal, S. Feliú Jr. "Influence of microstructure and composition on the corrosion behaviour of Mg/Al alloys in chloride media" *Electrochimica Acta* **53** (2008) 7890–7902.

10.   A.B. Gurcan, T.N. Baker "Wear behaviour of AA6061 aluminium alloy and its composites" *Wear* **188** (1995) 185–191.

11.   R. Zeng, J. Zhang, W.Huang, W. Dietzel, K.-U. Kainer, C. Blawert, W. KE. "Review of studies on corrosion of magnesium alloys" *Transactions of Nonferrous Metals Society of China* 16(2) (2006) s763–s771.

12.   H. Takahashi, K. Fujiwara, M. Seo, "The cathodic polarization of aluminum covered with anodic oxide films in a neutral borate solution- II. Film breakdown and pit formation" *Corrosion Science* **36** (1994) 689–705.

13.   Y. Baek G.S. Frankel "Electrochemical Quartz Crystal Microbalance Study of Corrosion of Phases in AA2024" *Journal of the Electrochemical Society* **150** (2003) B1–B9.

14.   I.L. Muller, J.R. Galvele, "Pitting potential of high purity binary aluminium alloys-I. Al-Cu alloys. Pitting and intergranular corrosion" *Corrosion Science* **17** (1997) 179–193.

15.   M. Bethencourt, F.J. Botana, M.J. Cano, M. Marcos, J.M. Sánchez-Amaya, L. González-Rovira "Behaviour of the alloy AA2017 in aqueous solutions of NaCl. Part I: Corrosion mechanisms" *Corrosion Science* **51** (2009) 518–524.

16.   W.A. Badawy, N.H. Hilal, M. El-Rabiee, H. Nady "Electrochemical behavior of Mg and some Mg alloys in aqueous solutions of different pH" *Electrochimica Acta* **55** (2010) 1880–1887.

17.   G.M. Abady, N.H. Hilal, M. El-Rabiee, W.A. Badawy, "Effect of Al content on the corrosion behavior of Mg–Al alloys in aqueous solutions of different pH" *Electrochimica Acta* **55** (2010) 6651–6658.

18.   K. Ogle, J. Baeyens, J. Swiatowska, P. Volovitch "Atomic emission spectroelectrochemistry applied to dealloying phenomena: I. The formation and dissolution of residual copper films on stainless steel" *Electrochimica Acta* **54** (2009) 5163–5170.

19.   M. Serdechnova, P. Volovitch, K. Ogle "Atomic emission spectroelectrochemistry study of the degradation mechanism of model high-temperature paint containing sacrificial aluminum particles" *Surface and Coatings Technology* 206 (2012) 2133–2139.

20.   P. Volovitch, M. Serdechnova, K. Ogle "Aqueous Corrosion of Mg-Al Binary Alloys: Roles of Al and Mg" *Corrosion* **68(6)** (2012) 93-106.

21.   F. Thebault, B. Vuillemin, R. Oltra, C. Allely, K. Ogle "Protective mechanisms occurring on zinc coated steel cut-edges in immersion conditions" *Electrochimica Acta* **56** (2011) 8347-8357.

22.   I. Puigdomenech, "Hydra/Medusa Chemical Equilibrium Database and Plotting Software", Version 18 August, 2009. Database update- 2/21/2011, *KTH Royal Institute of Technology* (2004).

23.   G. Mrówka-Nowotnik, J. Sieniawski, M. Wierzbińska "Analysis of intermetallic particles in Al-Si-Mg-Mn aluminium alloy" *Journal of Achievements in Materials and Manufacturing Engineering* **20** (2007) 155–158.

24.   M.J. Yang, L.M. Zhang, L.Q. Han, Q. Shen, C.B. Wang "Simple fabrication of Mg2Si thermoelectric generator by spark plasma sintering" *Indian Journal of Engineering and Material Sciences* **16** (2009) 277–280.

25.   P. Appendino, C. Badini, F. Marino, A. Tomasi "6061 aluminium alloy-SiC particulate composite: a comparison between aging behavior in T4 and T6 treatments" *Materials Science and Engineering: A* **135** (1991) 275–279.

26.   P. Volovitch, J.E. Masse, A. Fabre, L. Barrallier, W. Saikaly "Microstructure and corrosion resistance of magnesium alloy ZE41 with laser surface cladding by Al–Si powder" *Surface and Coatings Technology* **202** (2008) 4901–4914.

27.   A. B. M. Mujibur Rahman, S. Kumar, A.R. Gerson, "The speciation of Si and other alloying elements in the oxide surface film of galvanically corroded weld fusion zone of laser welded AA6061 aluminium alloy" *Corrosion Science* **50** (2008) 1267–1273.

28.   P.M. Dove, "The dissolution kinetics of quartz in aqueous mixed cation solutions" *Geochimica et Cosmochimica Acta* **63** (1999) 3715–3727.

29.   F. Norouzi Afshar, J.H.W. de Wit, H. Terryn, J.M.C. Mol "The effect of brazing process on microstructure evolution and corrosion performance of a modified AA4XXX/AA3XXX brazing sheet" *Corrosion Science* **58** (2012) 242–250.

Chapter VIII

Aqueous corrosion of Mg-Al binary alloys: role of Al and Mg

Polina Volovitch, Maria Serdechnova, Kevin Ogle

Aqueous corrosion of Mg-Al binary alloys: role of Al and Mg

The mutual effect of Al and Mg on the corrosion of model binary Mg-Al alloys (Mg from 0 to 100 wt %) in 3 wt.% NaCl aqueous solutions is studied by atomic emission spectroelectrochemistry (AESEC). Mg^{2+} ions retard the formation of passive oxide on Al and alloys during spontaneous reaction but inhibit the cathodic dissolution of Al from Mg-Al alloys. The ratio between cathodically generated OH^- and dissolved Al increases significantly with Mg^{2+} in the solution suggesting the formation of insoluble product. Al^{3+} in the solution does not influence the anodic current evolution on Mg but decreases the Mg dissolution rate indicating that oxidized Mg stays in insoluble form. The titration experiments and the XRD analysis confirm the co-precipitation of Al^{3+} and Mg^{2+}. The rapidly formed semiconducting spinel is supposed to be responsible for the reduced concentrations of soluble Al and Mg and delayed in comparison to Mg-free solution passivation of Al surface. The interpretation is made that key factor for the reactivity of Al-Mg binary alloys is the modified solution composition near the surface which is controlled by the chemical composition of the alloy via the selective dissolution processes.

8.1. Introduction

It is generally accepted [1] that the electrochemical behavior of alloys cannot be predicted from the chemical composition and electrochemical data of pure metals. Some models were proposed for binary alloys containing one noble and one active metal [2,3] but these models were not extended to include a combination of two active metals like Al and Mg. The coupling of Al and Mg is complicated due to the possibility of passivation of both metals: Al at neutral and slightly acid pH and Mg at high pH [4-7] and by the variation of solution composition by accumulation of cathodic and anodic reaction products. Further complicating the situation is the formation of mixed Al-Mg oxidized species often detected in corrosion products on Al-Mg compounds and on the Al alloys corroded in the presence of Mg^{2+} [8-11]. Another factor is that for Al-Mg alloys, the complex microstructure can result in galvanic potentials and interphase boundaries preventing the formation of barrier layers and enhancing corrosion [12-14]. As a result, the corrosion and pitting potential values are not sufficient to predict the current densities for Al and Mg alloys, Al-Mg binary layers in coatings, their intermetallics and mutual solid solutions [4-21]. Key factors that could determine the behavior of the binary (or more complex) Mg-Al compounds include a complex microstructure, the surface composition of which is modified by selective dissolution, oxide layer formation and/or precipitated corrosion products. Further the solution chemistry near the surface is modified by the corrosion reactions. The experimental resolution of such a problem requires separating the different phenomena of the corrosion process. The intrinsic reactivity of the alloy, the variation of the solution composition by accumulation cathodic and anodic reaction products, and the interactions between different ions in the solution resulting in the precipitation processes need to be measured independently.

The goal of this study is to evaluate the mutual role of Al and Mg on the elementary corrosion phenomena (dissolution, surface oxide formation, precipitation) by simultaneous, in-situ measurement of the elementary dissolution rates of binary Mg-Al alloys with from 0 wt % to 100 wt % of Mg and from pure Al or Mg with the addition of a small concentration of the second element in the solution. The direct measurement of the dissolution rates of Mg and Al and the potential-electrochemical current measurement are performed by atomic emission spectroelectochemistry (AESEC) technique [22]. This technique combines an electrochemical flow cell with an inductively coupled plasma optical emission spectrometer (ICP-OES) used to monitor in real time the elements released by the reactions in the flow cell. The electrolyte in the flow cell is permanently renewed which disfavors the accumulation of the reaction

products and hence discriminates precipitation processes, allowing us to measure the intrinsic reactivity of the alloy. The dissolution is measured at both spontaneous, open circuit potential and under polarization. The pH evolution of the electrolyte is also monitored downstream from the flow cell. The rate of hydroxide ion generation by the cathodic reaction is estimated from the difference between the total electrochemical current and the sum of elemental dissolution currents. The precipitation conditions are studied by titration experiments.

8.1.1. Principe of AESEC rate measurement for anodic dissolution and hydroxide ion generation

The principle of the AESEC measurement has been previously described in detail [22,23]. Briefly, it consists of an electrochemical flow cell coupled with an inductively coupled plasma optical emission spectrometer. In the flow cell, the reaction between the sample and the aggressive electrolyte occurs, leading to the production of dissolved ions. The electrolyte is transported to the inductively coupled plasma optical emission spectrometer (ICP-OES) where its composition is continuously analyzed. The instantaneous dissolution rate of an element M in the cell, v_M, is directly related to the instantaneous downstream concentration (in nmol s^{-1} cm^{-2}) as:

$$v_M = C_M f / A \qquad\qquad [8.1]$$

where f is the flow rate of electrolyte (in this work it was fixed at 3.02 cm^3 min^{-1}), C_M is a concentration of element M, and A is the surface area (0.51 cm^2) of the exposed surface. C_M is measured from the emission intensity at a specific wavelength using normal quantitative procedures for ICP spectrometry. The Faraday's law quality of the techniques was previously demonstrated for a number of chemical elements, including Al [23] and Mg [24].

Under electrochemical control, the total current, j_e, between working electrode and counter electrode is measured with the potentiostat. It can be expressed as an equivalent electron transfer rate (v_e) by Faraday's law:

$$v_e = j_e / n F \qquad\qquad [8.2]$$

where F is the Faraday constant and n = 1 for electron.

As the total current j_e is the sum of the cathodic and anodic components (j_{cat} and j_A respectively) the equivalent electron transfer rate can be decomposed into a cathodic electron transfer rate v_{cat} and anodic electron transfer rate v_A.

$$v_e = v_A + v_{cat} \qquad [8.3]$$

Under anodic potentials, in the absence of oxide film growth, the anodic electron transfer rate (with n=1 for electron), v_A, can be assumed to be equal to the sum of the instantaneous downstream dissolution rates v_M of all elements with coefficients corresponding to the cation charge n_M,

$$v_A = \Sigma n_M v_M = j_A / F \qquad [8.4]$$

In the presence of oxide film growth, the difference between v_A and $\Sigma n_M v_M$ can be used to estimate the rate of oxide formation [25]. There is a different time resolution between v_e and v_M. Therefore, for rapidly changing transients, it is necessary to transform one into the time resolution of the other by performing a numerical convolution. In current work we were mainly focused on the conditions at which the quasi steady-state can be obtained and the convolution was not performed because its influence in quasi steady state is less important than for rapid transients.

When the thickness of the oxide film can be neglected, assuming the cathodic reaction (solution is not de-aerated) in the form (5) or (6)

$$2H_2O + O_2 + 4e \rightarrow 4\ OH^- \qquad [8.5]$$

$$2H_2O + 2e \rightarrow H_2 + 2OH^- \qquad [8.6]$$

the OH^- generation rate, v_{OH}, can be estimated by the combination of the total electron transfer rate (v_e) and the sum of anodic electron transfer rates, v_A. Assuming no oxide film growth or dissolution, the OH^- generation rate can be calculated as:

$$v_{OH} = -\ (\ v_e - v_A) \qquad [8.7]$$

The hydroxide generation rate and the oxide formation rate in this work are calculated in assumption of Mg(II) and Al(III).

We do not measure the total cathodic current in this experiment, only the cathodic current in excess of that necessary to balance oxidation. A simultaneous volumetric measurement of hydrogen would correct this problem to the extent that hydrogen reduction (reaction 6) is certainly the major contribution to the cathodic current, j_{cat}. We have not however observed the visible gas formation occurs except for AlMg(65) and AlMg(50) during polarization experiments in the cathodic domain around -1.8 vs. Hg/Hg_2Cl_2. It can be understood if the reaction rates and times are taken into account. Cathodic current of 1mA cm^{-2} is expected to produce about 10^{-8} mol s^{-1} or about 0.1-0.2 µl s^{-1} of gas per cm^2 of reacting surface; in our experiment the active surface is 0.5 cm^2, the in-situ measurement of formed gas is hence not a trivial task. Moreover, the error bars can still be significant compared to the precision of ICP concentration measurement even for the total volume of gas collected during several hundreds seconds of the AESEC experiment (about 0.1 ml for 1000 s). The volumetric measurement of hydrogen formation can be also ambiguous because of possible formation and high stability of Mg hydride.

8.2. Experimental

8.2.1. Materials

The chemical composition and information about the microstructure of the materials used in current study is presented in **Table 1**. The intermetallic phase $Mg_{17}Al_{12}$ was prepared by powder technique as described in [10]. The binary alloys were prepared specially for this study by co-evaporation of Mg and Al by PVD. The phase composition and grain size was verified by scanning electron microscopy using a Zeiss Supra 55 VP microscope at accelerating voltage of 20 kV. The crystalline phases were determined by X-ray diffraction (XRD) using Cu Kα radiation ($λ = 1.5406$ Å) with a PANalytical diffractometer operating at 45 kV and 40 mA equipped with an incident beam Ge (111) monochromator and a linear PixCell detector (active length 14 mm). The XRD spectra were collected with an angular resolution of 0.02° and a scanning rate of 0.3 s per point. The phase identification was carried out by referencing the X'Pert HighScore software using PCPDFWIN version 2.02 containing the JCPDS (ICDD) database files.

TABLE 1
Materials

	Al Alloy 1199	Mg Alloy	AlMg I	AlMg II	AlMg III	AlMg IV	$Al_{12}Mg_{17}$
Name	Al	Mg	AlMg(20)	AlMg(50)	AlMg(50T)	AlMg(65)	βAlMg
Nominal Al/wt%	99.999	0.0066	80.0	48.6	48.6	34.8	37.5
Nominal Mg/wt%	<0.006	99.94	20.0	50.9	50.9	65.2	62.5
Possible impurities/wt%	Fe, Si, Cu, Zn, Mn<0.006	Si 0.0137 Mn 0.008 Fe, Ni<0.006	Fe < 0.07, Si < 0.4, Mn < 0.006, Zn < 0.06				Si 0.0137 Mn 0.008 Fe, Ni, Zn<0.006
Treatment	Polishing with 4000 grit SiC paper	Polishing with 4000 grit SiC paper	Plasma deposited, as-received and polished with 4000 grit paper	Plasma deposited, as-received and polished with 4000 grit paper	Plasma deposited, annealed at 250°C for 72 h under high vacuum	Plasma deposited, as-received and with 4000 grit paper	Polishing with 4000 grit SiC paper
Supposed structure	Al (XRD)	α-Mg (XRD)	Al with $Al_{12}Mg_{17}$	$Al_{12}Mg_{17}$ (XRD) + residual α-Mg	$Al_{12}Mg_{17}$ (XRD) + Al_3Mg_2?	$Al_{12}Mg_{17}$ (XRD) + α-Mg	$Al_{12}Mg_{17}$ (XRD)

For PVD coatings the grain size in order of 30 - 40 nm resulted in difficult phase identification by XRD. Metallic Al was detected in all PVD samples in as deposited state which can suppose for these samples non-equilibrium structure with Mg dissolved in α-Al as a solid solution even despite it high content. The large peak at about 36° accompanied by narrows peak at 65° were observed for 50 wt% and 65 wt% of Mg alloys. The two possible interpretations are the formation of β-$Al_{12}Mg_{17}$ intermetallic with thin grain size or formation of glassy Mg in α-Al as proposed for coatings obtained similarly in [17]. After heat treatment at 250°C for 72 h in secondary vacuum the peaks of intermetallic phase appear clearly.

8.2.2. Titration experiment.

All solutions used in this work were prepared using analytical grade reagents (AnalaR NORMAPUR, VWR ProLabo) in high purity water (resistance 18MΩ).

For titration experiments the $Al(NO_3)_3 \cdot 9H_2O$ and $Mg(NO_3)_2 \cdot 6H_2O$ were added into 3% NaCl solution in concentrations presented by **Table 2**. The choice of concentrations was based on the idea to respect the ratio between Al and Mg in the solution corresponding to chosen value (0 wt %, 20 wt %, 50 wt %, 65 wt % or 100 wt % of Mg).

The initial solution volume for the slow titration experiment was 30 ml. The titration was performed by 1 M NaOH prepared from the Titrisol® Merck KGaA (Germany) standard in 1000 ml ultra-pure water (Millipore, Synergy UV) using Ω Metrohm, 808 Titrando (Swiss) system at 23°C. Added volume for slow titration experiment was 10 µl of 1M NaOH every 1800 s; for rapid titration: 40 µl every 100 s.

TABLE 2
Solution Composition for Titration Experiment[A]

Line N	Wt% of Mg	Al(NO₃)₃·9H₂O (g)	Mg(NO₃)₂·6H₂O (g)	Al(NO₃)₃·9H₂O (mol L⁻¹)	Mg(NO₃)₂·6H₂O (mol L⁻¹)
6	0%	0.139	—	1.24×10^{-2}	—
5	20%	0.139	0.029	1.24×10^{-2}	3.77×10^{-3}
4	50%	0.139	0.107	1.24×10^{-2}	1.39×10^{-2}
2	65%	0.139	0.187	1.24×10^{-2}	2.43×10^{-2}
1	100%	—	0.105	—	13.65×10^{-3}

[A] 30 mL of solution was used in the experiment.

8.2.3. Analytical parameters of AESEC measurement.

The AESEC measurements were performed using Ultima2C Horiba JobinYvon ICP-OES spectrometer with 30 wavelengths measured simultaneously by a polychromator (focal distance 50 cm). In order to detect Al in the ultraviolet region the optical system was continuously purged by high purity nitrogen (less than 3 ppm of O_2). The solution flow rate was adjusted at 3.02 cm³/min. A 50 ml cyclonic chamber and MEINHARD® *K3* nebulizer were used as optimal for this flow rate. The sensitivity of the analytical system was evaluated by considering the standard deviation of the intensity in the electrolyte not contacted with the sample. We define the limit of the measurement to be twice the standard deviation of the background signal, $C_{2\sigma}$, expressed as concentration or equivalent rate [22]. The analytical parameters of AESEC during this study are presented in **Table 3**. The spectral lines chosen exclude any interferences between studied species in used spectral resolution (12 picometers in the monochromator and 24 in the polychromator). The calibration curves for Mg and Al obtained with the electrolyte passing through the cell before ICP analysis (points shown by squares) and with the electrolyte analyzed directly by ICP without contacting the cell (points shown by circles) are presented in **Figure 8.1a**. This figure demonstrates clearly the near 100% efficiency of the cell for 5 orders of magnitude of concentrations. The ICP OES signal is also known to show linear behavior between real solutions and colloidal solutions containing particles up to 7 μm in diameter allowing us to detect the initially dissolved ions even if they precipitate downstream. Indeed, the current densities in order of 1 mA cm⁻² form several nmols of metal ions per second and these ions are evacuated with typical time between 9 and 20 seconds (time necessary to bring solution from the cell to the ICP). The total experiment time is less than 1 h and even if the accumulating species are considered it seems to be unrealistic that precipitated particle size can exceed 7 μm in these conditions. The problem can be more difficult if some big parts of the sample are detached however, the

particle detachment is visible on the ICP signal as a sharp high picks associated only with one element [23] which were not observed in this work.

TABLE 3
Analytical Parameters of AESEC Experiment in 3% NaCl

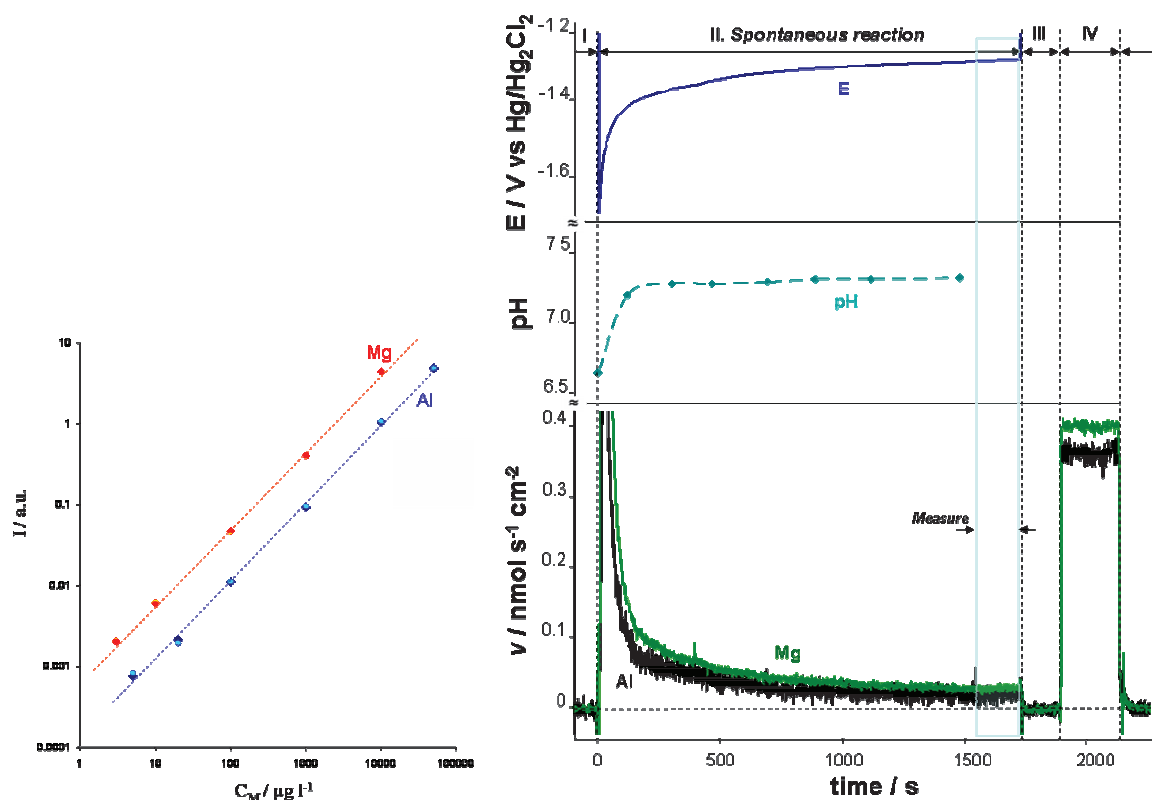|	Element			
	Al	Mg	Si	Fe
Wavelength (nm)	167.02	279.55	251.61	259.94
$C_{2\sigma}$ (nmol s^{-1} cm^{-2})	0.015	0.007	0.025	0.029
$C_{2\sigma}$ (µA cm^{-2})	4.6	1.4	4.8	5.7

Figure 8.1. Illustration of the analytical parameters and measurement principles.

a) Calibration measurement for Al and Mg obtained with the electrolyte passing through the cell before ICP analysis (points shown by squares) and with the electrolyte analyzed directly by ICP without contacting the cell (points shown by circles).

b) Example of OC reactivity measurement for AlMg(50) sample in downstream 3% NaCl aqueous solution at initial pH 6.3. The open circuit potential (E), pH and elemental dissolution rates of Al and Mg evolution (vM) are measured as a function of time during period II. Arrows indicate the zone for which the mean values of the dissolution rates and OCP are calculated for Table 3. See text for more details.

145

The total electrochemical current, j_e, and electrochemical potential, E, were measured with an EG&G M273A potentiostat/galvanostat. All potentials were measured relative to an Hg/Hg_2Cl_2 (in the saturated KCl solution) reference electrode (242 mV vs. SHE) unless otherwise stated. All experiments are made in 3% NaCl solution prepared from purified with a Millipore^{TM} system water and analytical grade NaCl (Normapur, VWR). The standard solution containing 100 ppb of Mg^{2+} and 100 ppb of Al^{3+} were prepared from 1000 ppm standards produced by SCP SCIENCE, PlasmaCAL, by dilution in purified water.The specificity of the ICP analysis is that only about 5% of solution is aspirated into the plasma, 95 % of the solution is removed with a second channel of the peristaltic pump. The solution was collected in separated recipients by portions about 9 ml (period of 3 min) and the pH in each portion was measured.

8.3. Results

8.3.1. Spontaneous reactivity of Al-Mg alloys in neutral and alkaline solutions of 3 wt % NaCl

An example of the measurement of the spontaneous reactivity at open circuit potential (OCP) at initial pH 6.3 is presented in **Figure 8.1b** for AlMg(50) alloy**.** The electrolyte passes through the cell during period II with sample contact at t=0. The OCP evolution, elemental downstream ICP concentrations and downstream pH are continuously recorded as a function of time (period II) until the OCP value is stable. Generally this was achieved at about 30 min. The mean values of the dissolution rates of Al and Mg and OCP are calculated for the last 100 s of the measurement (indicated with arrows). The final pH value was also assumed to correspond to the steady state. The periods I and III correspond to the measurement of the blank electrolyte, which passes directly to the ICP without contacting the sample before and after the dissolution experiment in order to verify the system stability.

The steady state dissolution rates for different Al-Mg compositions in unbuffered 3% NaCl with initially neutral and initially alkaline pH are summarized in **Table 4**. Each result represents the mean value and deviation between 3 independent experiments as described before and after 30 minutes of contact between surface and flowing electrolyte. At this time both OCP and elemental dissolution rates are stabilized for all compositions except pure Mg. For pure Mg the potential was stable, but the dissolution rate increased continuously in accordance with the literature [26]. For the re-circulating electrolyte the formed on the surface during the experiment phases detected by XRD are also presented. No XRD result for the

surfaces after the measurement in the renewed electrolyte is presented because the quantity of the product is too small to be detected by conventional XRD (thickness of several tens of nm). It can be also taken into account that the correlation between any post-experimental surface characterization with the kinetic measurement should be taken with caution because once the surface is no more in the contact with the electrolyte it can change considerably.

TABLE 4
Results of AESEC Measurement of Spontaneous Reactivity of Al, Mg, and Binary Al-Mg Alloys

Electrolyte	Initial pH	At 30 min	Mg	AlMg(65)	βAlMg	AlMg(50)	AlMg(50T)	AlMg(20)	Al
Continuously renewed 3 mL/min	6.3	Al (nmol cm^{-2} s^{-1})	0	0.012±0.006	0.055	0.014±0.007	0.010	0.008±0.004	DL – 0.002
		Mg (nmol cm^{-2} s^{-1})	0.73	0.045±0.007	0.069	0.024±0.012	0.025	0.007±0.004	<DL
		OCP (V$_{Hg/Hg_2Cl_2}$)	−1.64±0.02	−1.44±0.04	−1.35±0.05	−1.32±0.05	−1.18	−1.05±0.12	−0.75±0.02
		Downstream pH	9.4	7.28/6.9(p)	7.5	7.24/6.9(p)	6.9	5.0/7.07(p)	4.6
	9.5	Al (nmol cm^{-2} s^{-1})	0	0.022	0.034	0.031±0.003		0.005	0.005
		Mg (nmol cm^{-2} s^{-1})	0.5	0.067	0.036	0.040±0.004		0.012	—
		OCP (V$_{Hg/Hg_2,Cl_2}$)	−1.64±0.02	−1.51±0.06	−1.29	−1.45±0.01		−1.31	−1.56
		Downstream pH	9.9	9.15	—	9.2		9.2	???
30 mL, recirculated, 3 mL/min for 40 min	9.7	pH in stagnant solution	9.9	2.6	8.9	8.3		8.7	1.8
		XRD – crystalline phases	MgO, MgO$_2$	MgO, Al$_2$O$_3$	Not studied	Mg[AlO$_2$]$_2$		No detectable product	Al$_2$O$_3$

It can be noted from the results presented in **Table 4** that:

1. The spontaneous corrosion potential increases regularly with Al content. In alkaline solution for all Al-Mg compositions the OCP is systematically less noble than for the same composition in neutral pH and stays more noble than for pure Al and Mg.

2. When the OCP is stabilized, the pH of the electrolyte measured downstream after the contact with pure Mg becomes alkaline (close to 10), the pH of the electrolyte after contact with pure Al decreases to mildly acidic values (4.6 for initial pH 6.3). In contrast, for all binary compositions the solution pH after contact with the surfaces is slightly basic increasing till pH 7.1 ± 0.2 from initial pH 6.3, or decreasing till pH 9.2 ± 0.05 from initial pH 9.5-9.7.

3. The measured leaching of Mg decreases more than 10 times with addition of Al to the alloy, but between different Al compositions the difference is less marked. The measured dissolution rate of Al is systematically higher in Al-Mg alloys than in pure Al.

4. The pH evolution of alkaline solution in the experiment with re-circulated solution are similar to that in renewed solution for pure Al and Mg and for Al-Mg alloys with similar rates of Al and Mg dissolution. For 65 % Mg composition for which the Mg dissolution is strongly selective and the dissolution rate is maximal, the pH becomes acidic. This can be understood

from the rapid leaching of Mg and formation of an Al rich surface which undergoes the pitting attack resulting in pH decrease. Al oxide was detected on the surface of AlMg(65) and pure Al samples. For alloys with intermediate dissolution rates, XRD confirmed the formation of an Al-Mg spinel after the experiment. No visible corrosion products were detected on the AlMg(20) sample.

8.3.2. Potentiodynamic polarization behavior of binary alloys compared to pure metals

Figure 8.2 gives AESEC polarization curves for the investigated samples in neutral solution (initial pH 6.3) The initial potential was -1.8 V vs. Hg/Hg_2Cl_2 and was swept in the anodic direction at 1 mV /s. Some important effects can be seen from this figure.

1. The selective dissolution of Al under cathodic polarization and selective dissolution of Mg under anodic polarization when the anodic current is lower than several mA are clearly observed for all systems (**Figure 8.2d**). At high anodic currents the system dissolves with the bulk stoichiometric composition.

2. The decrease of pitting potential and the difference between corrosion and pitting potential are observed with increase of Mg content (**Figure 8.2a**). Such a form of the curve for binary allows is very similar to polarization curves of binary alloys containing one noble and one active metal presented by Pickering [2].

3. For all binary compounds a limiting current (passive) region on the anodic curve which is independent of potential corresponds to the selective dissolution of Mg (**Figures 8.2a-8.2d**). Contrary to pure Mg, the rate of Mg dissolution from Al-containing compounds doesn't increase with potential in this potential range (**Figure 8.2b**). During this period the surface should be depleted in Mg. At the same time the constant positive excess electron transfer rate about 10-20 $\mu A\ cm^{-2}$ is measured (the difference between the total current and the elemental dissolution rates expressed as currents). This positive value represents the oxidation reaction resulting in the formation of insoluble (or precipitated) products, probably passivating oxide film. The oxide formation rate is constant and limited to 10 - 20 μA **(Figure 8.2e).**
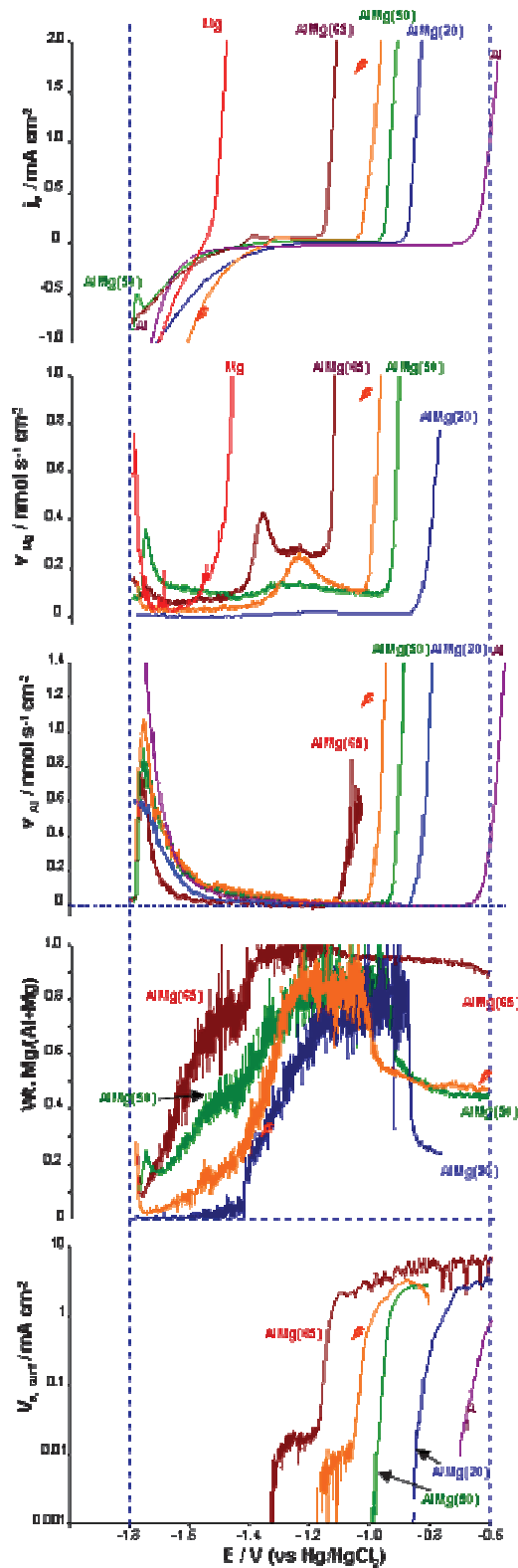
Figure 8.2. Evolution of total electrochemical current, j_e (a), Mg dissolution rate, v_{Mg2+} (b), Al dissolution rate, v_{Al3+} (c), Mg fraction in the solution (d) and calculated from (a-c) excess anodic electron transfer rate which can be associated to the oxide formation current (e) from the Al-Mg binary alloys during polarization experiment in anodic direction in 3% NaCl solution. The potential (OX axis) is the same for all graphs (a – e). Sweep rate 1 mV/s.

4. After the pitting potential, corresponding to the value at which Al anodic dissolution begins (**Figures 8.2a, 8.2c**), the current depends on potential and both Mg (**Figure 8.2b**) and Al (**Figure 8.2c**) dissolution rates increase rapidly. At the same time the rate of oxide formation increases sharply till several mA and than oscillates near this value. The high current density associated with this period indicates that the formed oxide is not passivating. In **Figure 8.2e**, the noise of the signal is shown only for AlMg(65), for AlMg(50) and β the smoothed dot lines represent the mean current level. This noise can indicate either gas formation or dissolution – precipitation processes.

5. The solution composition ratio $Mg^{2+}/(Al^{3+}+Mg^{2+})$ approaches that of the bulk composition for AlMg(20) sample. This ratio is lower than expected for the dissolution of Mg from AlMg(50) and the intermetallic composition is probably a consequence of significant Mg depletion of the surface layer. The anodic reactivity of AlMg(65) is so high that the depleted zone is not detected. The high dissolution rate is accompanied by the formation of insoluble corrosion products which can explain apparent selective dissolution of Mg from this sample at high anodic potentials.

6. No clear tendency in the influence of Mg content on the cathodic current can be drawn from this data; however the decrease of Al dissolution rate seems to correlate with lowering of Al content in the sample.

8.3.3. Behavior of Al-Mg alloys under applied cathodic potential

An example of typical dissolution profiles under applied cathodic potential is presented in **Figure 8.3.** After 30 minutes of OCP (period I) different cathodic potentials are applied (period II). The rate of OH⁻ generation, v_{OH}, is calculated from j_e and Al and Mg dissolution rates by using equations (2-4) and (7) with assumption of n=2 for Mg and n=3 for Al. In **Figure 8.3a** (sample AlMg(65)) the cathodic current is significant and the dissolution rate of Al^{3+} and Mg^{2+} decreases with time indicating passivation. In **Figure 8.3b** (sample AlMg(20)) the reactivity increases with time indicating the de-passivation of the system with increasing pH.
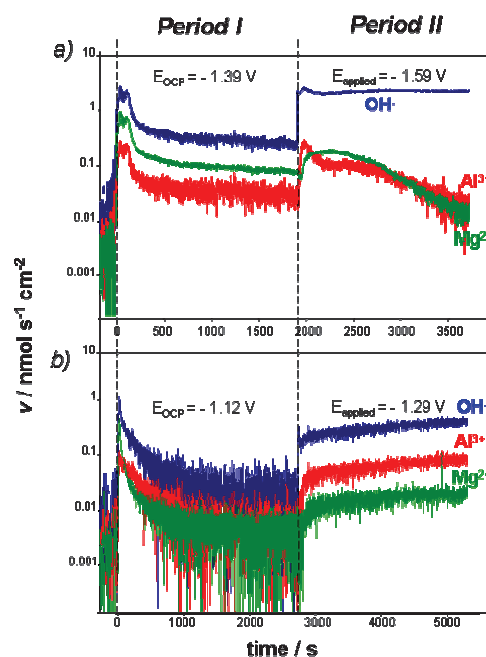
Figure 8.3. Typical reactivity of binary Mg-Al alloys at OCP (period I) and under applied cathodic potential (period 2): passivating behavior of AlMg(65) (a) and active dissolution of AlMg(20) (b). The measured elemental dissolution rates (v) of Mg and Al and calculated by equation (7) OH⁻ generation rate are shown as a function of time.

Similar experiments were conducted for alloys and intermetallics and the dissolution rates and hydroxide generation rates were calculated for different applied potentials and the active or passive behavior was noted. The ratios of hydroxide generated to Al dissolved were also calculated. The results are presented in **Table 5**. It seems from these results that for moderate cathodic current the dissolution rate of Al is significant and the dissolution rate of Mg also increases. At larger cathodic current densities both Al and Mg dissolution rates decrease rapidly. This behavior differs significantly with the behavior of pure Al and Al-Cu alloys for which the Al dissolution rate increased linearly with cathodic current [27] indicating a different mechanism of cathodic Al dissolution in the presence of magnesium. This behavior differs also with the behavior of pure Al and Al-Sn alloys described in literature [28,29]. The origin of such a behavior will be addressed in the discussion section.

Sample	E_{OCP} (V)	$E_{applied}$ (V)	j_e (µA cm⁻²)	j_{cat} (µA cm⁻²)	Measured Bulk pH₀	Calculated v_{OH} (nmol cm⁻² s⁻¹)	v_{Al} (nmol cm⁻² s⁻¹)	$v_{Mg,init}$ (nmol cm⁻² s⁻¹)	Ratio v_{OH}/v_{Al}	Calculated Precipitation pH	Calculated Surface pH	Passivation Under Applied Potential
AlMg(20)	−1.12	−1.29	−8.78	−32.10	7.00	0.40	0.08	0.02	5.00	12.7	11.18	No
AlMg(50)	−1.37	−1.59	−79.79	−139.78	6.90	1.40	0.10	0.10	14.00	11.66	12.27	Yes
AlMg(65)	−1.39	−1.59	−216.49	−222.44	7.25	2.30	0.01	0.18	230.00	11.67	12.63	Yes
β	−1.32	−1.39	−172.89	−218.61	8.20	1.35	0.18	0.15	7.50	11.7	12.07	Yes
β	−1.32	−1.49	−759.66	−767.07	8.70	4.60	0.02	0.20	230.00	11.67	12.93	Yes
β	−1.349	−1.356	−2.56	−17.45	6.30	0.17	0.02	0.05	8.50	11.91	11.24	No
β	−1.349	−1.377	−4.79	−29.82	6.30	0.34	0.05	0.07	6.80	11.91	11.45	No
β	−1.349	−1.387	−6.58	−44.02	6.90	0.47	0.07	0.10	6.71	11.66	11.58	No
β	−1.349	−1.408	−15.14	−62.48	7.25	0.63	0.10	0.11	6.30	11.66	11.66	No
β	−1.349	−1.460	−81.09	−146.42	7.60	1.54	0.13	0.11	11.85	11.66	12.29	Yes
β	−1.349	−1.563	−534.56	−559.40	7.89	5.71	0.04	0.01	142.75	11.67	13.02	Yes

[A] The passivity in the last column is considered for the end time of each applied potential domain. See text for details.

In order to verify if the evolution of the intrinsic reactivity of Al-Mg alloys can be determined by the chemical composition of dissolved ions rather than by the specific microstructure of selected alloys, similar experiments were made for pure Al with and without added Mg^{2+} and for pure Mg with and without added Al^{3+} into solution.

8.3.4. Effect of Mg^{2+} in solution on the electrochemical behavior of Al in 3% NaCl

Adding 1 ppm of Mg^{2+} ions to the solution results in a significant delay of the spontaneous passive film formation (**Figure 8.4**) as indicated by both the OCP evolution (**Figure 8.4a**) and Al dissolution rate (**Figure 8.4b**). This result is coherent with XPS study of the passive layer formation on Al alloys in presence of Mg impurities [30]. Interestingly, if the sample is exposed to air for 30 - 40 minutes after polishing (native oxide is assumed to be thicker), the effect on the OCP is less visible, however the dissolution rate of Al (**Figure 8.4b**) is increased. Al is not detected in the presence of Mg^{2+} even if the OCP is about 100 mV more cathodic. This may be interpreted as Al is precipitated but the oxide formed keeps the surface active, probably because of its semi-conducting nature.
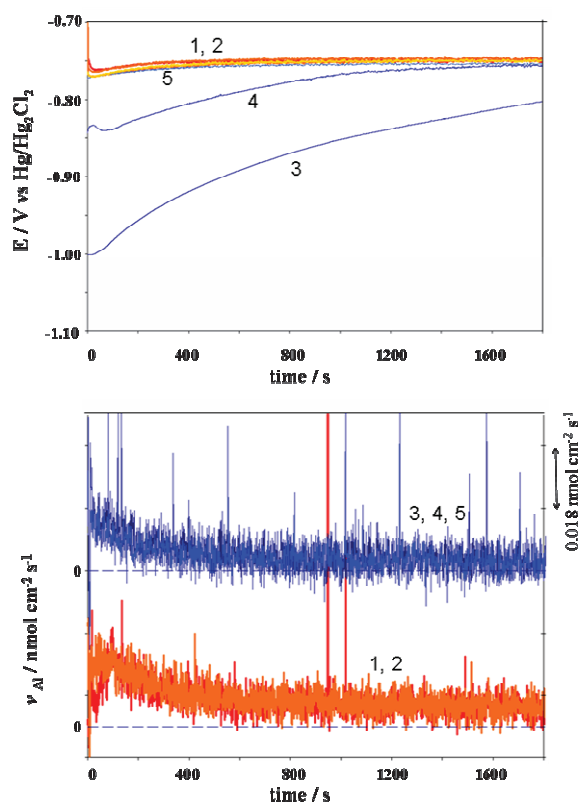
Figure 8.4. OCP evolution (a) and Al dissolution rate, v_{Al} evolution (b) for Al without (1 – fresh polished surface, 2 – after 40 min exposure to air) and with 5 ppm of Mg^{2+} in the solution (3 – fresh polished Al, 4 – after 40 min exposure to air). The $c_{2\sigma}$ limit is 0.011 nmol s^{-1} cm^{-2}.

The polarization curves of pure Al without and with Mg^{2+} are shown in **Figure 8.5**. A clear effect on the cathodic reaction is confirmed for both, total electrochemical current and Al dissolution rate. The stoichiometry of Al dissolution is also changed. Without Mg^{2+}, the ratio between OH generated and Al dissolved, $v_{OH} / v_{Al} = 3.6$ corresponds to the previously reported values for different Al alloys and Al-Cu intermetallics [27]. In contrast, the v_{OH} / v_{Al} ratio increases with potential when Mg^{2+} is added into solution indicating the modification of the cathodic reaction mechanism. The surface appearance after the polarization with Mg^{2+} in the solution is also very different, the thick layer of white corrosion product is visible by visual inspection in presence of Mg^{2+} **(Figure 8.6b)** when the corrosion product is not visible in absence of Mg^{2+} in the solution **(Figure 8.6a).**
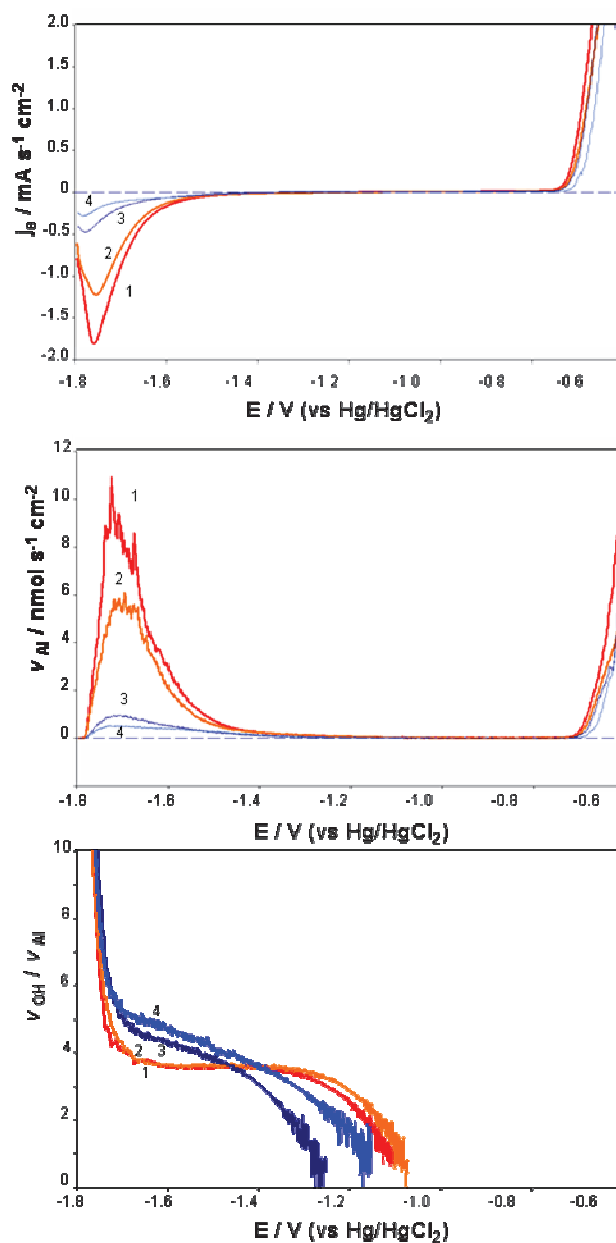
Figure 8.5. Polarization curves of Al without (1 – fresh polished surface, 2 – after 40 min exposure to air) and with 5 ppm of Mg2+ in the solution (3 – fresh polished Al, 4 – after 40 min exposure to air): the total current of the reaction (a); Al dissolution rate, vAl; (b), the ratio vOH/vAl between the calculated by eq. 7 rate of OH- generation and the Al dissolution rate (c).
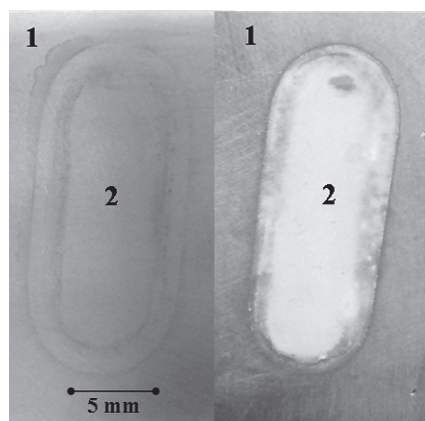
Figure 8.6. General view of aluminum sample after the polarization experiment in 3% NaCl solution (a) and in 3% NaCl + 5 ppm MgCl$_2$ (b) demonstrating visible formation of white corrosion product in presence of Mg^{2+}. The unreacted area (outside of the cell) is indicated as 1 and the exposed in the AESEC experiment area is indicated as 2.

8.3.5. Effect of Al^{3+} in solution on the electrochemical behavior of Mg in 3% NaCl

The presence of Al^{3+} in the solution does not influence the OCP evolution of Mg (**Figure 8.7a**) but decreases the Mg dissolution rate (**Figure 8.7b**). During potentiodynamic polarization (**Figure 8.8**) the only reproducible effect of Al^{3+} on the cathodic branch of the polarization curve is the decrease of the total current. At the same time, the Mg dissolution rate under low cathodic polarization seems not to be affected by the presence of Al^{3+}.
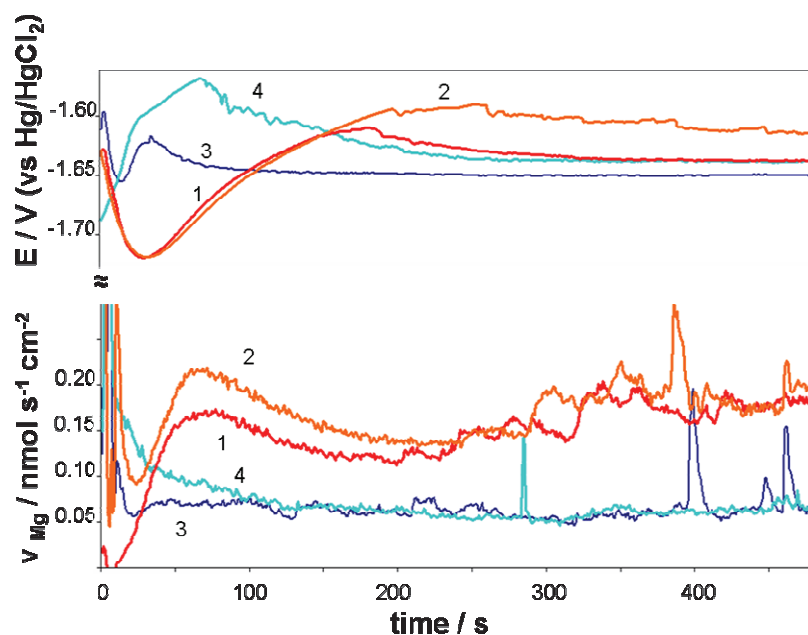
Figure 8.7. The OCP evolution (a) and Mg dissolution rate evolution (b) for Mg without (1 – fresh polished surface, 2 – after 40 min exposure to air) and with 5 ppm of Al^{3+} in the solution (3 – fresh polished Al, 4 – after 40 min exposure to air). The $c_{2\sigma}$ limit is 0.007 nmol s^{-1} cm^{-2}.

On the anodic branch (**Figure 8.8**) the most affected is the difference between the total current and Mg dissolution rate. Another reproducible effect is an anodic shift of about 50 mV of the corrosion potential. Both of these factors indicate that in the presence of Al^{3+} an oxide layer on the Mg surface is formed quicker than on pure Mg. Similar to Al in the presence of Mg^{2+}, this oxide seems not to influence significantly the anodic current which can be interpreted reflecting a conductive oxide film.
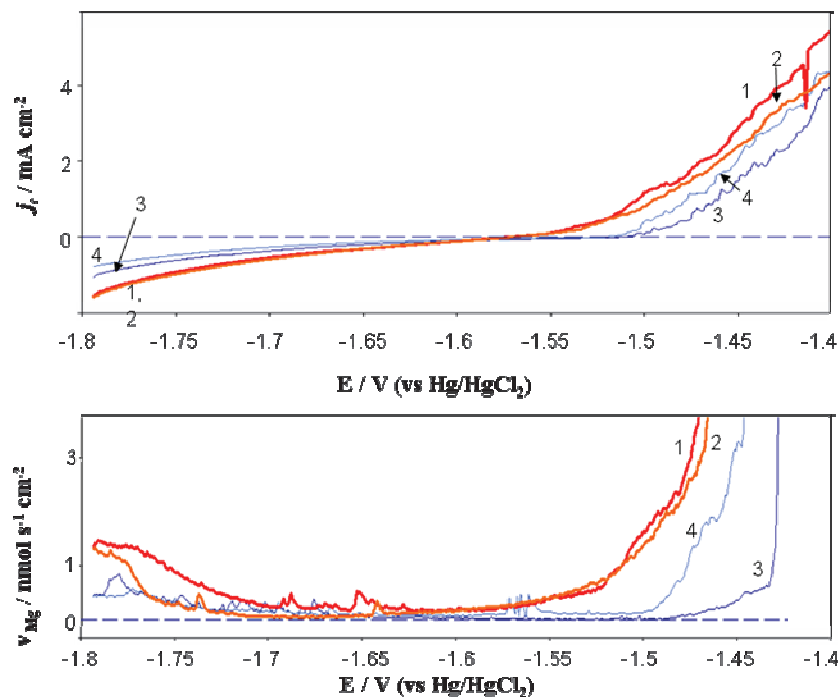
Figure 8.8. Polarization curve (a) and Mg dissolution rate evolution (b) for Mg without (1-fresh polished surface, 2 – after 40 min exposure to air) and with 5 ppm of Al3+ in the solution (3 – fresh polished Al, 4 – after 40 min exposure to air).

8.3.6. Trends in the co-precipitation of Al and Mg during titration experiment

In order to understand the oxide species formation and to understand the pH evolution, titration experiments were performed followed by XRD analysis of the precipitates. The titration curves and the expected endpoints calculated from the stoichiometry of the reaction products are presented in **Figure 8.9**. The plateau around pH = 9.5, obtained when $MgCl_2$ alone was titrated with NaOH, was due to the precipitation of $Mg(OH)_2$ (**Figure 8.9 curve 1**). The plateau between pH 4.0 and 4.5, obtained with the Mg^{2+} and Al^{3+} mixtures (curves 2-6), was due to the precipitation of $Al(OH)_3$. The precipitates appear at the ratio of OH/Al close to 2.5 indicating the formation of hydroxide complexes [31]. From both, rapid and slow titrations (**Figures 8.9 a and b**), the second plateau range between pH 7.7 and 8.5 on curves 2-5 is more than one pH unit below that obtained when $Mg(OH)_2$ is precipitated. This corresponds to the co-precipitation of Al^{3+} and Mg^{2+} in different ratios [32]. During rapid titration (**Figure 8.9 a**), the precipitation of Al at low pH is difficult to observe; the system evolves immediately to the high pH of mixed Al-Mg products. It seems from the comparison of rapid and slow titration results that the kinetics of formation of mixed oxides is quicker and

they can be initially formed and buffer the pH at values close to 8.5. The XRD analysis of the product formed by precipitation (arrow in the titration curve of **Figure 8.9 b)** confirmed the formation of $Mg_6Al_2(OH)_{18}$ $4.5H_2O$ and has also shown presence of $Al(OH)_3$ and $Mg(OH)_2$ **(Figure 8.9c)**. The formation of hydrated spinel-like structures in presence of Al and Mg is also in accordance with literature [33]. The observed mixture of products indicates the possible transformation of different species and local pH variations.
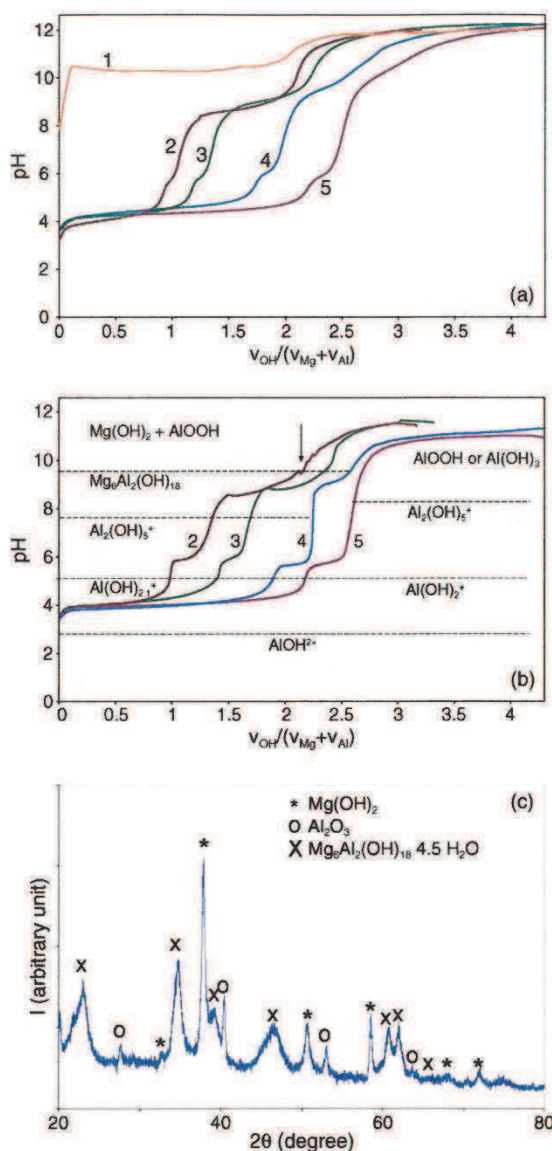

Figure 8.9. Rapid (a) and slow (b) titration curves for Al^{3+}-Mg^{2+} mixtures with different fractions of Mg^{2+} $\eta_{Mg} = m_{Mg2+} / (m_{Mg2+} + m_{Al3+})$: 1 – 100 wt %, 2 – 65 wt %, 3 –50 wt %, 4 - 20 wt %, 5 – 0 wt %; the OX axis corresponds to the ratio between the quantity of added hydroxide ions, VOH and the total metallic cations in the solution $\Sigma V_M = V_{Al} + V_{Mg}$. Figure 9 c represents the XRD pattern of the precipitates formed during slow titration at the point indicated by the arrow in Figure 9b.

158

8.4. Discussion.

As in our previous AESEC study of Mg reactivity in NaCl [24], the difference between the anodic electrochemical current and elemental dissolution currents calculated in assumption of Mg^{2+} stays positive. This observation can not give any credit in favor of formation of Mg^+ ions because considering Mg^+ will only increase this difference. In contrast, the oxide formation seems to be an important factor for dissolution kinetics of studied materials. From the experimental results presented below it seems that two main factors should be considered for the electrochemical behavior of Al-Mg binary compounds: the evolution of the oxide layer composition in presence of Mg^{2+} or Al^{3+} ions and the role of pH evolution during surface reactions.

8.4.1. Evidence of the surface oxide modification

Despite the similarities in the shape of anodic polarization curves obtained here with the curves described by Pickering [2], the main difference in the selective dissolution mechanism in case of Mg-Al alloys is that this mechanism should include the mass and charge transfer via passive oxide. It is generally accepted for both Al [34,35] and Mg [26] that the oxide film is present on the surface at all pH and applied potentials. Interpretation of the experimental results presented in this work clarifies the role of the passive oxide on the selective dissolution under cathodic and anodic polarization and allows extend the selective dissolution model to Mg-Al binary compounds including both, anodic and cathodic reactivity.

For all Al-Mg alloys investigated in this work, in unbuffered 3% NaCl solution, a strong selective dissolution of Al was observed under cathodic polarization and strong Mg selective dissolution was observed at OCP and under anodic polarization. The inhibitive effect of Mg^{2+} on the cathodic Al dissolution was confirmed for all Al/Mg ratios in the alloy composition and for pure Al in the presence of Mg ions. In contrast, the spontaneously formed oxide film in presence of Mg^{2+} is less protective than the Al oxide passive film and the OC dissolution rate of Al increases in presence of Mg^{2+}. This activation is in accordance with recently published results of Macanas at al. [36] demonstrated the improved hydrogen yield and shorter reaction time for Al reaction with slightly alkaline solutions in presence of Mg^{2+} as compared to the blank. On the basis of our results one can consider that the activation can be due to cathodic de-passivation.

There was no clear evidence of Al inhibition effect on the anodic current on Mg, however an increase of the oxide formation rate and the slowing of the cathodic reaction are systematically observed. It is irrelevant if the ions are initially present in the alloy composition or simply added to the solution. These results indicate that the common presence of Al^{3+} and Mg^{2+} ions results in the modified nature of the oxide layer and this oxide is formed more easily than on pure Al and Mg but it seems not to have a passivating effect. Titration results suggest that the rapid formation of spinel-like compounds occurs with buffering of the interfacial pH at about 8.5. Curiously, similar pH values were measured in flowing electrolyte after contact with the binary alloys surface at OCP for different compositions. The mixed oxide containing Mg^{2+} and Al^{3+} presents an increased number of point defects (anionic and cationic vacancies). Moreover, the spinel like structure in contact with solution should be systematically depleted in Mg^{2+} because of its high solubility and ion exchange capacity resulting in increased vacancy activity in aqueous media. These defects can play a significant role in anodic and cathodic passivation breakdown.

8.4.2. Anodic breakdown of Al-rich film due to the surface oxide modification

The mechanism of anodic and cathodic reactions on pure Al is well detailed [28-30, 34-35]. **A critical component of a passive layer on Al [37]** is a bohemite (AlOOH) based polymer in fibril form and a breakdown involving penetration of these fibrils by Cl^-, which displaces the OH^- therein and diffuses out again, in the form of an $AlCl_x^{n+}$ complex. One can expect as for Al-Sn alloys that the vacancies formed in the mixed oxide in presence of Mg^{2+} can help the migration of O^{2-} to the metal/oxide phase boundary or the migration of metal ions to the metal/solution phase boundary simplifying the oxide growth. The presence of Cl^- anion vacancies could help Cl^- migration and destabilize the passive film decreasing the anodic breakdown potential (compare **Figure 8.2**). The fact that the mixed oxides precipitate at lower pH (**Figure 8.9**) explains also the increased rate of oxide formation on Mg in presence of Al^{3+} (**Figures 8.4, 8.5**) and on Al in presence of Mg^{2+} (**Figure 8.7**).

8.4.3. Cathodic reactivity in low cathodic potential (LCP) through Al-rich film

The cathodic polarization of passivated Al [28] and Al–Sn alloys [29] in a chloride solution is characterized by two regions of potentials with distinctly different phenomena: the range of low and high cathodic potentials (LCP and HCP). In the LCP range, the oxide film retains its properties and the electrochemical reaction between electrons in the metal and the species in solution is controlled by the transport of electrons through the oxide film. The Tafel slope at this stage is relatively high. In this region the cathodic aluminum dissolution at a specific potential should depend on the cathodic current rather than the potential, therefore on the catalytic activity of the surface for cathodic reaction. The potential independent cathodic dissolution seems to be valid for previously studied Al-Cu alloys with the $v_{OH} / v_{Al} = 3.6$ stoichiometry independent of the catalytic activity for hydrogen reduction for over three orders of magnitude of cathodic activity for Al alloys [21] indicating that the reaction occurs in LCP. The presence of Mg^{2+} decreases significantly the cathodic dissolution of Al. In the case of the rapid formation of semi-conducting spinel-like compound by Al^{3+} and Mg^{2+} the film formed cannot completely inhibit the charge transfer but decreases the measured dissolution of Al and Mg because of the oxide layer formation. The oxide film breakdown places the system as reacting in the high cathodic potential (HCP) region. The modification of the cathodic reaction mechanism is also clear from the v_{OH} / v_{Al} ratio which increases with potential (**Figure 8.5c**) or with time (**Figure 8.3a**) and can achieve values more than 50 for several cases of polarization of intermetallic. The classic schema of low cathodic potential cannot hence be applied to Mg-Al alloy.

8.4.4. Role of pH in high cathodic potential region

After the breakdown, in HCP the pH increases by reactions (8.5, 8.6) lead to an enhanced solubility of aluminum oxide (reaction 8.8) following by the oxidation of the underlying metal to replace the dissolved portion of the film (reaction 8.9).

$$Al(OH)_3 + OH^- \rightarrow Al(OH)_4^- \qquad\qquad [8.8]$$

$$Al + 3OH^- \rightarrow Al(OH)_3 + 3e- \qquad\qquad [8.9]$$
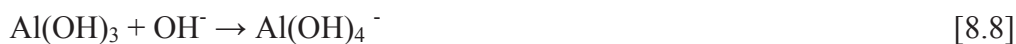
The overall reaction is thus (8.10)

$$Al + 4H_2O + e- \rightarrow 2H_2 + Al(OH)_4{}^- \qquad [8.10]$$

or in presence of oxygen (8.11)

$$Al + 2H_2O + O_2 + e- \rightarrow Al(OH)_4{}^- \qquad |8.11]$$

The modification of the reaction sequences in presence of Mg^{2+} can be understood by assuming the surface passivation reactions involve both Al and Mg. The later is in agreement with the observed correlation between the evolution of the cathodic current on Al-Mg intermetallic and dissolution rates of both Al and Mg (**Figure 8.3b**). The higher cathodic reactivity is followed by the rapid co-precipitation of Al and Mg forming an insoluble film. This film is reformed quicker and re-dissolved slower than $Al(OH)_3$ limiting the cathodic current.

$$(1-x)Al(OH)_4{}^- + xMg^{2+} \rightarrow Mg_xAl_{1-x}(OH)_zO_{4-4x-z} + ((4-4x-z)/2)\ H_2O \qquad [8.12]$$

At very high cathodic currents (and hence high pH) the transformation of the film can result in stabilization of an insoluble Mg hydroxide

$$Mg_xAl_y(OH)_zO_n + zOH^- \leftrightarrow yAl(OH)_4{}^- + xMg(OH)_2 \qquad [8.13]$$
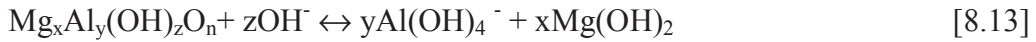
which can prevent the access to metallic Al and its dissolution by the reaction (8.10).

The passivation at high cathodic currents can hence be explained by Mg passive film formation at high pH. In order to verify that the repassivation of Al-Mg alloys is current and not potential controlled, we have recalculated from the OH⁻ generation rate presented in **Table 5** the surface pH considering the diffusion of OH⁻ formed by reactions (8.5, 8.6) in the assumption of a steady state reaction and stationary conditions on the interface as [21]

$$dC_{OH}/dt = (\ v_{OH} - (D_{AlOH}\ /\ \delta)\ (C_{SAl}\text{-}C_{0Al})\ 4\ v_{Al} - (D_{OH}\ /\ \delta)\ (C_S\text{-}C_0) = 0 \qquad [8.14]$$

where $D_{OH} = 5.27 \cdot 10^{-7}\ cm^2\ s^{-1}$ is the diffusion coefficient for the OH⁻ in presence of Cl⁻ [38], C_S – the concentration of OH⁻ on the surface, C_0 is the concentration on the OH⁻ far away from the surface measured downstream, δ is the interface "well mixed solution"/"diffusion area" estimated as 0.01 mm, v_{OH} is the rate of OH⁻ formation, $4v_{Al}$ is the rate of formation of $Al(OH)_4{}^-$ measured by ICP.

The surface pH in **Table 5** was calculated as

$$-\log(C_S) = -\log(D_{OH} / \delta \, (\, v_{OH} - 4 \, v_{Al} \,) + C_0) \qquad\qquad [8.15]$$

The pH of formation of $Mg(OH)_2$ was estimated from the solubility product of $Mg(OH)_2$ and the Mg^{2+} concentration measured downstream. In case of decreasing concentrations, the initial Mg dissolution rate was taken into account. The last column in **Table 5** indicates whether or not the inhibition of cathodic dissolution was experimentally observed.
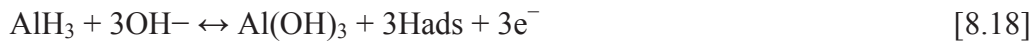
It can be seen from the data presented in **Table 5** that without exception the cathodic dissolution is blocked if the initial OH generation rate was sufficiently high to reach the $Mg(OH)_2$ formation pH and is active in all other cases. Interestingly, the cathodic current necessary for cathodic passivation of Al-Mg alloys is significantly lower than the cathodic current reported by Song [26] as necessary for cathodic passivation of pure Mg in 1 N NaCl. We suppose that this is because the reaction should be considered not in terms of the current but rather the interfacial pH which can be modified by the side reactions of the alloying elements. The comparison of this calculation results with titration data, the recirculation electrolyte experiment and the pH evolution was different indicating that the intrinsic reactivity can be masked significantly by changing solution composition.

8.4.5. Hydride mechanism and reactivity in high cathodic potential region before passivation by Mg

The transition to the HCP is determined by the oxide structure. For instance, for Al-Sn alloys the boundary between these two potential ranges shifts towards more negative potential values with Sn content [29]. From our results (**Figure 8.2**), the higher value of the Tafel slope (compared to pure Al) in potential range - 1.2 - -1.7V vs. Hg/Hg_2Cl_2 indicates that for studied Al-Mg alloys the potential shifts to nobler values.

At high cathodic potentials, the cathodic process occurring initially at the surface of the oxide is followed by oxide hydration and a transfer of the cathodic process to the metal-hydrated oxide interface, with a subsequent change of the properties of the metal surface (possible formation of the metal hydride). This hydride intermediate can explain some specific features of the cathodic dissolution in the potential range, when cathodic breakdown and hydration of

the oxide take place but the interfacial pH for Mg^{2+} precipitation has not been obtained. One of the possible explanations is the hydride formation as intermediate (reactions 8.16-8.19) including the interaction of adsorbed hydrogen with a vacancy site [39,40] in alkaline media

$$3H_2O + 3e- \leftrightarrow 3Hads + 3OH^- \qquad\qquad [8.16]$$

$$Al + 3Hads \rightarrow AlH_3 \qquad\qquad [8.17]$$

$$AlH_3 + 3OH- \leftrightarrow Al(OH)_3 + 3Hads + 3e^- \qquad\qquad [8.18]$$

$$3Hads \leftrightarrow Vac\text{-}Hx + (3\text{-}x)/2\ H_2 \qquad\qquad [8.19]$$

This reaction schema suggests that Vac-H defects may be created by anodic oxidation of interfacial hydride, followed by the movement of an Al atom into the hydride site.

If Mg is present in the alloy, the variation of the cathodic reactivity of intermetallics is logical. Because of the high hydrogen fugacity on Mg and high stability of MgH_2 (which is more stable than AlH_3 and is the only hydride species detected during cathodic charging or corrosion of Al-Mg intermetallics [26,41]) the Al dissolution through the reactions (8.16–8.19) should be reduced but hydrogen evolution maintained or even increased. This results in nobler than for pure Al HCP region. The Tafel slope in HCP region decreases compared to LCP. It should be kept in mind that this reaction sequence doesn't take into account the electron transport through the oxide and cannot be applied in presence of significant oxide film. The reactivity of Al decrease in the presence of Mg^{2+} ions (**Figures 8.4, 8.5**) as well as the observed potential dependence of v_{OH}/v_{Al} ratio during cathodic polarization of Al can not be considered through this mechanism because of significant oxide formation.

8.5. Conclusion.

1. During spontaneous reaction in neutral pH, Mg^{2+} ions retard the formation of passive film on Al which is confirmed by OCP evolution and Al dissolution rate.

2. The presence of Al^{3+} in the solution influences neither the OCP nor the anodic current on Mg but inhibits Mg dissolution suggesting that oxidized Mg stays in its insoluble form.

3. The inhibitive effect of Mg on the cathodic dissolution of Al-Mg alloys and the selective dissolution of Al in cathodic domain is confirmed for all Al/Mg ratios in the alloy composition and for the pure Al in the presence of Mg ions.

4. The measured ratio between OH$^-$ generated and Al dissolved corresponds to the previously reported value (3.6) for pure Al but increases significantly and evolves with potential in presence of Mg^{2+} in the solution for pure Al and from all binary alloys.

5. The titration experiment and the XRD analysis of the precipitated product confirm the possible formation of Al^{3+} and Mg^{2+} containing spinel-like compound at pH lower than Mg(OH)$_2$ formation. Close pH was measured in the renewed electrolyte after the contact with the binary alloy surface at OCP for different compositions. In the re-circulated electrolyte with initial pH 9.7 the pH decrease during experiment was more pronounced than renewed electrolyte, in particular for AlMg(65) the final pH in the re-circulated electrolyte was 2.6 and in renewed electrolyte 9.2. This indicates that the intrinsic reactivity can be masked significantly by evolving solution composition.

6. These results are interpreted in terms of changes in the solution composition near the surface which is controlled by the chemical composition of the alloy via selective dissolution processes. This is considered a key factor determining the reactivity of Al-Mg binary alloys.

7. The cathodic reactivity of Mg-Al alloys is proposed to be modified as compared to high Al alloys because of the different intermediate species. In the presence of Mg ions mixed Al-Mg spinels may be formed. These compounds precipitate at lower pH than Mg(OH)$_2$ and have low solubility product, which explains the significant decrease of the measured leaching rate. These oxide layers do not inhibit electron transfer because of high defect concentrations. This may explain the high anodic activity in the presence of Mg.

8.6. References

1. W. B. Nowak "Thin metallic films for corrosion control" *Surface and Coatings Technology* **49** (1991) 71—77

2. H.W. Pickering "Characteristic features of alloy polarization curves" *Corrosion Science* **23** (1983) 1107-1120

3. B. G. Ateya and H. W. Pickering "The effects of potential and kinetic parameters on the formation of passivating noble metal rich surface layers during the selective dissolution of binary alloys" *Corrosion Science* **38** (1996) 1245-1267

4. B. Mazurkiewicz "The electrochemical behaviour of the Al_8Mg_5 intermetallic compound" *Corrosion Science*, **23(7)** (1983) 687-690,

5. N. Birbilis and R. G. Buchheit "Investigation and Discussion of Characteristics for Intermetallic Phases Common to Aluminum Alloys as a Function of Solution pH" *Journal of the Electrochemical Society* **155(3)** (2008) C117-C126

6. M. Mokaddem, P. Volovitch, F. Rechou, R. Oltra, K. Ogle, "The cathodic and anodic dissolution of Al and Al-Cu-Mg alloy", *Electrochimica Acta* **55** (2010) 3779–3786

7. M.Ghada Abady, Nadia H. Hilal, Mohmmed El-Rabiee, Waheed A. Badawy "Effect of Al content on the corrosion behavior of Mg–Al alloys in aqueous solutions of different pH" *Electrochimica Acta* **55** (2010) 6651–6658

8. M. Liu, P. Schmutz, S. Zanna, A. Seyeux, H. Ardelean, G. Song, A. Atrens, P. Marcus "Electrochemical reactivity, surface composition and corrosion mechanisms of the complex metallic alloy Al_3Mg_2M" *Corrosion Science* **52** (2010) 562-578

9. A. Pardo, M.C. Merino, A.E. Coy, F. Viejo, R. Arrabal, S. Feliú Jr. "Influence of microstructure and composition on the corrosion behaviour of Mg/Al alloys in chloride media" *Electrochimica Acta* **53** (2008) 7890–7902

10. S. Mathieu, C. Rapin, J. Steinmetz and P. Steinmetz "A corrosion study of the main constituent phases of AZ91 magnesium alloys" *Corrosion Science* **45** (2003) 2741-2755

11. C. E. Austing. A. M. Pritchard and N. J. M. Wilkins "The formation and properties of Al/Mg scales on Al heat exchange surfaces in desalination plant" *Desalination* **12** (1973) 25 I-272

12. R K S Raman, N Birbilis, J Efthimiadis "Corrosion of Mg alloy AZ91 - the role of microstructure" *Corrosion Engineering Science and Technology* **39(4)** (2004) 346-350

13. M.-Ch. Zhao, M. Liu, G. Song, A. Atrens "Influence of the β-phase morphology on the corrosion of the Mg alloy AZ91" *Corrosion Science* **50** (2008) 1939–1953

14. G. Song, A. Atrens "Understanding magnesium corrosion: a framework for improved alloy performance" *Advanced Engineering Materials* **5** (2003) 837 - 858

15. S. Mathieu, C. Rapin, J. Steinmetz and P. Steinmetz "of main components" *Corrosion Science* **45** (2003) 2741-2755

16. M. Anik, P. Avci, A. Tanverdi, I. Celikyurek, B. Baksan and R. Gurler "Effect of the eutectic phase mixture on the anodic behavior of alloy AZ91" *Materials & Design* **27** (2006) 347

17. Y. Kyo, G.A. EL-Mahdy, A. Nishikata and T. Tsuru "Electrochemical Behavior of Al-Mg Alloy-coated Steel Prepared by PVD" 214th ECS Meeting, Abstract #1564

18. He Meifeng, Liu Lei, Wu Yating, Zhong Cheng, Hu Wenbin "Influence of microstructure on corrosion properties of multilayer Mg–Al intermetallic compound coating" *Corrosion Science* **53** (2011) 1312–1321

19. H. Yang, X. Guo, G. Wu, Sh. Wang, W. Ding "Continuous intermetallic compounds coatings on AZ91D Mg alloy fabricated by diffusion reaction of Mg–Al couples" *Surface & Coatings Technology* **205** (2011) 2907–2913

20. A. D. Südholz, N. T. Kirkland, R. G. Buchheit, and N. Birbilis "Electrochemical Properties of Intermetallic Phases and Common Impurity Elements in Magnesium Alloys" *Electrochem. Solid-State Lett*. **14 (2)** (2011) C5-C7

21. N. Birbilis, R.G. Buchheit "Electrochemical characteristics of intermetallic phases in aluminum alloys - An experimental survey and discussion" *J. of the Electrochem. Soc*. **152** (2005) B140-B151

22. K. Ogle, J. Baeyens, J. Swiatowska, P. Volovitch "Atomic emission spectroelectrochemistry applied to dealloying phenomena: I. The formation and dissolution of residual copper films on stainless steel" *Electrochimica Acta* **54** (2009) 5163–5170

23. M. Mokaddem, P. Volovitch, F. Rechou, R. Oltra, K. Ogle "The anodic and cathodic dissolution of Al and Al-Cu-Mg alloy" *Electrochimica Acta* **55** (2010) 3779-3786

24. J. Światowska, P. Volovitch, K. Ogle "The anodic dissolution of Mg in NaCl and Na2SO4 electrolytes by atomic emission spectroelectrochemistry" *Corrosion Science* **52** (2010) 2372-2378

25. C. Gabrielli, M. Keddam, F. Minouflet-Laurent, K. Ogle, H. Perrot "Investigation of zinc chromatation. I. Application of QCM-ICP coupling" *Electrochimica Acta* **48** (2003) 965-976

26. G. Song, A. Atrens, D. Stjohn, J. Nairn, Y. Li "The electrochemical corrosion of pure magnesium in 1N NaCl" *Corrosion Science* **39** (1997) 855-875

27. K. Ogle, M. Serdechnova, M. Mokaddem, P. Volovitch "The cathodic dissolution of Al, Al2Cu, and Al alloys" *Electrochimica Acta* **56** (2011) 1711–1718

28. A. R. Despic, D. M. Drazic, J. Balakina, LJ. Gajic, R. M. Stepanov "Investigation of oxidation potentials of substances accumulated during cathodic polarization of aluminum" *Electrochimica Acta* **35** (1990) 1747-1755

29. S. Gudic, J. Radossevic 1, I. Smoljko, M. Kliskic "Cathodic breakdown of anodic oxide film on Al and Al–Sn alloys in NaCl solution" *Electrochimica Acta* **50** (2005) 5624 – 5632

30. A. Csanady, T. Turmezey, I. Imre-BAAN, A. Griger, D. Marten, L. Fodor, L. Vitalis "The relationship between the corrosion resistance and impurity content of aluminum oxide layers" *Corrosion Science* **24** (1984) 237-248

31. A. C. Vermeulen, J. W. Geus, R. J. Stol, P. L. De Bruyn "Hydrolysis-Precipitation Studies of Aluminum (111) Solutions: I. Titration of Acidified Aluminum Nitrate Solutions" *Journal of Colloid and Interface Science* **51** (1975) 449-458

32. G. J. Ross , H. Kodama "Properties of a synthetic magnesium-aluminum carbonate hydroxide and its relationship to magnesium-aluminum double hydroxide, manasseite and hydrotalcite" *The American Mineralogist* **52** (1967) 1036-1047

33. C. E. Austing. A. M. Pritchard and N. J. M. Wilkins "The formation and properties of Al/Mg scales on Al heat exchange surfaces in desalination plant" *Desalination* **12** (1973) 25 I-272

34. Kim, Y.-S., Pyun, S.-I., Moon, S.-M. & Kim, J.-D. "The effects of applied potential and pH on the electrochemical dissolution of barrier layer in porous anodic oxide film on pure aluminum" *Corrosion Science* **38** (1996) 329-336

35. Moon, S.-M. & Pyun, S.-I. "The formation and dissolution of anodic oxide films on pure aluminum in alkaline solution" *Electrochimica Acta* **44** (1999) 2445-2454

36. J. Macanás, L. Soler, A. María Candela, M. Muñoz, J. Casado "Hydrogen generation by aluminum corrosion in aqueous alkaline solutions of inorganic promoters: The AlH-idrox process" *Energy* **36** (2011) 2493-2501

37. J. O' M. Bockris, Lj.V. Minevski "On the mechanism of the passivity of aluminum and aluminum alloys" *J. Electroanal. Chem.* **349** (1993) 375-414

38. E. Samson, J. Marchand, K.A. Snyder "Culation of ionic diffusion coefficients on the basis of migration test results" *Materials and Structures* **36** (2003) 156–165

39. S. Adhikari, K. R. Hebert "Factors controlling the time evolution of the corrosion potential of aluminum in alkaline solutions" *Corrosion Science* **50** (2008) 1414–1421

40. S. Adhikari, J. Ai, K. R. Hebert, K.M. Ho, C.Z. Wang "Hydrogen in aluminum during alkaline corrosion" *Electrochimica Acta* **55** (2010) 5326–5331

41. J.-C. Crivelloa, T. Nobukib, T. Kujic "Improvement of Mg–Al alloys for hydrogen storage applications" *International Journal of Hydrogen Energy* **34** (2009) 1937 – 1943

Chapter IX

Role of additives for sacrificial protection of steel by Al and Zn pigments in model high temperature coatings

M. Serdechnova, P. Volovitch, S. Franger, K. Ogle

Role of additives for sacrificial protection of steel by aluminum and zinc pigments in model high temperature coatings

M. Serdechnova, P. Volovitch, S. Franger, K. Ogle

Atomic emission spectroelectrochemistry (AESEC) was applied for the direct measurement of the aqueous reactivity of model sacrificial Zn or Al pigmented paints on steel. For the same binder formulation very different behavior of Zn and Al was observed: when Zn pigment offered sacrificial protection confirmed by both, open circuit potential and Zn and Fe dissolution rates measured by ICP, for the system with Al steel was corroded. These results were interpreted in terms of the loss of conductivity in the metal/oxide/polymer interface. In order to control the reactivity of Al, the formulation was modified by additives. To simulate the role of these additives the reactivity of bulk aluminum in their presence was investigated. It was demonstrated that some ions (Mg^{2+}, PO_4^{3-}, silicates) can activate Al either modifying the oxide structure or increasing the pH when released. After the modification in the paint composition by the additives the resistance of the oxide layer was reduced up-to the level of the coating with Zn pigments. As a result, the galvanic protection was observed in modified systems.

9.1. Introduction

The paint systems with sacrificial metallic pigments are widely used to prevent steel corrosion. One of the known systems contains zinc pigments in siloxane binder [1]. These coatings provide galvanic protection to the steel, as confirmed by electrochemical and salt spray tests. However, for several applications when the substrate is supposed to be heated, low Zn melting point (419 °C) makes it impossible to use these formulations.

To avoid the problem of thermal decomposition, Zn pigments could be replaced by Al pigments in the same binder with a similar average particle size. However, the replacement of one of the components can modify the reactivity of the whole system. The difficulty working with Al as a sacrificial metal is that its naturally formed oxide is nonconducting [2] preventing electrical contact between the particles and the steel substrate thereby making the galvanic protection ineffective [3]. For the good choice of the way to control the reactivity of metallic pigments in the complex system the mechanisms of the reactivity should be understood. Early it was shown that Mg^{2+} ions retard passive oxide formation on Al during spontaneous reaction and modify the oxide layer under anodic potential [4]. The results were interpreted as due to the rapid formation of a semiconducting spinel which is responsible for the resistivity decrease in the oxide layer. This concept of *in-situ* Al oxide layer modification by additives in formulation can be useful for coatings formulations.

In this work we apply an atomic emission spectroelectrochemistry (AESEC) to determine the individual rates of dissolution of Al and steel from the model system containing sacrificial Zn or Al pigmented paints on steel in presence of different additives in the paint formulation. In this way, we may determine the specific effect of different additives on the elementary degradation phenomena and demonstrate the role of Mg^{2+}, PO_4^{3-} and hydroxides in promoting the cathodic protection mechanism with Al particles

9.2. Experimental

The principle of the AESEC measurement has been previously described in detail [5,6]. Briefly, it consists of an electrochemical flow cell combined with an inductively coupled plasma atomic emission spectrometer. In the cell reactions between a sample and an aggressive electrolyte occur, leading to the production of dissolved ions. After the cell, the electrolyte is transported to an inductively coupled plasma optical emission spectrometer (ICP-OES) where its composition is continually analyzed. The instantaneous dissolution rate of an element M in the cell (v_M in nmol s^{-1} cm^{-2}) is directly related to the downstream concentration as (equation 9.1):

$$v_M = C_M f / A \qquad [9.1]$$

where f is the flow rate of electrolyte (in this work, 3.02 cm^3 min^{-1}), C_M is a concentration of element M (in mol l^{-1}), and A is the exposed surface area (0.51 cm^2). C_M is measured from the emission intensity at a specific wavelength using normal quantitative procedures for ICP spectrometry [7]. The dissolution rate of each elements can be expressed as equivalent electrical current (j_M) by Faraday's law (equation 9.2):

$$j_M = v_M \, n \, F \qquad [9.2]$$

where F is the Faraday constant, n is the charge of the element (n=3 for Al and Fe, n=2 for Zn).

The ICP-OES Ultima2C (produced by Horiba JobinYvon) with 30 lines of different element measured simultaneously by polychromator was used. The focus distance of the polychromator is 50 cm. The nebulizer *Meinhard K3* optimized for 3 ml/min flow-rate (Horiba JobinYvon) was used to aspirate the solution after the reaction into the plasma.

The electrochemical flow cell is equipped with three electrodes (Hg/Hg_2Cl_2 as a reference electrode, Pt wire as a counter electrode and the sample of the interest as a working electrode), which allow us to measure the potential and the total current of the reaction by potentiostat EG&G M273A.

The specificity of the ICP analysis is that only 5% of solution is aspirated into the plasma, 95 % of the solution removes from the system by the second channel of the peristaltic pump.

It allows us to analyze the pH of this residual solution. During the applied potential experiment, the solution was collected by portions of 9 cm^3 (during each 3 minutes) and the pH was measured.

The thickness of the coatings, the size of metallic pigments and their elemental composition were investigated by scanning electron microscope Zeiss Supra 55 VP, equipped with elemental microanalysis system (accelerating voltage is 5 keV for elemental microanalysis and 15 keV for dimension measurements).

The resistivity measurements were performed in a 2 electrodes configuration (2 points), in the frequency range 2 10^3 to 2 10^{-1} Hz, with a VMP3 (BioLogic) frequency response analyzer. The average value of resistivity was used and analyzed in this work.

9.3. Materials

All samples for this work were prepared in the laboratory with the intention of reproducing phenomena that might be observed with commercial materials. However, they should not be considered representative of any existing commercial product or products in development.

The model system consists of a 15CDV6 steel substrate (see table 9.1 for elemental composition) with an Al and Zn particles into the different rich silicone based coating of 50 to 80 µm thickness (**figure 9.1**). Commercial 99.8% Al particles (average diameter about 2-8 µm) or 99.99% Zn particles (average diameter about 9-13 µm) were combined with a polymer siloxane binder and applied by spray.

Table 9.1. Elemental composition of 15CDV6 steel

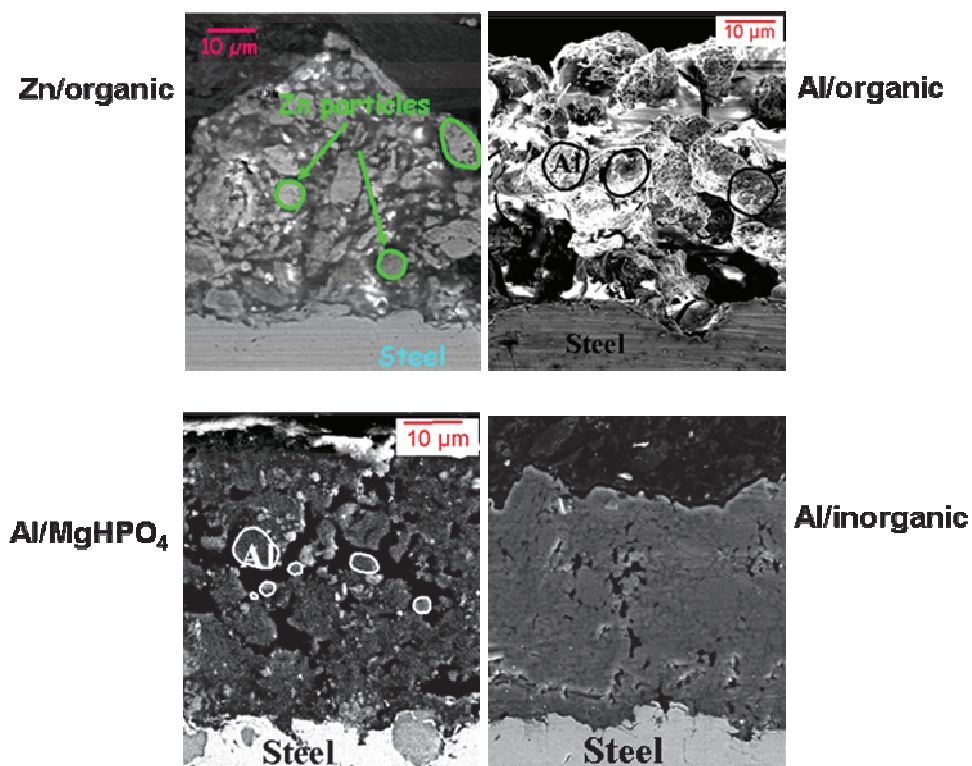| Metal	Fe	C	Si	Mn	Cr	Mo	V	S	P
Wt. %	Base	0.16	0.18	0.86	1.60	0.85	0.220	0.001	0.006

Figure 9.1. Cross-sections of the coating: (a) – Zn particles in the organic siloxane binder; (b) – Al particles in the organic siloxane binder; (c) – Al particles with additives of Mg^{2+} and PO_4^{3-} in the formulation; (d) – Al particles in the inorganic binder.

The coated samples were rinsed in purified water obtained with a Millipore[TM] system (resistivity of 18.2 MΩ·cm). Dissolution experiments were made in a 3 % NaCl electrolyte at room temperature (24 °C). All reagents were analytical purity grade produced by Analar Normapur VWR[®] BDH Prolabo[®].

9.4. Results

9.4.1. Spontaneous dissolution of the coated systems.

Figure 9.2 shows the result of the AESEC measurement of spontaneous dissolution for 4 types of investigated samples. The elemental dissolution was measured by ICP-OES while the potential of the reaction was measured by potentiostat.
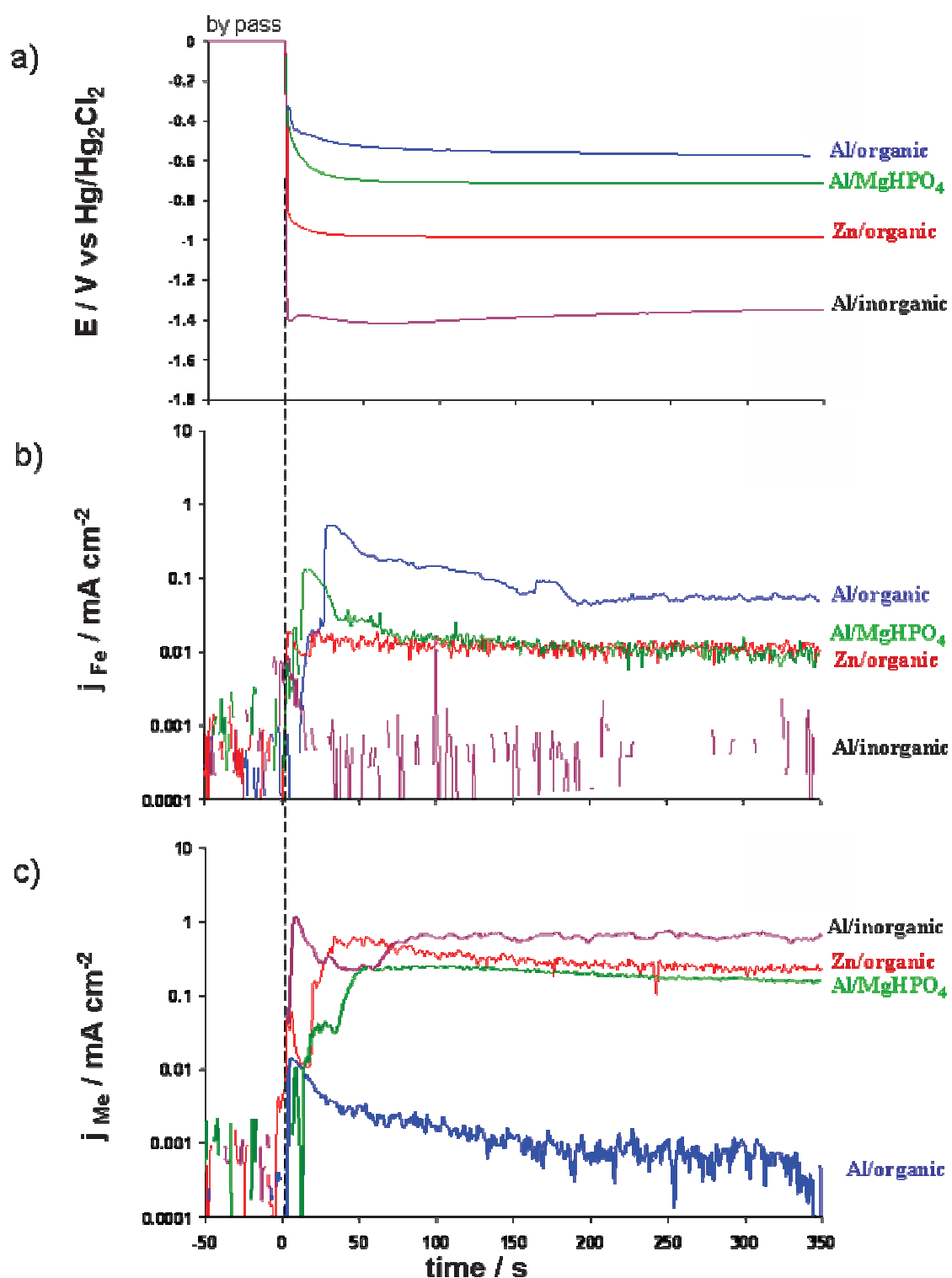
Figure 9.2. The dependence of OC potential and the dissolution rate of Fe and active metal (Al and Zn) for 4 types of the samples used in this work. The samples contact the electrolyte at t=0 s. The same time scale is used for three figures.

It is clear from **figure 9.2** that the potential of the spontaneous corrosion for the sample Al/organic corresponds to the potential of steel corrosion (-0.59 V), while for three other samples (Zn/organic, Al/MgHPO$_4$ and Al/inorganic) corresponds to the corrosion potential of active metals (-1.05 V, -0.71 V and -1.34 V respectively).

Initial pH of the NaCl electrolyte is 6.3; however the pH measurement in the electrolyte after the contact with a surface of Al/inorganic sample related the pH increases up to 10.7 during 30 minutes ICP experiment. The SEM observation of the Al/inorganic surface (**figure 9.3**) shows the presence of the unreacted monomer used for formation of the binder. The pH of the 0.25 vol.% solution of the monomer is 11.7 which corresponds well with the observed pH increase.
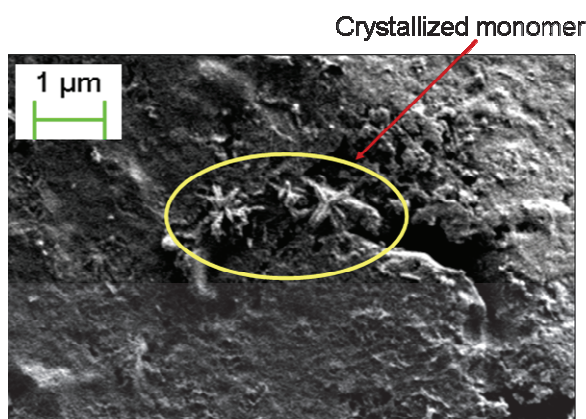
Figure 9.3. The SEM image of the coating with aluminum particles in the inorganic binder. The crystalline structure of monomer is marked.

The potential of the spontaneous reaction (-1.34V) indicates the activated Al pigments in the coating, the rate of the Fe dissolution is below detection limit. The relatively low Fe and high Al dissolution rates may be used to confirm the existence of galvanic coupling between two elements. For organic binder with Mg^{2+} and PO$_4^{3-}$ additives, the galvanic coupling is also observed even iron is still detected.

The XRD analysis of the coated samples shows the presence of metallic Al and Zn particles. The natural oxide on them was not detected probably due to its amorphous structure or its relatively small thickness. The additional peaks in the XRD spectra were observed for the Al/MgHPO$_4$ sample (**figure 9.4**). These peaks may be attributed to the formation of aluminum-magnesium spinel (MgAl$_2$O$_4$) on the surface.
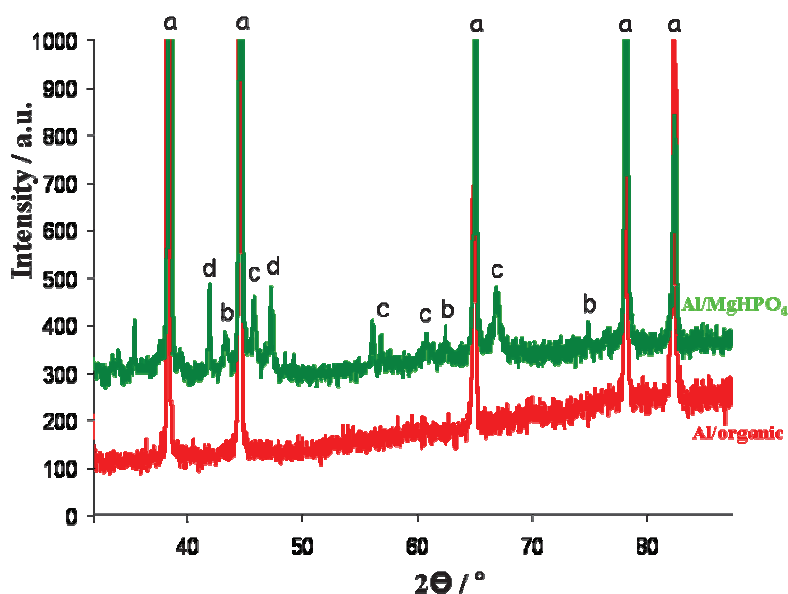
Figure 9.4. XRD analysis for the Al/organic (red) and Al/MgHPO$_4$ (green) coatings: (a) – Al, (b) – MgO, (c) - cubic MgAl$_2$O$_4$, (d) – Fe$_3$O$_4$ (we attributer it to the impurities after sample cutting).

9.4.2. The polarization experiment.

Figure 9.5 shows the typical AESEC result during the potentiodynamic experiment started at -1.3 V vs Hg/Hg$_2$Cl$_2$. The potential increase in the anodic direction with a sweep rate 1 mV/s. **Figure 9.5**(a) presents the typical AESEC polarization curve for each sample. **Figures 9.5 (b) and 9.5 (c)** show the ICP data of the dissolution rates of the active metal pigments (Al and Zn), j$_M$, and Fe from the steel substrate during the experiments.
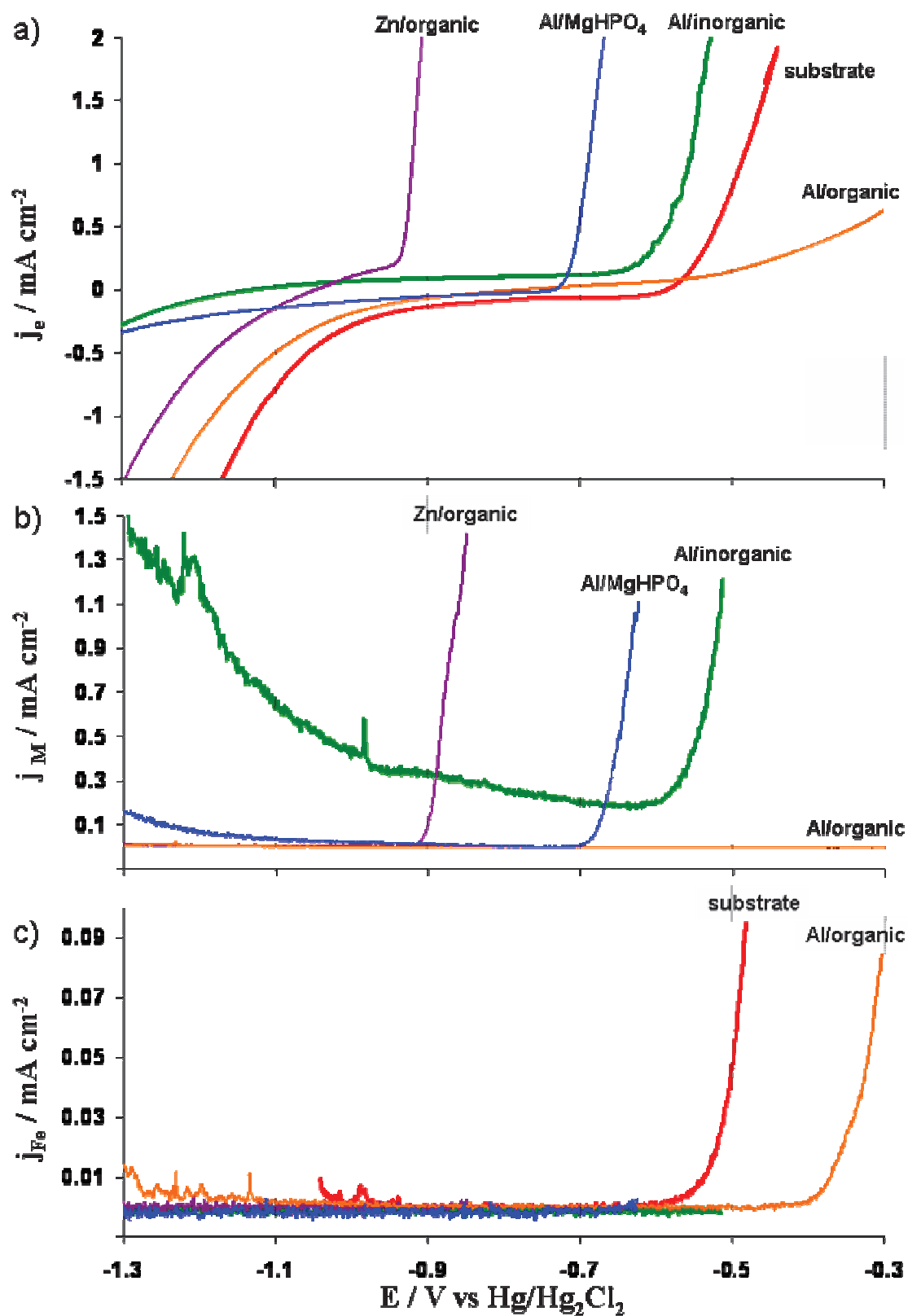
Figure 9.5. Typical polarization profiles for 4 types of coated systems and non-protected substrate as a reference. The potential scale is the same for all figures.

For the non-protected sample, the total current reflects steel corrosion in the anodic domain and water reduction in the cathodic domain. The close behavior was observed for the sample Al/organic, where Fe dissolves in the anodic domain and Al dissolution is negligible. In the both domains the total current of the reaction is slightly lower for the Al/organic sample then for the non-protected steel which can be related to a slow barrier protection. The barrier protection by Al/organic coating can be not effective due to the high porosity of the coating [8,9]. The high Fe dissolution in the anodic domain was interpreted as an absence of galvanic protection of the substrate by the coating.

For the Zn/organic, Al/MgHPO$_4$ and Al/inorganic samples the total current of the reaction in the anodic domain corresponds to the dissolution of active metal (Zn for the first sample and Al for the second and third). The dissolution of Fe substrate is below the detection limit and galvanic protection of steel by active metal pigments is observed. In the cathodic domain the total current of the reaction significantly decreases for the samples Al/MgHPO$_4$ and Al/inorganic. It was interpreted as the barrier protection of the steel due the compact structure of the coating.

9.4.3. The resistivity measurements

The galvanic coupling between the active metal and the steel is determined by the electrical contact between them. To quantify this contact, both the horizontal (on the surface of the coating, **figure 9.5(a))** and perpendicular (in the depth of the coating, **figure 9.5(b))** resistivities were measured and compared with AESEC result. The results of conductivity measurements are presented in Table 9.3.
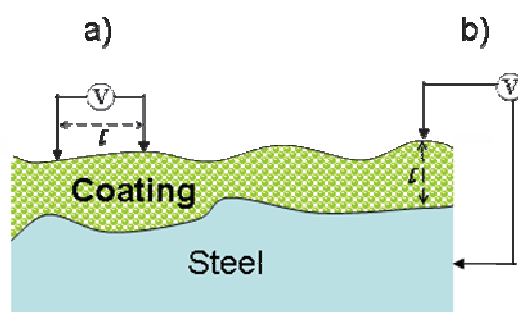

Figure 9.5. The two ways of the resistivity measurements: (a) – surface conductivity, (b) – cut-edge conductivity.

Table 9.3. The results of the resistivity measurement

Sample	Resistivity (cut-edge) / Ω m	Resistivity (surface) / Ω m	OCP / V	Corroding material	Galvanic protection
Al / organic	$1.0 \cdot 10^8$	$1.6 \cdot 10^9$	-0.59	Steel	-
Al / MgHPO$_4$	$2.0 \cdot 10^3$	$1.2 \cdot 10^2$	-0.75	Al pigment	+
Al / inorganic	$1.3 \cdot 10^3$	$1.0 \cdot 10^2$	-1.34	Al pigment	+
Zn / organic	$2.0 \cdot 10^5$	$1.0 \cdot 10^4$	-1.05	Zn pigment	+

For the Al particles in the organic siloxane binder the resistivity is very high. It means that the conductivity in the coating is very low and electrons could not effectively transfer from Al to steel. For this sample the galvanic protection was not observed. For others three samples the measured resistance is lower in orders of magnitude, the galvanic protection was observed for them during both the spontaneous reaction and the polarization experiment.

9.4.4. Spontaneous dissolution of pure bulk Al in the presence of Mg^{2+} and PO_4^{3-} (pH 9.4)

In the previous section we demonstrated that the addition of MgHPO$_4$ in the coating formulation enhances the galvanic couple between the Al particles and the steel substrate. To understand better this phenomenon, an experiment was performed in 3% NaCl solution in presence of Mg^{2+} and PO_4^{3-} ions.

Each experiment was repeated several times. Typical results are shown in **figure 9.6**. The curve without magnesium or phosphate is shown as a reference. The dissolution rate increases in the presence of Mg^{2+} and PO_4^{3-} (this effect was also previously demonstrated in [4]), however in the presence of phosphate the activation is much longer, requiring more then 1000 s to reach the steady state value. The potential of the spontaneous Al dissolution in presence of Mg^{2+} and PO_4^{3-} is shifted up to -1.0 V (table 9.4).
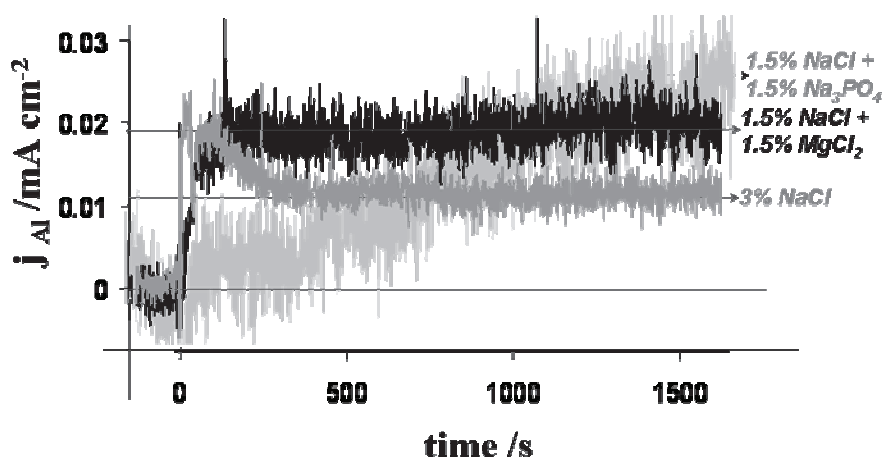
Figure 9.6. The dissolution rate of bulk aluminum with and without PO_4^{2-} and Mg^{2+} in the solution, pH 9.4.

The analysis of the dielectric constants data for compounds, which can be formed on the surface, is presented in table 9.4. The highest dielectric constant corresponds to the lowest dissolution rate of Al and was observed for the Al_2O_3 on the surface. During the corrosion of bulk Al in presence of Mg^{2+} and PO_4^{3-} the dielectric constants of the formed compounds decrease at the same time with potential decrease.

Table 9.4. The corrosion of the bulk metals in NaCl solution

Massive sample	Solution	Corrosion potential / V	Supposed structure	Dielectric constant [10]
Al	NaCl	-0.8	Al_2O_3	11.5
Al	$NaCl + MgCl_2$	-1.0	$MgAl_2O_4$ (XRD)	8.7
Al	$NaCl + Na_3PO_4$	-1.0	$AlPO_4 \cdot nH_2O$ (XRD)	2.5
Zn	NaCl	-1.05	ZnO (XRD)	9.3

9.5. Discussion

9.5.1. The resistance between active metal pigment and steel

For the galvanic protection of steel by the active metal from the particles in the coating, an electrical contact between them is necessary. This electrical interaction exists, if two metals have a direct contact. In our system, particles in the coating and substrate do not have direc contact due to a number of intermediate layers. These layers are the oxide layer on particle surface (the conductivity of the oxide is lower, than the conductivity of the metal) and the layer of the polymer binder between particles and steel.

Thus, the system can be represented as in **figure 9.7**. The substances, oxide layer and binder layer at which the electrical contact between active metal and steel can be interrupted are presented as resistances R_1 and R_2. Both these layers have non-zero resistance these resistances should be reduced to obtain the galvanic protection.
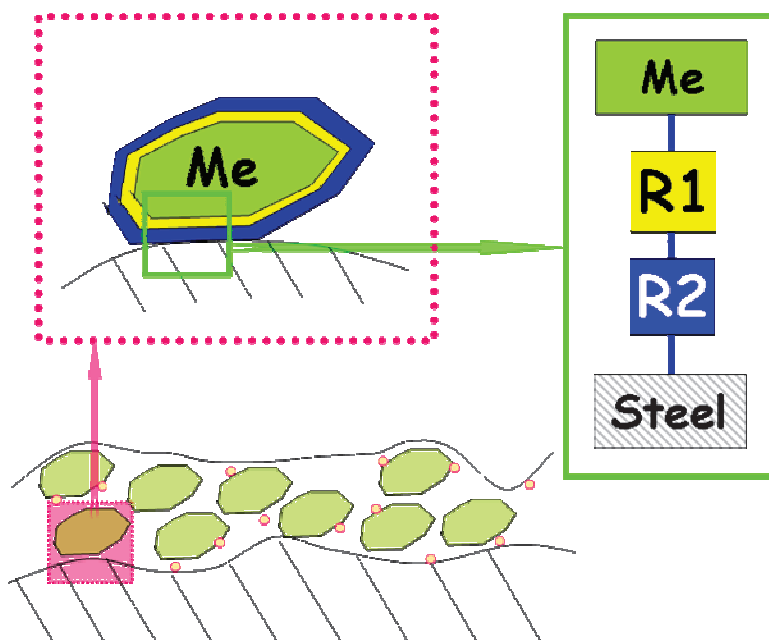

Figure 9.7. Schematic presentation of system: steel / coating with active metal pigment in the siloxane binder.

The coating with zinc pigments in the organic binder is enough conductive, that means that both the oxide layer and the binder on it have low resistance. The polymerization of the organic silicate monomer takes place in the presence of acids (or Lewis acids) (**figure 9.8**) [11,12]. Natural Zn oxide on the surface of pigments is appropriate as a Lewis acid.
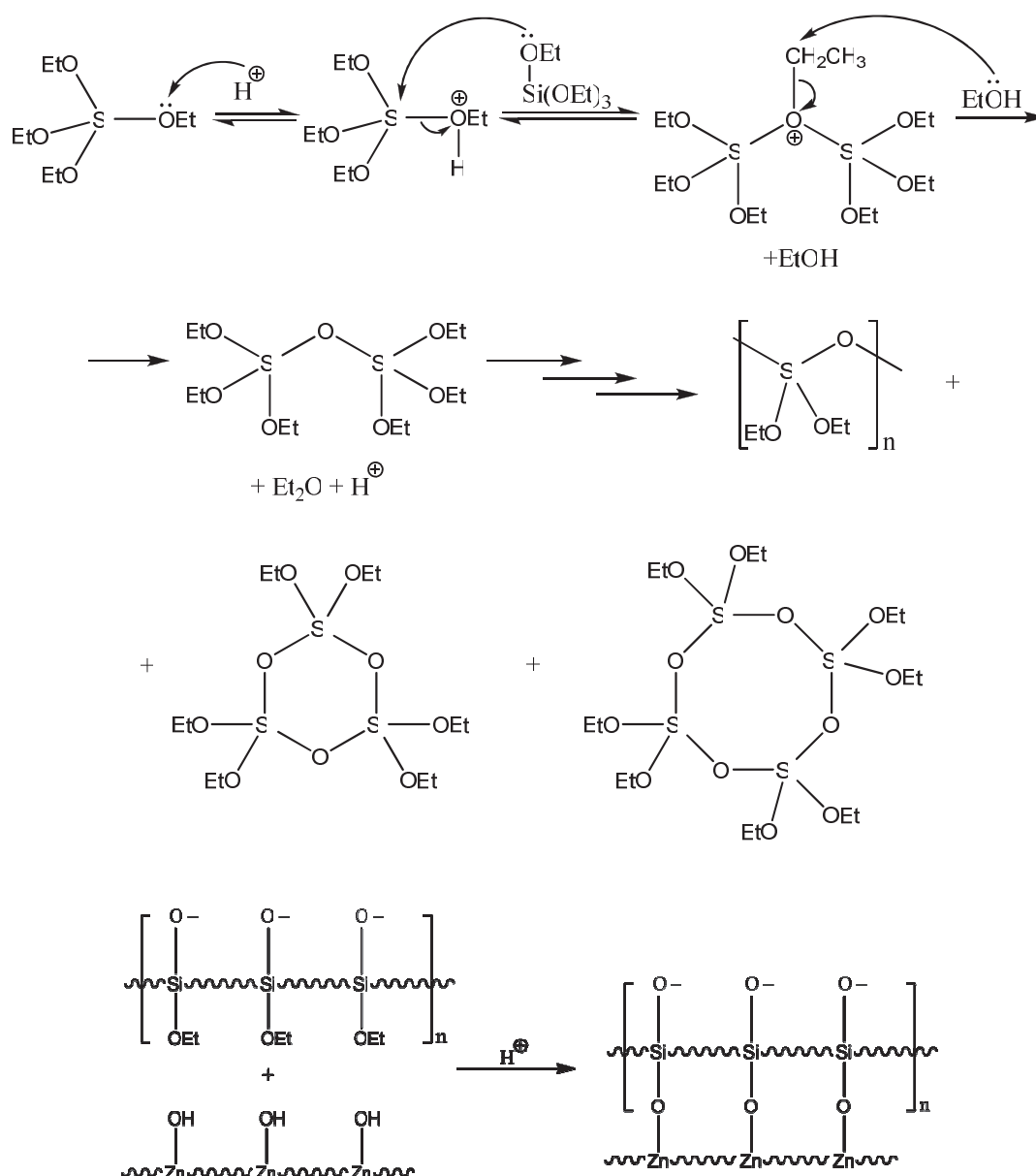
Figure 9.8. The polymerization of the organic silicate monomer in presence of Zn particles.

At the beginning of the polymerization the vacant orbital of the acid attacks the -OR group in the monomer. It leads to the formation of ROH and allows the silicate to react with one more molecule. This polymerization reaction leads to the formation of the chains (both rings and linear) with general formula –Si-O-Si-O-Si-… This mechanism occurs if the amount of Zn oxide (Lewis acid) is rather small and it is enough only to catalyze the reaction. If the system contains a much higher amount of ZnO then it is necessary for the catalysis, it can also be included in the structure of polymer [11]. In this case, the etherification reaction between Zn-OH groups on the surface of the zinc particles and Si-OR of the polymer occurs. It leads to the particles with ZnO on the surface become chemically bonding in the structure of the

polymer. Moreover, Grasset et al [13] have shown that the closest layer of polymer on the surface of oxide continues the structure of this oxide and keeps some its properties, such as conductivity. This implies that for a semi-conductive ZnO layer, the closest layer of binder is also semi-conductive.

However, if during formulation of the coating, the Zn pigments are replaced by the Al pigments in the same binder, the structure of the coating changes a lot. During the siloxane polymerization the noticeable reaction rate between Al_2O_3 and siloxane occurs only at very high temperature (more then 1000 °C [14]). Moreover, the resistivity of the Al_2O_3 is much higher than ZnO (table 9.4). Even if Al_2O_3 reacts with siloxane, conductivity in this system does not exist, because Al_2O_3 is an insulator. The siloxane polymer, which keeps the structure of oxide under it, also becomes an insulator.

If we come back to the proposed model of resistive layers between active metal and steel, it means, that total resistance R_1+R_2 is too high for electrons transfer occurs. The Al particles can be used for the galvanic protection of the substrate only in case if the sum of R_1 and R_2 decreases.

9.5.2. Ways to reduce the oxide resistivity

The experiment with the bulk aluminum explains the possible ways to reduce the resistivity of the Al oxide layer and to activate the Al pigments. The modification of the structure of Al_2O_3 takes place in presence of external ions. **Figure 9.6** shows the increase of the Al dissolution rate, when the solution contains Mg^{2+} or PO_4^{3-} ions. It was interpreted in terms of the formation of $MgAl_2O_4$ (magnesium-aluminum spinel) or $AlPO_4$ on the surface, which are much more conductive then Al_2O_3. Different defects in the structure of these compounds further increase their conductivity. As a result, the formulation modification for the $Al/MgHPO_4$ sample the Al_2O_3 layer properties also change and its resistance decreases ($MgAl_2O_4$ and $AlPO_4$ are semi-conductors in comparison with Al_2O_3, which is nonconductive). In the proposed model it means that R_1 is reduced. Moreover, using the approach that the structure of the closest layer of polymer continues the structure of the oxide; it means that the binder resistivity in near-surface layer decreases (the decrease of the R_2 in the proposed model).

The activation of the Al surface also occurs for the Al/inorganic sample. The isolative Al_2O_3 dissolves in presence of hydroxides according to the reaction (9.3) [15]. It can be due to the pH increase in presence of monomer:

$$Al_2O_3 + OH^- \rightarrow Al(OH)_4^-$$ [9.3]

The absence of the isolative oxide on the pigment surface decreases R_1 and allows the electrical contact and galvanic protection between Al and steel.

9.5.3. Ways to reduce the binder resistivity

The presence of the PO_4^{3-} ions in the solution increases the conductivity of the binder, including in its structure during polymerization (**figure 9.9**) [16].
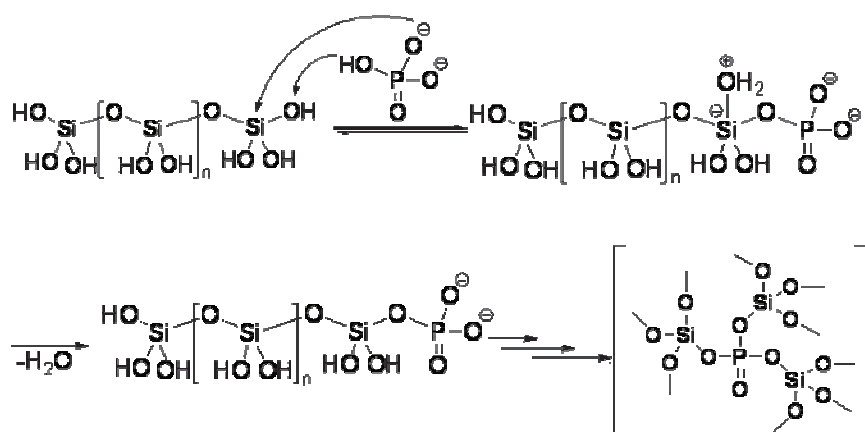
Figure 9.9. The polymerization of the organic silicate monomer in presence of PO_4^{3-} in the formulation.

Including of –O–P–O– in the structure of siloxane increases the ionic conductivity of the polymer because of the formation –Si–O–P– bond, which is close to ionic [17]. As a result of the ionic conductivity in the binder, the R_2 in the model decreases and the conductivity between the active metal (Al) and steel increases. For the sample with the PO_4^{3-} in the structure (Al/MgHPO$_4$) the galvanic protection was obtained (table 9.3).

9.5.4. The mutual layer influence

The formation of the intermediate layers between the oxide layer and the layer of the binder does not allow us to distinguish the resistivity R_1 and R_2 in the real samples according to the proposed model. The binder conductivity is strictly influenced by the oxide conductivity in the near-oxide layer and the porosity of the coating. For the real samples only average effective resistivity can be measured experimentally.

According to such type of measurement it was shown that the most conductive (less resistive) samples provide the best galvanic protection of the steel by active pigments in the coating. Probably, further experiments by impedance spectroscopy could be performed in order to distinguish between resistivities R_1 and R_2 for different thicknesses of both the oxide and the binder layers.

9.6. Conclusions

•   The AESEC method allows us to measure the rates of elementary degradation phenomena for model high temperature paint systems and distinguish the galvanic and barrier protection of steel by the active metal pigments.

•   The preliminary simple electrical model for the contact interruption was proposed.

•   The galvanic protection of steel by zinc pigment is possible even in the organic siloxane binder without additives, while the galvanic coupling between Al particles and a steel substrate is not achieved in the absence of additives due to the oxide film on the Al surface.

•   The addition of $MgHPO_4$ or hydroxide-ions enhances the galvanic coupling effect.

•   The model explaining the conductivity improvement and galvanic protection of organic systems with Mg^{2+} and PO_4^{3-} additives and in inorganic binder is proposed. The mechanism is the reducing the oxide resistance through the modification of the oxide structure.

9.7. Acknowledgement

9.8. References

1. Hare, C. H. Corrosion control of steel by organic coatings. *Uhlig's Corrosion Handbook* 1023–1038 (2000).

2. Palibroda, E., Lupsan, A., Pruneanu, S. & Savos, M. Aluminium porous oxide growth. On the electric conductivity of the barrier layer. *Thin Solid Films* **256**, 101–105 (1995).

3. Galvanic Corrosion Bimetallic Corrosion. *Corrosionist, The Website of Corrosion Protection and Corrosion Control* at <http://www.corrosionist.com/Galvanic_Corrosion.htm>

4. Volovitch, P., Serdechnova, M. & Ogle, K. Aqueous Corrosion of Mg-Al Binary Alloys: Roles of Al and Mg. (2012).

5. Ogle, K., Baeyens, J., Swiatowska, J. & Volovitch, P. Atomic emission spectroelectrochemistry applied to dealloying phenomena: I. The formation and dissolution of residual copper films on stainless steel. *Electrochimica Acta* **54**, 5163–5170 (2009).

6. Serdechnova, M., Volovitch, P. & Ogle, K. Atomic emission spectroelectrochemistry study of the degradation mechanism of model high-temperature paint containing sacrificial aluminum particles. *Surface and Coatings Technology* **206**, 2133–2139 (2012).

7. Mokaddem, M., Volovitch, P., Rechou, F., Oltra, R. & Ogle, K. The anodic and cathodic dissolution of Al and Al-Cu-Mg alloy. *Electrochimica Acta* **55,** 3779–3786 (2010).

8. Twite, R. L. & Bierwagen, G. P. Review of alternatives to chromate for corrosion protection of aluminum aerospace alloys. *Progress in Organic Coatings* **33**, 91–100 (1998).

9. Aksut, A. A. & Onal, A. N. The effect of some organic compounds on the corrosion of pure Fe, pure Cr and Fe---Cr alloys in acidic solutions. *Corrosion Science* **39**, 761–774 (1997).

10. Shannon, R. D. & Rossman, G. D. DIELECTRIC CONSTANT OF MgAl2O4 SPINEL AND THE OXIDE ADDITIVITY RULE. *J. Phys. Chem. Solids* **52**, 1055–1059 (1991).

11.   Kotecha, M., Veeman, W., Rohe, B. & Tausch, M. NMR investigations of silane-coated nano-sized ZnO particles. *Microporous and Mesoporous Materials* **95**, 66–75 (2006).

12.   Díaz, I. *et al.* Corrosion resistance of new epoxy–siloxane hybrid coatings. A laboratory study. *Progress in Organic Coatings* **69,** 278–286 (2010).

13.   Grasset, F. *et al.* Surface modification of zinc oxide nanoparticles by aminopropyltriethoxysilane. *Journal of Alloys and Compounds* **360**, 298–311 (2003).

14.   Waseda, Y. & Toguri, J. M. Phase diagrams of binary and tarnary silicate systems. *The structure and properties of oxide melts* 7–14 (1998).

15.   Ogle, K., Serdechnova, M., Mokaddem, M. & Volovitch, P. The cathodic dissolution of Al, Al2Cu, and Al alloys. *Electrochimica Acta* **56,** 1711–1718 (2011).

16.   Plotnichenko, V. G., Sokolov, V. O., Koltashev, V. V. & Dianov, E. M. On the structure of phosphosilicate glasses. *Journal of Non-Crystalline Solids* **306**, 209–226 (2002).

17.   Kim, S. H., Kim, J. Y., Kim, H. S. & Cho, H. N. Ionic conductivity of polymer electrolytes based on phosphate and polyether copolymers. *Solid State Ionics* **116**, 63–71 (1999).

Chapter X

Conclusions

Acknowledgements

Conclusions

- New methodology was developed for the rapid screening of sacrificial coatings giving access to the degradation mechanisms. The AESEC method allows us to distinguish and to quantify elementary degradation phenomena, such as the dissolution of metallic pigment, the detachment of the pigment particles, the dissolution of the siloxane binder and the corrosion of the steel substrate in a model high temperature paint system. The galvanic and barrier protection of substrate by a coating can be distinguished by AESEC.

- The main factors, controlling the reactivity of Al pigments were determined:

  1. The cathodic dissolution of Al was observed for all systems and was interpreted in terms of a simple model in which hydroxide generation, $Al(OH)_3$ formation/dissolution, and $Al(OH)_4^-$ diffusion are kinetically coupled.
  2. The role of noble additives during Al dissolution (like Cu or $Al_xFe_yMn_{1-y}Si$ is explained as giving rise to local cathodes which accelerate the Al dissolution rate.
  3. The active additives like Mg or Si decrease Al cathodic dissolution due to competitive reactions with cathodically generated hydroxides in the strong cathodic domain.

- The AESEC methodology was developed for measurement of particles release rate:

  1. The detachment of Al particles during the polarization experiment is observed by ICP and confirmed by SEM. It was shown, that the ICP technique detects only particles with diameter less then 7 µm under condition of the experiment (*Meinhard K3* nebulizer, 3 ml/min flow-rate).
  2. The calibration experiment for different particles size distribution (3.2, 13.1 and 38.4 µm) was performed and used for quantification of released particles.

- Using the new methodology for coated systems it was shown that:

1. No galvanic protection is observed during the anodic polarization by Al pigments in the organic siloxane binder. These results may be interpreted in terms of the presence of the passive Al oxide layer on the particles.

2. The presence of Mg^{2+} ions is observed to delay Al_2O_3 formation; this result was attributed to the formation of a semiconducting spinel responsible for the increase of conductivity.

3. The addition of $MgHPO_4$ or Lewis base (to increase pH) to the coating formulation enhances the galvanic coupling effect probably by reducing the oxide resistance through the modification of the oxide structure.

- The fundamental knowledge of Zn and Al reactivity were applied to propose a new coating formulation stable up to 550 °C and protective more then 1000 H of salt spray test.

1. The preliminary simple electrical model for the contact interruption was proposed comparing galvanic protection of steel substrate by Al and Zn pigments.

2. The barrier protection of steel by the coating with active metal pigments was distinguished and ameliorated by modification of particles size distribution.

Annex I

Peak calculation soft-ware

This program was developed together with N. Timofeev (Institute of bioorganic chemistry of the Russian Academy of Sciences, Russia) for calculation of the peaks on the ICP curves obtained during the experiments.

The program was written on C++ programming language using the following tools: cross-platform framework Qt, collection of widgets for technical applications Qwt and free library for arbitrary precision arithmetic GMP. Our software can be compiled on Windows, GNU/Linux and Mac OS X platform.

The original program text is avaliable on https://github.com/KblCb/particleicp

src/math/edittable.h

```cpp
#ifndef EDITTABLE_H
#define EDITTABLE_H

#include <QVariantMap>
#include "vectortable.h"
```

```cpp
// the functions of this name space perform the operations with numeric tables
// of double accuracy (double) which contain named columns. Reading the in-put
// file the program convert the data to the table, where the columns represent
// the data for different elements.
```

```cpp
namespace edt {

    VectorTable cuttable( const VectorTable& table, double start, double finish );
    VectorTable filtertable( const VectorTable& table, const QVariantMap& settings
);
    VectorTable correcttable( const VectorTable& table, const QVariantMap& settings
);

}
```

```cpp
#endif /* EDITTABLE_H */
```

src/math/correcttable.cpp

```cpp
#include <QtConcurrentMap>
#include <QVector>
#include <QDebug>
#include <gmpxx.h>
#include "edittable.h"
#include "falgorithms.h"
```

```cpp
// The function returns the table, which contain the in-put table (table) data
// with background level substraction, taken from the settings parameters
// (settings).
```

```cpp
// The functional part, which allows to work with MapReduce and accelerate the
// calculation procedure due to the concurrent processes...
class delta_mp
{
public:
    delta_mp(double b) : b_v( b ) {}

    typedef double result_type;

// ...which is calculatind as difference between in-put value and value a;
// the program performe this procedure with any value of the deviation, this
// allows to decrease the errors accumulation.
    double operator()( double a )
    {
        mpf_class a_mp = a, b_mp = b_v, c_mp = a_mp - b_mp;
        return c_mp.get_d();
    }

    double b_v;
};

VectorTable edt::correcttable( const VectorTable& table,
        const QVariantMap& settings )
{
// The table (containing one column, which is equal to zero column of in-put
// table) is created. Tha table has the same name.
```

194

```cpp
    VectorTable result( table.getTags().first(), *table.getColumn( 0 ) );

// For each column of the in-put table (exept column one)...
    foreach( QString tag, fp::tail( table.getTags() ) )
    {

// ...substract the average value of background from the each value, containing
// into the column for each column
        QVector<double> vec = QtConcurrent::blockingMapped( *table.getColumn(tag),
            delta_mp(settings[QString("%1_AverageNoise").arg(tag)].toDouble()));

// ...and add the obtained column to the table
        result.addColumn( tag, vec );
    }

// The out-put table is done.
    return result;
}
```

src/math/cuttable.cpp

```cpp
#include "edittable.h"

// The function substract from the table (table) the defined subtable, which
// corresponds to the X interval, defining by beginning (start) and final
// (finish) values.

VectorTable edt::cuttable( const VectorTable& table, double start, double finish )
{
// At the beginning, the defined interval is verified. If the beginning value
// more or equal to the final value...
    if ( start >= finish )
// ...the program immidiately closes.
        qFatal( "cuttable: start >= finish" );

// The acces to read the file with first column of the table is obtained (where
// the X values are kept). The access is performed due to the constant reference
// to QVector<double>. This reference is made by the invocation of VectorTable
// function.
    const QVector<double>* scale = table.getColumn( table.getTags().first() );

    int pos = -1, length = -1;

// Define: i is a first cell of the column, which contains X values; j is the
// last cell of the same column; k is equal to first i value. Check all cells of
// the column untill i < j.
    for ( QVector<double>::const_iterator i = scale->begin(), j = scale->end(),
                                          k = i; i != j; i++ )
    {
// For each cell…
//
// If the the number of the firs cell does not change from the beginning of
// searching (e.g. equal to -1) and the value of the cell of interest is higher
// than the interval beginning...
        if (( pos == -1 ) && ( *i > start ))
// ...than the number of the first line of the small cell is equal to the number
// of gaps between first cell and current cell.
            pos = i - k;

// If the the number of the firs cell does change from the beginning of
// searching (e.g. does not equal to -1) and the value of the cess of interest
// is higher than the end of the interval...
        if (( pos != -1 ) && ( *i > finish ))
        {
// ...than the lengths of the obtained table is equal to the cell of interest
```

```
// position, minus the position of the first (start) cell, minus 1...
            length = i - k - pos - 1;
// ...and searching is immidiately finishes.
            break;
        }
    }

// The table (converted from the original table) started from pos line and with
// lengths lengths is created. The section of the table is performed due to the
// internal function.
    return table.mid( pos, length );
}
```

src/math/filtertable.cpp

```cpp
#include <QDebug>
#include <QVector>
#include <QString>
#include <QMap>
#include <QStringList>
#include "falgorithms.h"
#include "edittable.h"

// The function creates the subtable, which contains all values of in-put table
// (table) greater than the maximal background deviation (settings).

VectorTable edt::filtertable( const VectorTable& table, const QVariantMap& settings
)
{
// The empty subtable, containing the names of columns from the original table,
// is created.
    VectorTable result( table.getTags() );

// Define the list of lines, which keep the names of the chosen columns of
// in-put table.
    QStringList tags;

// Define the list of pairs key-value for keeping of maximal background
// deviation associated with in-put table colums names.
    QMap<QString,double> limits;

// For each column name from whole lists of column names of in-put table (exept
// first column, where do we have the X values, which are out of our
// interest)...
    foreach( QString tag, fp::tail( table.getTags() ) )
    {
// ...if it is marked in settings that the signals should be analysed...
        if ( settings[QString("%1_State").arg(tag)].toBool() )
        {
// ...to add the column name to the list of chosen column of the in-put table...
            tags << tag;
// ...and associate the limit value for this column (taken from settings) with
// the name of this column.
            limits[tag] = settings[QString("%1_MaxNoise").arg(tag)].toDouble();
        }
    }

// For each line of the in-put table...
    for ( int i = 0, j = table.getHeight(); i < j; i++ )
    {
// ...we assume that into the each cell the signal value is contained
        bool check = true;

// For each column of interest...
        foreach( QString tag, tags )
        {
```

196

```
// ...if the value in the cell on the intersection of the cell of interest and
// column of interest is lower than the background deviation for the respective
// column...
            if ( table.getColumn(tag)->at(i) < limits[tag] )
            {
// ...the signal value of all cell of this line corresponds to the background
// deviation...
                check = false;
// ...and the searching continious through the next line.
                break;
            }
        }

// If the cells contain the measured signal...
        if ( check )
// ...than the line is added to the out-put subtable
            result << table.getRow(i);
    }

// The out-put small-table is created.
    return result;
}
```

src/reuseable/vectortable.h

```
#ifndef VECTORTABLE_H
#define VECTORTABLE_H

#include <QVector>
#include <QStringList>
#include <QString>
#include <QMap>

class VectorTable
{
public:
    VectorTable( const QStringList& tags  );
    VectorTable( const VectorTable& table );
    VectorTable( const QString& tag, const QVector<double>& col );
    virtual ~VectorTable();

    int                    getWidth() const;
    int                    getHeight() const;
    QVector<double>        getRow( int i ) const;
    const QVector<double>* getColumn( const QString& str ) const;
    const QVector<double>* getColumn( int i ) const;
    const QStringList&     getTags() const;
    virtual VectorTable    mid( int pos, int length = -1 ) const;
    virtual void           addRow( const QStringList& row );
    virtual void           addRow( const QVector<double>& row );
    virtual void           addColumn( const QString& tag, const QVector<double>&
col );

    VectorTable& operator = ( const VectorTable& table );
    VectorTable& operator << ( const QStringList& table );
    VectorTable& operator << ( const QVector<double>& table );


private:
    int                            width;
    int                            height;
    QMap<QString,QVector<double>*> table;
    QStringList                    tags;
};

#endif /* VECTORTABLE_H */
```

src/reuseable/vectortable.cpp

```cpp
#include <QDebug>
#include <QList>
#include "vectortable.h"

VectorTable::VectorTable( const QStringList& tags ) :
    width( tags.size() ), height( 0 ), tags( tags )
{
    foreach( QString str, tags )
        this->table[str] = new QVector<double>;
}

VectorTable::VectorTable( const VectorTable& table ) :
    width( table.getWidth() ), height( table.getHeight() ), tags( table.getTags() )
{
    QList<QVector<double>*> tmp = this->table.values();
    this->table.clear();
    foreach( QString str, tags )
        this->table[str] = new QVector<double>( *table.getColumn( str ) );

    qDeleteAll( tmp );
}

VectorTable::VectorTable( const QString& tag, const QVector<double>& col ) :
    width( 1 ), height( col.size() ), tags( tag )
{
    this->table[tag] = new QVector<double>( col );
}

VectorTable::~VectorTable()
{
    qDeleteAll( this->table.values() );
}

int VectorTable::getWidth() const
{
    return this->width;
}

int VectorTable::getHeight() const
{
    return this->height;
}

QVector<double> VectorTable::getRow( int i ) const
{
    if ( i < 0 || i > this->height )
        qFatal( "VectorTable: row does not exist" );

    QVector<double> vec;
    foreach( QString tag, this->tags )
        vec << this->table[tag]->at(i);

    return vec;
}

const QVector<double>* VectorTable::getColumn( const QString& str ) const
{
    if ( ! this->table.contains( str ) )
        qFatal( "VectorTable: table does not contain this column" );

    return this->table[str];
}
```

```cpp
const QVector<double>* VectorTable::getColumn( int i ) const
{
    if ( this->tags.size() <= i )
        qFatal( "VectorTable: table does not contain this column" );

    return this->table[this->tags.at(i)];
}

const QStringList& VectorTable::getTags() const
{
    return this->tags;
}

VectorTable VectorTable::mid( int pos, int length ) const
{
    if ( this->height < pos || this->height < pos + length )
        qFatal( "VectorTable: incorect mid" );

    VectorTable result( this->getTags() );
    for ( int i = pos, j = this->height; i < j; i++ )
    {
        if ( length == 0 )
            break;

        result << this->getRow( i );
        length--;
    }

    return result;
}

void VectorTable::addRow( const QStringList& row )
{
    if ( this->width != row.size() )
        qFatal( "VectorTable: incorect row" );

    foreach( QString str, this->tags )
        *this->table[str] << row.at( this->tags.indexOf( str ) ).toDouble();

    this->height++;
}

void VectorTable::addRow( const QVector<double>& row )
{
    if ( this->width != row.size() )
        qFatal( "VectorTable: incorect row" );

    foreach( QString str, this->tags )
        *this->table[str] << row.at( this->tags.indexOf( str ) );

    this->height++;
}

void VectorTable::addColumn( const QString& tag, const QVector<double>& col )
{
    if ( this->height != 0 && col.size() != this->height )
        qFatal( "VectorTable: incorect column — column's size != height" );

    if ( tag.isNull() || tags.contains( tag ) )
        qFatal( "VectorTable: incorect tag" );

    this->tags << tag;
    this->width++;
    this->table[tag] = new QVector<double>( col );
}

VectorTable& VectorTable::operator = ( const VectorTable& table )
```

```cpp
{
    if ( this != &table )
    {
        this->width  = table.getWidth();
        this->height = table.getHeight();
        this->tags   = table.getTags();
        QList<QVector<double>*> tmp = this->table.values();
        this->table.clear();
        foreach( QString str, tags )
            this->table[str] = new QVector<double>( *table.getColumn( str ) );

        qDeleteAll( tmp );
    }

    return *this;
}

VectorTable& VectorTable::operator << ( const QStringList& row )
{
    this->addRow( row );

    return *this;
}

VectorTable& VectorTable::operator << ( const QVector<double>& row )
{
    this->addRow( row );

    return *this;
}
```

src/reuseable/falgorithms.h

```cpp
#ifndef FALGORITHMS_H
#define FALGORITHMS_H

#include <stdexcept>

namespace fp
{
    template <typename T, class iterator>
    inline bool elem( const T& value, iterator first, iterator last )
    {
        for ( iterator i = first; i != last; i++ )
            if ( *i == value )
                return true;

        return false;
    }

    template <typename T, template <typename> class C>
    inline bool elem( const T& value, const C<T>& list )
    {
        return elem( value, list.begin(), list.end() );
    }

    template <typename T, class iterator>
    inline void uniq( iterator first, iterator last, T& list )
    {
        for ( iterator i = first; i != last; i++ )
            if ( ! elem( *i, first, i ) )
                list << *i;
    }

    template <typename T>
    inline T uniq( const T& list )
```

```cpp
{
    T result;
    uniq( list.begin(), list.end(), result );
    return result;
}

template <typename T, class iterator>
inline void tail( iterator first, iterator last, T& result )
{
    for ( iterator i = first + 1; i != last; i++ )
        result << *i;
}

template <typename T>
inline T tail( const T& list )
{
    T result;
    tail( list.begin(), list.end(), result );

    return result;
}

template <typename T, class iterator>
inline void take( int length, iterator first, iterator last, T& result )
{
    while ( first != last && length > 0 )
    {
        result << *first;
        first++;
        length--;
    }
}

template <typename T>
inline T take( int length, const T& list )
{
    T result;
    take( length, list.begin(), list.end(), result );

    return result;
}

template <class iterator>
inline iterator maximum( iterator first, iterator last )
{
    iterator max = first;
    for ( iterator i = first; i != last; i++ )
        if ( *max < *i )
            max = i;

    return max;
}

template <typename T, template <typename> class C>
inline T maximum( const C<T>& list )
{
    return *maximum( list.begin(), list.end() );
}

template <class iterator>
inline iterator index( iterator first, iterator last, int i )
{
    if ( last - first < i || i < 0 )
        throw std::invalid_argument( "index: bad index" );

    return first + i;
}
```

```cpp
    template <typename T, template <typename> class C>
    inline T index( const C<T>& list, int i )
    {
        if ( list.size() - 1 < i || i < 0 )
            throw std::invalid_argument( "index: bad index" );

        return *(list.begin() + i);
    }

    template <typename T, class iterator, class iterator1>
    inline void rebuild( iterator first, iterator last, iterator1 first1, iterator1
last1, T& value )
    {
        for ( iterator1 i = first1; i != last1; i++ )
            value << *index( first, last, *i );
    }

    template <typename T, template <typename> class C>
    inline T rebuild( const T& list, const C<int>& ilist )
    {
        if ( list.size() < maximum( ilist ) )
            throw std::invalid_argument( "rebuild: bad index" );

        T result;
        rebuild( list.begin(), list.end(), ilist.begin(), ilist.end(), result );
        return result;
    }
}

#endif /* FALGORITHMS_H */
```

Annex II

Other methods

Other methods

1. Scanning electron microscopy (SEM)

The "first" Scanning Electron Microscope (SEM) image was obtained by Max Knoll, in 1935 on a steel material showing electron channeling contrast using a sort of backscattered electron detector (BSE). The "first" SEM was further developed by Professor Sir Charles Oatley and his postgraduate student Gary Stewart and was first marketed in 1965 by the Cambridge Scientific Instrument Company as the "Stereoscan" microscope (**figure 1**).
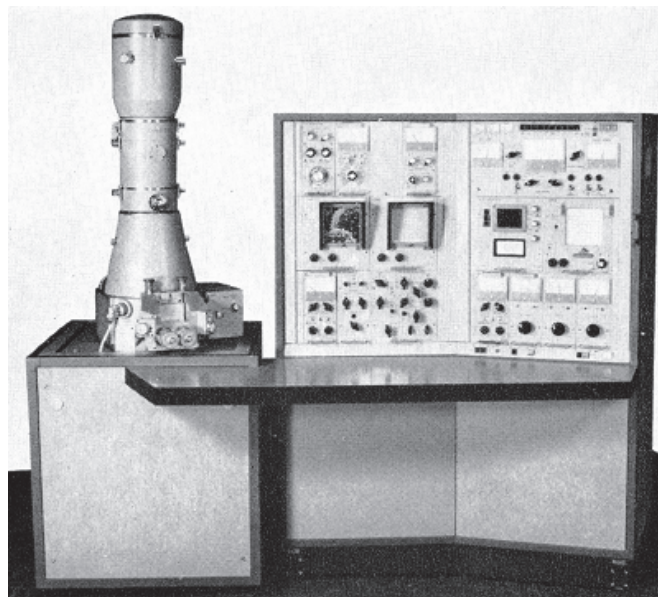

Figure 1. The photo of the old electron microscope, obtained at 1965.

The SEM is a type of electron microscope that images a sample by scanning it with a high-energy beam of electrons usually from about 1 to 30 kV. The electrons interact with the atoms (see figure 2) that make up the sample producing signals that contain information about the sample's surface topography, composition and other properties. The later can be obtained with different sorts of specialized detectors.
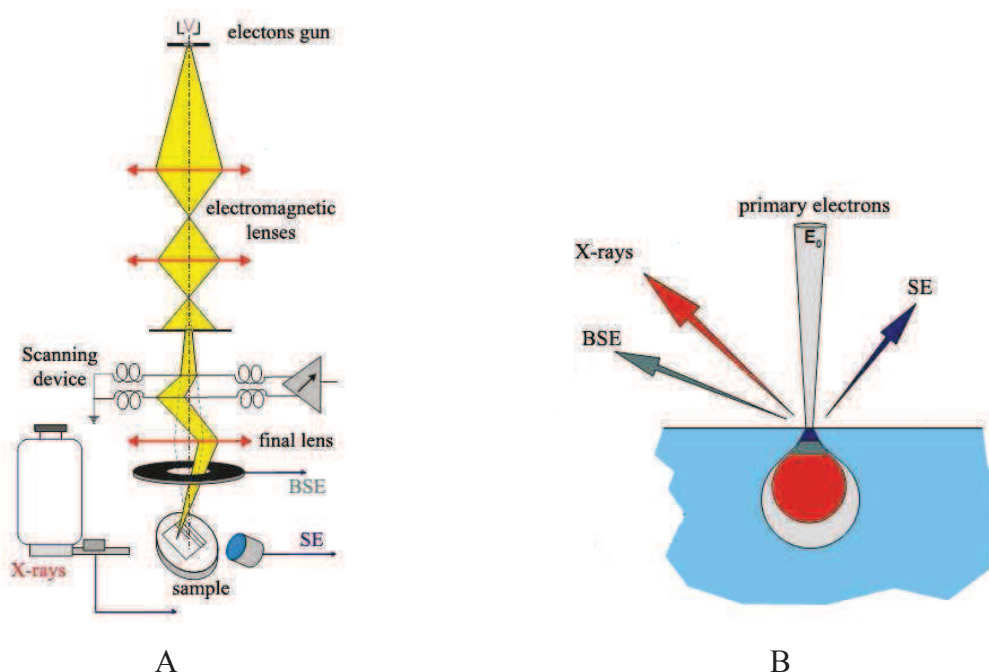
Figure 2. The principle of the SEM column (A) and the interactions between electron and material (B); BSE – backscatteres electrons, SE – secondary electrons.

The main types of signals produced by an SEM include secondary electrons (SE), backscattered electrons (BSE), characteristic X-rays (photons), electrons backscattered diffraction (EBSD), specimen current and transmitted electrons (STEM - scanning transmitted electron microscopy), light (cathodoluminescence) and now many detector types allowing work in a SEM chamber at variable pressure (from 1 to 4000 Pa).

Secondary electron (SE) detectors are common in all SEMs, but it is rare that a single machine would have detectors for all possible signals. The signals result from interactions of the electron beam with atoms at/or near the surface of the sample. In the most common or standard detection mode, secondary electron imaging, the SEM can produce very high-resolution images of a sample surface, revealing details about less than 1 to 5 nm in size. Due to the very narrow electron beam, SEM micrographs have a large depth of field yielding (as compared to light microscopy) a characteristic "three-dimensional" appearance useful for understanding the surface structure of a sample (in the case of an in-chamber SE detector as opposed to an in-lens SE detector). A wide range of magnifications is possible, from about 10 times (about equivalent to that of a powerful hand-lens) to more than 500,000 times, about 250 times the magnification limit of the best light microscopes.

BackScattered Electrons (BSE) are beam electrons that are reflected from the sample by elastic scattering. BSE are often used in analytical SEM along with the spectra made from the characteristic X-rays. Because the intensity of the BSE signal is strongly related to the atomic number (Z) of the specimen, BSE images can provide information about the distribution of different elements in the sample. It is important to note that this type of detector can also give crystallographic information (these detectors can be in-chamber or in-lens).

Characteristic ***X-rays*** are emitted when the electron beam removes an inner shell electron from the sample, causing a higher energy electron to fill the shell and release energy. These characteristic X-rays are used to identify the composition and measure the abundance of elements in the sample. As we have not used the other types of detectors, we will not discuss them further.

The ICMMO FEG-SEM. The scanning electron microscope (SEM) used during our experiments is a Zeiss Supra 55 VP (**figure 3**). It is fitted with a field emission gun (FEG) to allow a very good resolution (a few nanometers depending on samples, experimental conditions, etc) and work at very low voltage (from 0.1 to 30 kV). The instrument is used to characterize the structure at the nanometer-scale in optimal conditions and the composition of materials with the help of the EDS (Energy Dispersive Spectrometer) detector.

Figure 3. The electron-microscope Zeiss Supra 55 VP.

The main characteristics of this FEG-SEM are:

Pressure	2 – 133 Pa, adjustable in steps of 1 Pa
VP Vacuum	1.0 nm if 15 kV 1.7 nm if 1 kV
Emitter	Thermal field emission type
Main detectors	In-lens Detector Secondary Electron Detector VPSE Detector Backscatter Detector EDS Detector EBSD Detector

2. X-ray diffraction

X-ray diffraction (XRD) is a versatile, non-destructive technique that reveals detailed information about the chemical composition and crystallographic structure of natural and manufactured materials. In 1919 A.W.Hull gave a paper titled, "A New Method of Chemical Analysis", where he pointed out that "… every crystalline substance gives a pattern; the same substance always gives the same pattern; and in a mixture of substances each produces its pattern independently of the others". In order to understand better the role of the compounds, from which the samples consist or which form during the corrosion of Al, Al alloys and coated systems, the analysis of products on the surface was performed during this PhD work. Solid matter can be described as:

1. *Amorphous:* The atoms are arranged in a random way similar to the disorder we find in a liquid. Glasses are amorphous materials;
2. *Crystalline:* The atoms are arranged in a regular pattern, and there is as smallest volume element that by repetition in three dimensions describes the crystal. This smallest volume element is called a unit cell.

The X-ray diffraction pattern of a pure substance is, therefore, like a fingerprint of the substance. The powder diffraction method is thus ideally suited for characterization and identification of polycrystalline phases. Today about 50,000 inorganic and 25,000 organic single components, crystalline phases and diffraction patterns have been collected and stored on magnetic or optical media as standards. The main use of powder diffraction is to identify components in a sample by a search/match procedure. Furthermore, the areas under the peak

are related to the amount of each phase present in the sample. About 95% of all solids can be described as crystalline.

How does X-ray diffraction work? When an X-ray beam hits an atom, the electrons around the atom start to oscillate with the same frequency as the incoming beam. In almost all directions we will have emission, resulting in no energy leaving the solid sample. However the atoms in a crystal are arranged in a regular pattern, and in a very few directions we will have constructive interference. The waves will be in phase and there will be well defined X-ray beams leaving the sample at various directions. Hence, a diffracted beam may be described as a beam composed of a large number of scattered rays mutually reinforcing one another. In 1913 English physicists Sir W.H. Bragg and his son Sir W.L. Bragg developed a relationship to explain why the cleavage faces of crystals appear to reflect X-ray beams at certain angles of incidence (theta, Θ), **figure 5**.
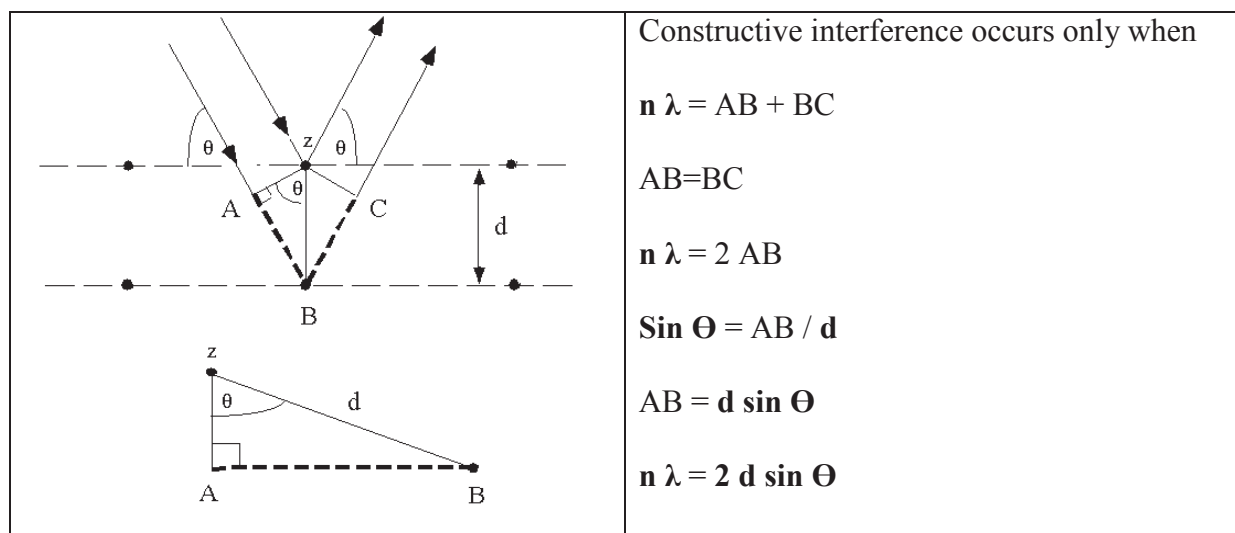

	Constructive interference occurs only when
	$n\,\lambda = AB + BC$
	$AB = BC$
	$n\,\lambda = 2\,AB$
	$\sin\Theta = AB / d$
	$AB = d\,\sin\Theta$
	$n\,\lambda = 2\,d\,\sin\Theta$

Figure 5. The principal schema of XRD technique

The variable **d** is the distance between atomic layers in a crystal, and the variable lambda λ is the wavelength of the incident X-ray beam; n is an integer number.

This observation is an example of X-ray wave interference, commonly known as X-ray diffraction (XRD), and was direct evidence for the periodic atomic structure of crystals postulated for several centuries.

XRD difractometer at l'ENSCP. The PANalytical diffractometer operating at 45 kV and 40 mA equipped with an incident beam Ge (111) monochromator and a linear PixCell detector (active length 14 mm was used during this work to determine the crystalline phases by X-ray diffraction (XRD) using Cu Kα radiation line ($\lambda = 1.5406$ Å).

The XRD spectra were collected with an angular resolution of 0.02° and a scanning rate of 0.3 s per point. The phase identification was carried out by referencing the X'Pert HighScore software using PCPDFWIN version 2.02 containing the JCPDS (ICDD) database files.

3. Titration experiment

Titration is a common laboratory method of quantitative chemical analysis that is used to determine the unknown concentration of an identified *analyte* or the stoichiometry of the reaction if the concentration of both components is known. Because volume measurements play a key role in titration, it is also known as volumetric analysis. A reagent, called the *titrant* is prepared as a standard solution. A known concentration and volume of titrant reacts with a solution of analyte to determine concentration by the equation (1).

$$C_a = \frac{C_t V_t M}{V_a}$$

[1]

where C_a is the concentration of the analyte [/ mol/l]; C_t is the concentration of the titrant [/ mol/l]; V_t is the volume of the titrant used [/ l]; M is the mole ratio of the analyte and reactant from the balanced chemical equation; and V_a is the volume of the analyte used [/ l].

Titration in l'ENSCP was performed using a Titrando 808 automatic titration system (Methohm) with the Tiamo software in jacketed glass cell with constant stirring (Grade 4 in the software). The initial solution volume for the slow titration experiment was 30 ml. The titrations were done by 1 M NaOH prepared from the Titrisol® Merck KGaA (Germany) standard in 1000 ml ultra-pure water (Millipore, Synergy UV) at 23°C. Added volume for slow titration experiment was 10 µl of NaOH every 1800 s; for rapid titration: 40 µl every 100 s. The reference electrode was Ag/AgCl (3M KCl, 207 mV vs SHE) from VWR.

The aim of this work is the reactivity of Al that is why the titration of Al^{3+} was the typical experiment (**figure 6**).
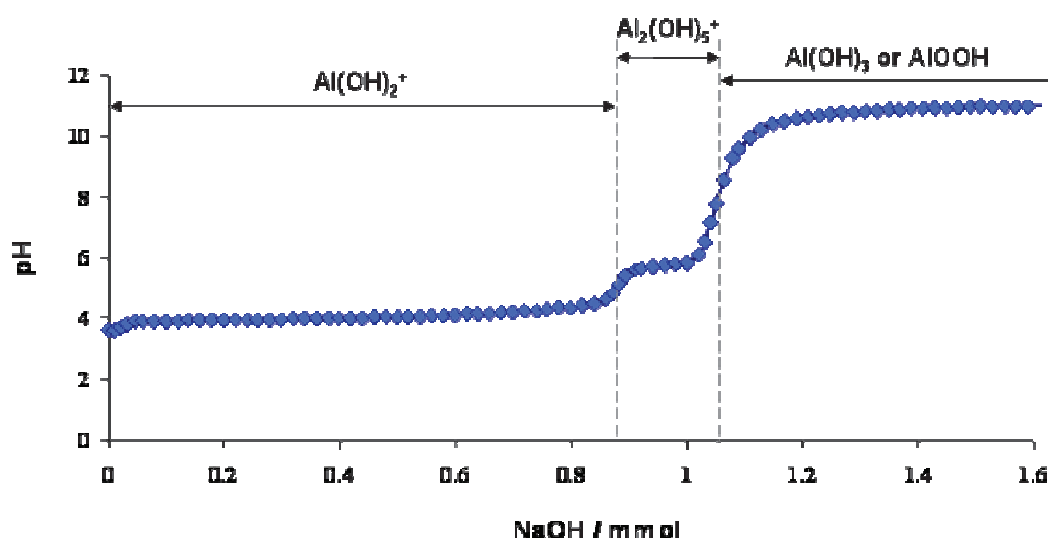
Figure 6. The definition of the stoichiometry of Al reaction with hydroxide during titration experiment of 0.4 mmol of Al^{3+} by NaOH.

The two steps in the experimental titration curve for 0.4 mmol Al^{3+} t correspond to two plateaus with a midrange pH of 4.06 and 5.67. The third dissociation is not observed as the upper pH limit obtainable in this experiment (pH ≈ 11) is insufficient. The reactions, associated with titration endpoints, are following:

$$Al^{3+} + 2OH^- \leftrightarrow Al(OH)_2^+ \qquad\qquad (pH\ 4.1) \qquad\qquad [2]$$
$$2Al(OH)_2^+ + OH^- \leftrightarrow 2Al_2(OH)_5^+ \qquad (pH\ 5.7) \qquad\qquad [3]$$

The application of the titration method and obtained results will be shown in the **chapter 6**.

4. Contact angle measurement

The measurement of contact angle reflects the ability of a liquid to spread on a surface. The method consists in measuring of the angle of the drop profile deposited on the substrate and corresponds to the free surface energy of the system. It also allows to distinguish the nature of polar or non-polar interactions at liquid-solid interface, showing the hydrophilic or hydrophobic surfaces.

The contact angle is defined as the angle made by the intersection of the liquid/solid interface and the liquid/air interface. It can be alternately described as the angle between solid sample's surface and the tangent of the droplet' solvate shape at the edge of the droplet. A high contact angle indicates a low solid surface energy or chemical affinity. This is also referred to as a low degree of wetting. A low contact angle indicates a high solid surface energy or chemical

affinity, and a high or sometimes complete degree of wetting. For example, a contact angle of zero degrees will occur when the droplet has turned into a flat puddle; this is called complete wetting.

The theoretical description of the method can be done in the assumption of a thermodynamic equilibrium between the three phases: the liquid phase of the droplet (L), the solid phase of the substrate (S), and the gas/vapor phase of the ambient (G) (which will be a mixture of ambient atmosphere and an equilibrium concentration of the liquid vapor, **figure 7**). The gaseous phase could also be another (immiscible) liquid phase. At equilibrium, the chemical potential in the three phases should be equal. It is convenient to frame the discussion in terms of the interfacial energies. We denote the solid–vapor interfacial energy (see surface energy) as γ_{SG}, the solid–liquid interfacial energy as γ_{SL} and the liquid–vapor energy (i.e. the surface tension) as simply γ, we can write an equation that must be satisfied in equilibrium (known as the Young Equation):

$$0 = \gamma_{SG} - \gamma_{SL} - \gamma \cos\Theta_C$$

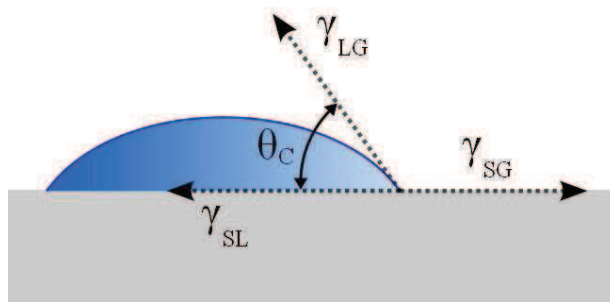where Θ_C is the equilibrium contact angle.

Figure 7. A contact angle of a liquid sample.

The Young equation assumes a perfectly flat surface, but in many cases surface roughness and impurities cause a deviation in the equilibrium contact angle from the contact angle predicted by Young's equation.

The simplest way of measuring the contact angle is with a goniometer, which allows the user to measure the contact angle visually. The droplet is deposited by a syringe pointed vertically down onto the sample surface, and a high resolution camera captures the image, which can then be analyzed either by eye (with a protractor) or using image analysis software.

5. Conductivity measurement

Electrochemical impedance spectroscopy (EIS) (sometimes also called AC impedance) is an electrochemical technique that surfaced in the late 1960's but did not become extensively studied until the late 1970's and early 1980's when computer controlled laboratory equipment became the norm. The reason is that the technique is most easily controlled with a laboratory computer. While many of the idiosyncrasies of the technique are now reasonably understood, the ability to use the technique to model all corrosion systems remains elusive.

The technique itself is conceptually rather simple. Low amplitude alternating potential (or current) wave is imposed on top of a DC potential (often the corrosion potential with zero imposed current). The frequency is varied from as high as 105 Hertz to as low as about 10-3 Hertz in one experiment in a set number (often between 5 and 10) steps per decade of frequency. Varying frequency from low to high frequency is also possible. The corrosion process usually forces the measured current to be out of phase (denoted by the phase angle) with the input voltage. Dividing the input voltage by the output current furnishes the impedance. The variation in impedance (magnitude and phase angle) is used for the interpretation. This technique is in essence built on the DC polarization resistance technique in which a direct current voltage (or current) ramp is imposed. The out-of-phase relationship between the input voltage and output current is analyzed by the frequency response analyzer.

The technique has found practical application in such areas as:

- estimating corrosion rates especially low corrosion rates
- examining corrosion inhibitor functionality
- examining coatings on metal surfaces

This technique has been used in a number of areas beyond corrosion including battery research.

Most corrosion practitioners have attempted to analyze impedance spectra using combinations of analogous circuit elements. The reasoning used to justify this approach might be summarized as follows:

- Corrosion of alloys and related conductive materials is an electrochemical degradation process governed by kinetics and thermodynamics.
- This chemistry is often difficult to interpret in real-life complex and often poorly characterized systems normally encountered.
- Analogous circuit elements enable the corrosion practitioner to bridge gaps in knowledge.

- Such bridging enables use of electrochemical impedance spectroscopy to estimate corrosion rates and corrosion mechanisms in poorly characterized systems.

The specific circuit elements often used are the capacitor, resistor, and inductor. One point that cannot be emphasized enough is that corrosion is an electrochemical process involving molecules and ions. The analogous circuit components provide a way of modeling and discussing the corrosion process. They are not components of the corrosion process itself. An example of a simple circuit that can model a very passive alloy (e.g. titanium in water) is a parallel combination of a resistor and capacitor in series with a resistor.

The resistivity measurements in this work were performed in a 2 electrodes configuration (2 points), in the frequency range $2 \cdot 10^3$ to $2 \cdot 10^{-1}$ Hz, with a VMP3 (BioLogic) frequency response analyzer. The average value of resistivity was used and analyzed.

The control of Al reactivity for high temperature anticorrosion paint formulation

The aim of this work is to understand Al reactivity at a fundamental level and to use this knowledge for the development of Cr(VI)-free sacrificial paints for high temperature aeronautic applications.

Pure Al, Al intermetallics and alloys are studied. The *atomic emission spectroelectrochemistry* is used to isolate the individual phenomena during paint degradation. A linear relationship between cathodic current and Al dissolution is shown and interpreted with a simple model where OH^- generation, $Al(OH)_3$ formation/dissolution and $Al(OH)_4^-$ diffusion are kinetically coupled. For early formulations significant binder dissolution is measured under cathodic polarization, while Al reactivity is suppressed. Similar Al behavior is observed for Al-Mg intermetallics. In terms of the cathodically generated hydroxide mechanism these results are interpreted as the reaction of either Si or Mg with OH^-. These results confirm the cathodic Al reactivity model. The loss of anodic activity is explained by the loss of electrical contact at the metal/oxide/polymer/substrate interfaces and the oxide layer modifications are studied to circumvent this problem. It is found that Mg^{2+} ions retard Al passivation and improve conductivity due to the formation of semiconducting spinel.

Finally, two major factors are found to be critical for the Al reactivity control: solution pH and oxide properties. Using additives to control them, the new coating formulation stable up to 550°C and protective more than 1000H in salt spray test is developed.

Le contrôle de réactivité d'aluminium en peinture anticorrosion résistant à la haute température

L'objectif de ce travail est de comprendre le mécanisme fondamentales de la réactivité d'Al et d'utiliser ces connaissances pour développer une peinture sacrificielle sans Cr(VI).

L'Al pur, ses alliages et intermétalliques sont étudiés. La *spectroélectrochimie atomique à émission de plasma* est utilisée pour isoler les phénomènes individuels au cours de la dégradation. La relation linéaire entre le courent cathodique et la vitesse de dissolution d'Al est démontrée et interprétée par un modèle dans lequel OH^- génération, $Al(OH)_3$ formation/dissolution et $Al(OH)_4^-$ diffusion sont cinétiquement couplées. La dissolution significative du liant de première formulation a été accompagnée de la passivation d'Al pendant la polarisation cathodique. Un comportement similaire est observé pour des intermétalliques Al-Mg. Ceci est interprété comme la réaction des composants (du Mg ou du Si) avec OH^-. Ces résultats confirment le modèle de réactivité cathodique d'Al. La perte d'activité anodique est expliquée par la perte de contact électrique au niveau des interfaces métal/oxyde/polymère/substrat. Les façons de modification de la couche d'oxyde sont étudiées. Les ions de Mg^{2+} retardent de la passivation d'Al par la formation de spinelle semi-conductrice qui est responsable de l'amélioration de la conductivité.

Finalement, deux facteurs principaux sont jugés essentiels pour la réactivité d'Al: pH de la solution et la conductivité de l'oxyde. Utilisant des additifs pour contrôler ces facteurs, la formulation de nouvelle peinture est proposée, qui est stable jusqu'à 550°C et sacrificielle plus de 1000 H en brouillard salin test.